creative commons

COMMONS DEED

저작자표시-비영리-변경금지 2.0 대한민국

이용자는 아래의 조건을 따르는 경우에 한하여 자유롭게

- 이 저작물을 복제, 배포, 전송, 전시, 공연 및 방송할 수 있습니다.

다음과 같은 조건을 따라야 합니다:

저작자표시. 귀하는 원저작자를 표시하여야 합니다.

비영리. 귀하는 이 저작물을 영리 목적으로 이용할 수 없습니다.

변경금지. 귀하는 이 저작물을 개작, 변형 또는 가공할 수 없습니다.

- 귀하는, 이 저작물의 재이용이나 배포의 경우, 이 저작물에 적용된 이용허락조건을 명확하게 나타내어야 합니다.
- 저작권자로부터 별도의 허가를 받으면 이러한 조건들은 적용되지 않습니다.

저작권법에 따른 이용자의 권리는 위의 내용에 의하여 영향을 받지 않습니다.

이것은 이용허락규약(Legal Code)을 이해하기 쉽게 요약한 것입니다.

Disclaimer

dCollection

Doctoral Thesis

Development of Optical Devices for Digital Medicine

Jung Kweon Bae

Department of Biomedical Engineering

Graduate School of UNIST

2020

Development of Optical Devices for Digital Medicine

Jung Kweon Bae

Department of Biomedical Engineering

Graduate School of UNIST

ULSAN NATIONAL INSTITUTE OF SCIENCE AND TECHNOLOGY

Development of Optical Devices for Digital Medicine

A thesis/dissertation
submitted to the Graduate School of UNIST
in partial fulfillment of the
requirements for the degree of
Doctor of Philosophy

Jung Kweon Bae

12.09.2019

Approved by

Advisor

Woonggyu Jung

ULSAN NATIONAL INSTITUTE OF SCIENCE AND TECHNOLOGY

Development of Optical Devices for Digital Medicine

Jung Kweon Bae

This certifies that the thesis/dissertation of Jung Kweon Bae is approved.

12.09.2019

signature

Advisor: Woonggyu Jung

signature

Hyun-Wook Kang

signature

Jung-Hoon Park

signature

Seungah Lee

signature

Hoyoung Yun

ULSAN NATIONAL INSTITUTE OF SCIENCE AND TECHNOLOGY

Abstract

Advances of technology have made a revolution that interconnects industrial devices and fuses the boundaries of digital, physical and biological spaces. These technologies such as cloud computing, 3D printing technology, big data, internet of things (IOT), artificial intelligence (AI), and maturity of system integrations have been improved every year, changing our daily life quickly in intelligent and convenient ways. In this days, these explosions of technology, changing the way we live and think, is referred to 4th industrial revolution. As we know, every industry is affected by the new waves of technologies, digitalization and connectivity, and the biomedical or medical field is no exception. Healthcare fields have benefited mostly from recent technical improvements, revolutionizing the medical systems in many terms in cost-effective ways. Particularly, "digital medicine" has been recently came into the limelight as one of the uprising fields. In digital medicine, traditional medical devices and diagnostic programs have become miniaturized, digitalized, and automated. As taking advantages of digital medicine, specific fields related to digital pathology, point-of-care (POC) diagnostics, and application of deep learning or machine learning technologies have shown the great potentials not only in biomedical academia but also in the revenues of their markets. It allows to connect devices, hospital equipment, and to accelerate efficiencies in health service such as diagnosis, and to reduce the cost of services. Moreover, interconnection between advanced technologies has been improved the access of healthcare to the places where hospital or medical services are limited. Furthermore, artificial intelligence has shown promising results related to disease screening especially using medical images.

Although fields in digital medicine are prospering, still there are limitations that needs to be overcome in order to provide further advanced health services to patients in the various situations. In digital pathology, improvements of microscopic technologies, internets, and storage capabilities have reduced the time-consuming processes. The simple transformation of microscopic image to digital have successfully alternated many limitations in the analogue histopathology workflow to efficient and cost saving ways. However, tissue staining is currently referred as one of the bottleneck that makes workflow still lengthy, labor-intensive, and costly. In the POC diagnostic fields, various digitalized portable smartphone-based diagnostic devices have been introduced as alternatives to conventional medical services. These devices have provided the quality assurance of diagnostics by taking advantages of sharing, and quantitative analysis of digital information. However, most of these works have been focused on replacing diagnostic process which mostly done in laboratory settings. As medical imaging devices and trained clinicians or practitioners are limited, there are also high demands on clinical imaging-based diagnostics in developing countries.

In this thesis, computational microscope using patterned NIR illumination was developed for label-free quantitative differential phase tissue imaging to bypass the staining process of the pathology workflow. This system overcame the limitations found in the conventional quantitative differential

ULSAN NATIONAL INSTITUTE OF SCIENCE AND TECHNOLOGY

phase contrast in a LED array microscope, allowing to captured light scattering and absorbing specimen while maintaining weak object approximation. Moreover, portable endoscope system was developed integrating the additive production technologies (3D printing), ICT, and optics for POC diagnostics. This innovative POC endoscope demonstrated comparable imaging capability to that of commercialized clinical endoscope system. Furthermore, deep learning and machine learning models have been trained and applied to each devices, respectively. Generative adversarial network (GAN) was applied to our NIR-based QPI system to virtually stain the label-free QPI which look comparable to image that is captured from bright field microscope using labeled tissue. Lastly, POC automated cervical cancer screening system was developed utilizing smartphone-based endoscope system as well as training the machine learning algorithm. 3-5% of acetic acid was applied to the suspicious lesion and its reaction was captured before and after application using smartphone endoscope. This screening system enables to extract the features of cancers and informs the possibility of cancer from endoscopic images.

ULSAN NATIONAL INSTITUTE OF
SCIENCE AND TECHNOLOGY

ULSAN NATIONAL INSTITUTE OF SCIENCE AND TECHNOLOGY

Table of Contents

Abstract ..... **i**

Table of Contents ..... **iv**

List of Figures ..... **vii**

List of Tables ..... **xii**

Chapter 1. Introduction **1**

1.1 Digital medicine 1

1.2 Digital pathology 2

1.3 Portable medical devices for point-of-care diagnostics 4

1.4 Artificial intelligence in biomedical fields 6

1.5 Research motivation & approaches 10

Chapter 2. Development of computational microscope for label-free digital imaging **14**

2.1 Development of RGB matrix based multi-contrast microscope 14

2.1.1 Introduction 14

2.1.2 Single-shot BF, DF, DPC image reconstruction 15

2.1.3 Weak object transfer function (WOTF) 16

2.1.4 Quantitative phase reconstruction from DPC 18

2.1.5 System configuration 20

2.1.6 Effect of illumination patterns 21

2.1.7 Result & Discussion 22

2.1.8. Conclusion 27

2.2 Development of QPI system using diffuser based NIR illumination 28

2.2.1 Introduction 28

2.2.2 System configuration 29

2.2.3 Gradient source calculation 30

2.2.4 Partially coherent NIR-Illumination based on diffuser implementation 31

2.2.5 Comparison of different diffuser-based illumination patterns on phase transfer function and DPC images 34

2.2.6 Result & Discussion 39

2.2.7 Conclusion 47

Chapter 3. Development of mobile medical device for point-of-care digital medicine **48**

3.1 Smartphone-based endoscope for advanced point-of-care diagnostics 48

ULSAN NATIONAL INSTITUTE OF SCIENCE AND TECHNOLOGY

3.1.1 Introduction 48
3.1.2 Endoscope system using smartphone 48
3.1.3 Designing for lens system 51
3.1.4 User interface software development 53
3.1.5 In-vivo imaging protocol at otolaryngology 53
3.1.6 Result & Discussion 55
3.1.7 Conclusion 60
Chapter 4. Application of artificial intelligence in digital medicine 61
4.1 Machine Learning Technology 62
4.1.1 K-nearest neighbor 62
4.1.2 Supportive vector machine 63
4.1.3 Decision tree 65
4.1.4 Deep Learning 66
4.2 In-silico tissue staining using NIR-based computational phase microscopy and deep learning technique 69
4.2.1 Introduction 69
4.2.2 Quantitative phase imaging 71
4.2.3 Sample preparation and imaging 73
4.2.4 Data processing methods 74
4.2.5 GAN architecture and training 75
4.2.6 Implementation details 78
4.2.7 Results & Discussion 79
4.2.8 Conclusion 89
4.3 Quantitative Screening of Cervical Cancers for Low-resource Settings: Pilot Study of Smartphone-based Endoscopic VIA using Machine Learning Technique 90
4.3.1 Introduction 90
4.3.2 Smartphone-based endoscope system 91
4.3.3 Image acquisition from clinic 92
4.3.4 Pre-image processing 94
4.3.5 Feature analysis and selection 96
4.3.6 Classification training and validation 97
4.3.7 Result & Discussion 98

ULSAN NATIONAL INSTITUTE OF SCIENCE AND TECHNOLOGY

4.3.8 Conclusion 105

Chapter 5. General conclusion and future perspectives 106

5.1 General conclusion of thesis 106

5.2 Future perspectives 107

References 113

ULSAN NATIONAL INSTITUTE OF SCIENCE AND TECHNOLOGY

List of Figures

Figure 1.1 Brief illustration of industrial revolutions [2] 2
Figure 1.2 Digital pathology imaging process 3
Figure 1.3 Comparison of traditional and digital pathology workflow 3
Figure 1.4 Recent POC microscope devices. a-b) Smartphone based microscope system adapting optical components before camera. c) Lens-free stand-alone microscope systems d) Lens-free smartphone-based microscope. 4
Figure 1.5 Smartphone based POC devices in bioanalytical sciences. a) POC fluorescence- and magnetophoresis-based cytometry b) Device for colorimetric assay. c) Smartphone-imaged microfluidic biochip for measuring CD64 expression from whole blood. d) Smartphone based fluorescence device and optofluidic fluorescent imaging cytometer. 5
Figure 1.6. The number of papers published from 2012 to 2017 in bio-medical image analysis community with deep learning approach applications. Figure adapted from ref. [9]..... 6
Figure 1. 7 Example of computer assisted diagnosis application using deep learning. The developed module detecting specious region in whole histopathogy slice image and grading the level of patient. Figure adapted from reference [26] 7
Figure 1. 8 Example of the cell segmentation using deep convolution neural network architecture. The U-net in reference [27] detect the boundary of cell in the image and segment. Figure adapted from ref. [27] 8
Figure 1. 9 Conceptual description of learning process in the generative adversarial networks. Through the training process distribution of generated data converges to real data distribution by adversarial learning process. Figure modified from ref. [32] 8
Figure 1. 10 Super-resolution of the florescence microscope image using deep learning architecture which consist of CNN based on GAN and virtual staining of label-free image. Figure adapted from ref. [16, 33] 9
Figure 1.11 Motivation points of thesis related to digital medicine. a) Limitations in current histopathology workflow. Staining procedure still takes long time and requires delicate laborious steps. b) Limitations in conventional medical device as POC. Many demands of imaging-based diagnosis are existing in low-resource setting. But these conventional devices are not appropriate. c) Advances of artificial intelligence are offering promising outcome that benefits the healthcare in many ways. This technologies could be applied to the fields in a-b), making devices intelligence and autonomous. 10

Figure 2.1 Multi-contrast microscope using RGB color patterns in LED matrix. From single shot mixed color image, each colors representing different contrast images. With simple computations, DPC and BF could be realized. 15
Figure 2.2 Summarization of quantitative phase reconstruction. 19
Figure 2.3 System configuration of single-shot multi-contrast microscopy. 20
Figure 2.4 Relationship between illumination and phases in freqeuncy spectrum. Point source located near (a) NA of object, (b) NA/2 of object, and (c) center. PTF is difference of convolution and corss-correlation between illumination source and pupil function. 21
Figure 2.5 Effects of spatial coherence parameter **σ** to the imaging system. Larger coherence parameter provide stabilized phase contrast as well as qunatitative phase estimation. 23
Figure 2.6 Phase measurement accuracy using single-shot multi-contrast illumination pattern. DF is provided to compare the structural deformations or missings from QPI. Phase delay is measured from distribution of line crossing the center of micorsphere. 24
Figure 2.7 Result of noise reduction in QPI using live fibroblast cells. 25
Figure 2.8 Result of multi-contrat microscope uisng cheek cells. BF, DF, QPC, and QPI was reconstructed with single microscope setup. 10x/0.25 NA objective was utilized for this imaging. ... 26
Figure 2.9 Result of multi-contrat microscope uisng c.elegans. 40x/0.55 NA objective was utilized for this imaging. 27
Figure 2.10. System schematic of quantitative phase imaging system diffuser based gradient NIR

ULSAN NATIONAL INSTITUTE OF SCIENCE AND TECHNOLOGY

illumination. Asymmetric patterns were generated from the physical filter with single NIR ($\boldsymbol{\lambda c}$=780 nm) illumination source. Diffuser is placed before sample to create scatterings that act similar to partial coherent light source. Patterned filter was developed by printing 3D models that intentionally designed in prior. For this system, customized infinity-corrected invert type of microscope was developed. L1: collimator lens; F; 3D printed filter; D: diffusers; S: sample; Obj: objective; L2; tube lens. 30
Figure 2.11 Schematic of diffuser based NIR illumination. Filtered light from point LED source passes the diffuser and randomly scatters with gradient effect due to near Lambertian (more similar to elliptical shape). Captured background image and its 3D surface plot clearly shows gradient amplitude, where white arrows denote gradient directions. 31
Figure 2.12 Illustration of Haralcik's texture feature calculation. From gray level image, pixel combinations were counted only considering the neighbor pixels on the right and marked in GLCM matrix. After marking all the combinations in GLCM from grayscale image, each element is divided by sum of all elements in GLCM to create the probability of combinations in matrix form (normalized GLCM). Using GLCM, texture features can be calculated. 32
Figure 2.13 Background comparison using different illuminations. All images were cropped at corresponding position in 760 x 760 pixels from original 2048 x 2048 images. Background was captured using partially coherent (a) blue LED, (b) green LED, (c) red LED, (d) single NIR LED with diffuser employed, and (e) NIR LED without any diffuser attached (low coherence parameter). 33
Figure 2.14 Surface plot under different illuminations and quantitative measurement of the background. 3D surface plot of computed from backgrounds from Fig. 2.4. Partially coherent (a) blue LED, (b) green LED, (c) red LED, (d) single NIR LED with diffuser employed, and (e) NIR LED without diffuser was visualized intuitively showing the noises. (f) Graph illustrates the Haralick's texture features which was calculated form (a-d). 34
Figure 2.15 Illustration of illumination apparatus with beam path and measurements from illumination patterns. (a) Image describing the scattering characteristics of employed diffuser in terms of intensity and angle. (b) Intensity measurements of diffuser surface for each illumination pattern. 35
Figure 2.16 Comparison of different illumination patterns on phase transfer function (PTF) model and intensity sum of every PTF axis. Four patterns (Half, Gradient amplitude, Gradient annulus, sectors) were designed and two different superimposing methods (2-axis or 3-axis) were simulated..... 37
Figure 2.17 Deviations between illumination patterns in frequency spectrum. 38
Figure 2.18 Quantitative phase measurement of each illumination pattern on the variations of target thickness. 39
Figure 2.19 Quantitative phase images of star targets (unable to visualize with BF) for characterizing the performance of each illumination patterns. 40
Figure 2.20 Comparison of QPI performance quantitatively 41
Figure 2.21 Representative QPI of cervix epitheial cells acquired by half and annulus pattern 42
Figure 2.22 Analysis of QPI frequency response depending on implementation of diffusers. 42
Figure 2.23 Analysis of the performance of QPI according to distance between sample and diffuser (or $\sigma\ coherence$). 43
Figure 2.24 Comparison of QPI by wavelength capturing chromatic stained cervical cells. Images were taken using all red/gree/blue, blue, green, red, and NIR illuminations with half asymmetric cirlce pattern. Performance was analuzed from DPC and FFT of DPC images. 45
Figure 2.25 Demonstration of QPI using diffuser-bsaed illumination for CIN2+ sample. Images were capured by NIR and visible illuminations to compare the reuslt. Yellow arrow denotes suspicious abnormal cells. 45
Figure 2.26 Demonstration of H&E stained mouse brain tissue using NIR-QPI system. (a-b) Magnified images for NIR QPI, NIR BF and color BF image comparison. 46

Figure 3.1 Smartphone-based endoscope system setup. Smartphone-based endoscope system setup. (a) Schematic of smartphone-based endoscope system. A photography of (b) rigid type endoscopic system, (c) flexible type endoscopic system, (d) android based HMD, and (e) the smartphone-based endoscope system vs clinical endoscope system. 50
Figure 3.2 Beam path of smartphone-based endoscope system. Schematic of assembled lens system in

ULSAN NATIONAL INSTITUTE OF SCIENCE AND TECHNOLOGY

smartphone-based endoscope system. 50
Figure 3.3 Image simulation and distortion analysis according to designed lens system with different combinations. 51
Figure 3.4 Simulation of lens system. Achromatic lens (L1) having f=40 mm, Ø25.4 mm and aspherized achromatic lens (L2) having f=14 mm, Ø12.7 mm were utilized. Smartphone lens (SM) was simulated to deliver the image to complementary metal-oxide semiconductor sensor. Spot diagram, field curvature, distortion, and details of SM are presented. 52
Figure 3.5 Evaluation of the lens system by comparing the magnification results from simulation and real endoscopic image. 53
Figure 3.6 Android based software for the smartphone-based endoscope system. (a) Main capturing screen, (b) Gallery mode of the software 54
Figure 3.7 Result of the smartphone-based endoscope evaluation. At 20 mm away from the target, the USAF resolution was captured with (a) smartphone-based endoscope without lens, (b) with customized lens, and (c) commercial endoscope system. (d) At the corresponding distance, field-of-view was measured by capturing the ruler with (d) smartphone-based endoscope without lens, (e) with customized lens, and (f) commercial endoscope system. (g) Graph of the measured resolution and (h) field-of-view according to the working distance. 55
Figure 3.8 Result of human in-vivo imaging at Otolaryngology. Otoscope, sinuscope, and flexible endoscope were utilized. The corresponding sites were captured with smartphone-based endoscope and commercial endoscope system in clinical settings. (a, b) normal tympanic membrane. (c, d) postoperative state of tympanomastoiedectomy. (e, f) chronic otitis media, central large perforation. (g, h) normal middle turbinate. (i, j) chronic rhinosinusitis with nasal polyp. (k,l) normal nasal vestibule. (m,n) normal vocal cord. (o,p) normal larynx. (q,r) postoperative state of thyroid cancer surgery in larynx. 57

Figure 4. 1 Explanation of KNN 62
Figure 4. 2 Explanation of SVM 63
Figure 4. 3 SVM hyperplane analysis according to cost parameter. 64
Figure 4. 4 Explanation of kernel function in SVM 65
Figure 4. 5 Illustration of neural network architecture 67
Figure 4. 6 General convolution neural network architecture 67
Figure 4. 7 Result of CNN models in the image classification challenge. 68
Figure 4. 8 In-silico tissue staining flow work. (a) Compare to histology assay procedure, label-free histology procedure with deep learning model allows to bypass the conventional histology staining process. (b) Our innovative method simply captures only stained tissue section for both brightfield and QPI. This allows to train deep learning model without taking bright field image of tissue after staining procedure and without applying complicated image registration process. 70
Figure 4. 9 Quantitative phase imaging using NIR LED array. (a) Optical configuration for the direct in-silico histology staining. Near-infrared (NIR)-/White-LED array is installed on the conventional inverted microscope setup. (b) Incoherent light emission of 850nm wavelength is from NIR-LED array (red line) and no hematoxylin/eosin absorption is shown. (c) QPI is carried out by illuminating NIR in four patterns, i.e. P1 to P4 in NIR-LED array patterns, which forms four transfer functions accordingly. Four patterned illuminated images are processed to create a quantitative phase image. (d) Brightfield image with NIR, QPI with NIR, and brightfield image with white LED illumination at a hematoxylin and eosin (H&E) stained kidney section. Scale bar: 100 μm or 50 μm for inset images. 71
Figure 4. 10 Illustration of registration methods for analysis of effects on phase deviations between stained and unstained tissues according to illumination wavelength variations 75
Figure 4. 11 Architecture of in-silico staining algorithm using GAN structure. In-silico staining is carried out using four deep neural networks (DNNs), i.e. (a) generator network, (b) discriminator network, (c) feature extraction network. (a) The generator network performs in-silico staining from input image (NIR-QPI). (b) The discriminator network evaluates the difference of the stained image (White-BF) and the generated image. (c) Image features are extracted using ImageNet pre-trained VGG19 network in (c). The outcome of (b) and (c) are used to train (a) in adversarial manner. (d)

ULSAN NATIONAL INSTITUTE OF SCIENCE AND TECHNOLOGY

Generative adversarial network (GAN) losses over training. Two models were trained, i.e. In-silico BF to in-silico staining of NIR-brightfield image (NIR-BF), or In-silico QPI to in-silico staining of NIR-QPI image. 77
Figure 4. 12 Analysis of DPC driven QPI of mouse kidney tissue before and after H&E staining 80
Figure 4. 13 Phase variation measurements on various illumination wavelength and tissue thickness using mouse kidney tissue before and after staining 80
Figure 4. 14 Scattering coefficient on various illumination wavelength and tissue thickness using mouse kidney tissue before and after staining 81
Figure 4. 15 In-silico staining of mouse kidney tissue using GAN frameworks..... 82
Figure 4. 16 In-silico staining of mouse brain tissue using GAN frameworks 83
Figure 4. 17 In-silico staining from NIR-BF image NIR-BF or NIR-QPI image for a kidney section. (a, b) Images of NIR-BF or NIR-QPI followed by in-silico stained image of each (In-silico BF or In-silico QPI, subsequently) with a correspond stained kidney section image (White-BF). Yellow boxed regions are shown in (b). (c, d) Intensity profile along yellow dotted line in (b) are shown and the correlation coefficient between In-silico stained images (In-silico BF or In-silico QPI) and the stained section image (white-BF). (e) Quantitative analysis of image similarity between In-silico stained images (In-silico BF or In-silico QPI) and the stained section image (white-BF) by mean square error (MSE), peak signal to noise ratio (pSNR), structure similarity (SSIM), or mean opinion score (MOS) from six histopathologists. Scale bar: 100 μm. 85
Figure 4. 18 In-silico staining from NIR-BF image NIR-BF or NIR-QPI image for a brain section. (a, b) Images of NIR-BF or NIR-QPI followed by in-silico stained image of each (In-silico BF or In-silico QPI, subsequently) with a correspond stained brain section image (White-BF). Yellow boxed regions are shown in (b). (c, d) Intensity profile along yellow dotted line in (b) are shown and the correlation coefficient between In-silico stained images (In-silico BF or In-silico QPI) and the stained section image (white-BF). (e) Quantitative analysis of image similarity between In-silico stained images (In-silico BF or In-silico QPI) and the stained section image (white-BF) by mean square error (MSE), peak signal to noise ratio (pSNR), structure similarity (SSIM), or mean opinion score (MOS) from six histopathologists. Scale bar: 100 μm. 86
Figure 4. 19 Schematic of the system. (a) 3D modeling of the smartphone-based endoscope system. (b) Optics of the customized zoom lens. (c) Images of the resolution target taken by without any optics adapter and our system, respectively and group 2, element 4 from each image was described as line plot. 92
Figure 4. 20 Smartphone-based endoscopic cervicogram. (a) Cervicogram of before acetic acid application. (b) Cervicogram of after acetic acid application. (c) VIA- patient (d-e) VIA+ patients with predictions from best among four physicians. Prediction labeled the precancerous regions with colors at each clock position. 93
Figure 4. 21 Block diagram of image processing and classification. (a) Pre-image processing method, (b) Feature analysis and classification. 94
Figure 4. 22 Image pre-processing procedures with representative images. 95
Figure 4. 23 Result of image processing result. 99
Figure 4. 24 Result of feature extraction. (a) Extracted VIA features from sliced VIA-/VIA+ images, showing graphical information in different color spaces. In addition, correlation map was calculated form Haralick's texture feature. (b,c) Representative histogram of green-to-red ratio in VIA-/VIA+. (d) Summarization of selected features as predictors for classifying model. 100
Figure 4. 25 Comparison & selection of classification model. (a) Graph of training performance comparing the VIA results from each classifier. (b) ROC curves comparing the VIA+ performances. (c) Box plots of prediction scores for each classifying method. (d) Confusion map of testing for KNN model. 101
Figure 4. 26 Analysis of KNN for smartphone-based endoscopic VIA. (a) Visualization of KNN classifying result for 10 patients with VIA+/VIA-. Lines inside of annulus ring indicates the results of golden standard for each clock position. Annulus ring presents the result of KNN classification according to each clock position. Outer yellow mark represents the position where both golden standard and prediction results are matched. (b) Graph presenting the agreement of KNN to each physician. (c)

ULSAN NATIONAL INSTITUTE OF SCIENCE AND TECHNOLOGY

Graph comparing the screening performance for 10 patients interpreted by KNN and physicians. .. 102

Figure 5.1 Smartphone-based QPI system for POC diagnostics 108
Figure 5.2 Development of QPI software in Android platform. a) Image capture screen. b) Real-time DPC computation screen imaging cells. 109
Figure 5. 3 Future perspective of POC-QPI system implemented on smartphone. a) automated cervical cancer cell screening. b) In-silico tissue staining from label free smartphone-QPI. 109
Figure 5.4 Development of portable high-throughput DPC-based QPI system. a) Real image of portable system connected to laptop. b) Simple schematic of proposed system. Reconstruction of large field-of-view (c) QPI and (d) color bright field image from a single platform. 110
Figure 5.5 Development of phase contrast optical projection tomography. a) Schematic of phase contrast OPT, b) LCD for pattern filter, c) real image of the system. 111
Figure 5.6 QPI reconstruction using LCD patterned illumination in OPT. a) Bright field, and phase contrast images are available in this OPT system. 112

ULSAN NATIONAL INSTITUTE OF SCIENCE AND TECHNOLOGY

List of Tables

Table 3.1 Cost of smartphone-based endoscope system 58

Table 4. 1 Comparison of machine learning and deep learning 61
Table 4. 2 Training details for the in-silico staining of QPI images using GAN..... 78
Table 4. 3 Blind mean opinion score (MOS) testing for In-silico and H&E histological staining for kidney and brain sections..... 87
Table 4. 4 Sensitivity, specificity, and cohen's kappa value, P-value for smartphone-based endoscopic VIA among all observers (n=20)..... 98

ULSAN NATIONAL INSTITUTE OF SCIENCE AND TECHNOLOGY

Chapter 1. Introduction

1.1 Digital medicine

Recently, various innovative technologies such as cloud computing, 3D printing technology, big data, internet of things (IOT), artificial intelligence (AI), and system integrations have been rising along with markets, making the manufacturing and production chain faster, smarter, ubiquitous, and autonomous. Furthermore, it changes our daily life by offering intelligent functionalities and technologies related to our livings and works, which couldn't achieve before. In this days, these technical explosion, changing the way we live and think, is referred to 4th industrial revolution [1, 2]. Brief history of the industrial revolutions is described in Figure 1.1. This term "4th industrial revolution" was initially announced at the World Economic Forum in 2016, which has been released as a technological revolution that fuses the boundaries of digital, physical, and biological spaces based on the 3rd industrial revolution ("digital revolution") [3]. As mentioned in the forums, its unique characteristics of connectivity and intelligence would transform many conventional technologies into interconnected and more intelligent.

Every industry is affected by the new waves of technologies, digitalization and connectivity, and the biomedical or medical field is no exception. According to a survey conducted by The Economist, healthcare was expected as the highest to benefit from the 4th industrial revolution. Such technologies of IoT, cloud computing, big data, digitalization, additive manufacturing, and artificial intelligence has offered the great promises to the field of medicine [4]. Among the medical application fields, "digital medicine" has been highlighted as one of the uprising field that earns the benefits in speed, sharing, connection, and performances from 4th industrial revolution. Conventional/analogue medical devices and diagnostic programs have become miniaturized, digitalized, and automated, suggesting the technical revolution in the field of medicine [5, 6]. Particularly, digital pathology, point-of-care (POC) diagnostics, and application of deep learning or machine learning technologies have shown the great potentials not only in academia but also in the revenues of their markets. It allows to connect devices, hospital equipment, and to accelerate efficiencies in health service such as diagnosis, and to reduce the cost of services. Moreover, interconnection between advanced technologies has been improved the access of healthcare to the places where hospital or medical services are limited [7, 8]. Recently, artificial intelligence has shown promising results related to disease screening especially using medical images [9].

ULSAN NATIONAL INSTITUTE OF SCIENCE AND TECHNOLOGY

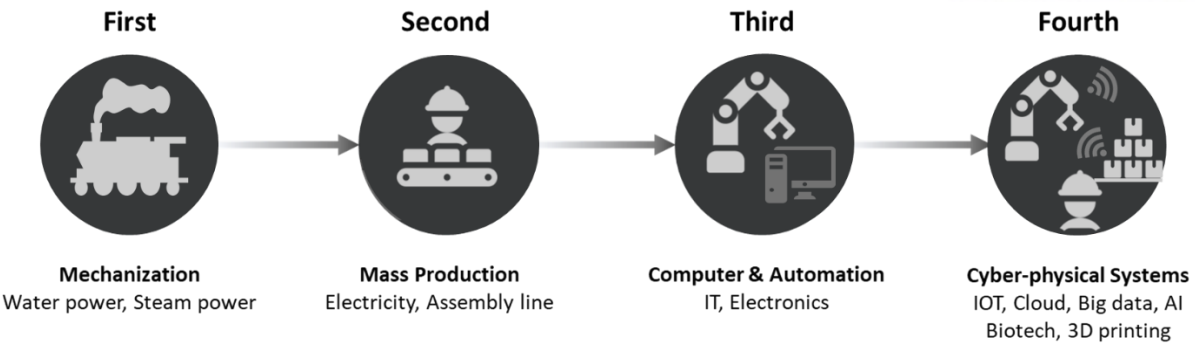

Figure 1.1 Brief illustration of industrial revolutions [2]

1.2 Digital pathology

As a result of technical advances many innovative optical device has been introduced in the field of pathology. Some of these devices, in this days, have been settled as a part of hospital system, significantly giving benefits and efficiencies as improved medical services to patients. Particularly, the introduction of whole-slide imaging (WSI) had brought a major impact in the medical fields, opened a new era of digital pathology [10]. Analogue pathology, inspecting the specimens under conventional microscopes, had changed to digitalized pathology, acquiring the images in digital manner that has been transformational and engendered numerous clinical, educational, and research applications. The capacity to rapidly capture the large field-of-view of pathology slide has become feasible as a result of technical advances in optical imaging technologies [11]. Today, WSI scanners performs in automatic ways that takes images less than 1 minute per whole slide. This imaging system produces high-resolution images, replicating the glass slides in digital [12]. Equally dramatic improvements of internet infrastructures and cloud data technologies that derived from 4th industrial revolution have made possible for sharing and storing the large WSI datasets in current hospital's pathology system. As a result, traditional workflow has become efficient, relatively less time-consuming, and simple which makes the whole pathological diagnostic process less complicated and improved as shown in Figure 1.3. Now with digital pathology process, pathologist doesn't need to inspect each specimens and make notes for final conclusion. Computer software analysis and sharing images electronically with doctors would offer supportive information which improves the diagnosis accuracy [11]. Moreover, digital pathology system would also benefit to save the costs, estimating to save at $12.4 million for the laboratories or institutions that had 219,000 orders per year [13]. Therefore, digital pathology has developed into a thriving field as well as their revenue are growing quickly in the markets. According to survey conducted by Mordor Intelligence, global digital pathology market was valued at $516 million and expected to reach $1,054 million by 2024 [14].

ULSAN NATIONAL INSTITUTE OF SCIENCE AND TECHNOLOGY

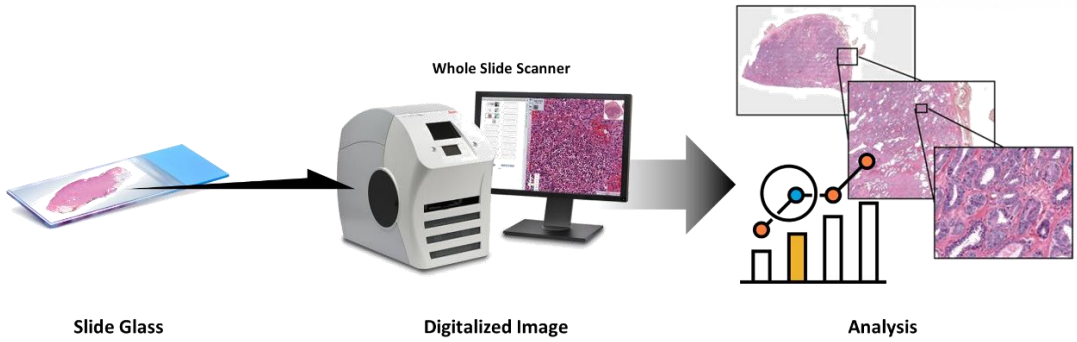

Figure 1.2 Digital pathology imaging process

Although intelligent workflow of digital pathology process may improve quality and efficiency as well as streamline, and harmonize the processes, there are still bottleneck that delays the whole process along with cost and labor issues [15, 16]. Staining is very essential and efficient process in pathology workflow that labels the molecular constituents of tissues and cells with chemical reactions to visualize the transparent specimens under bright field microscope. However, this process requires multiple time-sensitive steps to follow, uses various kinds of chemical reagents depending on the characteristics of specimen, hence, takes high labors, times, and costs [17]. For example, for the histochemical staining process, average time of staining procedure of a tissue specimen was spent around ~ 1 hour for H&E, and 2-4 hours for Masson's Trichrome, and Jones stain. Estimated cost for each staining process, including the labors and material costs, was ~$5-10 and >$15-40 for H&E, and

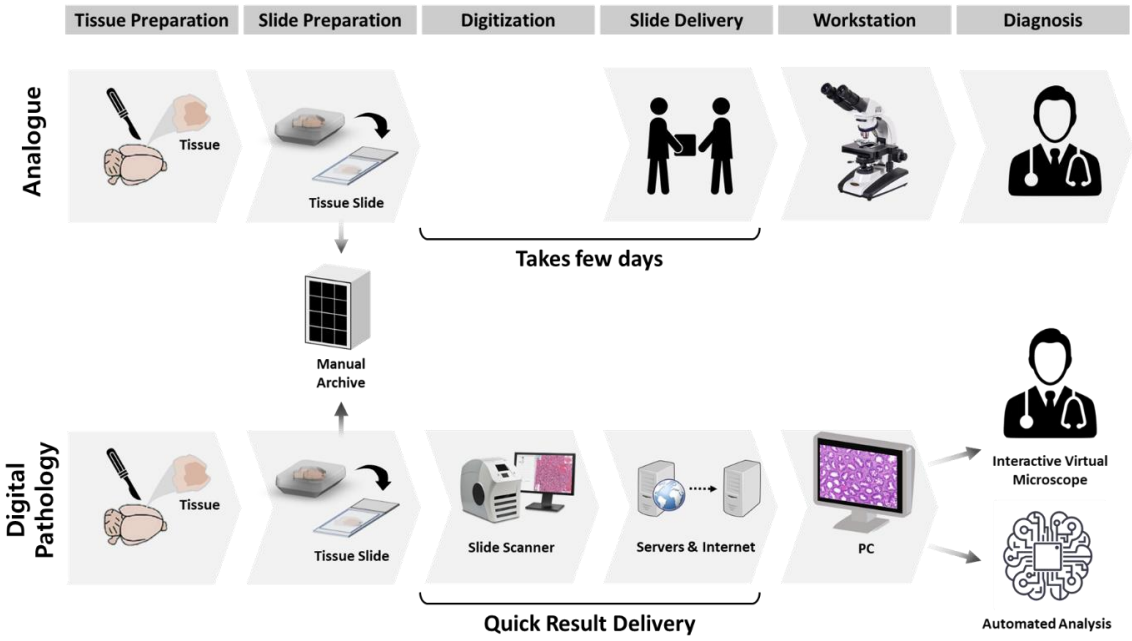

Figure 1.3 Comparison of traditional and digital pathology workflow

Masson's Trichrome and Jones stain, respectively [16]. As we can expect, if staining method could be totally bypassed or shrunk, digital pathology workflow could be further capable to eliminate the delays, leading to saving additional time and cost as well.

1.3 Portable medical devices for point-of-care diagnostics

During the last few years, point-of-care (POC) diagnostic devices have benefited from the rapid advancement of technologies that derived from 4th industrial revolution. Leveraging advances in IOT, additive manufacturing technologies, and wireless telecommunications, low-cost, portable medical devices have the potential to improve screening and detection of disease at the POC in the settings in both low- and high-resource countries [7, 8]. Similarly, recent state-of-the-art smartphones including the technologies such as high-resolution camera, computing power, high definition of display, ubiquitous connective technologies, have been introduced as a candidate that could alternate the computing devices in the conventional medical devices. Adapting with other engineering components, current systems could be further miniaturized as well as provide simple, cost-effective, and corresponding functionalities for improving diagnosis quality and treatment at the POC [7, 18, 19].

In the developing countries, medical resources and treatments are highly demanded. There is a shortage of trained healthcare workers in low-resource settings or developing countries. Hence, patients may have to travel long distances to receive medical services unfortunately. However, frontline health care is often served by community healthcare providers in low-resource settings which lacks electricity,

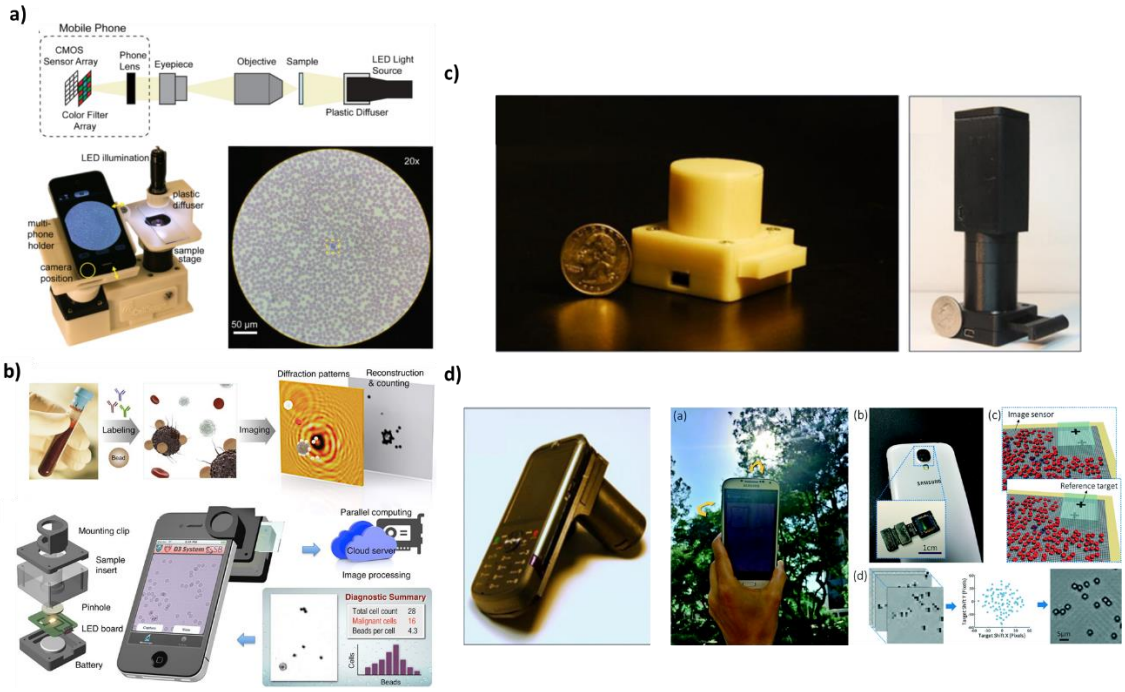

Figure 1.4 Recent POC microscope devices. a-b) Smartphone based microscope system adapting optical components before camera. c) Lens-free stand-alone microscope systems d) Lens-free smartphone-based microscope. .

ULSAN NATIONAL INSTITUTE OF SCIENCE AND TECHNOLOGY

water, chemicals, and access to laboratory apparatus for screening. It is feasible that real-time POC such as telemedicine could be conducted with compact, low-cost medical devices that can be connected with to expert through internet infrastructures [7]. Therefore, POC markets grow fast, and faster than the average of the in vitro diagnostics industry, which is one of largest market in diagnostic fields. In 2018, sales of POC testing reached $22.3 billion, increasing 7.5% from $20.7 billion in 2017 [20].

Recently, many smartphone based POC devices in a compact form factor have been introduced and provided promising performances related to biophysical, biochemical, or biological components or properties from biological samples. Many devices in the markets offers efficient measurements related to primary cares such as glucose, urine, blood pressure in remote settings or out of clinical office by applying connective devices to smartphone and make analysis. Moreover, integration of optical techniques offers an additional means for imaging biological properties or biomarkers, providing spatially resolved information across cell or tissue samples or specimens, as well as providing in vivo screening and diagnostic capabilities. However, these POC imaging technologies are mostly focused microscopy (fluorescence, bright field) and flow-based system (lab on a chip cytometry, microfluidic channels, lens free system) [7, 21]. Currently, in the low-resource settings, there are still great amount of demands in such fields related to medical imaging, which are accessible by other medical imaging tools.

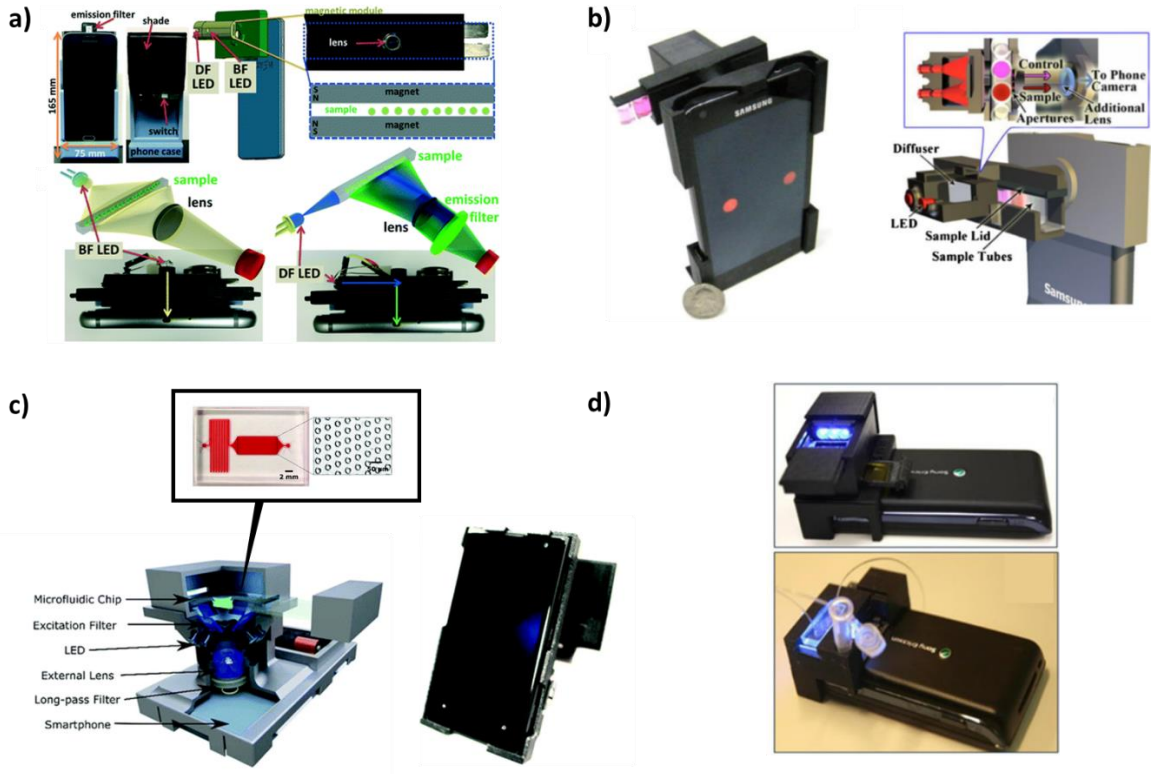

Figure 1.5 Smartphone based POC devices in bioanalytical sciences. a) POC fluorescence- and magnetophoresis-based cytometry b) Device for colorimetric assay. c) Smartphone-imaged microfluidic biochip for measuring CD64 expression from whole blood. d) Smartphone based fluorescence device and optofluidic fluorescent imaging cytometer.

Mostly these diagnostic imaging demands may be performed with devices that are more bulky, expensive than conventional microscope or flow cytometry systems. For example, endoscope system plays essential role diagnosing various diseases in real-time which are not access by human eye or other surface measurements. Although this routine endoscopy shows promising performances in high-resource settings, it is mostly difficult to operate in the developing countries where infrastructure, and expert physicians or nurse practitioners are deficient. In this context, we believe that there are still many application of medical imaging fields including cancer screening, primary care, telemedicine that require state-of-the-art POC devices in the developing countries.

1.4 Artificial intelligence in biomedical fields

Recently Moore's Law has been broken as technologies of graphic processing unit (GPU) improved dramatically every year. This directly influenced many engineering felids, allowing heavy computational process with improved speed [22]. Not only in electronic, but also fields of artificial intelligence have been improved significantly, enabled to perform the heavy task in these days. Particularly, a subset of artificially intelligence called deep learning has been improved and started to provide promising outcome in various fields. The increased computational speed has expanded the capability of deep learning model to design complex models of neural networks. Thus, this new waves in artificial intelligence have also made many influence in biomedical engineering fields, especially related to medical imaging and pathology [9]. From 2015, publications of papers related to artificial intelligence using deep learning for medical imaging has been increased. In 2016, numbers of publication have been increased more than four times from previous years.

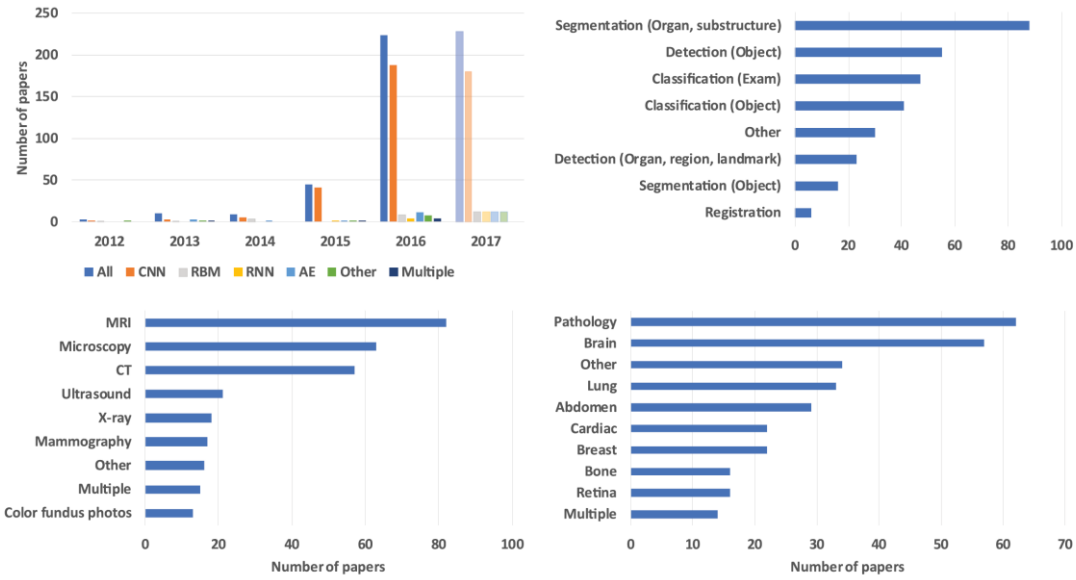

Figure 1.6. The number of papers published from 2012 to 2017 in bio-medical image analysis community with deep learning approach applications. Figure adapted from ref. [9]

Deep learning technique in bio-medical engineering

In biomedical engineering fields, the post image processing after taking an image using observation tools, such as MRI, CT, and microscopes, is crucial to extract desired information from taken images for intended purposes. Initially from the 1970s and the 1990s, those techniques were developed as an application of low-level processing based on pixel values, for example, the edge and line detector filters, and mathematical models. After 1990s, supervised techniques, where data is used for training a system for a specific task, were becoming majority in post processing. The most popular example is the statistical classifiers for detection and diagnosis purposes. This machine learning or pattern recognition approach is still very powerful and forms the basis of image analysis techniques, however, it requires extracting features or labeling by human, so called handcrafted features as the reference so that machines can learn from given data to determine the optimal decision boundary in the high-dimensional feature space [9]

Recent explosive development of advanced concepts and techniques in the deep learning community are dramatically changing the landscape of bio-medical image processing applications and taking over previous commercial and traditional rule-based and mathematical model-based image processing algorithms. The successful image analysis with deep learning approach lies on many contributions from different fields, however, the convolutional neural networks (CNNs) is at the center. CNNs consist of many layers which transform their input with convolution filters, and it learn the features that optimally represent the data for a given task during the training. Although the concept of CNN had been released in early 1980s [23] and initial successes of real-world application to medical image analysis, which detecting lung nodule using CNN, were released in 1995 [24], the attention of bio-medical community to CNN were not stimulated until the contribution of AlexNet [25] in 2012 to the ImageNet challenge in 2012, because of the inefficient training of deep networks and limited computing power by that time.

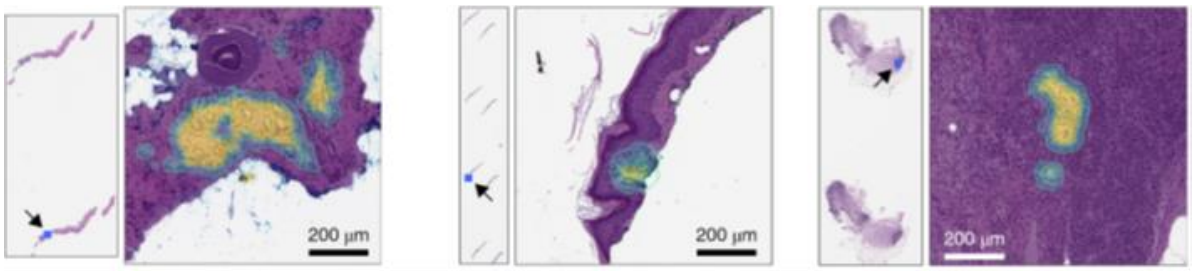

Figure 1. 7 Example of computer assisted diagnosis application using deep learning. The developed module detecting specious region in whole histopathogy slice image and grading the level of patient. Figure adapted from reference [26]

ULSAN NATIONAL INSTITUTE OF SCIENCE AND TECHNOLOGY

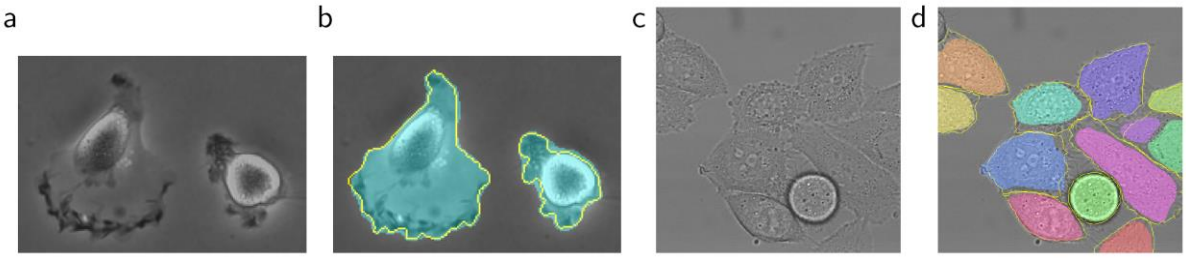

Figure 1. 8 Example of the cell segmentation using deep convolution neural network architecture. The U-net in reference [27] detect the boundary of cell in the image and segment. Figure adapted from ref. [27]

Applications of deep learning to bio-medical image processing/analysis divided into several subcategories which are the image classification, the semantic segmentation, the noise reduction, the image generation and enhancement etc. All these applications can be formulated based on CNN, however, the details in training and validation procedure, for example, the type of loss function, the structure of network, the quantitative metric for validate and comparison between the output and the reference, should be carefully designed depends on the purpose of desired task. In general, the image classification and the segmentation are the classification problem, which distinguishing a given image or subarea of given image into one of classes, and thus these jobs require the labeled answer for supervising the network during the train. The classifier network based on CNN learns and extract the features from the data that helpful for distinguishing task during the training through the back propagation of loss to minimize the error from the output layer to the input layer. Examples of classification problem in biomedical image analysis are the segmentation of cell or colon grands [27-29], the nucleus detection and classification [30, 31], and computer assisted diagnosis [26].

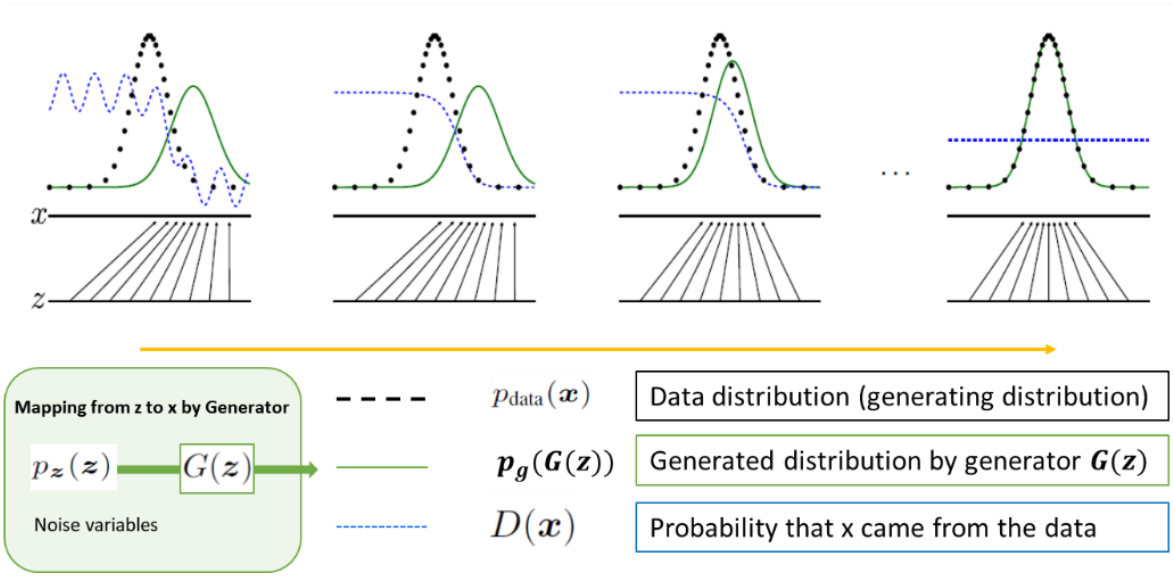

Figure 1. 9 Conceptual description of learning process in the generative adversarial networks. Through the training process distribution of generated data converges to real data distribution by adversarial learning process. Figure modified from ref. [32]

ULSAN NATIONAL INSTITUTE OF SCIENCE AND TECHNOLOGY

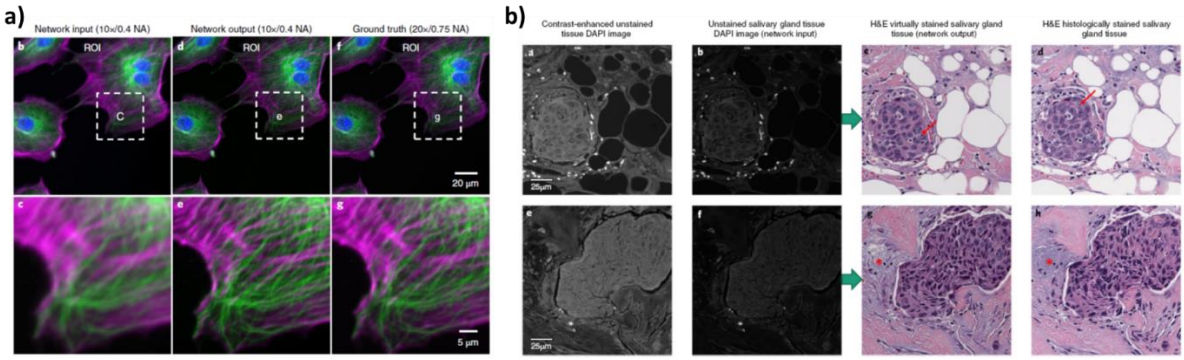

Figure 1. 10 Super-resolution of the florescence microscope image using deep learning architecture which consist of CNN based on GAN and virtual staining of label-free image. Figure adapted from ref. [16, 33]

In terms of probabilistic perspective, the classification problem addresses a discriminative model: a model of conditional probability of the target Y, given an observation X, P(Y|X=x), while the problems such as the noise reduction, the resolution enhancement, or the virtual staining in bio-medical image processing are application of generative models. Generative problem addresses a model of the conditional probability of the observation X, given a target Y, P(X|Y=y). In general, generative model is much more difficult compare to a discriminative model, that generating data that fall close to their real counterparts in the data space, thus, it has to model the distribution throughout the data space. The breakthrough of generative model approach introduced in 2014 by Ian Goodfellow with his concept, the generative adversarial network (GAN) [32]. GAN is composed with two neural networks, a generator, G(z), for generating a data x from input or noise z, and a discriminator, D(x), for evaluating the difference in real and generated data. The key idea in GAN is the adversarial learning that a generator network learns toward generating more realistic data while a discriminator learns toward distinguishing better between real and synthesized. As the results of this adversarial learning process, a generator could be trained as much as it can generate realistic data, since the distribution of generated data converges to the real data distribution. Many of application in biomedical image processing based on GAN published recently, including the noise reduction [34], the super resolution [33, 35], and the virtual staining [16]. These applications occupied the concept of adversarial learning and built the generator and discriminator based on CNN.

1.5 Research motivation & approaches

Research motivation

As technologies has been improved every years, many fields of healthcare took the advantages, solving various demands which was not achievable in previous works. One of the promising field is digital medicine which transforms analogue clinical system to digital, improving healthcare services in terms of performance quality, cost-effectiveness, and speed. Moreover, advanced technologies affect in positive ways especially to the tissue diagnosis process, point-of-care diagnosis, and artificial intelligence. Integration of various engineering techniques leads to eliminate the delays in traditional pathology analysis process, to miniaturize the conventional diagnostic laboratory devices, to enhance the computational power which allows to perform complicate learning models for biomedical fields. However, there are still limitations or opportunities to overcome in terms of hardware and software wise to provide stability, cost-effectiveness, and quick process for quality improvement of the healthcare service

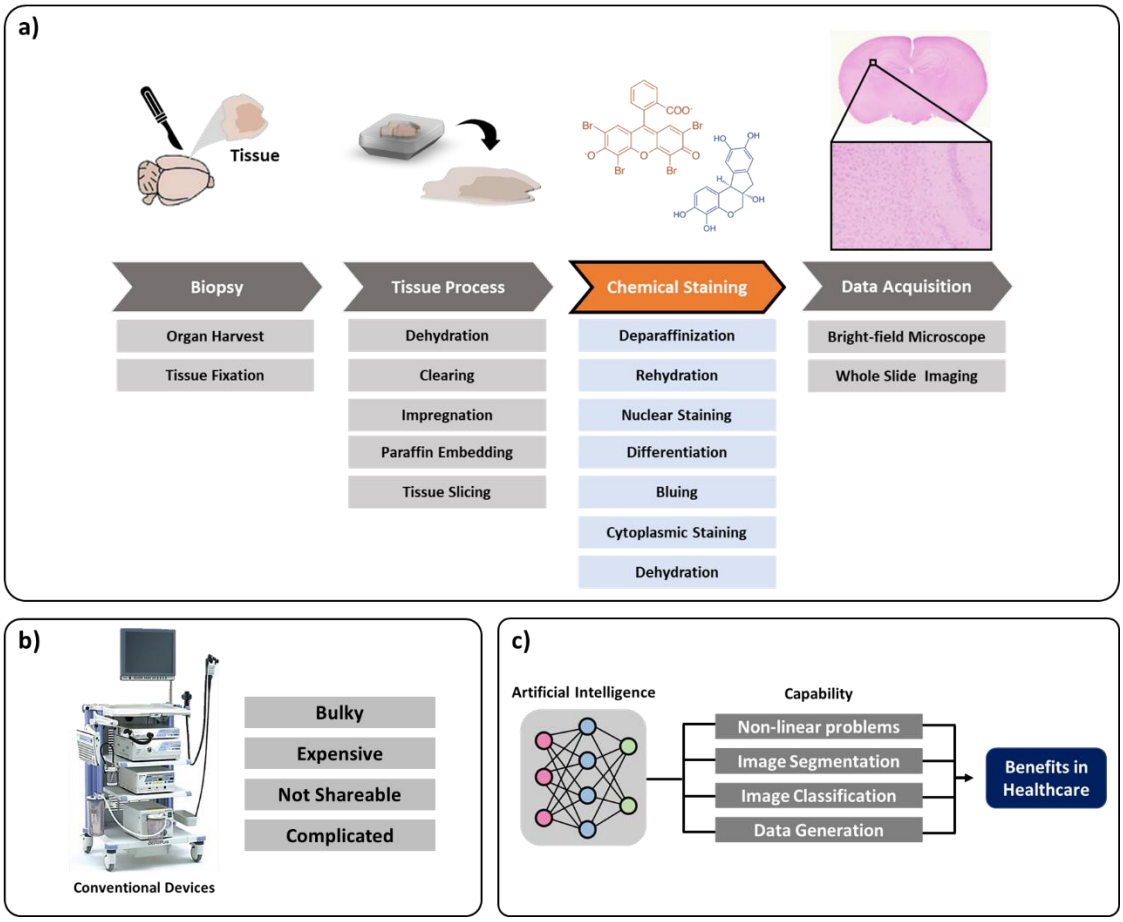

Figure 1.11 Motivation points of thesis related to digital medicine. a) Limitations in current histopathology workflow. Staining procedure still takes long time and requires delicate laborious steps. b) Limitations in conventional medical device as POC. Many demands of imaging-based diagnosis are existing in low-resource setting. But these conventional devices are not appropriate. c) Advances of artificial intelligence are offering promising outcome that benefits the healthcare in many ways. This technologies could be applied to the fields in a-b), making devices intelligence and autonomous.

ULSAN NATIONAL INSTITUTE OF SCIENCE AND TECHNOLOGY

Although introduction of digital pathology shrunk the total process of workflow, some sub-process requires lengthy steps and costs which makes pathology process still lengthy. For example, in order to acquire images from transparent tissue, chemical staining method is inevitable. However, this method requires time-sensitive steps and long processes, which leads to increase of costs as shown in Figure 1.6a. Therefore, we believe that implementation of label-free imaging device could address this problem, bypassing the staining process which leads to less cost, time in total pathology workflow.

Currently, most of POC research and markets has been mainly focused on biophysical signal and microscope applications. These devices have offered promising performances in low-resource settings with portability that could alternate the primary care devices or diagnostic process that is based on laboratory settings. Recently portable optical devices for POC medical imaging have been introduced. As taking advantages of internet infrastructures, cloud storage, improved computational powers, POC medical imaging devices could demonstrate tele-medicine, and automated analysis in the low-resource settings. However, in developing countries, there are still many demands of diagnostic fields related to real-time medical imaging. Especially, such imaging-based diagnosis for cervical cancer screening are currently limited due to heavy, and expensive limitations of conventional devices. Even though, portable devices are ready, it is true that trained clinicians and practitioners are limited to interpret the images.

Lastly, as result of technical explosions, artificial intelligence has shown great potentials in various biomedical applications. As computational power increase, deep learning networks are now capable to solve very deep, complicated, and non-linearized medical imaging analysis. Recently, machine learnings and deep neural networks allows to classify the diseases with high accuracy by finding features from various types of medical images. Deep learning technologies, nowadays, shows promising outcome in automated disease segmentations from radiology images and generative models were technically matured enough to transform and elaborate images to different images that could not perceptually differentiate between them. Therefore, recent artificial intelligence has become smarter and more stable. We believe that these techniques could be applied to digital pathology as well as POC device.

Research approaches

The research aim in this study is developing the optical devices to provide benefits in the fields of digital medicine by addressing the limitations mentioned above. Moreover, the machine learning and deep learning technologies has shown great potentials, hence, they were applied to the devices for each fields, providing more mature solutions to the problems.

Label-free imaging for digital pathology

In this thesis, label-free imaging device was developed utilizing one of the computational microscopes. This microscope system was implemented in the simple conventional bright field configuration, only replacing the illumination part with LED matrix. For this system, partially coherent LED matrix was utilized for patterning the illumination and to provide contrasts to the transparent object for visualization. With assumption of use of slowly varying phase specimen, complex field of object illumination was linearized, and phase of object was retrieved quantitatively (quantitative phase imaging; QPI) by computing simple deconvolution process using measured phase shifted images (differential phase contrast; DPC). Prior to label-free tissue imaging QPI device, in this thesis, multi-contrast imaging system was developed in a single microscope configuration, offering bright field, dark field, differential phase contrast, and quantitative phase contrast simultaneously. Furthermore, we have addressed the limitation in conventional DPC-based QPI system (illumination in visible range) by utilizing NIR illumination and developing its customized apparatus. Therefore, this device allows to provide QPI regardless to scattering and absorptions of light which enables to demonstrate not only label-free thick tissue imaging but also acquiring QPI of chromatic stained specimens. Therefore, we expected our label-free imaging computational microscope would skip the staining process, resulting in improvements of the digital pathology workflow.

Smartphone-based endoscope for point-of-care diagnostics

Second, herein, portable endoscope system was developed utilizing smartphone that addresses problems of cost, size, and connectivity as POC diagnostics. To provide corresponding performance on smartphone, magnifying lens system was developed in small form and homebuilt software was developed control imaging parameters as well as rotate the images that were flipped from designed lens system. This system provides optical magnification up to ~3x and allows to reach up to ~12x with digital zoom function in camera. Pilot study of proposed endoscope system was conducted in the Otolaryngology, capturing the human subjects. We compare the imaging capability of smartphone-based endoscope system to conventional clinical endoscope system.

Application of deep learning-based virtual staining method for digital pathology

Third, although proposed NIR based QPI system successfully demonstrated label free tissue imaging, quantitative phase information could be only visualized in monochromatic manner. Hence, even though label free tissue imaging is capable, it is somewhat difficult to apply in real world application in digital histopathology. In order to overcome this limitations, one of the state-of-the-art deep learning techniques named generative adversarial network (GAN) was applied to our system to generate the virtually staining image which look comparable to image that is captured from bright field microscope using labeled tissue. Basically, GAN transforms the label free QPI image to histochemical stained tissue image. In this study, utilizing NIR based QPI system engendered many advantages to virtual staining methods. It enables to train the GAN model very quickly since stained samples imaging was available as phase contrast, which eliminates additional image registration methods or any image compensation algorithms. Moreover, partially coherence illumination which used in our system allows to achieve better resolutions, creating more stable and accurate model outcome which look similar to brightfield stained image. Throughout this approach, costly, lengthy, and laborious tissue staining methods could be fully bypassed while providing equivalent outcome as tissue staining method.

Application of machine learning technology for automated cancer screening method

Lastly, POC automated cervical cancer screening system was developed utilizing smartphone-based endoscope system as well as training the machine learning algorithm. This system offers non-invasive, non-contact imaging method with high resolution imaging capability in digitalized format. To train the classification model, we took endoscopic images from patients in clinic before and after application of acetic acid on lesion and conduct biopsy to achieve golden standard results. Then, image processing methods was performed to derive multiple precancerous features from endoscopic images. With these features, machine learning algorithm was trained and validated. As a result, higher overall accuracy of machine learning model classifying normal and abnormal patients was shown compared to that of physicians. This cervical cancer screening system for POC diagnostics is very promising, which allows to provide quality assured digital images. Moreover, machine learning-based classification results may assist those health care workers who are minimally trained in developing countries.

ULSAN NATIONAL INSTITUTE OF SCIENCE AND TECHNOLOGY

Chapter 2. Development of computational microscope for label-free digital imaging

2.1 Development of RGB matrix based multi-contrast microscope

2.1.1 Introduction

Optical microscopes are the most common devices used to visualize the label-free biological specimens [36]. Among the functional modalities, bright field, dark field, and phase contrast imaging were the most common method for visualizing the transparent specimens in non-staining manner. Using each of these contrast microscopes may offer complementary information about the specimens, however, it is not available to acquire multiple contrast images simultaneously in single microscope configuration. Each contrast modality requires different optical path with hardware configurations such as annulus ring in condenser lenses, polarization apparatus, and specialized objective [37]. Moreover, some optical elements for contrast images may difficult to afford or to install that accompany by expensive price of optical elements and cumbersome or time-consuming task.

Recently, programmable LED matrix was utilized as an illumination with post-processing algorithms to provide diverse imaging capabilities [37-40]. Matrix of LED, which is controllable with micro controller unit (MCU), could provide the pattern for illumination in diverse form. With intention of giving oblique angles from illumination to specimen, BF, DF, DPC can be realized in a single configuration [39]. BF images could be achieved by turning on the central part of LEDs in matrix. DF contrast could be obtained through illuminating LEDs with angles outside of the numerical aperture (NA) of the objectives. Moreover, illuminating the specimens with asymmetric circular shape would offer differential phase contrast images (DPC). In DPC, two images from complementary illumination angles are needed to recover the phase through simple post-processing algorithm. The result of DPC is qualitative similar to differential interference contrast (DIC) image which transform the invisible sample phases into measurable intensity, emphasizing the structural information and variations of densities of specimens [41, 42]. Both sequential illumination of different patterns and simultaneous illumination using all patterns with different color combinations enabled real-time multi-contrast imaging [37, 43].

Quantitative phase contrast imaging (QPI) is one of the significant contrast modalities that can be additionally realized through computation algorithm using the LED-based multi-contrast microscopes. Contrary to qualitative information given by Zernike phase contrast or DIC/DPC, QPI offers quantitative information of specimens relate to the optical path length from intensity measurements. Among diverse methods of QPI, interferometry and holography are the common that uses coherent illumination and reference beam. However, these methods are mostly expensive, sensitive to optical alignments, speckle noises, and vibration of the system [44-46]. Alternatively, partially

ULSAN NATIONAL INSTITUTE OF SCIENCE AND TECHNOLOGY

coherent illuminated QPI systems such as transport-of-intensity equation (TIE) [47-49], Fourier ptychography (FP) [50-52], and DPC-based approaches [37-40] have been introduced to overcome the limitations found in coherent illumination-based QPI approaches. Utilizing the partial coherence illumination in QPI makes the system having imaging resolution up to incoherent resolution limit (2x better than coherent diffraction), better optical sectioning, and reduction of speckle noises. Especially, DPC-based QPI approach presented advantage of less imaging number needs for phase recovery compare to others approaches. With four images with asymmetric illuminations in opposite directions and assumption based linearized model from weakly scattering object, complex optical models from qualitatively measurements of DPC could be simplified to recover the phase in quantitative ways [37-40].

In this section, LED matrix-based multi-contrast microscope is introduced as preliminary research. Here, all RGB colors were assigned for each LED pattern to perform the single-shot multi-contrast imaging [37, 43]. Inversion model of weak object transfer function (WOTF) [40], which explains the connection between illumination and pupils for image formation of quasi-transparent object, was derived to quantify the phase information from intensity-based images. Instead capturing the four series of images, only two images from vertical and horizontal directions were captured, hence, improving the imaging speed. Prior to image acquisition, influence of the illumination shape or coherence parameter to the QPI was studied through simulations and experiment. Moreover, we denoised the residual noise amplifications from QPI by combining Tikhonov and total variation (TV) regularization at deconvolution process [53]. To evaluate the multi-contrast modalities, quasi-transparent biological specimens were utilized in this section.

2.1.2 Single-shot BF, DF, DPC image reconstruction

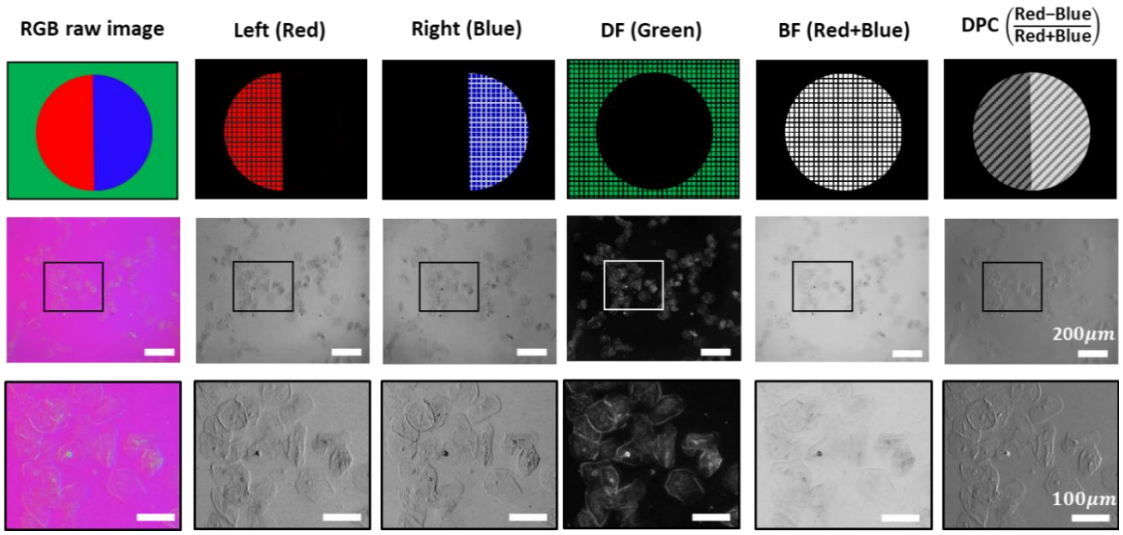

Figure 2.1 Multi-contrast microscope using RGB color patterns in LED matrix. From single shot mixed color image, each colors representing different contrast images. With simple computations, DPC and BF could be realized.

ULSAN NATIONAL INSTITUTE OF SCIENCE AND TECHNOLOGY

Here, we controlled each source on the LED matrix to light up the half circle asymmetric patterns to provide phase shifting illumination scheme. For DF imaging, LEDs located out of the objective NA were programmed to illuminate the specimen. However, all patterns were assembled by assigning the individual colors to each pattern to integrate all contrast images in a single illumination. For most of color camera sensors, to separately measure the color intensities, R, G, B color filters (or Bayer filter) are employed. Therefore, if each pattern on LED matrix purely contains R, G, B colors, multiple contrast images could be acquired from color camera with single-shot image. Due to leakage or crosstalk between each color pixels, color wavelength used for half circle should be separated to avoid the interference, hence, blue and red color was assigned [37]. Then, green was assigned the outer side of objective NA to provide DF images.

As shown in Figure 2.1, multiplexed contrast image could be acquired by separating each color from raw data. With simple operators such as add, subtract, and divide, BF and DPC could be generated. Bright field could be acquired from $I_{BF} = I_{red} + I_{blue}$, where I_{red}, I_{blue} denotes image from red half circle, and blue half circle, respectively. I_{green} could be utilized to visualize the DF image without additional computations. $I_{DPC} = \frac{I_{red} - I_{blue}}{I_{BF}}$ was computed to generate the DPC image which transfer the invisible phase into measurable intensity by shifting the sample's spectrum in Fourier domain [54]. Other than these contrast images, phases could be recovered in quantitative ways by utilizing measured phase information from DPC. Compare to DPC, QPI allows better contrast in image, and further opportunity for data analysis. DPC uses linearized forward model or weak object transfer function (WOTF) to describe measurable phase intensity that was acquired from sample's complex-field. Solving the forward model through the inverse problem could derive phase in quantitative value.

2.1.3 Weak object transfer function (WOTF)

Consider a weak scattering object with complex transmission function $\mathrm{t(r)} = e^{-\mu(r)+i\phi(r)}$ [40], where μ denotes the absorption of the sample and ϕ characterizes the phase with r= (x, y) spatial coordinates. Applying the weak phase approximation allows complex transmission function can be simplify as $\mathrm{t(r)} \approx 1 + -\mu(r) + i\phi(r)$ by solving the Taylor series [55]. For partially coherent which consists of multi-angle spatially incoherent illuminations, the images were formed by superimposing all intensity spectra corresponding to each coherent illumination or point source. Therefore, the intensity is initially analyzed at the camera regarding to single coherent illumination. The intensity captured of the transmitted complex wave-front in camera plane is [38, 40]:

$$\mathrm{I(r)} = \left|\mathcal{F}\{\mathcal{F}\left[\sqrt{S(u)}e^{i2\pi ur} \cdot \mathrm{t(r)}\right] \cdot P(u)\}s\right|^2 \tag{2.1}$$

ULSAN NATIONAL INSTITUTE OF SCIENCE AND TECHNOLOGY

where $\mathcal{F}$ denotes the Fourier transfer function, u spatial frequency coordinates in Fourier domain. Input field after light from single point source passes the sample can be achieved by the product of illumination S(u) and complex transmission function t(r). In general, illumination from each point source is approximated by a uniform plane wave at the sample, resulting overall illumination could be written in $\sqrt{S(u)}e^{i2\pi ur}$. After light passes the objective, filed is filtered from circular pupil at the Fourier plane before reaching the camera plane. P(u) represents the pupil function which is defined as $\mathrm{p(u)} = \mathrm{circ}(\mathrm{u}/\rho_o)$, where $\rho_o = NA_{obj}/\lambda$ serves as low-pass filter from objective [56] and $\mathrm{circ}(\psi)$ is defined as:

$$\mathrm{circ}(\psi) = \begin{cases} 0, & |\psi| > 1 \\ 1, & |\psi| \leq 1 \end{cases} \tag{2.2}$$

At the camera, field intensity of 2D image is then could be written as taking integral of each intensity of each point source [38, 40]:

$$\mathrm{I(r)} = \iint \left| \mathcal{F}\{\mathcal{F}\left[\sqrt{S(u)}e^{i2\pi ur} \cdot \mathrm{t(r)}\right] \cdot P(u)\}v \right|^2 d^2u \tag{2.3}$$

Furthermore, approximation assumption could simplify the intensity in to 3 terms, including background term, absorption contrast term, and phase contrast term [38, 40]. Then, we took Fourier transform of Eq. (2.3) to produce spectrum of intensity $\tilde{\mathrm{I}}(\mathrm{u})$:

$$\tilde{\mathrm{I}}(\mathrm{u}) = \mathrm{B}\delta(\mathrm{u}) - H_{ab} \cdot \tilde{\mu}(u) + iH_{ph} \cdot \tilde{\phi}(u), \tag{2.4}$$

where i is imaginary unit; B, background term, H_{ab}, absorption transfer function, H_{ph}, phase transfer function (PTF or WOTF). Express of B, H_{ab}, H_{ph} are given by

$$\mathrm{B} = \iint S(u')|P(u')|^2 \, d^2u', \tag{2.5}$$

$$H_{ab} = \iint S(u')P^*(u')\, P(u'+u)d^2u' + \iint S(u')P(u')\, P^*(u'-u)d^2u', \tag{2.6}$$

$$H_{ph} = \iint S(u')P^*(u')\, P(u'+u)d^2u' - \iint S(u')P(u')\, P^*(u'-u)d^2u', \tag{2.7}$$

where $S(u')$, and $P(u')$ denotes intensity distribution of illumination source and pupil function of the objective lens in Fourier space, respectively. Ideally, $P(u')$ is low-pass filter with a cutoff frequency of $\frac{NA_{obj}}{\lambda}$ (coherent diffraction limit). Eq. (2.6) and (2.7) is general expression, allowing

ULSAN NATIONAL INSTITUTE OF SCIENCE AND TECHNOLOGY

application to any illumination patterns and pupil functions [38, 40]. For DPC image I_{DPC} along specific direction of phase gradient, two images from complementary illumination S(u) were considered for calculation

$$\mathrm{I}_{lr}^{DPC} = \frac{I_l - I_r}{I_l + I_r} \ , \tag{2.8}$$

where I_l and I_r present the image acquired from left- and right-half circle (could be blue and red half circle or gradient amplitude pattern or annulus pattern). To facilitate further analysis of phase transfer function, Fourier transform of numerator and denominator from Eq. (2.8) was derived by substituting Eq. (2.4) [38]

$$\mathcal{F}(I_l - I_r) = [H_l^{ph} - H_r^{ph}] \cdot i\tilde{\phi}(u) \tag{2.9}$$

$$\mathcal{F}(I_l + I_r) = [B_l + B_r] \cdot \delta(\mathrm{u}) - [H_l^{ab} + H_l^{ab}] \cdot \tilde{\mu}(u) + [H_l^{ph} + H_r^{ph}] \cdot i\tilde{\phi}(u). \tag{2.10}$$

In the aberration-free system, ideally DPC image doesn't contain any absorption information, leading $H_{ab} = 0$. Moreover, symmetrically designed illumination patterns on the corresponding axis would make phase term, $H_l^{ph} = -H_r^{ph}$, and background term $B_l = B_r$. Thus, Eq. (2.9) and (2.10) can be rewritten as $\mathcal{F}(I_l - I_r) = 2i\tilde{\phi}(u) \cdot H_{ph}$ and $\mathcal{F}(I_l + I_r) = 2B$. Finally, Fourier spectrum of DPC image can be defined as

$$\tilde{\mathrm{I}}_{lr}^{DPC} = \frac{H_{ph}}{B} \cdot i\tilde{\phi}(u), \tag{2.11}$$

where background B can be approximated by sum of two images or brightfield image. Throughout this model, forward linear model such as A=Bx to has been established and the quantitative phase information can be calculated from it by solving phase retrieve inverse problem [38, 40, 53, 54, 56]. Furthermore, phase transfer function model will be used to analyze the relationship between coherence parameter of illumination and difference of spatial pattern. These methods were summarized in Figure 2.2.

2.1.4 Quantitative phase reconstruction from DPC

For reconstruction of phase from Eq. (2.11), inverse problem could be solved by simple deconvolution of the multi-axis DPC images with phase transfer function [38, 40, 53, 54, 56]. However, calculation of the optical transfer function H_{ph} in Eq. (2.7) would result in zero at frequencies along the axis of

ULSAN NATIONAL INSTITUTE OF SCIENCE AND TECHNOLOGY

asymmetry and over the bandwidth of the spectrum, providing an amplified noise information when direct deconvolution has been computed. Therefore, least squares method with regularization term was utilized to solve our forward model [38, 40, 53, 54, 56]:

$$\min \sum_i \left|\tilde{I}_{DPC,i}(u) - \tilde{H}_i(u) \cdot \tilde{\phi}(u)\right|^2 + \gamma\left|\tilde{\phi}(u)\right|^2, \tag{2.12}$$

where i denotes the number of DPC measurements, which is $i = 1, 2$ for 2-axis DPC images; $\tilde{H}_i(u)$ denotes $\frac{H_{ph}}{B}$ for each DPC measurement; γ denotes a Tikhonov regularization term to avoid singularity. Therefore, inverse problem can be solved

$$\phi(r) = \mathcal{F}^{-1}\left\{\frac{\sum_i \tilde{H}_i(u) \cdot \tilde{I}_{DPC,i}(u)}{\sum_i |\tilde{H}_i(u)|^2 + \gamma}\right\} \tag{2.13}$$

here $\mathcal{F}^{-1}$ corresponds to inverse Fourier transform. We compared the difference of the phase transfer functions referring to shape of illumination masks such as gradient amplitude, conventional half circle, and annulus circle using synthetic intensity of the phase transfer function for $\sum_i \left|\tilde{H}_i(u)\right|^2$ in multi-axes.

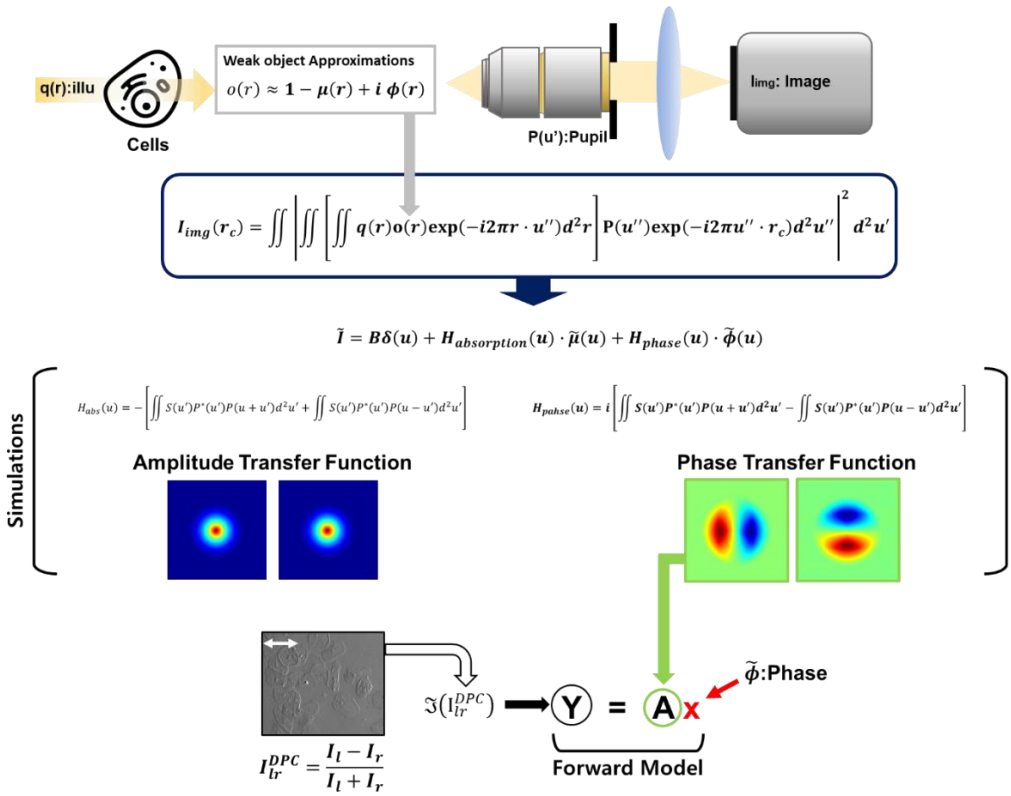

Figure 2.2 Summarization of quantitative phase reconstruction.

2.1.5 System configuration

Figure 2.3 illustrates the schematic of multi-contrast microscope, which was built on custom inverted microscope. For the custom microscope, off-the-shelf optic components were utilized. Mirror reflected the light in 90 degree and 0.5x tube lens was employed in this system to shrink down the overall dimension, providing the portability to the system. Instead using condensers, array of LED (Adafruit, 32x32 RGB LED matrix panel) was adopted to the system. Matrix had 4 mm spacing between LEDs and was placed 70 mm above the sample where illumination could be expected as planewave on the sample. Each LED in the matrix panel was controlled by MCU board (Arduino, Arduino UNO) to provide the patterns that illuminate the sample in a given angle. In this study, LEDs were not synchronized through sending trigger signals with the color camera (Thorlabs, CS505MU), instead controlled the exposure time to 32 ms to eliminate the rolling shutter effect. Using color calibration algorithm given by manufacturer, intensity of each red, green, blue was balanced from flat microscope slide glass illuminated by pattern shown in Figure 2.3. This calibration makes camera equally sensitive to each color, making each color image similar to condition of single-color illumination. All image was

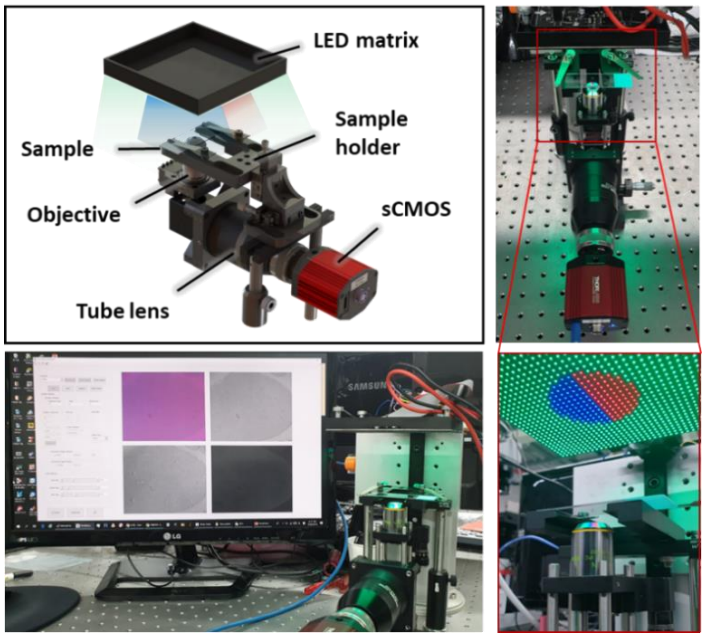

Figure 2.3 System configuration of single-shot multi-contrast microscopy.

captured using full sensor (2448 x 2048) with 12-bit ADC resolution. With this configurations, 1-axis single-shot multi-contrast image could be acquired within ~ 30 fps, which could be reduced in half in ideal case when 2-axial images are captured for reconstruction of QPI.

ULSAN NATIONAL INSTITUTE OF SCIENCE AND TECHNOLOGY

2.1.6 Effect of illumination patterns

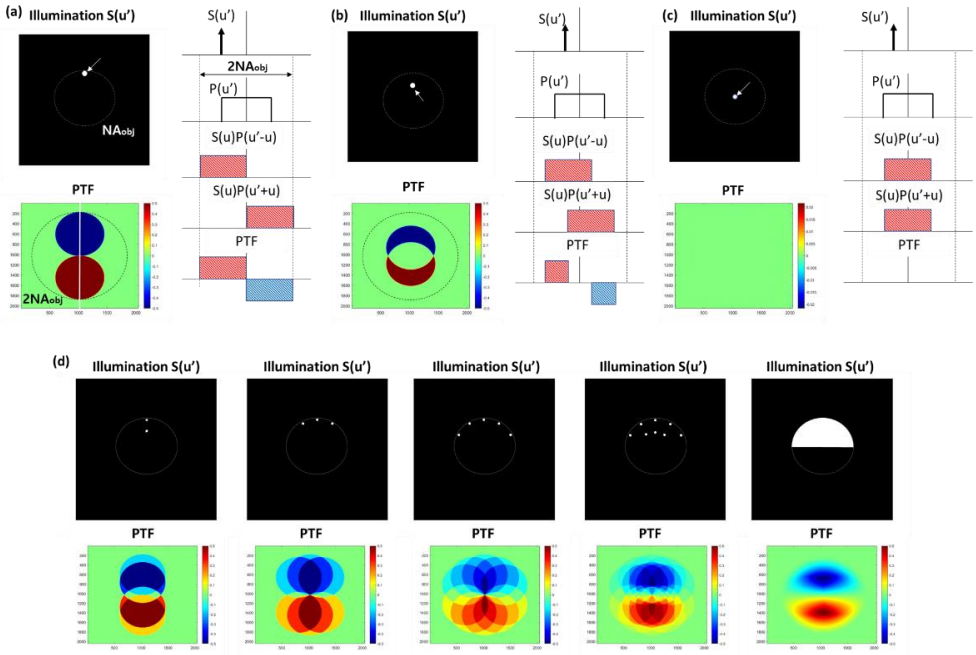

Figure 2.4 Relationship between illumination and phases in freqeuncy spectrum. Point source located near (a) NA of object, (b) NA/2 of object, and (c) center. PTF is difference of convolution and corss-correlation between illumination source and pupil function.

In DPC-based QPI, PTF or WOTF play as crucial role that directly matters to phase visibility in intensity form. Particularly, illumination characteristics and pattern are the key that affects the frequency responses in PTF. Therefore, understanding PTF and relationship of illumination patterns are significant to realize the quantitative phase imaging. In this section, we explored the effect on PTC through tuning the illumination patterns by simulation according to Eq. (2.10).

S(u) or illumination was assigned as single point source, making it equivalent to single LED illumination in real setup, and adjusted its location in order to analyze the phenomena in PTF. In Figure 2.4, we explored the PTF that related to single point source placed in various location within the objective NA. Since WOTF can be extracted by subtraction between cross-correlation function and convolution of pupil and source, we illustrate correlations and its subtraction at the side of each illumination images. Figure 2.4a illustrates the effect of PTF when point source is located near objective NA (coherence parameter $\sigma = \frac{NA_{illumination}}{NA_{objective}} \approx 1$ [40]). For this case, no overlaps were found, resulting all phases has been shifted without distortions. Radius of intensity spectrum is corresponding to NA of object and summation of both would make 2 times of NA. This explains why system with incoherent illumination has resolution two times better than that of system using coherent illumination. If point source moves toward center with low oblique angle $\sigma = 0.5$, as shown in Figure 2.4b, PTF start to have overlapping area where it could be found near axis. As point source illuminates at the center $\sigma \sim 0$, no

ULSAN NATIONAL INSTITUTE OF SCIENCE AND TECHNOLOGY

phase responses were found. In Figure 2.4d, we described the PTF under multiple illuminations.

Furthermore, effect of illumination patterns was tested to real microscope setup using unstained cervix cells as shown in Figure 2.5. We captured DPCs and reconstructed the phase according to σ which was tuned from 0.3 to 1.3 by changing the radius of asymmetric half circle patterns. At the low coherence parameter, diffraction from cells were shown in BF image, but no contrast was found in DPC images. Low and high frequency response is lost in this scenario. Therefore, QPI showed background amplified images with corrupted phase information. When coherence parameter $\sigma > 1.0$, contrast has been enhanced in DPC images as well as in QPI reconstruction. Moreover, depth sectioning was enhanced while artifacts were reduced (cancelling the diffracted images behind the focus). Interestingly, $\sigma = 0.9$ illumination provided structural information in DPC, but signal to noise ratio was still low compare the that of $\sigma > 1.0$. Throughout this experiment, we now understood that coherence parameter should always be larger than 1.0 that illuminates the specimen from high angles in order to fully reconstruct the QPI without any artifacts.

2.1.7 Result & Discussion

Phase calibration using microbeads

Tikhonov's regularization term γ is generally introduced to stabilize the deconvolution process in DPC-based QPI. Thus, optimizing the regularization γ is significant for accurate recovery of the phase along with noise reduction [40, 57]. By capturing the silica microspheres with a size of 5 μm (Sigma Aldrich, 44054) immersed in 86-89% glycerol solution (Sigma Aldrich, 49781) between microscope cover glass and cover glass, we optimized the regularization parameter to correlate the recovered phase to ideal phase delay. Two DPC imaging in the vertical and horizontal direction were performed using color assigned illumination pattern and QPI was performed to retrieve phase in quantitative manner. 10x/0.25NA objective lens was utilized for this experiment. The refractive index of microsphere and glycerol was found as $n_s = 1.46$ and $n_g = 1.45$, respectively. In this case, the ideal phase delay induced by specimen could be estimated as $\Delta\varphi = \frac{2\pi}{\lambda}(n_s - n_g)T = 0.593$ rad, where T was 5 μm , and wavelength (λ) of 530 nm was given by the average of RGB [37]. Here, both DF and QPI were shown in Figure 2.6. Compare to DF, microspheres were all correctly matched each other, and no eliminated structures were found in QPI. For this system, regulation parameter γ was $5\text{x}10^{-2.3}$ was utilized. The phase information measured along the white solid line crossing the microsphere is shown as purple solid line in the graph. Our measured phase delay was 0.597, which corresponds to less than 1% of phase difference from ideal phase delay. However, tuning regulation parameter γ to 1 makes system uncalibrated and makes phase large errors as shown in purple dash line in the graph. One should know that there could be variations in measurements due to uncertainties in size, refractive index of microspheres, and aberration in optics [37, 57].

Noise reduction for QPI using regularization method

Tikhonov's regularization (Tik) method introduced in deconvolution process guarantees the stability in the reconstructed images, suppressing the noises from low-frequencies and over incoherent diffraction limits. However, noises were not fully removed and were still visualized across whole FOV in the QPI. This may be caused by low-sampling frequency in the imaging system which correlates to the physical size of pixels in camera sensors. According to Nyquist-Shannon sampling theorem, the image pixel should be half smaller than the size of object which we wish to visualize. If we think this in frequency domain, it corresponds that maximum sampling frequency should be at least two times higher than obtained frequency. Maximum sampling frequency could be provided by $\mathrm{F}_{cam} = \frac{magnification}{2*pixel\ size}$, where magnification is magnification of system, and pixel size of imaging sensor. In order to provide phase information within the incoherent diffracted limits in Fourier spectrum, we need to satisfy the Nyquist criteria condition $\mathrm{F}_{cam} > \mathrm{F}_{PTF}$, where F_{PTF} denotes frequencies inside of $2 * NA_{obj}/\lambda$ [38]. Using 40x/0.55NA objectives, pixel size of $3.5\ \mu\mathrm{m}$ in CCD and 530 nm of wavelength for the system, $\mathrm{F}_{cam} = 0.006 > \mathrm{F}_{PTF} = 0.002$ was satisfied. Although, small size of pixel increases the SNR from limited illumination throughput. Furthermore, sampling frequency computed by small pixel size are more sensitive to noises, picking up more details from the object frequency. Therefore, noises after deconvolution process were not clearly eliminated. To make our deconvolution stable and

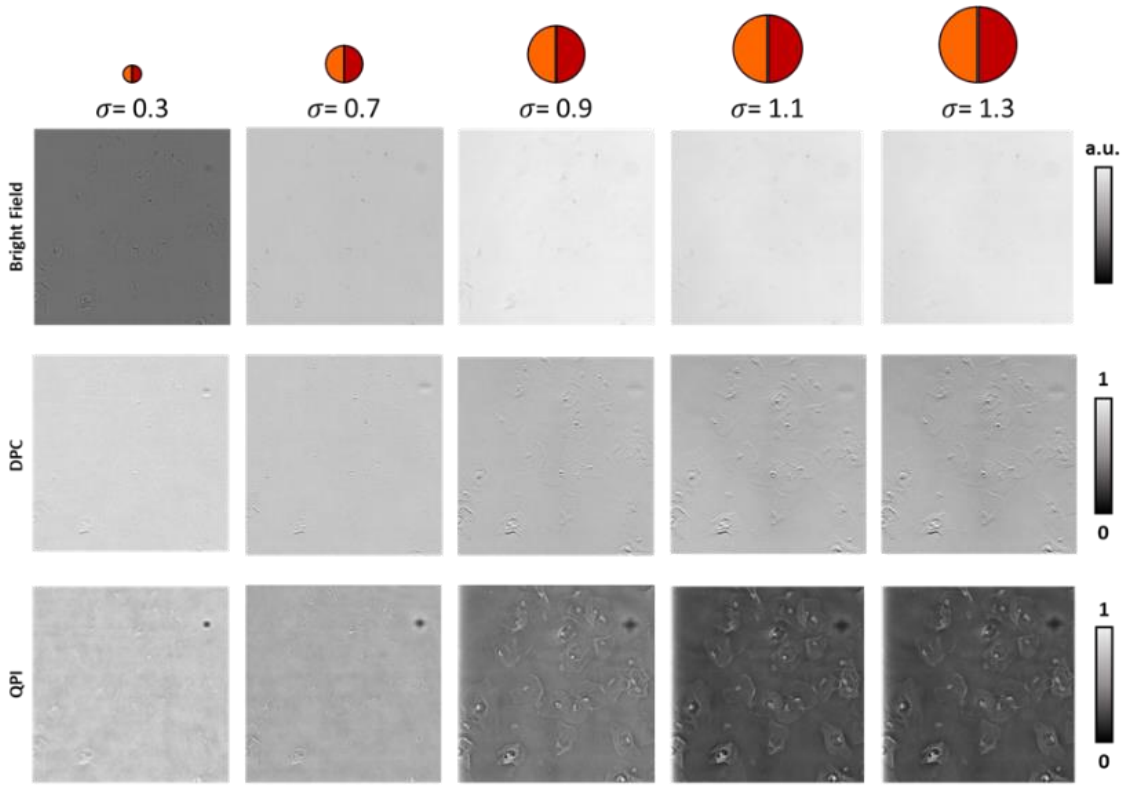

Figure 2.5 Effects of spatial coherence parameter σ to the imaging system. Larger coherence parameter provide stabilized phase contrast as well as qunatitative phase estimation.

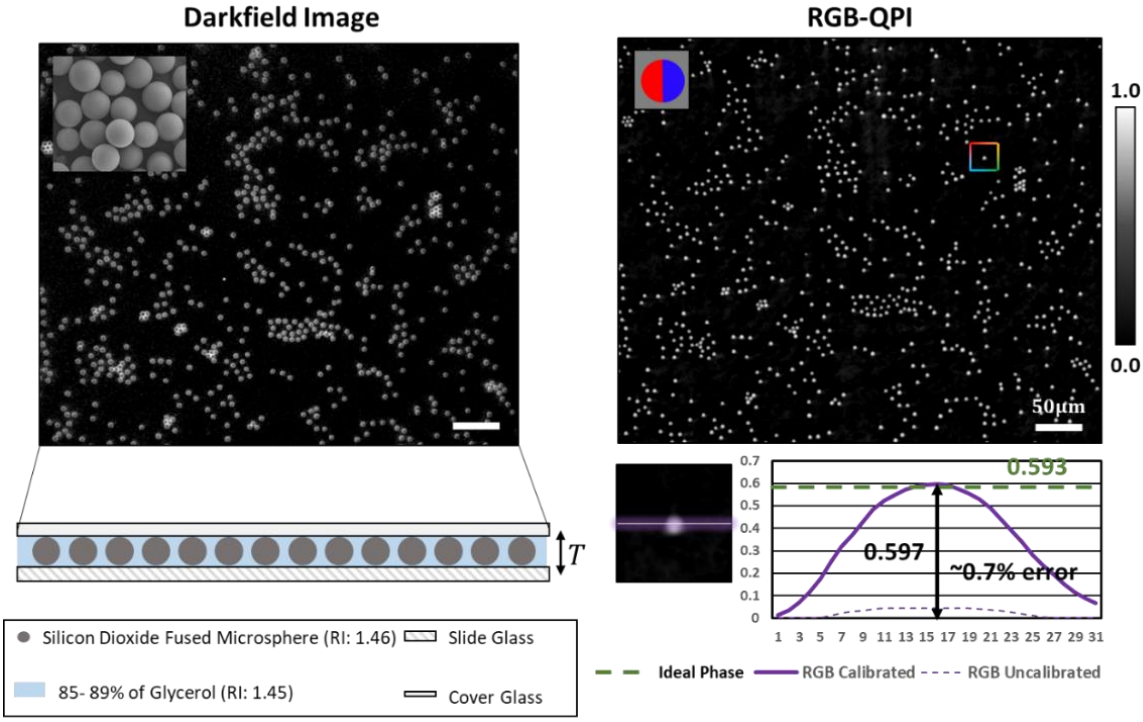

Figure 2.6 Phase measurement accuracy using single-shot multi-contrast illumination pattern. DF is provided to compare the structural deformations or missings from QPI. Phase delay is measured from distribution of line crossing the center of micorsphere.

robust to noises, we utilized hybrid regularization method based on total variation (TV) regularization and Tikhonov's regularization . TV-regularization is well known signal processing method that has great ability to eliminate noises while preserving the geometry of object. Here, we empirically selected 0.022 for TV-regularization term and performed 20 iteration using alternating direction method of multipliers for noise reduction [53]. To test out the processing, this time, we captured fibroblast cells using our imaging system. Top row of Figure 2.7 presents the QPI using Tikhonov regularization method only. Amplified noises could be found in the retrieved phase image by looking at the magnified images. However, application of hybrid regularization method had significantly reduced the noises from the image. In addition, no distortions or undesired reconstruction of objects in terms of geometrical shape was were not found in TV-Tik regularization result. Therefore, overall image looks smoother with hybrid method. At the bottom of the Figure 2.7, we compared QPI to negative phase image captured by conventional Zernike phase contrast microscope. Reconstructed QPI demonstrates correlated geometrical information compare to that from conventional phase microscope, while offers more details in cell constituents.

ULSAN NATIONAL INSTITUTE OF
SCIENCE AND TECHNOLOGY

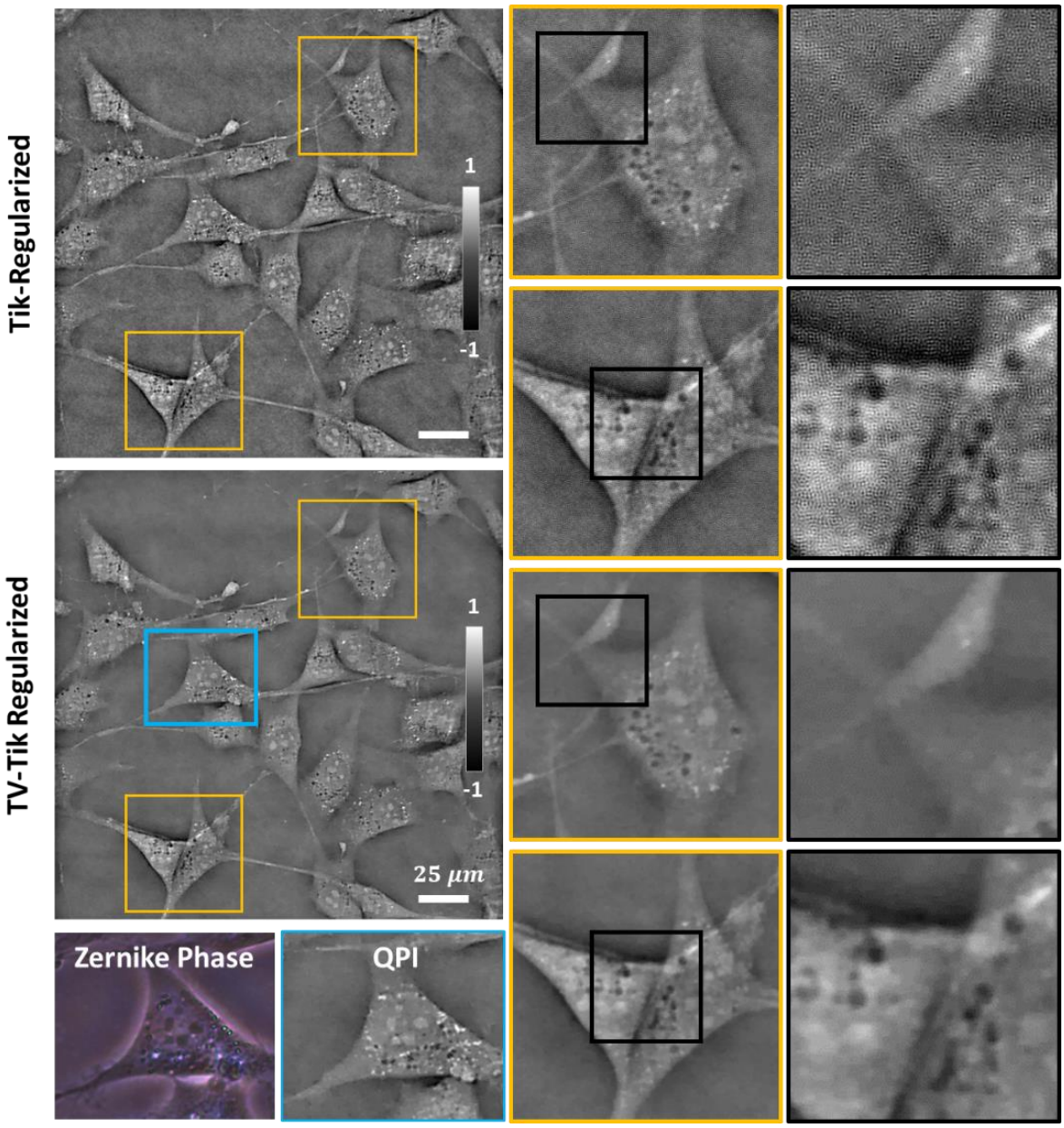

Figure 2.7 Result of noise reduction in QPI using live fibroblast cells.

Single-shot multi-contrast imaging of biological specimens

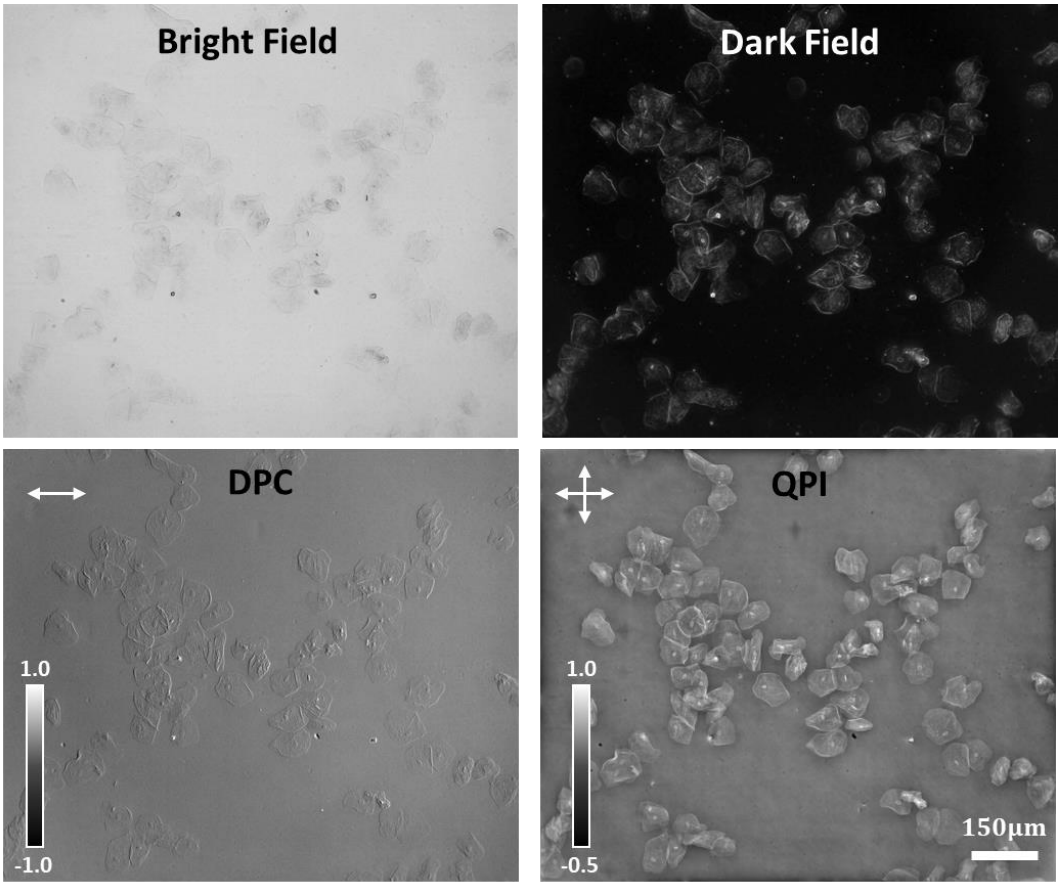

Figure 2.8 Result of multi-contrat microscope uisng cheek cells. BF, DF, QPC, and QPI was reconstructed with single microscope setup. 10x/0.25 NA objective was utilized for this imaging.

Multi-contrast imaging capability was evaluated using various biological specimens. First, we acquired images from human epithelial cheek cells. Since cheek cells are transparent with refractive index similar to that of surrounding medium, it is very quick and useful sample for evaluating the multi-contrast imaging. Therefore, it is very difficult to see the details through bright field image presented in the top left corner of Figure 2.8. On the other hand, dark field image clearly visualized the contrast that arises from the scatterings at the cell boundaries. Because light is illuminated outside of the numerical aperture of objective lens, there are no signals at the background, hence, visualized only black. DPC of horizontal where black small features were found in bright field image. Solving inverse problem using horizontal and vertical DPC measurements, quantitative phase image was obtained. Bottom right of Figure 2.8 presents QPI of cheek cell. In QPI, cellular constituents were clearly visualized with great contrast.

We also captured the transparent small animals to perform in-vivo imaging. Wild-type Caenorhabditis elegans (C. elegans) was utilized for this case. C. elegans was immersed in microscope immersion oil on the top of the slide glass to suppress its motions. As shown in Figure 2.9, some contrasts were found in bright field, dark field, and DPC images, but not much details were presented.

ULSAN NATIONAL INSTITUTE OF SCIENCE AND TECHNOLOGY

However, QPI provided significantly higher contrast compare among other imaging modalities. Anatomical structure of C. elegans was clearly discerned in QPI.

2.1.8. Conclusion

Throughout this study, multi-contrast imaging was evaluated and presented the great imaging capability that offers complementary information of specimens in the single microscope setup. Advantage of this system is according to its simplicity and cost-effectiveness which only requires color LED matrix implementation on the illumination part. Assigning the colors on the illumination pattern that corresponds to each color channel of imaging sensor allowed single exposure for acquiring multiple contrast modalities. Using regularized devolution method with two-axis qualitative phase contrast images, noise suppressed quantitative phase was successfully recovered. Once quantitative phase was calibrated through correlating to the ideal phase delay by capturing the microsphere, our system offered stable performance in the various range of magnifications. On the other hand, few issues were found to be considered for using simultaneous multi-contrast imaging system. Although objectives were designed to correct the chromatic aberrations, minor deviations in the structures of object for each image channel. Due to this reason, slightly unfocused or blurred image would be presented in QPI which is sensitive to focus misalignment, thickness of specimen, and higher magnification. Another issue in this system was difference in sensitivity of chromatic absorption. This may critically affect DPC/QPI, which may strictly limit the specimen to totally translucent specimens.

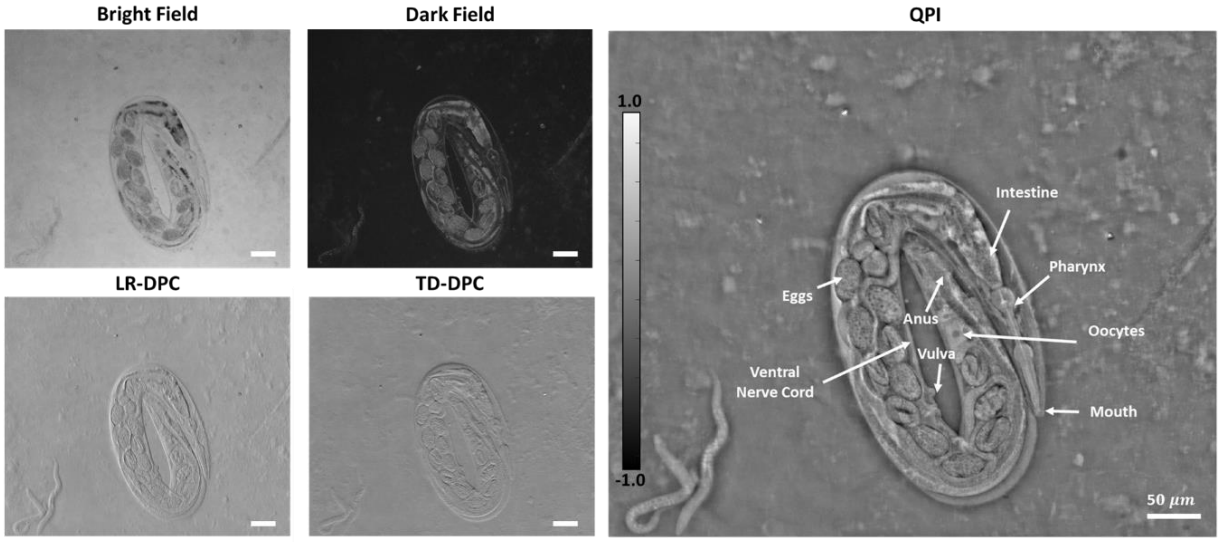

Figure 2.9 Result of multi-contrat microscope uisng c.elegans. 40x/0.55 NA objective was utilized for this imaging.

ULSAN NATIONAL INSTITUTE OF SCIENCE AND TECHNOLOGY

2.2 Development of QPI system using diffuser based NIR illumination

2.2.1 Introduction

Phase imaging has become a valuable tool in biomedical fields. Phase of specimens is somewhat difficult to acquire from intensity-based images or conventional bright-field microscopy, hence, some imaging modalities, such as Zernike phase contrast, differential interference contrast, have been provided to translate the phase information into measurable intensity [40]. However, these two classical methods provide information of the phase qualitatively, leading to difficulties in data interpretations or further analysis [58]. In recent years, quantitative phase imaging (QPI) technique has been introduced as alternative method that recovers the optical path length or phase of specimen from intensity measurements in quantitative manner [37, 40, 53]. Label-free imaging is one of the great advantages of QPI, allowing variety of applications to visualize the quasi-transparent specimens without any damages of photo-bleaching and phototoxicity from labeling [17].

During the last decades, various QPI approaches such as interferometric microscopy, digital holography (DH), transport-of-intensity equation (TIE), Fourier ptychography (FP), and differential phase contrast (DPC) have been developed [37, 40, 53]. Each of these techniques is based on different principles for imaging to recover phase of biological samples in quantitative manner. DH or interferometric approaches, in general, uses coherent light source, making the system expensive, sensitive to misalignments, speckle noises, and vibration [54, 56]. Alternative to coherent illumination system, TIE had been introduced as a well-established non-interferometric phase retrieval approach that uses partial coherent illumination. TIE is 2D second-order elliptical partial differential equation that uses multi-axial defocused images and inverse method-based Poisson solver to recover phases of object. TIE is fully compatible method with bright-field microscope configuration and allows resolution up to the incoherent resolution limit [54, 59]. FP is another QPI technique to retrieve the complex field of an object using multiangle coherent illumination in microscopic imaging. Using the low-resolution images captured from each different incident angle of illumination, the bandwidth of the Fourier spectrum can be expanded with an iterative phase retrieval algorithm. Without any mechanical scanning, FP allows to provide large field-of-view (FOV) with enhanced resolution in either amplitude or phase image [51, 52, 54]. Among others, DPC approach-based QPI, however, uses only four images from asymmetric partial coherent illumination patterns and provides promising non-interferometric performance with better system stability. Due to illumination properties, DPC approach offers twice better lateral resolution limit ($\frac{2NA_{obj}}{\lambda}$), better optical sectioning, and less speckle noise [52, 54]. In addition, the first-order derivative response to phase in DPC based QPI system has less sensitivity to frequency noise [54, 56]. By utilizing the weak object transfer function, complex field of weakly scattering specimen can be simplified and further able to be separated into phase and amplitude in the transfer function. Through a

ULSAN NATIONAL INSTITUTE OF SCIENCE AND TECHNOLOGY

simple deconvolution method with regularization term, phase could be quantified from multi-axes DPC measurements [37, 40, 53].

Typically, illumination patterns in DPC based QPI system has been designed with a half-circle [40], which was later expanded to annulus [54], sector-form [60], radial [57], and gradient amplitude [56]. These patterns were implemented using various methods including physical amplitude masks, programmable LCD or LED matrix [61], and spatial light modulator (SLM) [62]. Moreover, there were efforts to utilize partially coherent multi-color patterns to improve the imaging speed and reduce the complexity of system [37, 60]. Although these methods in DPC successfully have been quantified the phase, application of QPI is mostly restricted to live cell imaging which resulted from the utilization of weak-object approximation. Moreover, absorption is another factor of limiting application field. Highly absorbing object causes phase error while recovering the phase information through calculating the DPC images from complementary pattern with asymmetric illumination sources [40]. In order to solve the issue, shifting the illumination wavelength to near-infrared spectrum (NIR) would allow to assume the highly absorbing sample as weakly scattering object as using the visible spectrum [17, 63]. However, not only there are no off-the-shelf NIR based programmable LED matrix to afford but also developing NIR-based LED matrix is labor-intensive task and expensive. In addition, using NIR illumination for LCD based pattern is not appropriate because LCDs are commonly designed for visible lights, leading to the phase vanishing from illumination leakage. Using physical amplitude mask with NIR illumination may be available, yet, still it requires condenser lens which is still expensive and cumbersome to align the optics. Therefore, applications in thick tissues or stained object are not appropriated and have been avoided to capture with conventional DPC based QPI system.

In this study, a new approach of DPC microscopy is proposed by using diffuser based NIR illumination with single LED source. Our novel approach to the DPC incorporates diffuser with physical patterns made out of 3D printed material to generate the scattering effect which converts the coherent characteristics of single point source from to partial coherent. Without adapting expensive apparatus to the system, partial coherent illumination condition was maintained, which enhances the lateral resolution up to incoherent limit. Moreover, utilizing NIR illumination may lower the scattering, avoiding absorption and attenuation of the transmitted light from the thick specimens or highly absorbing samples. Therefore, weak-object approximation was still valid for computing the phase from 2-axis DPC measurements. Herein, various illumination patterns were realized in our illumination configuration and performances were explored and studied. In addition, proposing QPI was evaluated and experimentally demonstrated using stained cervix cells and stained mouse brain tissue.

2.2.2 System configuration

Figure 2.10 shows a schematic of the proposed QPI system setup, consisting of single NIR LED with

ULSAN NATIONAL INSTITUTE OF SCIENCE AND TECHNOLOGY

center wavelength of 780 nm (Thorlabs, M780L3), series of optical diffusers (Thorlabs, DG20-120-MD, DG20-220-MD) as illumination apparatus. At the filter for generating the illumination pattern, customized shapes of ABS block were made utilizing 3D printer in this study. This 3D printed object efficiently blocks the illumination on the non-opened area, hence, offering the desired shape without any TFT/LCD panels or programmable circuits for DPC acquisition. In order to capture the image, customized microscope was employed, incorporating 10x objective (Olympus, PlanN10X) with 0.25 numerical aperture (NA), infinity-corrected tube lens (Thorlabs, ITL200). All the data was collected by a 16-bits sCMOS (Andor, Zyla 4.2 Plus, 2048×2048 pixels, 6.5μm pixel pitch). 3D printed filter was manually rotated at 0,90,180,270 degrees for capturing the 2-axis DPC images with condition of short exposure time of 30 ms.

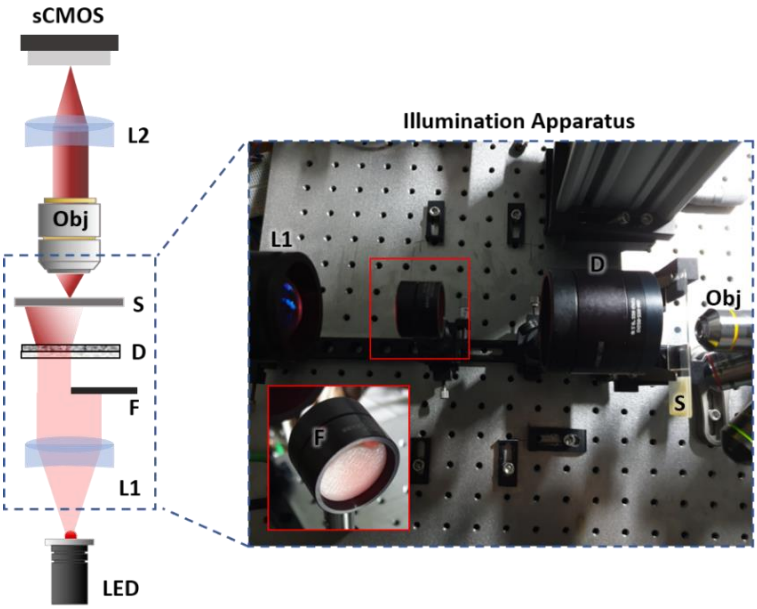

Figure 2.10. System schematic of quantitative phase imaging system diffuser based gradient NIR illumination. Asymmetric patterns were generated from the physical filter with single NIR (λ_c=780 nm) illumination source. Diffuser is placed before sample to create scatterings that act similar to partial coherent light source. Patterned filter was developed by printing 3D models that intentionally designed in prior. For this system, customized infinity-corrected invert type of microscope was developed. L1: collimator lens; F; 3D printed filter; D: diffusers; S: sample; Obj: objective; L2; tube lens.

2.2.3 Gradient source calculation

Principle of the system is following the 2.1.3 Weak object transfer function (WOTF) section. For the gradient amplitude patterns, gradient mask was applied to the partially coherent illumination. We redefine the S(u) as following:

$$S(u) = A(u) \cdot \mathrm{circ}(\psi) \tag{2.14}$$

where A(u) is amplitude mask that corresponds to following:

$$A(u) = \begin{bmatrix} \alpha(n) \\ \alpha(n) \\ \vdots \\ m \end{bmatrix} \mathcal{T}(k), \quad (\alpha(n) = \frac{(s \cdot n - 1024)}{1024}) \tag{2.15}$$

$\alpha(n)$ with slope s is a linear function to create a gradient slope by stacking $\alpha(n)$ in 2D matrix form; n, m denotes pixels (if we use 2048x2048) in u_x, u_y, repectively. Moreover, $\mathcal{T}(k)$ is a transformation function for 2D matrix which rotates amplitude mask in four different directions to capture, and it is define here:

$$\mathcal{T}(k) = \begin{bmatrix} \cos(k) & -\sin(k) \\ \sin(k) & \cos(k) \end{bmatrix} \begin{bmatrix} u_x \\ u_y \end{bmatrix} \quad (k = 0,180,90,270) \tag{2.16}$$

For gradient annulus pattern, we adjust the $\mathrm{circ}(\psi)$ function as following:

$$\mathrm{circ}(\psi) = \begin{cases} 0, & |\psi| < 0.9, |\psi| > 1 \\ 1, & 0.9 \leq |\psi| \leq 1 \end{cases} \tag{2.17}$$

2.2.4 Partially coherent NIR-Illumination based on diffuser implementation

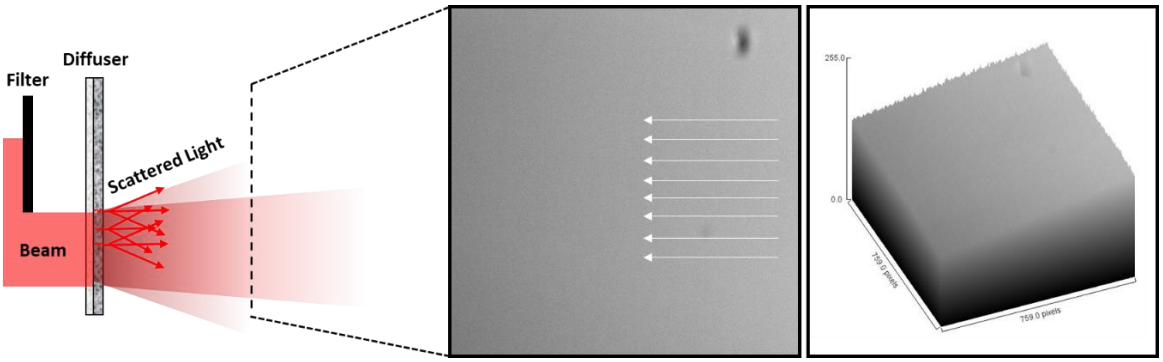

Figure 2.11 Schematic of diffuser based NIR illumination. Filtered light from point LED source passes the diffuser and randomly scatters with gradient effect due to near Lambertian (more similar to elliptical shape). Captured background image and its 3D surface plot clearly shows gradient amplitude, where white arrows denote gradient directions.

Series of diffusers in illumination apparatus randomly scatters the light that offers spatially less coherent illuminations with multiple oblique angles. To provide the phase shift to the specimen, we applied 3D printed physical patterns between diffuser and LED to create the patterns on the sample. From this apparatus, intensity of the patterned illumination will gradually decrease toward the center of the image as shown in Figure 2.11. In general cases, speckle noises were caused when highly spatial coherence

ULSAN NATIONAL INSTITUTE OF SCIENCE AND TECHNOLOGY

light such as laser passes the diffuser. However, typical LED sources have low coherence volume which is the product of coherence length and area. Coherence photon from different coherence volume cannot interfere each other; hence, LED would provide speckle patterns [64, 65]. Therefore, we utilized single LED source with characteristics of low temporally and spatially coherence to generate the low speckle noises after light traveled diffusers. To evaluate the effect of diffuser based partially coherent illumination, background images were captured without any sample placements using both with and without application of diffuser on the illumination apparatus. Herein, RGB LED-matrix was also applied for further comparative evaluation of the diffuser effect in background. Haralick's feature based on gray-level co-occurrence matrices (GLCM) was also computed to measure the texture of the noise in quantitative and statistical ways. Utilizing the probability of GLCM elements, texture statistics such as contrast, correlation, energy, and homogeneity can be calculated [66, 67]. Figure 2.12 illustrate how GLCM could be measured form gray scale image and equations are described as well.

Evaluation of effect applying the diffuser to provide partially coherence illumination using single LED source was compared in qualitative and quantitative manners. In qualitative manner, we captured images under different illumination conditions and cropped the original image consist of 2048 x 2048 pixels to 760 x 760 pixels to see details as shown in Figure 2.13. Intuitively, fine speckle noises were found in the background of diffuser based NIR illumination which minimally elevated the noises compare to that without diffusers (Figure 2.13e). Compare to images obtained using R,G,B LED-matrix,

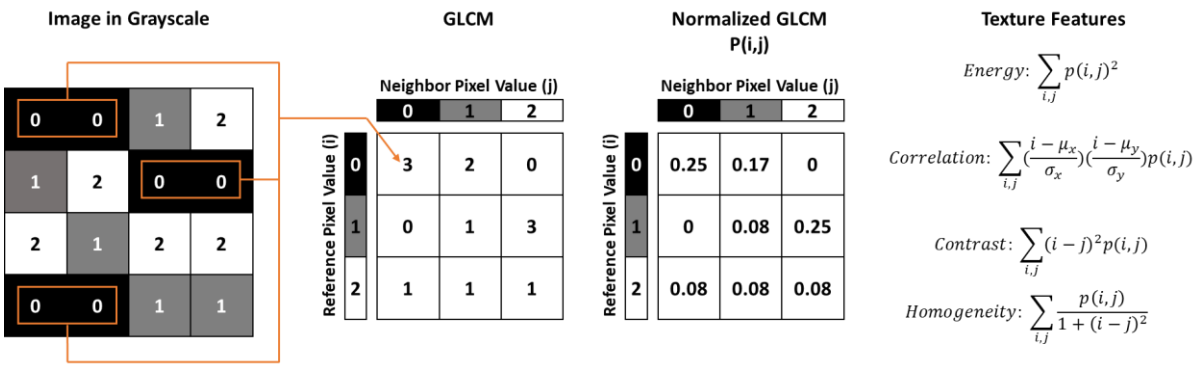

Figure 2.12 Illustration of Haralcik's texture feature calculation. From gray level image, pixel combinations were counted only considering the neighbor pixels on the right and marked in GLCM matrix. After marking all the combinations in GLCM from grayscale image, each element is divided by sum of all elements in GLCM to create the probability of combinations in matrix form (normalized GLCM). Using GLCM, texture features can be calculated.

higher SNR was expected using NIR-based illumination and clear qualitative background was able to observe. Due to spherical shape of illumination in each point source of RGB LED-matrix, intensity across the entire image in Figure 2.13(a-c) was found inhomogeneous [40]. Moreover, 3D surface plot was demonstrated to provide intuitive perception of noise in Figure 2.14. In quantitative ways, contrast, correlation, and homogeneity was calculated and described in Figure 2.14f. Background using NIR

ULSAN NATIONAL INSTITUTE OF SCIENCE AND TECHNOLOGY

shows significantly low contrast, higher correlation and homogeneity compare to these from RGB LED-matrix. These were expected that contrast in Haralick's texture features corresponds to variations between neighbor pixels. Usually constant image shows 0 in contrast; hence, higher values can be expected where noises were localized. Correlation is value that measures the mutual relationship or linear dependency between pixels range in -1 to 1 where NaN for constant image. In addition, Homogeneity provides extent of smoothness of gray level distribution of the image. Both correlation and homogeneity are expected to be high when there is low noise ratio (NIR backgrounds) as shown in Figure 2.14f. Comparatively, NIR with diffuser shows significantly low noises in quantitative measurements but it shows difference from NIR without diffuser application. However, these noises are found to be very small which can be neglected to capture DPC images. Furthermore, noises in NIR background is not expect for speckle noises patterns.

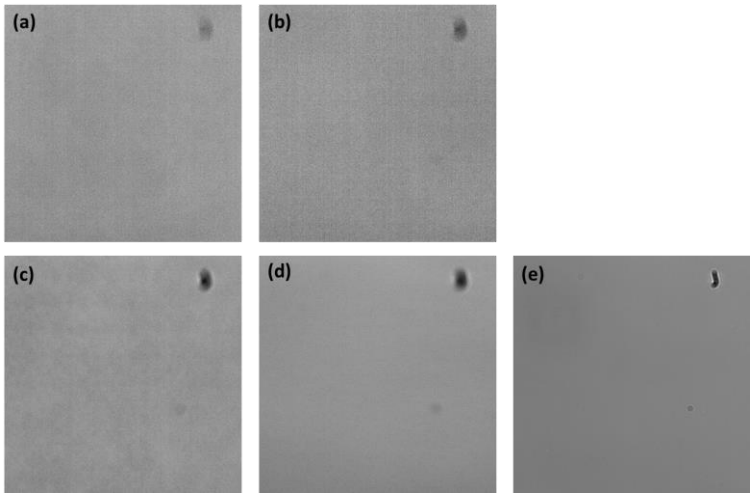

Figure 2.13 Background comparison using different illuminations. All images were cropped at corresponding position in 760 x 760 pixels from original 2048 x 2048 images. Background was captured using partially coherent (a) blue LED, (b) green LED, (c) red LED, (d) single NIR LED with diffuser employed, and (e) NIR LED without any diffuser attached (low coherence parameter).

ULSAN NATIONAL INSTITUTE OF SCIENCE AND TECHNOLOGY

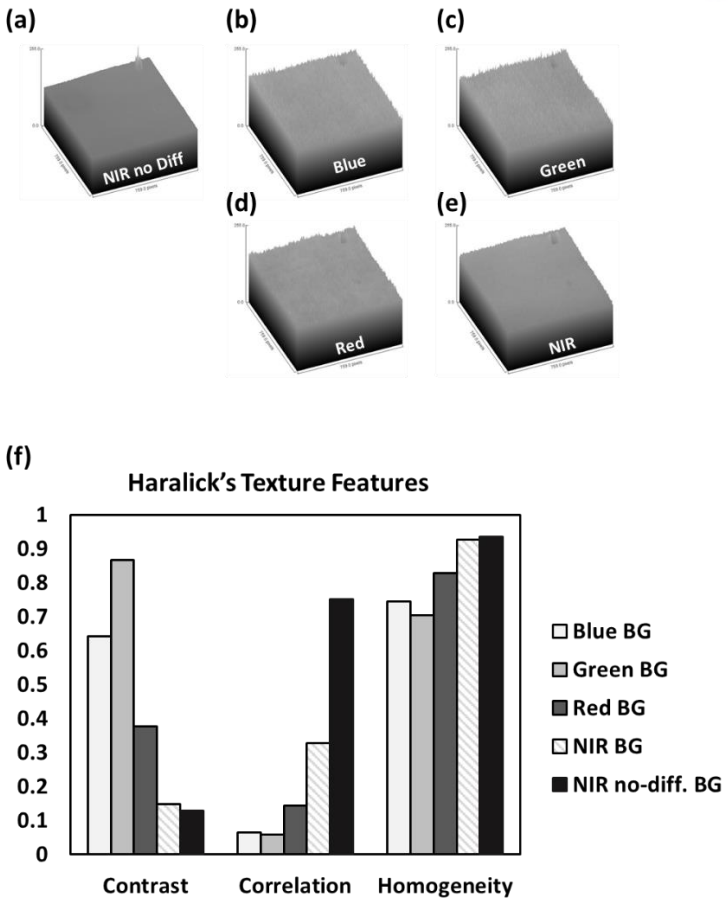

Figure 2.14 Surface plot under different illuminations and quantitative measurement of the background. 3D surface plot of computed from backgrounds from Fig. 2.4. Partially coherent (a) blue LED, (b) green LED, (c) red LED, (d) single NIR LED with diffuser employed, and (e) NIR LED without diffuser was visualized intuitively showing the noises. (f) Graph illustrates the Haralick's texture features which was calculated form (a-d).

2.2.5 Comparison of different diffuser-based illumination patterns on phase transfer function and DPC images

Validation of illumination patterns

Due to random vectors with phase variations caused by scattering effect, diffuser provide partially coherent illumination. When 1/2 of illumination is blocked before the light reaches the diffuser, light wave starts to diffract at the edge of the illumination stop or mask which creates diverging wave. The waves behind the stops contains less intensity compare to that of waves from opened areas. From this effects, gradient amplitude patterns can be generated for our system. If we block the middle part of illumination with size less than NA from gradient amplitude, gradient annulus patterns can be generated.

ULSAN NATIONAL INSTITUTE OF SCIENCE AND TECHNOLOGY

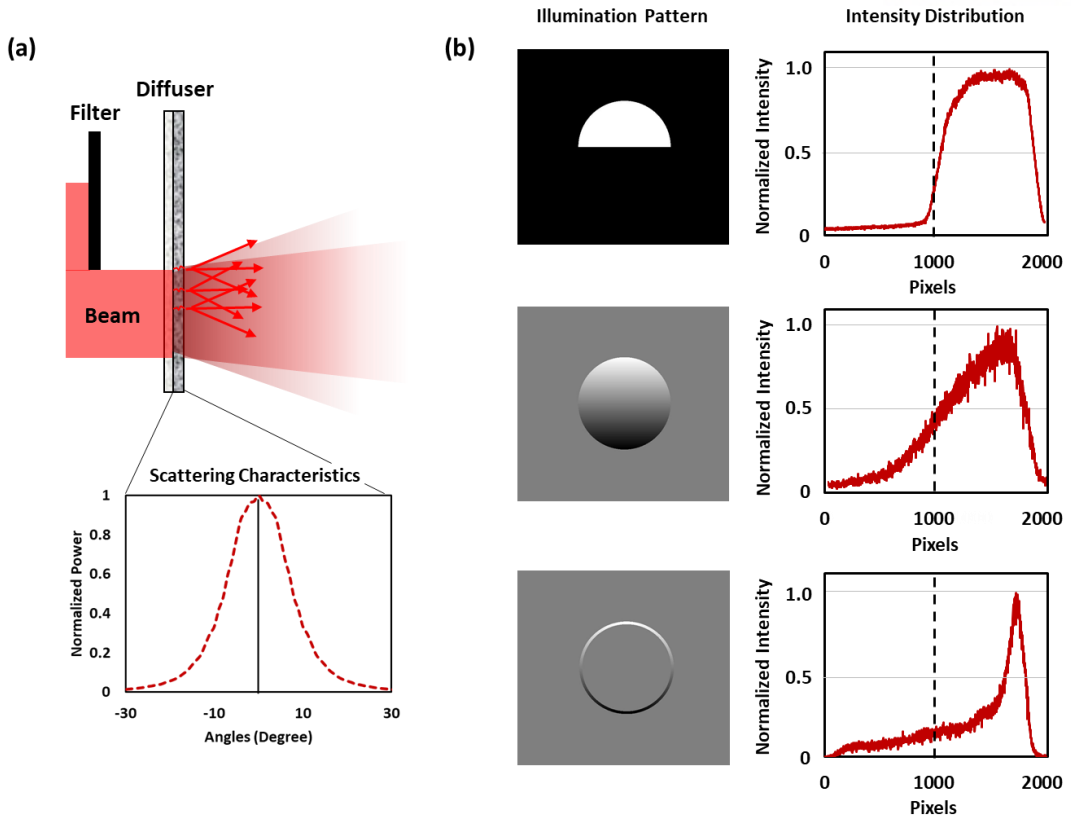

Figure 2.15 Illustration of illumination apparatus with beam path and measurements from illumination patterns. (a) Image describing the scattering characteristics of employed diffuser in terms of intensity and angle. (b) Intensity measurements of diffuser surface for each illumination pattern.

In order to validate this scenario from our microscope system, we capture the surface intensity of the diffuser. Normalizing the line profile crossing the center of the image, intensity variation of each the illumination pattern was evaluated as shown in Figure 2.15b. Compare to conventional half asymmetric pattern, intensity profile of gradient amplitude on the second column of the Figure 2.15b has shown the gradual increment after the middle of the diffuser surface which allows to create gradient amplitude illumination pattern. In addition, annulus pattern has shown highest intensity peak on the edge of the line profile. Throughout this measurement we can validated that illumination patterns are able to be designed and realized on real optical system through 3D printed objects.

Effect on PTF according to illumination patterns

In DPC based QPI system, illumination pattern is significant that induces different spatial frequency shifts in terms of phase. Different patterns are directly corresponding to transfers of the qualitative phase to measurable intensity with different contrast. Thus, exploring the efficient illumination pattern for transferring the isotropic phases over the broad frequency spectrum would be essential, resulting in enhanced resolution and visibility on the quantitatively retrieved phase image. Relationship between illumination and transferred phase in frequency spectrum could be studied through eq. 2.10. Since we are using wavelength of low scattering and absorbing characteristic, weak object transfer function is

ULSAN NATIONAL INSTITUTE OF SCIENCE AND TECHNOLOGY

still available for stained or thick samples.

Four different patterns such as half asymmetric [40], gradient amplitude [56], gradient annulus [54], and sectors [60] were designed and assigned for S(u) as shown in Figure 2.16. Furthermore, two different superimposing methods corresponds to different PTF axis was further analyzed. Most of the conventional DPC based QPI system captures complementary four images from asymmetric illuminations to compensate frequency loss mostly found on the central axis regions of PTF [40, 56]. However, 1/3 sector of the circle for illumination pattern only requires three images that can generate PTF of 3-axis covering the whole frequency spectrum after superimposition [60]. Similar to sector illumination pattern, we believe deign of gradient annulus pattern that covers the 1/3 of the circle will also available to offer 3-axis of PTF with advantages of using annulus pattern and reduced number of image acquisition. In Figure 2.16, intensity summation of half circle PTF shows phase losses on the low frequency regions and damping area on each corner. Gradient amplitude also requires 2-axis to cover whole frequency spectrum, however, shows better stability and accuracy with isotropic intensity in the intensity summation of PTF. Annulus pattern provides the best performances of retrieving the whole frequency spectrum within the incoherent diffracted limit, especially in low frequency regions. For capturing the three images with sectors, this avoids damping regions that was shown in the conventional half illumination, yet, still low frequency information is missing, and anisotropic phase transfer are shown in both low and high frequency regions. 3-axis gradient annulus pattern has advantage of reducing the number of image while offering the same phase transfer effect using four images with same pattern. Among the PTF models based on the illumination pattern, gradient annulus for either 2 or 3-axis was the optimal for effectively transferring the phase in terms of stability and accuracy within incoherent diffraction limits of spectrum. Comparing the line plot of PTF of half asymmetric circle, gradient amplitude and sectors, gradient annulus offers better transferring performances in high frequency region using all incoherent diffraction limit. Moreover, gradient annulus pattern provides the highest gradient (slope) within coherent region ($\frac{NA_{obj}}{\lambda}$), meaning better transfer of the phase in the low frequency regions.

ULSAN NATIONAL INSTITUTE OF SCIENCE AND TECHNOLOGY

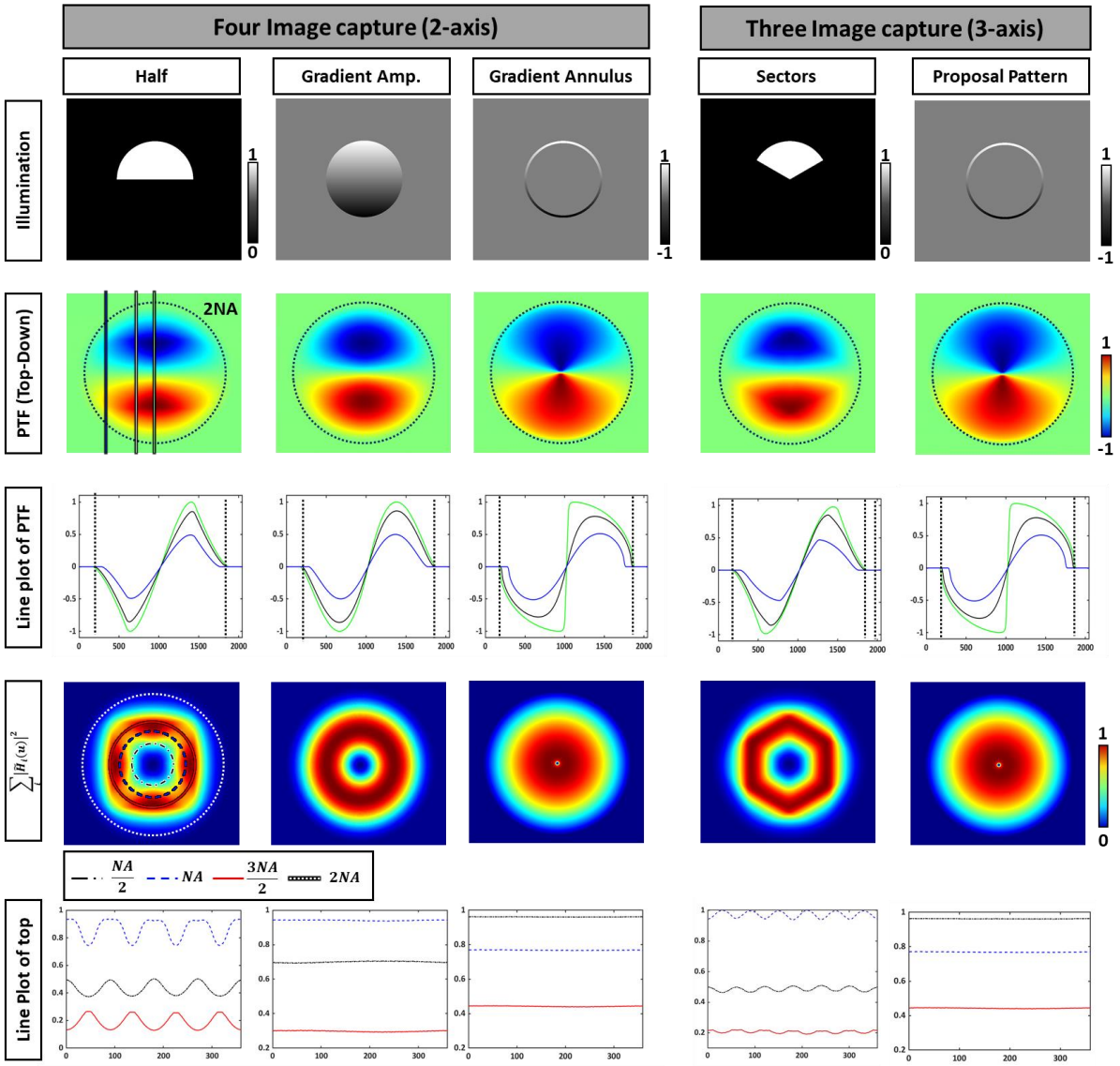

Figure 2.16 Comparison of different illumination patterns on phase transfer function (PTF) model and intensity sum of every PTF axis. Four patterns (Half, Gradient amplitude, Gradient annulus, sectors) were designed and two different superimposing methods (2-axis or 3-axis) were simulated.

ULSAN NATIONAL INSTITUTE OF
SCIENCE AND TECHNOLOGY

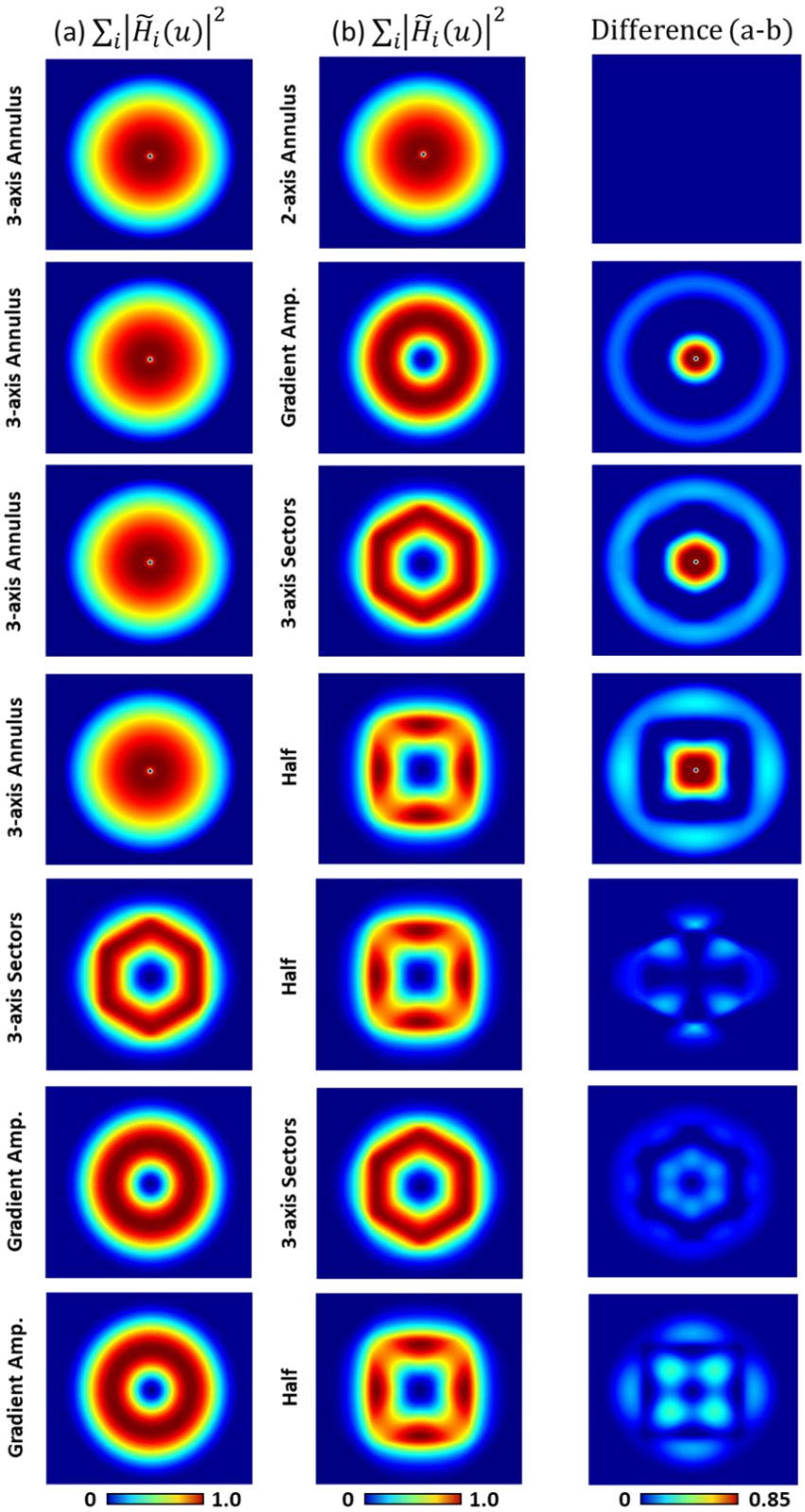

Figure 2.17 Deviations between illumination patterns in frequency spectrum.

ULSAN NATIONAL INSTITUTE OF SCIENCE AND TECHNOLOGY

In Figure 2.17, we further analyzed the deviations between different illumination patterns. It is clearly visualized that conventional half asymmetric and sector patterns have lowest phase transferred accuracy and stability after deviation from other patterns. Phase gradient amplitude shows smother and broader phase responses compare to half circle, but still limitations are remained in the low frequency. For annulus patterns, both 2-axis and 3-axis methods offers equivalent frequency responses, resulting no difference between their PTF summations. Moreover, annulus patterns show the best overall frequency responses. Particularly, annulus pattern delivers more information in high frequencies, compare to gradient amplitude which demonstrates the isotropic phase transfers.

2.2.6 Result & Discussion

Phase measurements by different illumination patterns

In order to verify the expected performances of PTF models above, we retrieved the phase quantitatively by capturing constituents of phase resolution target (Benchmark Technology, Quantitative phase microscopy target). Phase target contains both USAF 1951 resolution target and star target for validating the resolution and performance for QPI system. Moreover, phase target consists of 7 equivalent targets with different height that increases with interval of 50 nm. Each target with different height was utilized for phase calibration by optimizing the regularization term γ to correlate measured phase to calculated phase from $\phi = \frac{2\pi}{\lambda} d(n_1 - n_2)$, where λ is illumination wavelength, $(n_1 - n_2)$ is deviation of refractive index of object to surrounding, d is thickness of the object. The target is constructed with acrylate polymer (n=1.52) on the glass and each height is 56.8 nm, 109.9 nm, 168.2 nm, 215.6 nm, 272.2 nm, 328.4 nm, and 387.4 nm, respectively. Fig 2.9 summarizes the calibrated phases according to each height of target captured by each illumination patterns. Ideal phase was computed from real measurement of height and wavelength of 780 nm. First to seventh target has ideal phase (rad) of 0.237, 0.460, 0.704, 0.903, 1.140, 1.376, and 1.623, respectively. Since DPC based QPI system linearized the complex transmission function using Taylor-expansion, predicted phase was assumed by taking natural

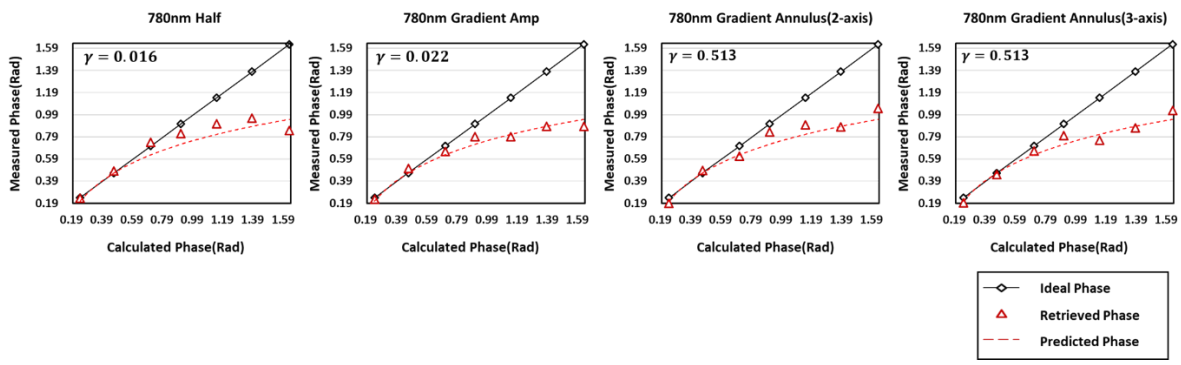

Figure 2.18 Quantitative phase measurement of each illumination pattern on the variations of target thickness.

ULSAN NATIONAL INSTITUTE OF SCIENCE AND TECHNOLOGY

log of weak object approximation on phase term, resulting in real phase and retrieved phase are related to $\ln(1 + i\phi)$ [68]. Therefore, we found that phase measurements from all patterns were found slightly lower than ideal phase. Error of phases above 1.0 radian starts to increase which is considered inaccurate in DPC-based QPI system. From Figure 2.18, our system was validated for capturing the weak scattering or slowly varying phase samples such as biological cells. While observing the retrieved phase, we adjusted regularization term to correlate retrieved phase to ideal phase. The gradient annulus was optimized with more general regularizations which values are much higher than that of half and gradient amplitude patterns.

In addition, star shaped object was captured from same quantitative phase microscope target and compared the performance relate to illumination patterns. Figure 2.19 demonstrates the resolution and frequency response in phase depending on the illumination patterns. Captured target height was approximately 150 nm. Target was found invisible when ordinary brightfield illumination was given. Utilizing the annulus pattern here also provides best performances as expected from PTF modeling. We validated that annulus pattern resolves better structure in the middle part of the star target though structure from half circle pattern was not well defined. Structure of phase target captured from gradient amplitude pattern was not as blurry as that from half circle pattern, however, slightly blurred areas were still visible in the central rings. For 3-axis annulus pattern, resolution and frequency response are similar to those of 2-axis annulus pattern, though comparatively higher intensities were distributed along the illumination axis. Additional quantitative analysis was demonstrated in Figure 2.20 using half and , gradient amplitude, 2 and 3-aix annulus patterns. Annulus pattern offers significantly higher contrast in high frequency response compare to other patterns. Furthermore, the annulus pattern results in less information loss on the line plot obtained in the low frequency range. In order to demonstrate the annulus pattern, we captured biological epithelial cells in Figure 2.21 and compared with half asymmetric pattern. Qualitatively, QPI retrieved from annulus pattern presents smoother image and better contrast across the FOV. Fourier transform of

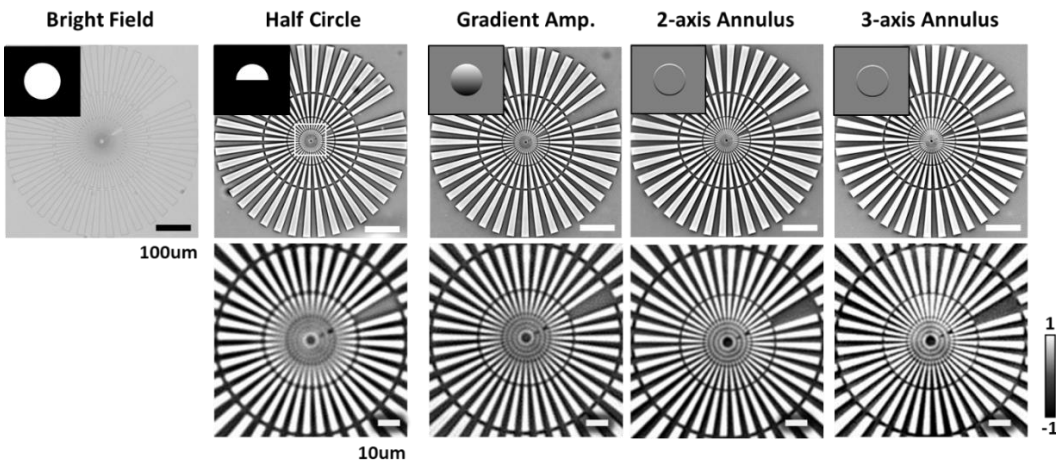

Figure 2.19 Quantitative phase images of star targets (unable to visualize with BF) for characterizing the performance of each illumination patterns.

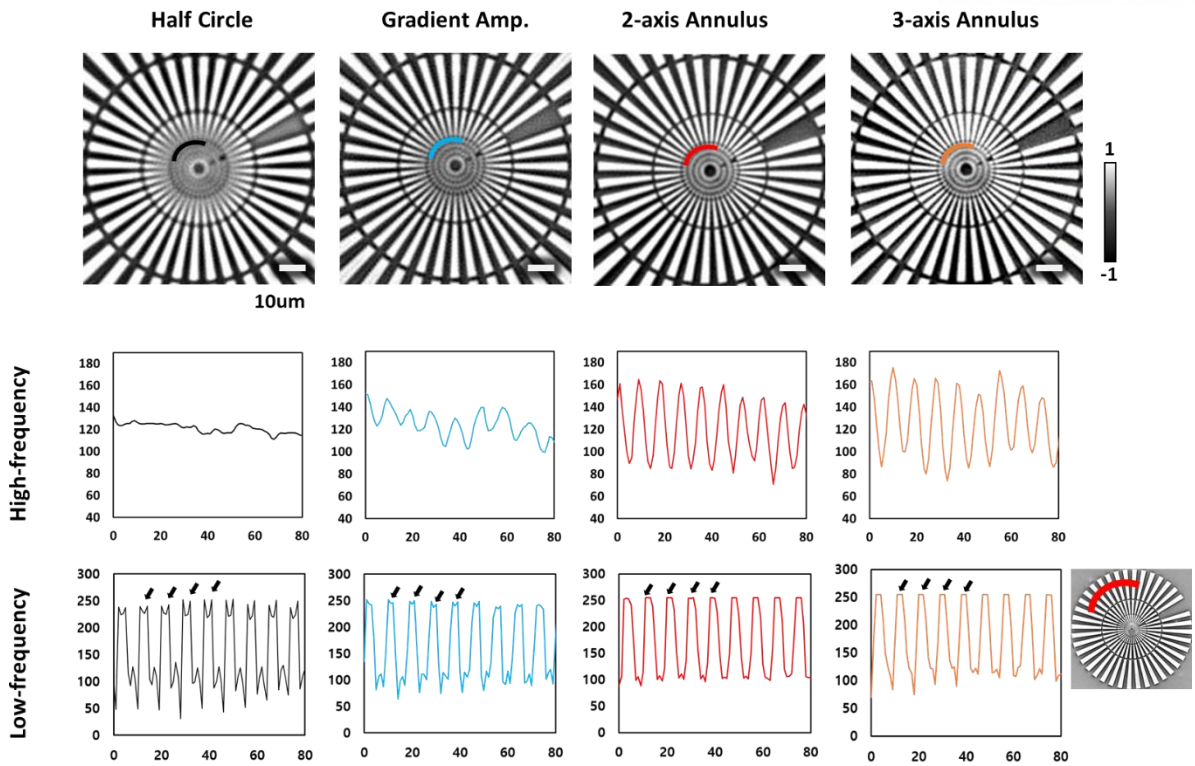

Figure 2.20 Comparison of QPI performance quantitatively

measured DPC clearly illustrate higher frequency distribution and area from annulus pattern which follows characteristics of PTF.

System characteristics using diffuser-based illuminations

Although use of NIR wavelength allows to maintain weak object assumption, at the same time, light itself has low scattering coefficient which may not provide sufficient expansion of illumination after transmitting diffuser. Thus, this could limit the coherent parameter less than 1 ($\sigma_{coherence} < 1$), breaking phase shift effect in DPC. In our NIR-based QPI system, number of implemented diffuser and distance between sample to diffuser were main parameters for determining $\sigma_{coherence}$.

In general DPC imaging system, increasing illumination NA or size of active LED diameter could increase $\sigma_{coherence}$. However, for this system, extent of scattering is the crucial factor to expand the light as well as to generate partial coherence illumination. Depending on number of diffusers for implementation, frequency response was different. Figure 2.22 presents relationship between frequency response and number of diffusers that was implemented to expand the illumination. Here we employed annulus pattern which is more sensitive to extent of $\sigma_{coherence}$. Upper row of the Figure 2.22 demonstrates Fourier transform of QPI image using cervical epithelial cells. Numerical value of grits indicates a particle size on the diffuser ground surface. Higher value employs smaller or fine particle and lower value incorporates larger or coarse particle in diffuser. Frequency response were found low

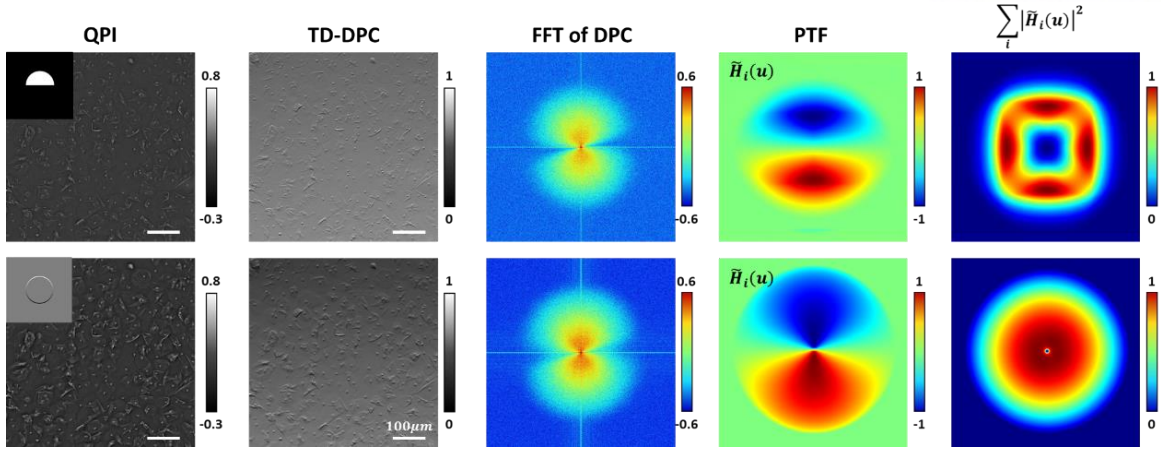

Figure 2.21 Representative QPI of cervix epitheial cells acquired by half and annulus pattern

especially bound in lower are for single diffuser implementation setup. 120- and 220-grit shows similar frequency response with average intensity value of 136.02, and 138.60, respectively. Use of 1500-grit illustrates lowest frequency response with average of 128.7. If we coupled 120- and 220- grit diffuser with distance 10 mm space, higher scattering effect were found, which enhances the frequency response. Average intensity found in Fourier spectrum of QPI was 142.22. Furthermore, line plot cross-sectioning the spectrum of QPI of combination diffuser configuration quantitatively indicates the highest performance compare to those from single diffuser implementation setup. Throughout this experiment, we concluded that using double diffuser was optimal and expressed the best frequency response which indicates the best $\sigma_{coherence}$.

We believe that distance between surface of diffuser to sample is another key parameter that generates the partial coherence illumination with scattering characteristics in our configuration. Figure 2.23 illustrates the phase retrieval performance according to distance between sample and diffuser. LED,

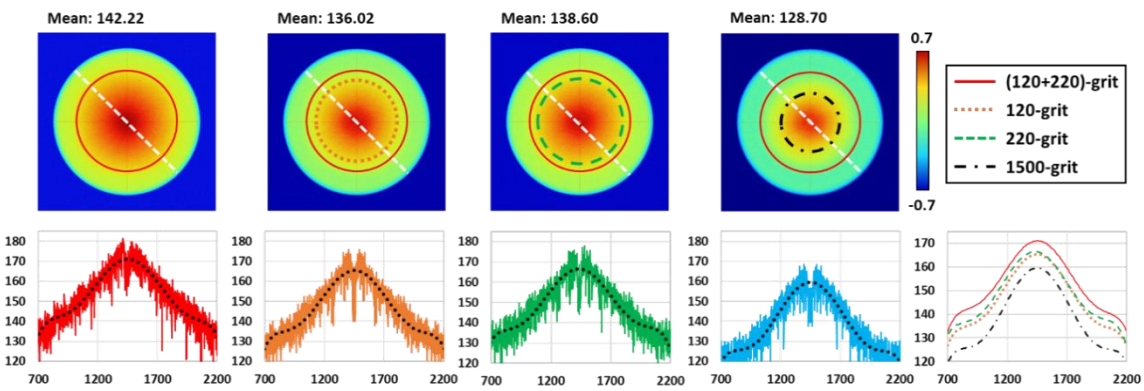

Figure 2.22 Analysis of QPI frequency response depending on implementation of diffusers.

ULSAN NATIONAL INSTITUTE OF SCIENCE AND TECHNOLOGY

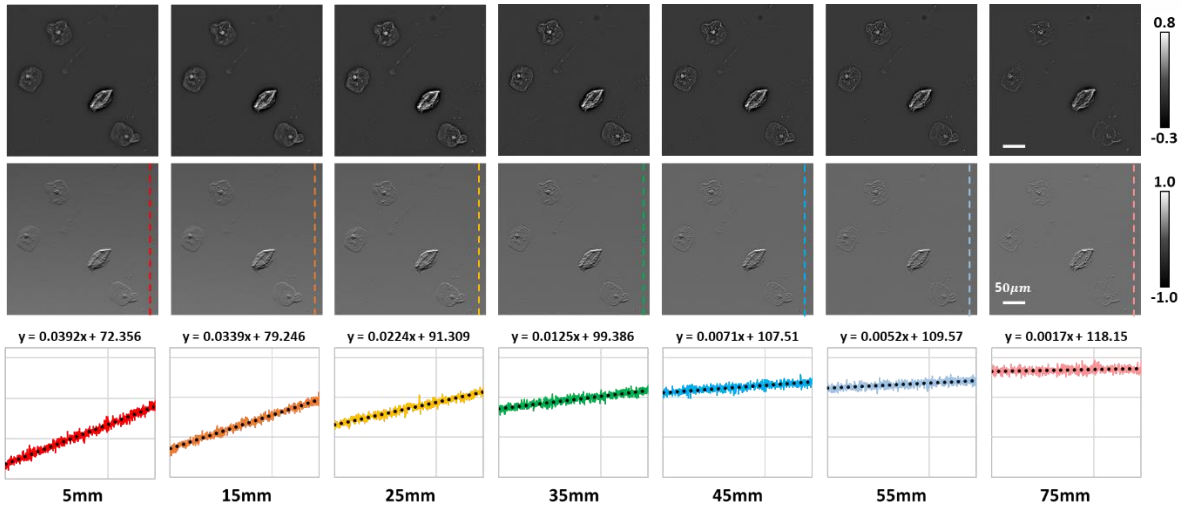

Figure 2.23 Analysis of the performance of QPI according to distance between sample and diffuser (or $\sigma_{coherence}$).

pattern, and diffuser parts in our illumination apparatus was bounded in single aluminum rail which can be moved at the same time whenever image was captured. Total 7 DPC images for vertical axis were captured from 5 to 75 mm from the interval of 10 mm using half pattern. QPI was also generated to highlight the difference between images. Here, we fixed all parameters in QPI algorithm to find out how phase recovery has been changed depends on the variation of real $\sigma_{coherence}$. Moreover, gradient indicating the phase contrast was analyzed by taking line plot of DPC background. Throughout this experiment, we found closer the sample to diffuser creates better gradient illumination, resulting in higher QPI performance. As shown in Figure 2.23, contrast of both QPI and DPC has been decreased and phase starts to break as distance increases. Since we utilized the half asymmetric circle pattern, gradient angle was not steep but still decreasing slope could be determined as distance increases. This indicates that intensity of scattered light from large oblique angle vanishes at the sample, eliminating the phase shifts from light near the $\mathrm{NA}_{illum} = \sim\mathrm{NA}_{objective}$. In addition, increasing the distance could be interpreted as decreasing the illumination NA from $\mathrm{NA} = \frac{\mathrm{D}}{2\mathrm{w}}$, where D is illumination area, which is fixed in this setup; w is working distance from illumination to sample. Therefore, we concluded that increasing distance between diffuser and sample are found inversely relate to $\sigma_{coherence}$ in this optical configuration.

NIR QPI using stained cervical cancer cells

To evaluate the performance of QPI system using diffuser based NIR illumination, stained cervical cancer cell images were captured and compared to that from visible wavelength-based QPI system. Furthermore, we identified the cervical cancer cells by comparing the color-based images. In Figure 2.24, RGB-coded single-shot QPI, single wavelength QPIs, and NIR-based QPI system were utilized to capture normal cervical epithelial cells. We also captured bright field color image using incoherent

ULSAN NATIONAL INSTITUTE OF SCIENCE AND TECHNOLOGY

white light source (Thorlabs, HPLS245). In this study, asymmetric half circle pattern and 10x objective was utilized for all imaging sessions. In RGB-coded single-shot QPI system, corrupted quantitative phase images were shown. As shown in top-down or vertical-directional DPC (TD-DPC) image, gradient illuminations were lost. We believe this was caused by different absorptions depending on wavelength. Therefore, different absorption makes each complementary image in different aspect, rejecting the weak-object assumption. Moreover, any phase shift was not found from RGB-coded DPC result when we analyzed in FFT of DPC image. On the other hand, blue, green and red LED based QPI was computed without corruption of phases but still phase errors were existed which depends of the wavelength absorption. At the places where cells stained with different colors were overlapped, QPI using visible wavelength could not recover the phase, which made structures invisible. However, using NIR wavelength avoids absorptions and phase was transferred thoroughly as we can found in FFT of DPC image. FFT of NIR-based DPC illustrates much higher frequency responses and follows much similar shape to PTF. In quantitative phase recovered image, NIR wavelength provided clear structural visibility as well as reduced phase errors at the area where multiple cells with different chromatic stains were located.

In addition, high grade of CIN was utilized for NIR based QPI and its image was compared to that from green wavelength QPI. As shown in Figure 2.25, similar to normal cervix cell QPI, structures of cell clusters are well distinguished, providing more feasibility of NIR QPI system for absorbable specimen in various situation. Investigating the morphological information of cell is one of the essential factors for abnormal cell identifications, which is equally important as the chromatic information of abnormal cells. Through QPI system, structural information is provided from phase contrast, hence, abnormal cervix cells are distinguishable in label free manner. In most cases, abnormal cells have high nucleus to cytoplasm ratio. Here, abnormal cells, marked with yellow arrows, were confirmed with physicians, and validated the result from patient's medical report.

NIR QPI using H&E stained thick tissue

With our innovative QPI system, we also validate to perform the QPI using H&E stained tissue. In this section, 5 μm thick mouse brain slice was H&E stained to provide as thick specimen with highly scattering and absorbing materials. Annulus pattern was applied for imaging to enhance the resolution and phase contrast. Brain that we captured mostly contains putamen and cortex which are known as grey matters. Refractive index (RI) of these regions were average between 1.361 to 1.369 found in [69]. With this numerical information, we can derive phase deviation within 5 μm thick brain corresponds to 0.322 rad, making our QPI system suitable for tissue application as well. As shown in Figure 2.26, NIR

ULSAN NATIONAL INSTITUTE OF SCIENCE AND TECHNOLOGY

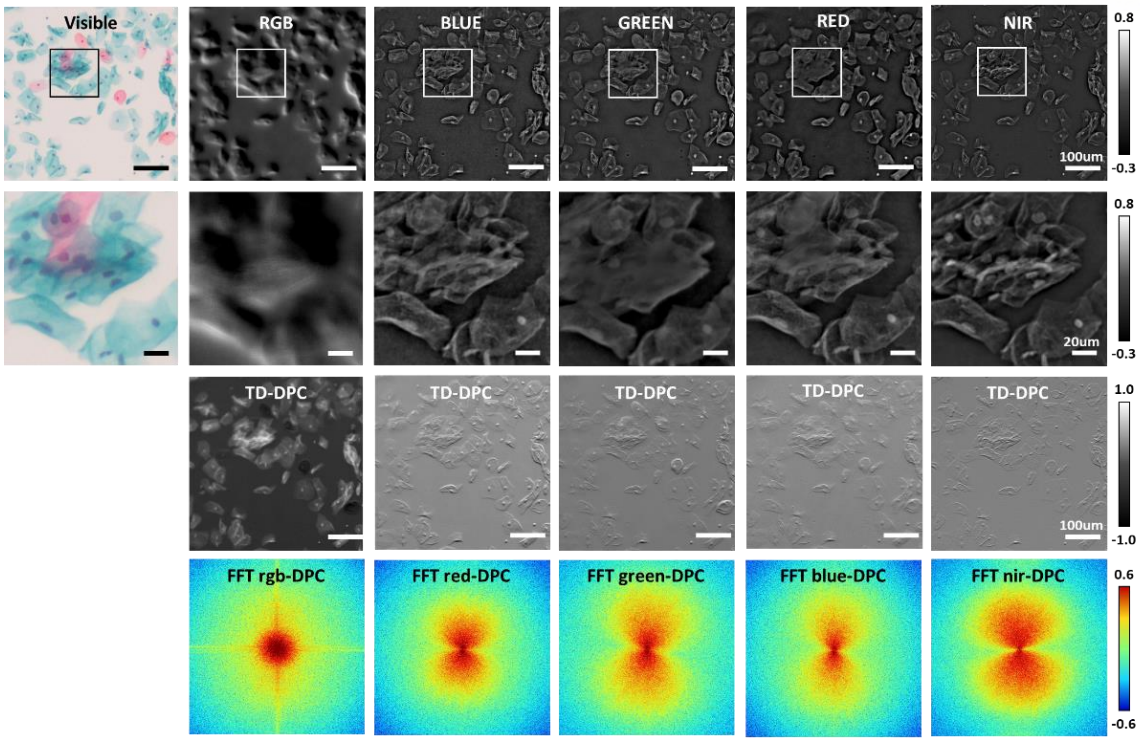

Figure 2.24 Comparison of QPI by wavelength capturing chromatic stained cervical cells. Images were taken using all red/gree/blue, blue, green, red, and NIR illuminations with half asymmetric cirlce pattern. Performance was analuzed from DPC and FFT of DPC images.

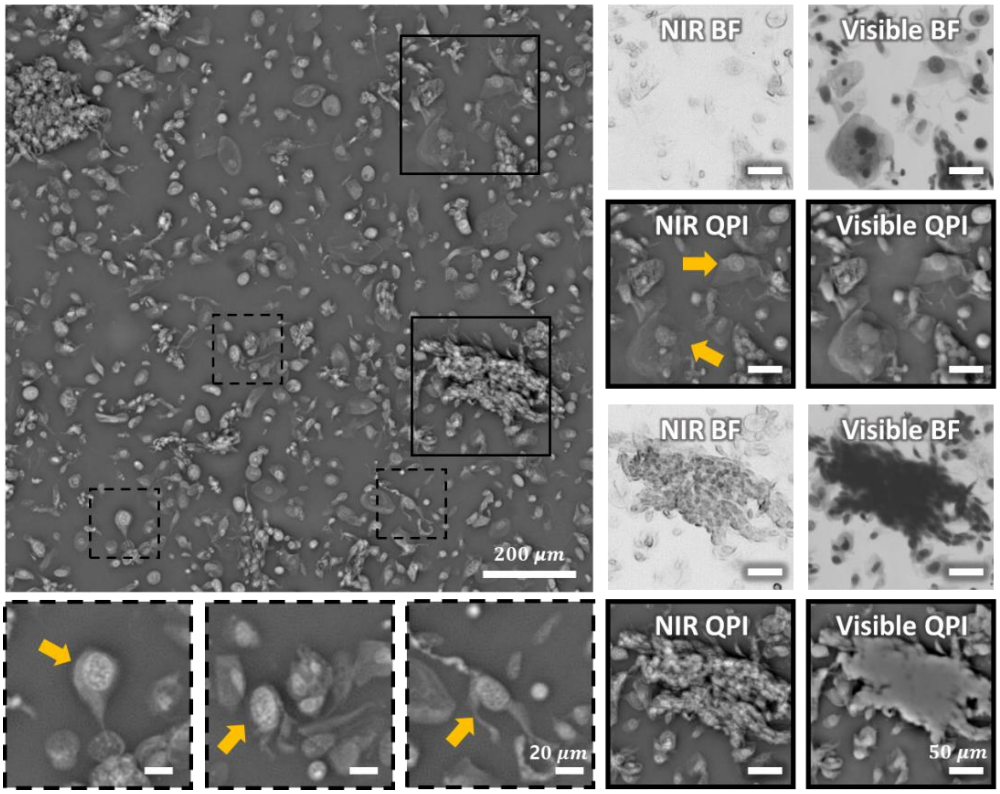

Figure 2.25 Demonstration of QPI using diffuser-bsaed illumination for CIN2+ sample. Images were capured by NIR and visible illuminations to compare the reuslt. Yellow arrow denotes suspicious abnormal cells.

ULSAN NATIONAL INSTITUTE OF
SCIENCE AND TECHNOLOGY

QPI successfully recovered the phase contrast in quantitative method. In the amplitude of NIR image, chromatic absorption was not appeared, which can be assumed that lights are passing the unstained tissue with low scatterings. Compare to H&E staining images as shown in Figure 2.26(a,b), NIR QPI shows comparable structural information. QPI shows more sharper image texture which makes image somewhat volumetric.

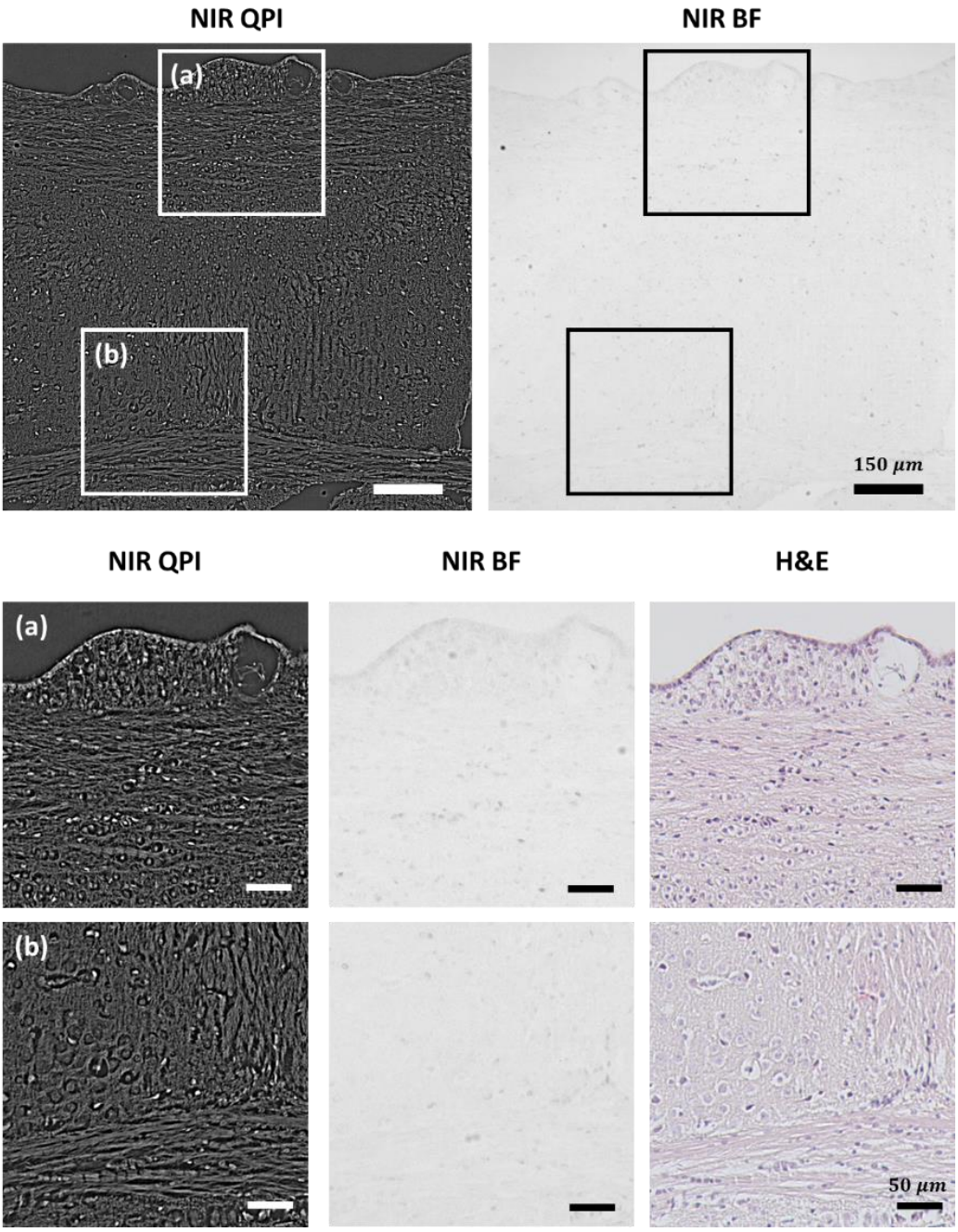

Figure 2.26 Demonstration of H&E stained mouse brain tissue using NIR-QPI system. (a-b) Magnified images for NIR QPI, NIR BF and color BF image comparison.

ULSAN NATIONAL INSTITUTE OF SCIENCE AND TECHNOLOGY

2.2.7 Conclusion

Throughout this study, utilization of our simple NIR illumination device successfully retrieved phases from thick and highly absorbing materials without any manipulations in QPI algorithm. Great advantage of using this method was that weak object transfer function was still available along with partial coherence illumination characteristics, resulting in simplification of complex field of object in optical system. In addition, using single LED source was another feature what makes our system fascinating. Although LED itself provides partial coherent illumination, illumination as point source would be considered as spatially coherent illumination which does not have phase response. Increasing only beam size would not provide solution for this situation. Increasing illumination area while affording spatially incoherent coherence condition with oblique illumination angle was our key tasks for phase stability and accuracy. With multiple diffuser implementation, randomly scattering on the surface of diffuser creates phase variations in the light propagation, which creates incoherent conditions while giving uniformity in illumination distribution. As light passes the physical mask, phase gradient was generated and use of single LED with this configuration could provide DPC images. Since multiple LEDs are not required anymore, not only NIR wavelength but also various illumination spectrum could be applied. This could offer advantages cost issue, provides possibility to develop QPI system in compact platform. However, although speckle noises were not crucially in NIR wavelength, scattering phenomena from diffusers could induce noises on the image in other wavelength, especially in visible range. We believe that, to the best of our knowledge, this work was the first method for not only imaging the tissue but also using only single point source illumination in DPC-based QPI system.

ULSAN NATIONAL INSTITUTE OF SCIENCE AND TECHNOLOGY

Chapter 3. Development of mobile medical device for point-of-care digital medicine

3.1 Smartphone-based endoscope for advanced point-of-care diagnostics

3.1.1 Introduction

Over the past decade, endoscope has become an essential medical instrument that enables physicians to access the internal organs with magnified visualization. The endoscopy was mainly purposed to investigate the unusual symptoms of the interior of the body, but now it has been utilized in various medical procedures, not only diagnosis, but also staging of diseases, biopsy, local therapy and minimally invasive surgery [70-72]. Endoscope has been applied in numerous fields including gastroenterology, orthopedics, urology, obstetrics/gynecology, otolaryngology, neurology, and anesthesiology [73-75]. Currently, endoscope system incorporates advanced technologies to provide the enhanced diagnosis by offering the high-definition, fast, quantitative and wide viewing images [76]. Despite the multiple benefits of using endoscope, the routine endoscopic procedures are usually confined inside clinics . Moreover, most of the endoscope system itself is not suitable for remote consultation and point-of-care diagnosis at developing areas or low-resource settings [77, 78].

Recently, there have been efforts to integrate smartphones into various medical devices [73, 79-86]. Thanks to the recent advances in mobile computing electronics, smartphones' performance is now comparable to personal computers while also featuring the state-of-the-art engineering components such as micro sensors, high-resolution camera, powerful CPU, GPU, and high-speed data communication chips [79, 86]. The infrastructure of mobile data communications has now become fast and ubiquitous, which can efficiently deliver the data between remote sites. Thus, the technical integration between ICT and medical device has opened the new opportunity for the next-generation diagnostic protocols through telemedicine and big medical data analysis.

In this study, we introduce a new complete smartphone-based endoscope system and evaluate its feasibility for clinical applications. Smartphone was already applied to the endoscopic devices, but previous works showed the only proof of concept while not considering its diagnostic value as well as the user interface. Furthermore, previously developed smartphone endoscope devices utilized the built-in camera software in the smartphone that only provides limited functionalities for the endoscopic imaging [76, 87]. Here, we developed a smart-phone based endoscope system combined with the home-built hardware, software as well as a head-mounted display (HMD). The performance of developed new endoscopic device was compared with one from the commercial endoscope system.

3.1.2 Endoscope system using smartphone

We developed a low-cost and portable endoscope based on a smartphone as illustrated in Figure 1. Our

ULSAN NATIONAL INSTITUTE OF SCIENCE AND TECHNOLOGY

system comprised 6 pieces of components aligning in series, including a conventional endoscopic probe, compact light source, customized adapter, magnifying relay-lens, packaging holder, and smartphone. Both holder and adapter were designed by three-dimensional (3D) modeling software (Solid Works) reflecting the actual dimensions of the smartphone and the endoscope eyepiece. The endoscopic probe can be detached from the adapter, which is compatible to most of the commercial rigid and flexible endoscopes. For delivering light to the interiors of body cavities, a portable light source (Medit, SPARK) was attached to the illumination port of an endoscopic probe. The smartphone holder was built for a specific smartphone model (Samsung Electronics, Galaxy S5) and made by a 3D printer (Stratasys, Objet260 Connex2) with the spatial precision of ±16 μm. For the magnification of endoscopic image, we customized the lens system that was located between the eyepiece of endoscope probe and smartphone camera. The customized lens system enabled the manual focus by employing the zoom housing (Thorlabs Inc, SM1NR05) to correspond to the different endoscopic probe. Off-the-shelf lenses were designed and selected by the optics designing software (ZEMAX LLC, Optic Studio) as shown in Figure 3.2. A smartphone camera–mimicking lens (L3) was simulated with 4.8 mm, f/2.2 as a constant parameter, which was set to infinite-focus. To deliver the image to the camera, we utilized 2 achromatic lenses (L1, L2) to reduce the chromatic aberrations while sustaining the portability as well as cost-effectiveness. Thus, tradeoff between length of the lens system and magnification was optimized. We assembled the achromatic lens and the aspherized achromatic lens with 40 mm and 14 mm focal lengths, respectively, to achieve approximately 3× optical magnification, which could be further enhanced up to 12× magnification approximately via software-based digital zoom. The final image was captured by the complementary metal–oxide–semiconductor sensor of the smartphone with specifications of 16.0-megapixels, MP (5312 × 2988 pixels), 1/2.6 inches (1.12 μm pixel size), incorporating 4.8 mm focal length and f/2.2 optical lens.

For replacement of the conventional display and enhancement of the portability, a newly designed commercialized HMD module (Green Optics Co., GO Glass) was employed in our system (Figure 3.1d). The operation of HMD is based on the Android OS which allows seeing the live endoscopic images through the glasses with 50% transparency, 45-degree sight angle, and 114 x 22 x 14 mm viewing optics. In addition, HMD is able to project the images which uses resolution of XGA (1024 x 768) in front of the eyes. HMD was interfaced wirelessly with smartphone via a mirror casting technology and displayed the endoscope images to clinicians. As shown in Figure 3.1c, a clinician would attach either rigid or flexible endoscope probe to the system and wear a HMD on the head while manipulating the smartphone-based endoscope system.

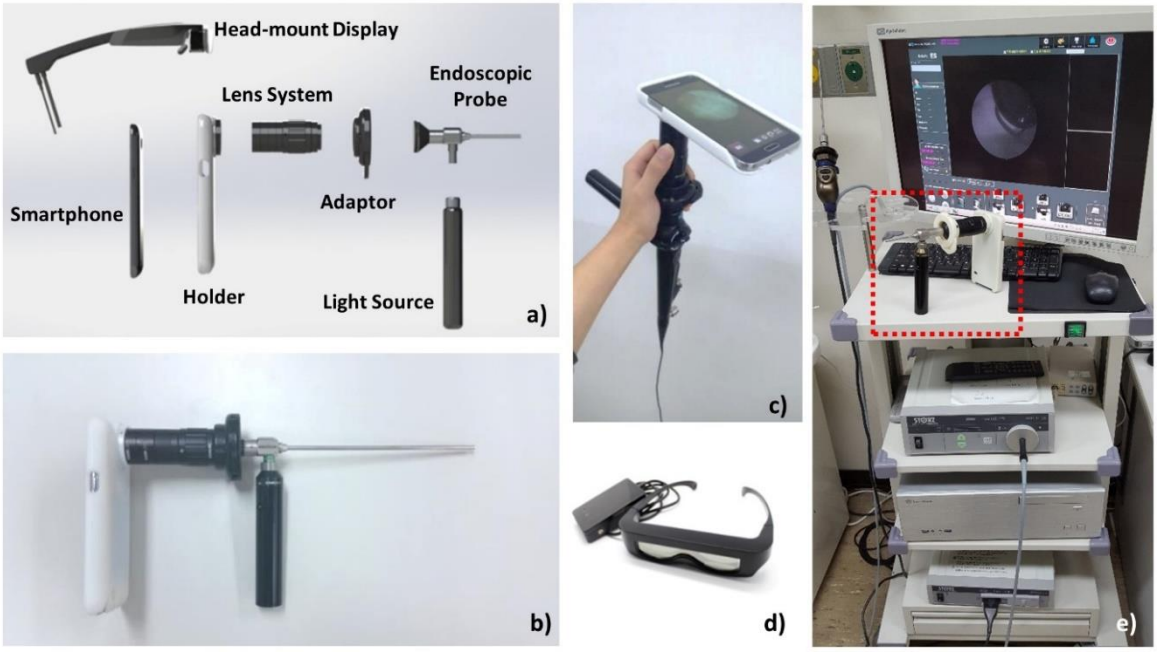

Figure 3.1 Smartphone-based endoscope system setup. Smartphone-based endoscope system setup. (a) Schematic of smartphone-based endoscope system. A photography of (b) rigid type endoscopic system, (c) flexible type endoscopic system, (d) android based HMD, and (e) the smartphone-based endoscope system vs clinical endoscope system.

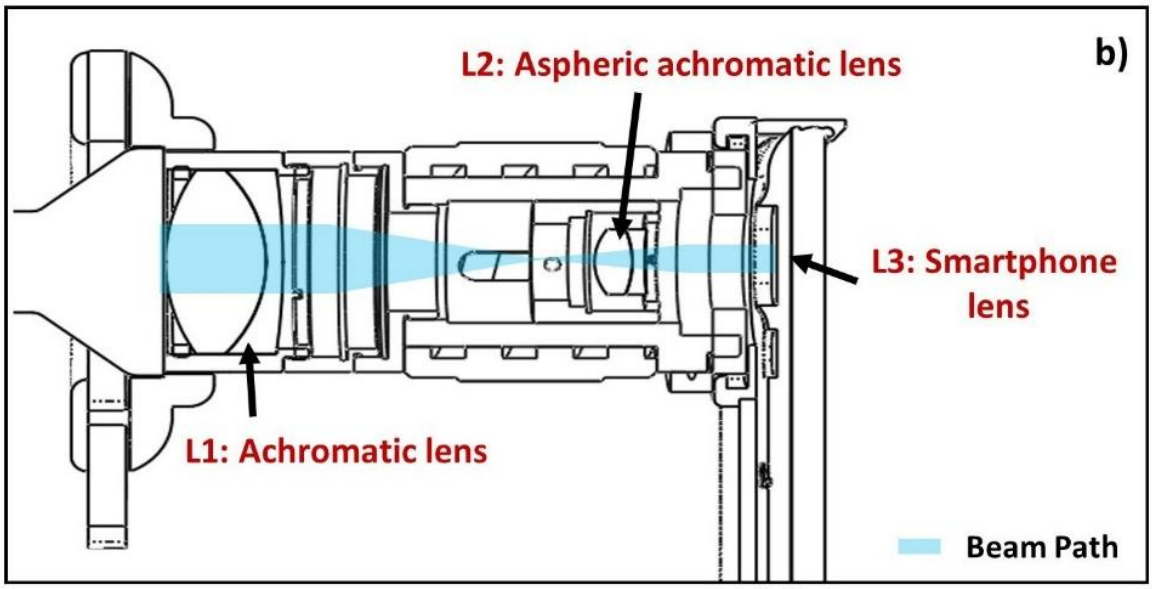

Figure 3.2 Beam path of smartphone-based endoscope system. Schematic of assembled lens system in smartphone-based endoscope system.

3.1.3 Designing for lens system

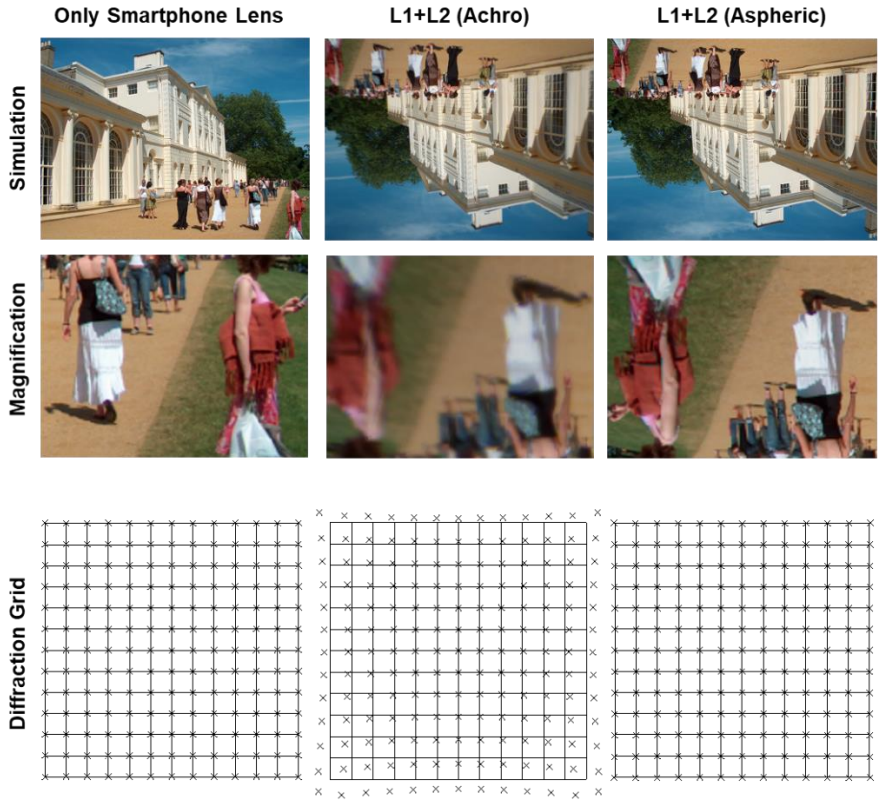

Figure 3.3 Image simulation and distortion analysis according to designed lens system with different combinations.

In order to find the appropriate combination of the lenses to magnify the endoscopic image, several lenses were designed through Zemax lens designing software. First, diverging angle of ray from the endoscope eyepiece was found through matching the image ratio (image area/sensor area) between empiric and simulation data. We utilized the otoscope of 0°, Ø4, 50 mm length. Largest diverging angle was found 4 degree that has beam diameter of ~2 mm. Then used the off-the-shelf lens data to design the simulations by combining them all together. Here, smartphone lens was designed referring to specifications given in the patent [43]. The biggest concern while selecting the lenses was development cost, total length of lens system, and lens aberrations. For manipulation convenience, we decided to not over 100 mm for the total length including the thickness of endoscope coupler. Therefore, first lens (L1) should be lower than 50 mm to have spaces for assembly parts. With a survey, we decide to use achromatic lens having f=40 mm, Ø25.4 mm for L1. We chose Ø25.4 mm lens and only utilized small portion of lenses in the central parts which have very low influences from spherical, comma aberration. Therefore, we focused to choose the L2 lens through analysis outcome of lens simulation. For candidate for L2, achromatic having lens f=14 mm, Ø12.5 mm and aspherized achromatic lens having f=14 mm, Ø12.7 mm were compared. Figure 3.3 illustrates the analysis result of designed lens system with different off-the-shelf lens combinations. Total length of lens system excluding the smartphone lens module was designed ~93.5 mm. Analysis was performed on the ray including 4 degree of divergence

ULSAN NATIONAL INSTITUTE OF SCIENCE AND TECHNOLOGY

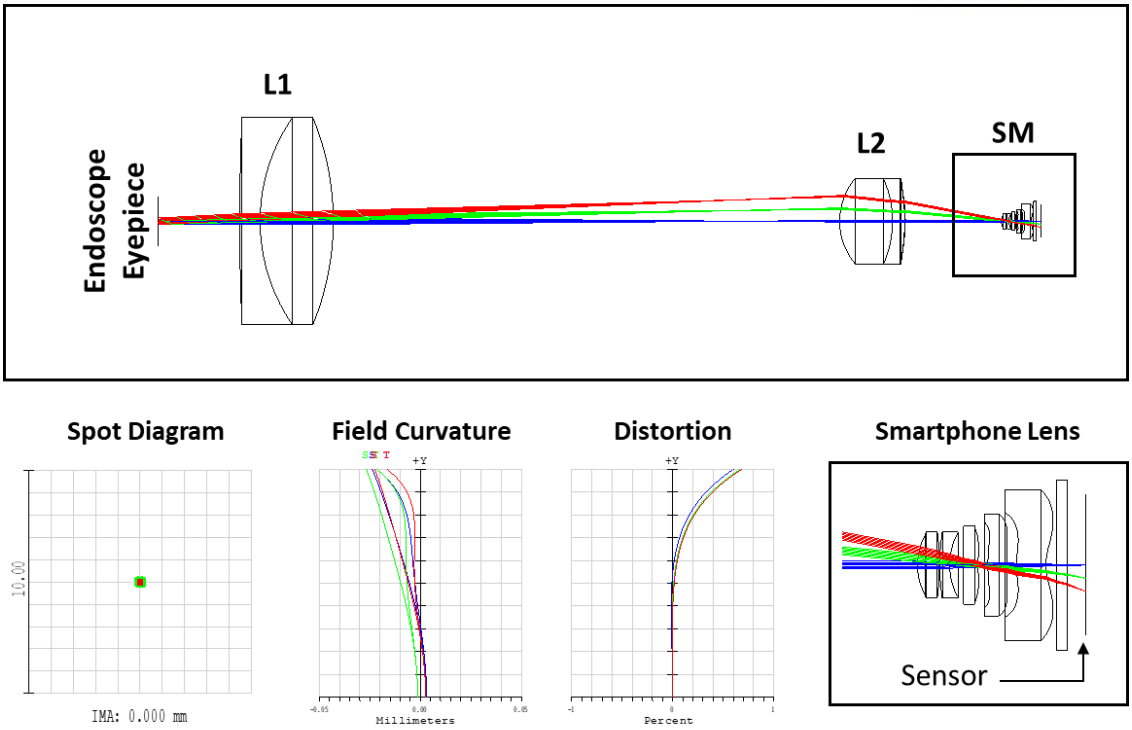

Figure 3.4 Simulation of lens system. Achromatic lens (L1) having f=40 mm, Ø25.4 mm and aspherized achromatic lens (L2) having f=14 mm, Ø12.7 mm were utilized. Smartphone lens (SM) was simulated to deliver the image to complementary metal-oxide semiconductor sensor. Spot diagram, field curvature, distortion, and details of SM are presented.

angle to see more closely about the aberrations. If we use only smartphone lens and attach to endoscope eyepiece, simulated image looked uniformly focused without a rotations and marks were fitted well in diffraction grid, which mean no aberrations were found in this situation. However, combinations using achromatic and aspherized achromatic lens both reverts the image 180 degree in image simulations. Moreover, achromatic lens shows aberrations at the edge of the image. Distortions were found critically at the edges. On the other hand, L2 with aspherized achromatic lens showed uniformly focused over whole FOV and no distortion was found. Using this simulation analysis, Figure 3.3 shows the final outcome of the lens simulation. Low filed curvature errors, and low astigmatism could be estimated from this combination by looking at the field curvature graph. Especially, ray angle below 6 degree (up to 3rd grid in vertical axis) shows low field curvature with error less than ~5 %, and distortion as well. To evaluate the simulation outcome, we simply compared magnification results as shown in Figure 3.5. From simulation, vertical length of the image focused on the sCMOS using only smartphone and lens system adaptation was found 0.28 mm and 0.83 mm, respectively, which gives around 3X in magnification. For empirical data, endoscope was attached, and images were captured using both without and with lens system. Similar to simulation, empirical data also showed magnification of 3X when image proportion ratio in horizontal direction was compared.

ULSAN NATIONAL INSTITUTE OF SCIENCE AND TECHNOLOGY

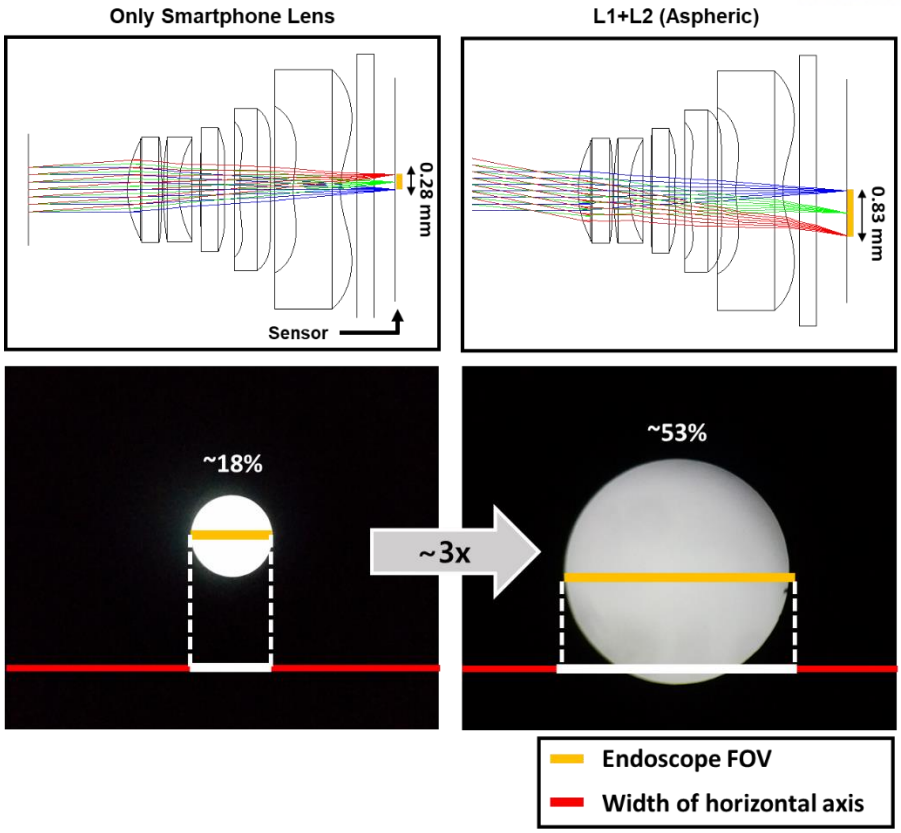

Figure 3.5 Evaluation of the lens system by comparing the magnification results from simulation and real endoscopic image.

3.1.4 User interface software development

We developed a JAVA-based Android software for a simple and intuitive user interface which allows an operator to control essential imaging parameters such as display brightness, image resolution, digital zoom, and focusing adjustment (Figure 3.66a). We also added multiple user-friendly features. For example, user can be set for either left- or right-handed operation for easier control of the display parameters during endoscope manipulation. Displayed endoscopic images are automatically flipped for better coordination between the endoscope movement and the display orientation. Furthermore, captured images and videos can be visualized in comprehensive gallery mode (Figure 3.6b). For convenient operation of system, the software was also enabled for simultaneous wireless casting on HMD.

3.1.5 In-vivo imaging protocol at otolaryngology

In accordance with a protocol approved by the institutional review board of the Kyungpook National University Hospital, the smartphone-based endoscope system was tested in human subjects. Each imaging session was conducted immediately after subjects' routine endoscopic examinations at an ENT

ULSAN NATIONAL INSTITUTE OF SCIENCE AND TECHNOLOGY

(ear, nose, and throat) doctor's office in Kyungpook National University Hospital. Routine endoscope procedures performed in the ENT departments were followed while utilizing our system as well. Before performing the endoscopy, the system was adjusted to get a fine focus for clear images through software and optics. Then, endoscope probe was wiped with a disinfectant to avoid the cross-contamination between patients. The whole procedure took less than a minute, thus avoiding undue burden on volunteers. Volunteer patients were verbally introduced to the risks and goals of this research study and agreed to participate and released the right to their endoscopic data to be used for the publication. For this research, 50 patients aged 20 or older were asked for participation, and of these, 30 volunteers agreed to participate in this research. As this was an initial pilot clinical study, we did not attempt to achieve statistical significance in data.

As it is shown in Figure 3.1, each human subject was imaged using both smartphone-based endoscope and commercial endoscope system that comprised a charge-coupled device camera head (Stryker, 1188HD), light source (Stryker, X8000), and information management system (Stryker, SDC ULTRA). Various types of endoscope probes such as 0°, Ø4, 50 mm length rigid otoscope (Medstar, Otoscope), 0°, Ø4, 175 mm sinuscope (Medsatar, Sinuscope), 70°, and Ø3.4, 300 mm flexible endoscope (Olympus, ENF-P4) were utilized.

Then, we chose several clear representative endoscopic pictures, including the healthy and diseased models corresponding to each endoscopic probe. The entire process was observed via the smartphone's liquid crystal display screen as well as the HMD in real time. In addition, the images from the commercial endoscope system were captured and archived via a computer for additional analysis. Thereafter, all captured images were cropped for resizing to better visualize the image for the manuscript. Moreover, the brightness and light contrast were manually adjusted for each image to enhance the visibility. No other image process was implemented in this study.

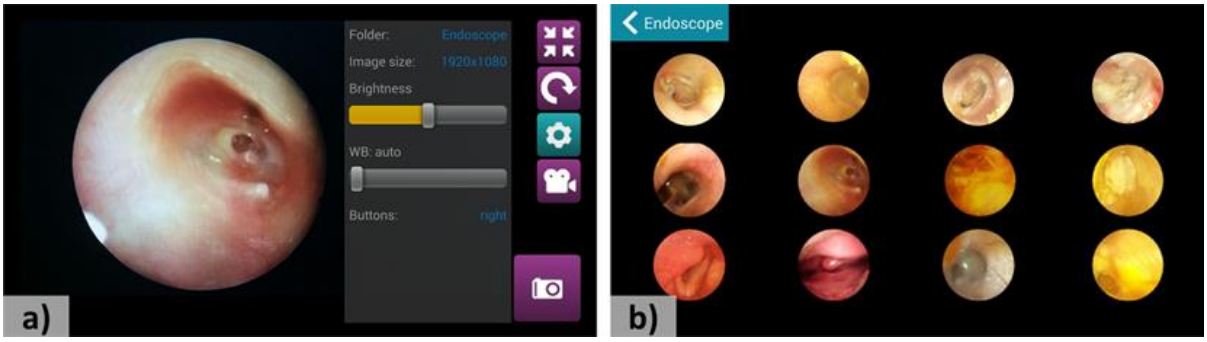

Figure 3.6 Android based software for the smartphone-based endoscope system. (a) Main capturing screen, (b) Gallery mode of the software

ULSAN NATIONAL INSTITUTE OF
SCIENCE AND TECHNOLOGY

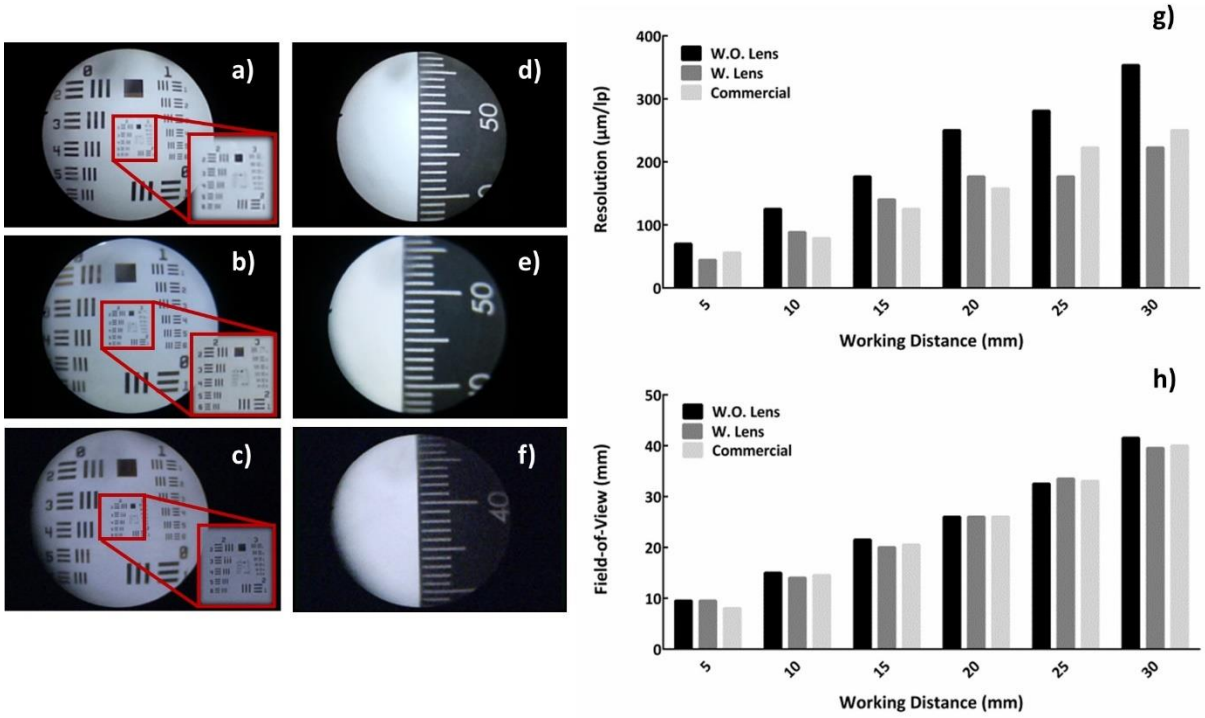

Figure 3.7 Result of the smartphone-based endoscope evaluation. At 20 mm away from the target, the USAF resolution was captured with (a) smartphone-based endoscope without lens, (b) with customized lens, and (c) commercial endoscope system. (d) At the corresponding distance, field-of-view was measured by capturing the ruler with (d) smartphone-based endoscope without lens, (e) with customized lens, and (f) commercial endoscope system. (g) Graph of the measured resolution and (h) field-of-view according to the working distance.

3.1.6 Result & Discussion

System characterization

To evaluate the imaging performance of our system, the US Air Force resolution target was imaged as shown in left side of the Figure 3.77 [76, 88]. Three different images were acquired and compared with smartphone-based endoscope with/without lens and the clinical version of commercial endoscope system. The distance between the end of endoscope probe and resolution target was 20 mm, which was sufficient to preserve the optical field-of-view (FOV).

Image captured by the smartphone-based endoscope without lens showed the lowest imaging capability in terms of resolution. It was able to resolve 4.0-line pairs per millimeter (lp/mm), which corresponds to 250.0 μm. When custom lens system was applied, the imaging performance improved and was able to resolve 5.66 lp/mm (corresponds to 176.7 μm). The clinical version of endoscope system showed the highest imaging performance among the 3 systems by resolving 6.35 lp/mm (corresponds to 157.5 μm).

In addition, a ruler was captured to identify the FOV as shown in Figure 3.77. Similar to the resolution measurement, images were captured at 20 mm of working distance using our device with/without lens and the clinical version of endoscope system. Measurements of resolution and FOV

ULSAN NATIONAL INSTITUTE OF SCIENCE AND TECHNOLOGY

at the working distance between 5 mm and 30 mm can be seen in right side of the Figure 3.77, respectively. They show that the smartphone-based endoscope with lens has imaging capability similar to that of a clinical endoscope system. Moreover, it can be ascertained that the features of the lens system did not critically influence the FOV.

HMD based endoscopy performance

Routine endoscopic procedure can be sometimes cumbersome the clinician due to mismatched eye-hand coordination. Manipulating the endoscope probe while observing the monitor forces a divergence between site of manipulating hand and field-of-view, which requires extensive training. Moreover, clinicians easily experienced the ocular strain from endoscopic procedures. To overcome above addressed issues, HMD has been applied to endoscopic procedures [88-91].

We tested the feasibility of endoscopic diagnosis using our device that includes a see-through type of HMD. Images were acquired with 3264 x 2176 (8MP), ISO 100, lowest exposure (-4) settings using the smartphone-based endoscope in routine endoscope procedure. Android-based HMD controller successfully duplicated the screen of the smartphone; hence, images can be seen through the viewing optics in the HMD. Clinician was able to detect the lesions in front of the eyes and successfully manipulated the endoscopic probe. Moreover, through this system setting, clinician had a benefit of observing the endoscopic image simultaneously at the manipulation site reducing the spatial disorientation. HMD during endoscopic procedure has been shown a potential of improvement on the eye-hand coordination. Clinician had impression that diagnosis time had been reduced compare to observing through the monitor. Especially, it was found that the manipulation time for flexible endoscope probe was significantly reduced when clinician wore HMD.

In-vivo human subject imaging

The smartphone-based endoscope was tested in a routine otolaryngology examination to evaluate its clinical value and performance. The images of human subjects were captured and compared with a clinical endoscope system. Our device used 3264 × 2176 (8MP) image resolution at the automatic ISO mode (ISO 100), and the lowest exposure (−4) setting to suppress the saturation of light and to achieve clear images. For the clinical endoscope system, the 1280 × 1024 (1.3MP) was used for camera resolution settings. The images were obtained at the same location with the corresponding probes that were utilized in the commercial system.

Images captured with the smartphone-based endoscope are shown in the columns on the left side, whereas images acquired from the clinical endoscope system are shown in the columns on the right under each subcategory of endoscopic probes (Figure 3.88). To examine different areas in otolaryngology, different types of endoscope probes were applied. Images of tympanic membranes were captured using the otoscope probe (the 1st two columns in Figure 3.8). Images from both systems clearly

ULSAN NATIONAL INSTITUTE OF SCIENCE AND TECHNOLOGY

showed the structures of the tympanic membrane compared with that of the normal patient. For nasal examination, a sinuscope was applied (2nd and 3rd coulmns in Figure 3.88). Several images were captured during the endoscopic examination to observe the feasibility of our system. Among the nasal endoscopic images, both systems particularly highlighted the nasal polyps of patient with chronic rhinosinusitis (g, h). The flexible endoscope was also applied to examine the larynx (the last two columns in Figure 3.88). Flexible endoscope was inserted first through the nose and then through nasopharynx to reach the larynx of the patients. Some images obtained by the fiber-optic endoscope probe displayed the pixelation throughout the entire FOV affecting the image quality and limiting the spatial resolution by undersampling because of core-to-core spacing between fibers [92]. Despite the pixelation, the smartphone-based endoscope still provided sufficient contrast and image quality for detecting the lesions. The smartphone system showed an acceptable level of clarity for an ENT specialist to distinguish the healthy and the diseased or damaged tissue regions through the

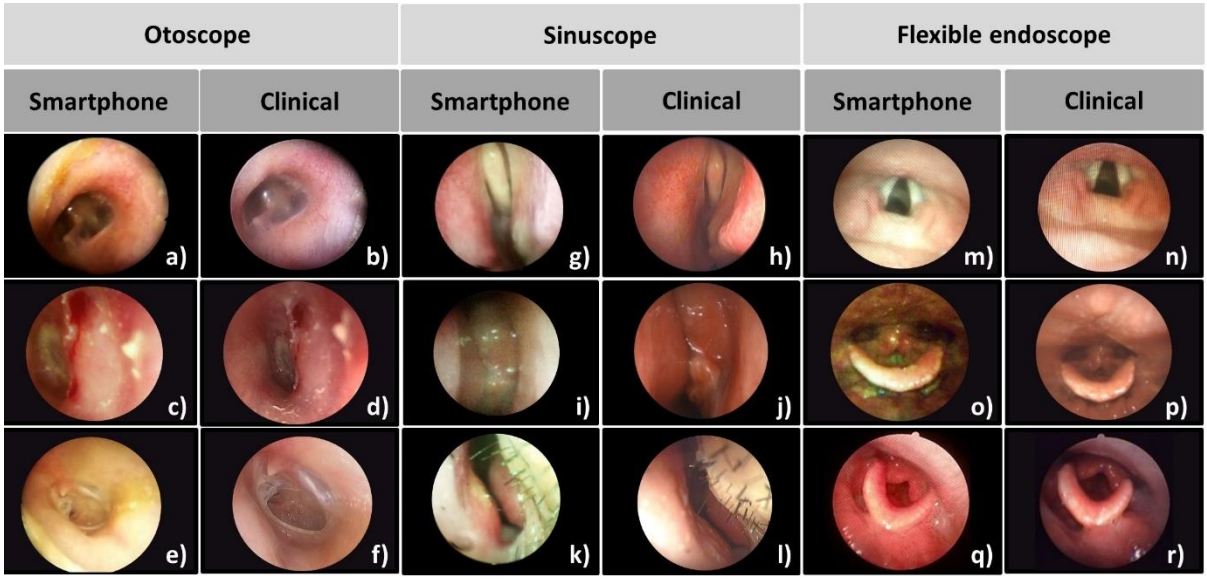

Figure 3.8 Result of human in-vivo imaging at Otolaryngology. Otoscope, sinuscope, and flexible endoscope were utilized. The corresponding sites were captured with smartphone-based endoscope and commercial endoscope system in clinical settings. (a, b) normal tympanic membrane. (c, d) postoperative state of tympanomastoiedectomy. (e, f) chronic otitis media, central large perforation. (g, h) normal middle turbinate. (i, j) chronic rhinosinusitis with nasal polyp. (k,l) normal nasal vestibule. (m,n) normal vocal cord. (o,p) normal larynx. (q,r) postoperative state of thyroid cancer surgery in larynx.

ULSAN NATIONAL INSTITUTE OF SCIENCE AND TECHNOLOGY

Table 3.1 Cost of smartphone-based endoscope system

Components	Price (USD)
Lens system (two off-the-shelf lenses, adjustable lens tube, additional lens components)	~$ 400
3D printing parts (smartphone case, adapter, coupler, etc.)	~$ 50
External light source	~$ 300
Miscellaneous components (spring, screws, battery, etc.)	~$ 30
Smartphone (Samsung Galaxy S5 16GB)	~$ 200
Total	~$980

Discussion

In this study, we demonstrated the use of a novel endoscope system based on a smartphone in clinical applications. The benefits of various aspects of our device have been observed throughout the study. Our device was fabricated in a compact form factor, so it can be used as a carry-on or standalone medical device in a clinical environment. Furthermore, significant safety guards or chemical protection were not necessary for this device. However, additional precaution was taken by wiping the probe with an antiseptic fluid to avoid the cross-contamination. The 3D printed case offered the robustness as well as the reliability with familiar coupling mechanism compared with that of the conventional system for endoscope probe. It was much simpler to set up the device for endoscopic diagnostics. The use of smartphone for endoscopy further simplified the system by providing the state-of-the-art sensors and hardware, thereby eliminating the need for expensive ancillary devices [79, 86]. In addition, cumbersome image processing or device control algorithm was unnecessary for endoscopic diagnosis with smartphone. Thus, the smartphone-based endoscope significantly reduced the overall cost compared with the price of conventional endoscope system equipped with essential apparatuses. The average price of the conventional system, with our survey from three major endoscope companies, was over US $ 50,000, whereas our system only costs under US $1000, including the smartphone (Samsung Galaxy S5) and the endoscopic probe. Even the additional cost related to commercial product delivery were taken into account, making the estimated price substantially lower for the smartphone-based system. Table 1 clearly presents the prices of components in our smartphone-based endoscope system.

Unlike other devices available in the market, the smartphone-based endoscope presented in this study provides a full endoscopic capability with a potentially customizable endoscope platform. Rather than simply capturing endoscope images with enhanced mobility, our system has shown a possibility to provide more advanced imaging modalities with various contents to the field applications. It can be easily modified for various needs in every aspect (optics, 3D printed cases, and light source) or made compatible with various accessories to the system for expanding the functionalities. We demonstrated the HMD as an example of a seamless integration of an accessory for endoscopy procedure. The integration of the next-generation wearable display such as an HMD can provide several

ULSAN NATIONAL INSTITUTE OF SCIENCE AND TECHNOLOGY

advantages to the smartphone-based endoscope system. An HMD allows clinicians to monitor digital information that is superimposed over the real-world view, thereby eliminating the need to view a monitor away from the patient and reducing the discomfort in the working position. Furthermore, the HMD completely rendered the smartphone-based endoscope system more portable and compact. However, some clinicians have experienced dizziness when they utilized an HMD for a long time because of ghost images caused by inherent structure of HMD design (static distance between optical windows). We anticipate that the future model of HMD will address these limitations and provide more advantages in our system.

The results shown in this study demonstrate the potential of the smartphone-based endoscopy for various clinical applications outside the conventional ones. In particular, the HMD-integrated system may offer more benefits outside the clinic. Faster diagnostics may be enabled with fascinating ease and safety, with considerable reduction in mismatch of the eye-hand coordination through HMD. The linkage between biosensors and HMD-integrated smartphone-based endoscope system could be beneficial for endoscopic surgeries. The extremely low price of the system could make it a cost-effective education tool for endoscope training. Furthermore, ubiquitous telecommunication infrastructure enables smartphone-based endoscope to be useful even in medical emergencies in the ambulance or field hospitals. It is still difficult to arrange an emergency operation in a timely manner. For this reason, sending the diagnosed endoscopic images to specialists while transporting the patient could shorten the delays and help manage urgent situations more efficiently using the smartphone-based endoscope.

Throughout the experiments, the great potential of the integration of smartphone technologies with medical devices has been observed because of the tremendous reduction in costs while sustaining health benefits for the patients. Many literatures have described them as the most prospective devices for the next-generation POC diagnostics [21, 86, 93-95].The smartphone-based medical devices may complement the quality of the services such as medical and health informatics. Moreover, recently developed mobile-picture archiving and communication system allows to connect remote locations to the central patient database in a secure fashion [96-98]. Now, real-time on-site diagnostics are available with a secure transmission of personal and sensitive medical data in a format specific to the health care industry [98]. These mobile devices show the possibilities of providing assistance to the patients in their medical records to improve coordination among health care providers who use telecommunication technologies such as short message service, calls, and Internet-based video links [21, 86, 94]. With advances in technologies, many devices tested in the laboratory settings have been translated to clinically or commercially available products [21, 86, 93-95]. The smartphone-based medical devices, especially for imaging device such as endoscope, will soon be utilized in the surgical settings for providing reliable results.

ULSAN NATIONAL INSTITUTE OF
SCIENCE AND TECHNOLOGY

3.1.7 Conclusion

Recent advances in smartphone technology have enabled the realization of cost-effective, portable medical devices. In this study, we introduced an endoscope system using a smartphone as an imaging sensor and display suitable for the POC diagnostics and offering the unique advantages such as mobility and flexibility. Experimental results showed that our device could potentially provide sufficient imaging performance as a diagnostic tool in a wide range of nonclinical settings and ultimately, in some clinical settings. In particular, our device would be a very useful tool for health providers in low-resource settings and at remote locations with limited health care service.

ULSAN NATIONAL INSTITUTE OF SCIENCE AND TECHNOLOGY

Chapter 4. Application of artificial intelligence in digital medicine

Artificial intelligence (AI) is designed to mimic the human brain in terms of decision making and learning, so with the computing power to learn the complex tasks in days, it is possible to create AIs that could surpass human in certain tasks [99, 100]. Hence, AI has been popularly contributed in various fields such as image processing, natural language process, robotics, image analytics etc. As technologies has been advanced, AI has recently become more powerful which allows enhanced AI technologies to handle sophisticated task that needed more computational process, resulting in increasing possibility of wider application fields [99-102]. In recent days, use of AI has become significantly promising especially in the medical fields such as medical image processing, computer-aided diagnosis, image interpretation, and image segmentation/registration [102]. Particularly, among the AI methods, conventional machine learning and state-of-the-art deep learning techniques such as convolutional neural network (CNN) were widely utilized and shown outstanding performance with large amount of medical imaging data in various applications. With advantages shown in AI, in the coming future, we believe that AI could help make the digital pathology more robust, more producible, and also help in providing more quantitative data. This will allow pathologists to make more accurate and consistent diagnoses with advantage in cost-effective and less time-consumption.

In this chapter, machine learning and deep learning from AI technique were applied to the developed medical imaging devices which were introduced in the previous chapters. With conventional machine learning methods, disease was predicted and classified from given feature data which was derived from image processing algorithms. For machine learning methods, most common three classification models such as supportive vector machine (SVM), k-nearest neighbor (KNN), and decision tree (DT), were trained in the study. For deep learning technique, instead of disease classification, data elaboration was performed to multiplex the information, offering cost-effective and

Table 4. 1 Comparison of machine learning and deep learning

Category	Model	Characteristics
Machine Learning	Decision Tree	▪ Simple to implement ▪ Good with small data sets ▪ Quick to train a model ▪ Requires manual feature data ▪ Gives less accuracy ▪ Limited tuning capabilities
	K-nearest Neighbor	
	Supportive Vector Machine	
	Artificial Neural Network	
Deep Learning	Deep Neural Network	▪ Requires large data sets ▪ Provides high accuracy ▪ Learns features and classifiers automatically ▪ Computationally intensive
	Convolutional Neural Network	
	Recurrent Neural Network	
	Auto-encoder	

quick medical images. Through application of one of the deep learning techniques called generative adversarial network (GAN), the input image data is generated as if it were taken from other imaging modality. Further details would be explained in the subchapters.

4.1 Machine Learning Technology

Currently, machine learning is the most common approach of AI. It builds mathematical algorithms from given data and automatically classify and predict diseases to offer aid healthcare related workers for decision making in uncertain conditions. Mostly, machine learning methods such as KNN, SVM and, DT have been used and shown robust performance in classification problems [99]. The KNN that represents the non-parametric model used for both classification and regression is one of the most popular and intuitive supervised machine learning algorithms. The SVM, which was introduced in late 1990s, is a discriminative model that formally separates the attribute space with hyperplane. The DT is one of the simplest machine learning models that splits the data in a shape of tree trying lower the data entropy [99, 100]. All these models require to tune hyperparameters with different characteristics for each model for the best performance. More details will be discussed in following sub-sections.

4.1.1 K-nearest neighbor

The KNN is known as lazy learner or instance-based learner where it memorizes all training data sets instead learning discriminative functions. Thus, it is fast and not much computations were required in prediction. It computes the similarity of the k numbers of neighbor data from the new cases to make a

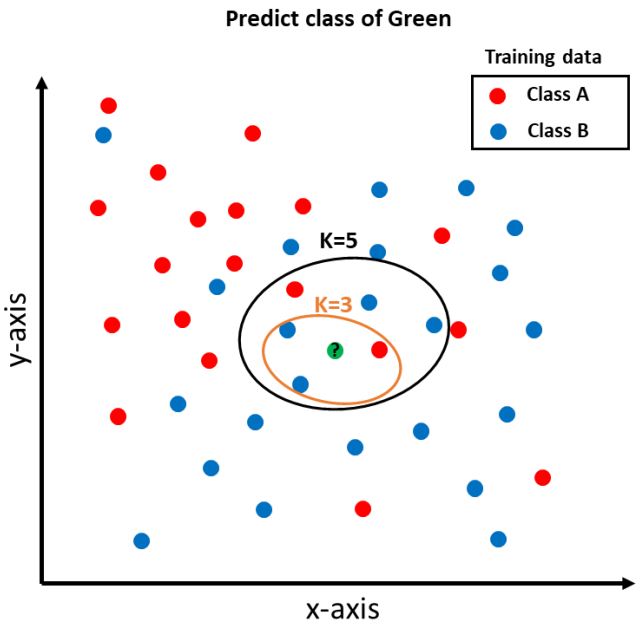

Figure 4. 1 Explanation of KNN

ULSAN NATIONAL INSTITUTE OF SCIENCE AND TECHNOLOGY

prediction as shown Figure 4. 1. In the graph, when k=3, three nearest data from green (new input) are chosen and predict the class of green by calculating the majority labels (voting) of selected neighbors. Therefore, green can be predicted as class B for both K=3, and K=5. In KNN, nearest neighbor data are measured by a distance function. For continuous variables, a common distance functions are defined as following [103].

$$\text{Euclidean distance: } \sqrt{\sum_{i=1}^{k}(x_i - y_i)^2}$$

$$\text{Manhattan: } \sum_{i=1}^{k}|x_i - y_i|$$

$$\text{Minkowski: } \left(\sum_{i=1}^{k}(|x_i - y_i|)^q\right)^{1/q}$$

4.1.2 Supportive vector machine

SVM classifies the data using a boundary known as the hyperplane that is driven by mathematical algorithm as shown in Figure 4. 2. A good separation is achieved by the boundary that maximizes the margin between the two classes. The data points that define the hyperplane are the supportive vectors. Suppose there is a vector w that is normal to hyperplane. Then, distance between sample to hyperplane could be determined by projecting the position vector of the sample on to the vector w. If position vector

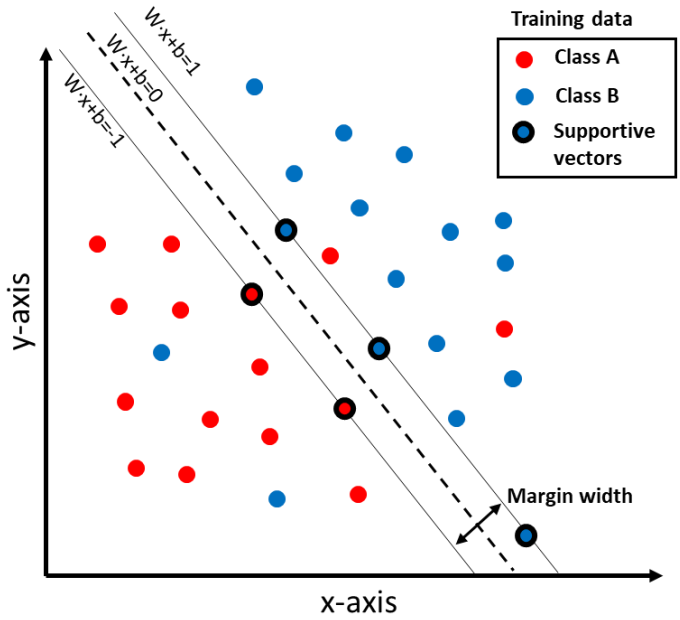

Figure 4. 2 Explanation of SVM

ULSAN NATIONAL INSTITUTE OF SCIENCE AND TECHNOLOGY

is a positive, the proceeding decision function $(\vec{w} \cdot \vec{x_i} + b)$ would return ≥ 1. On the other hand, if vector is negative, the proceeding decision function would return ≤ 1. By introducing an additional variable $y_i = \begin{cases} +1\ for + samples \\ -1\ for - samples \end{cases}$, the proceeding decision function could be simplified by multiplying them [104, 105].

$$y_i(\vec{w} \cdot \vec{x_i} + b) \geq 1$$

The objective of SVM is to maximize the margin of the hyperplane, which could be defined as $max \frac{2}{\|w\|_2}\ or\ min \frac{1}{2}\|w\|_2^2$ [104, 105]. Using quadratic programming for objective function, w and b could be solvable in proceeding decision function. In a perfect SVM model, ideally hyperplane would separate the classes clearly into distinct groups. However, perfect separation cannot be expected in real cases or models may separate in many cases which causes misclassification. In order to minimize the misclassification errors, cost is introduced in here. Cost is parameter that controls the margin size and training errors which decides how much error should the model will accept to generate the hyperplane. However, cost has tradeoff between margin size and error as shown in Figure 4. 3. The more penalty SVM gets when it makes misclassification which makes margin narrow and involves fewer supportive vectors. Furthermore, sometimes data could not be perfectly separated by linear boundary. Nonlinear boundaries which is known as kernel function could be applied and increase the training accuracy. Using different order of degree and shape in kernel function would give more dramatic and various shape of the hyperplane as shown in Figure 4. 4. Similar to cost, gamma in kernel also functions as parameter that penalize the model. The higher the gamma more influence the feature data points will have on the decision boundary as shown in Figure 4. 4 [104, 105].

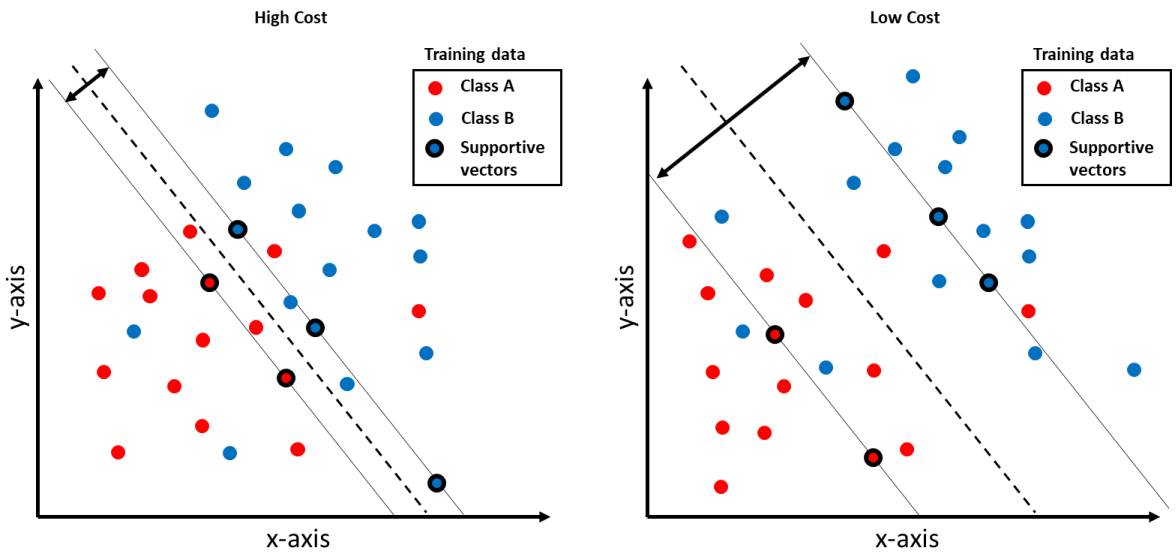

Figure 4. 3 SVM hyperplane analysis according to cost parameter.

ULSAN NATIONAL INSTITUTE OF SCIENCE AND TECHNOLOGY

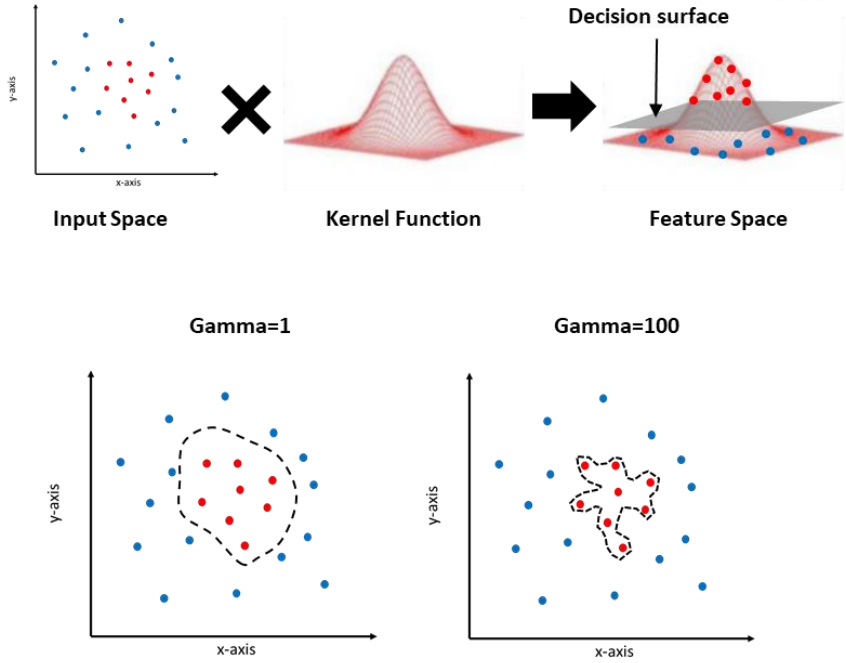

Figure 4. 4 Explanation of kernel function in SVM

4.1.3 Decision tree

Decision tree (DT) breaks down a data into smaller subsets and creates the classification or regression models that looks similar to form of a tree structure. The greatest advantage of decision tree is t hat results can be visually analyzed through tree diagram. When DT splits the data, conditions (ex. patient age > 30?) were given to the features to grow two or more branches. DT stops growing when the model reached the maximum depth that user set as training condition. To decide the conditions of splitting, DT calculates the entropy of the data which is level of disorder . In addition, DT tries to earn the highest information gain to decide the splitting from different attributes, which is decrease in entropy after a data set is split on an attribute. Other than information gain, Gini Index is also another choice to decide the splitting in every branch. Following equations are entropy and information gain:

Entropy (one attribute): $E(s) = \sum_{i=1}^{c} -p_i log_2 p_i$,

Entropy (two attributes): $E(T, X) = \sum_{c \in X} P(c)E(c)$

Information Gain: $\mathrm{Gain(T, X) = E(T) - E(T, X)}$

where p_i denotes probability of Ii, P(c) denotes c as one attribute. Gini Index is defined as following:

Gini Index: $\mathrm{Gini} = 1 - \sum_{i=1}^{c} (p_i)^2$

4.1.4 Deep Learning

Artificial neural networks with multiple hidden layers between input and output layer was introduced in 1980s which learns features and classify automatically [100]. This network was structured similar to human nerve system and offers performance to solve complex problems (non-linear problems). The general architecture of neural network is illustrated in Figure 4. 5. Each neuron in the network adds up the input data and applies the activation functions to the summed data, and finally provides an output that can propagate to the next layer. Therefore, adding more hidden layer in neural network allows to handle more complex problems as hidden layer deals with more non-linear relationships [100, 102]. With more large number of layers in the model, deep network can make intelligent predictions in complex problem by memorizing all the possible combinations of nodes after training with a sufficiently large data set.

Recently, deep learning has been shown significant impact in medical imaging fields. For medical imaging applications, various types of deep learning algorithms are utilized such as convolution neural network (CNN), deep neural network (DNN), recurrent neural network (RNN), deep autoencoder (dA), etc. Among them, CNN is showing a promising performance in digital image recognition, analysis, and classification problems. CNN takes an input image, assign importance to various features in the image and differentiate one from other. CNN generally have architecture similar to Figure 4. 6. CNN composes two part, one with feature learning and another with classification. In the feature learning, CNN consist of convolution filter layer, non-linear activation function, which is rectified linear unit (ReLU), and pooling layer. When input passes through sets of convolution, ReLU, and pooling layers in series, the output will be activations that represent higher level features. Convolution layer functions as image filter by shifting the small patches on the whole FOV. It extracts features such as edges, shapes of objects from the input image through the matrix calculation. ReLU takes low computation, lack of gradient vanishing problems, hence, now it's been common or could be said default function that activates the data for all positive values. Pooling layer were used after ReLU layer, reducing the dimension of the activation map. Pooling is significant in CNN which reduces computational cost by

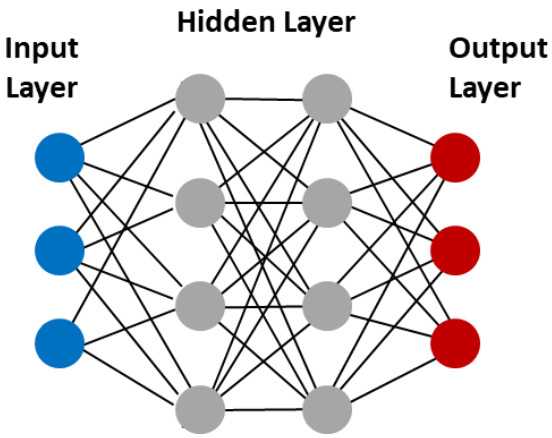

ULSAN NATIONAL INSTITUTE OF
SCIENCE AND TECHNOLOGY

Figure 4. 5 Illustration of neural network architecture

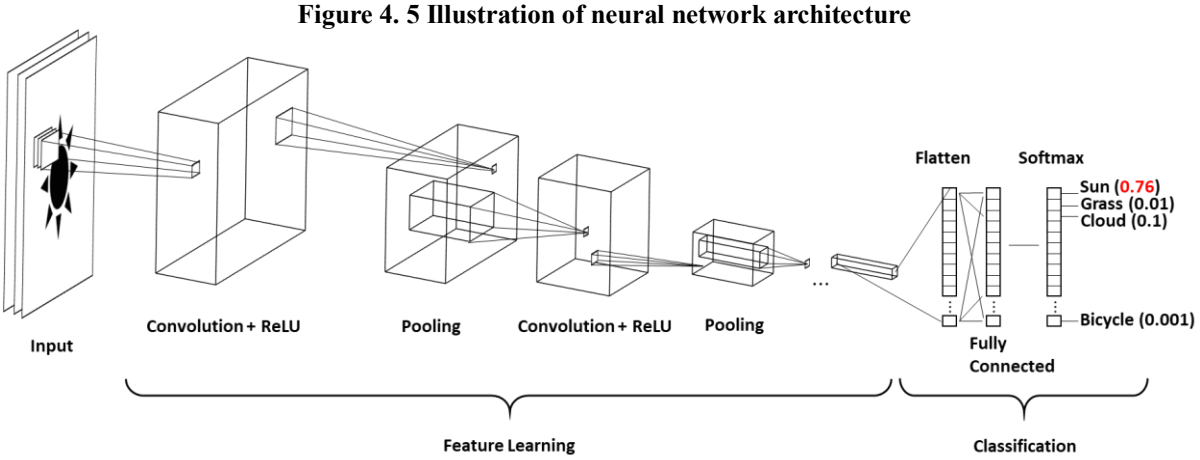

Figure 4. 6 General convolution neural network architecture

reducing number of parameters to learn. In the classification part, the fully connected layer connects all the neurons in one layer to all the neurons in the other layer. In principle, it is the same as the traditional artificial neural network. The flattened matrix goes through fully connected layers to classify the images [101]. The way this fully connected layer works is that it looks at the output of the previous layer and determines which features most correlate to a particular class. By training the model, it determines the weight of feature and make a relationship to its feature to each class.

Excellent success of CNN was shown demonstrating its great performance at the ImageNet Large Scale Visual Recognition Competition (ILSVRC) [106] as shown in graph in Figure 4. 7. Use of CNN

ULSAN NATIONAL INSTITUTE OF SCIENCE AND TECHNOLOGY

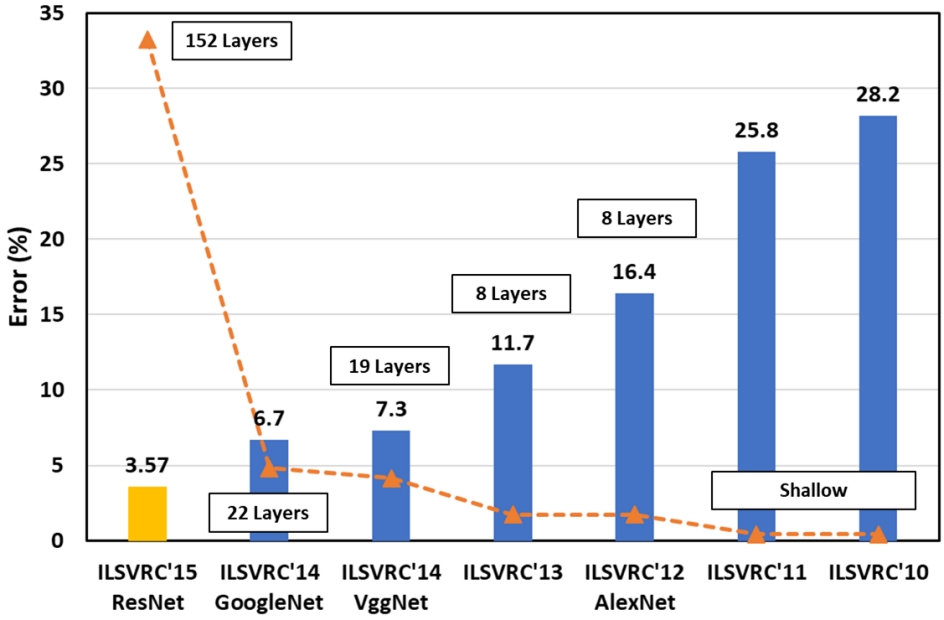

Figure 4. 7 Result of CNN models in the image classification challenge.

along with graphic processing units (GPU) has significantly dropped the error rate of image classification performance from 25% down to approximately 10%. This CNN model was called AlexNet developed by group from the University of Toronto. Since after AlexNet, continuous improvements were achieved in deep learning society. In 2015, ImageNet winner, ResNet, overcome human-level accuracy (5%) with error rate below 3% [102]. This CNN model was developed very deeply with 152 convolution layers avoiding gradient vanishing problem which was shown usually in deep layered training networks. Through these results are contributing to the wide range of application, some combining with other DNN models for various objectives.

ULSAN NATIONAL INSTITUTE OF SCIENCE AND TECHNOLOGY

4.2 In-silico tissue staining using NIR-based computational phase microscopy and deep learning technique

4.2.1 Introduction

Histological analysis of tissue is essential and has been widely utilized for diagnosing abnormalities [17]. It is known as golden standard for visualizing the structural details of tissue sections. In order to explore the tissue to find the abnormal features, laborious multiple procedures are required such as fixation, embedding, sectioning, and staining, which make patients to pay large amount of money and to wait for long time to get results [15-17]. However, without any labeling, pathological details are difficult to identify from the tissues under conventional brightfield (BF) microscope system. There are several imaging systems visualizing the tissue in label-free methods such as confocal, multi-photon, autofluorescence, holographic quantitative phase imaging microscopes. Although label-free imaging system offers structural information of tissues, these systems visualize image intensities in monochromatic [16, 17]. Due to these reason, pathologists who were familiar with chromatic stained images, need new training session to learn interpreting the monochromatic images. Moreover, many algorithms and automatic interpreting software were developed for color histology images, which inherently is not appropriate for label-free monochromatic images [15].

Deep learning has recently been successfully provided promising results in various fields such related to data-driven approach and solving inverse problems in optics [15, 107-109]. Recently, label free imaging system integrated with deep learning technique has been demonstrated, offering the virtual staining which successfully transforms the gray-scale image similar to H&E stained images [15, 16]. Along with quantitative analysis, virtually stained tissue image was difficult to perceptually differentiate from real bright field stained tissue images. However, there are still some issues that could be contributed to improve the virtual staining method in terms of simplicity and robustness of deep learning training. Both studies [15, 16] commonly have challenges in data preparation for matching label-free tissue sample and their corresponding bright-field images after histology staining process as shown in Figure 4. 1b. Some tissue constituents could be loss or deformed which will mislead the loss function in training deep learning process [110]. Moreover, images captured with different imaging modalities require complicated image registration algorithm to match the orientation and location of structural features [15, 16]. In addition, holographic quantitative phase imaging system itself is limited by speckle noises by using coherent illumination [15]. Hence, additional noise reduction network or algorithm is still required to enhance the visibility of the phase contrast.

Here we introduce “In-silico QPI” providing training material for virtual staining “directly” from the stained tissue section. Quantitative phase imaging (QPI) system was configured by simply alternating the illumination apparatus to programmable near infrared (NIR) LED matrix. Due to use of

ULSAN NATIONAL INSTITUTE OF SCIENCE AND TECHNOLOGY

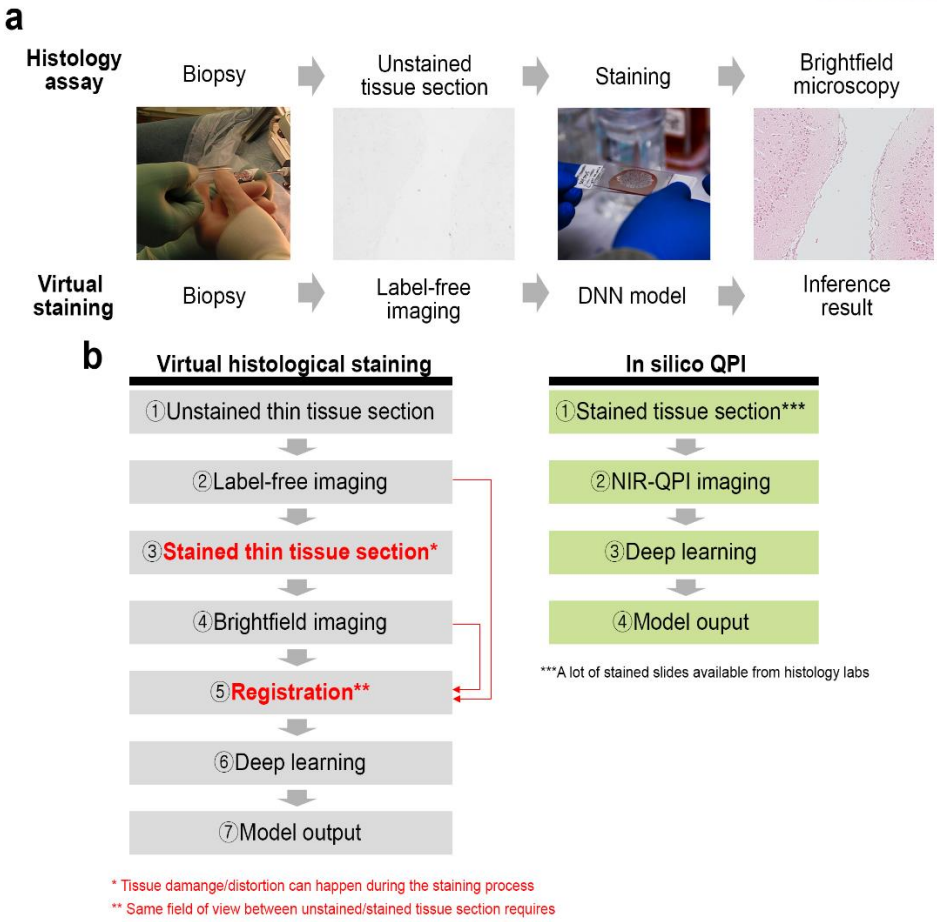

Figure 4. 8 In-silico tissue staining flow work. (a) Compare to histology assay procedure, label-free histology procedure with deep learning model allows to bypass the conventional histology staining process. (b) Our innovative method simply captures only stained tissue section for both brightfield and QPI. This allows to train deep learning model without taking bright field image of tissue after staining procedure and without applying complicated image registration process.

partially coherent illumination, our phase image allows 2x better imaging performance in terms of resolution and speckle noise-free imaging compare to that of other coherent QPI systems [40]. Thus, additional algorithm or ancillary methods were not required for noise reductions. After acquiring the structural information through quantitative phase images, we trained generative adversarial network (GAN) [111] and conventional neural network (CNN) [101] to transform the gray scaled phase to RGB color that corresponds to conventional golden standard. In order to avoid tissue deformations after staining process, we provide both QPI and bright field images utilizing already stained tissue. We believe this method may improve performance as well as robustness in training, eliminating the additional complex image registration methods. Therefore, we applied near-infrared (NIR) illumination to effectively acquire both color and phase images by avoiding the scattering and absorptions from stained tissue. With our DPC-based QPI system, now, not only transparent tissue but also stained tissue could be visualized in quantitative phase contrast, which was not available in previous systems. To evaluate the NIR effect in QPI, we further analyzed QPI by acquiring the stained tissues in various

ULSAN NATIONAL INSTITUTE OF SCIENCE AND TECHNOLOGY

thickness and different wavelength of light. To the best of our knowledge, it is the first-time not only visualizing tissue images in DPC based QPI system but also utilizing this system to perform in-silico tissue staining using deep learning technique. We believe this technique provides great advantage for clinical application especially in label-free imaging, cost-effectiveness and quick diagnosis through bypassing the cumbersome staining process in histology screening.

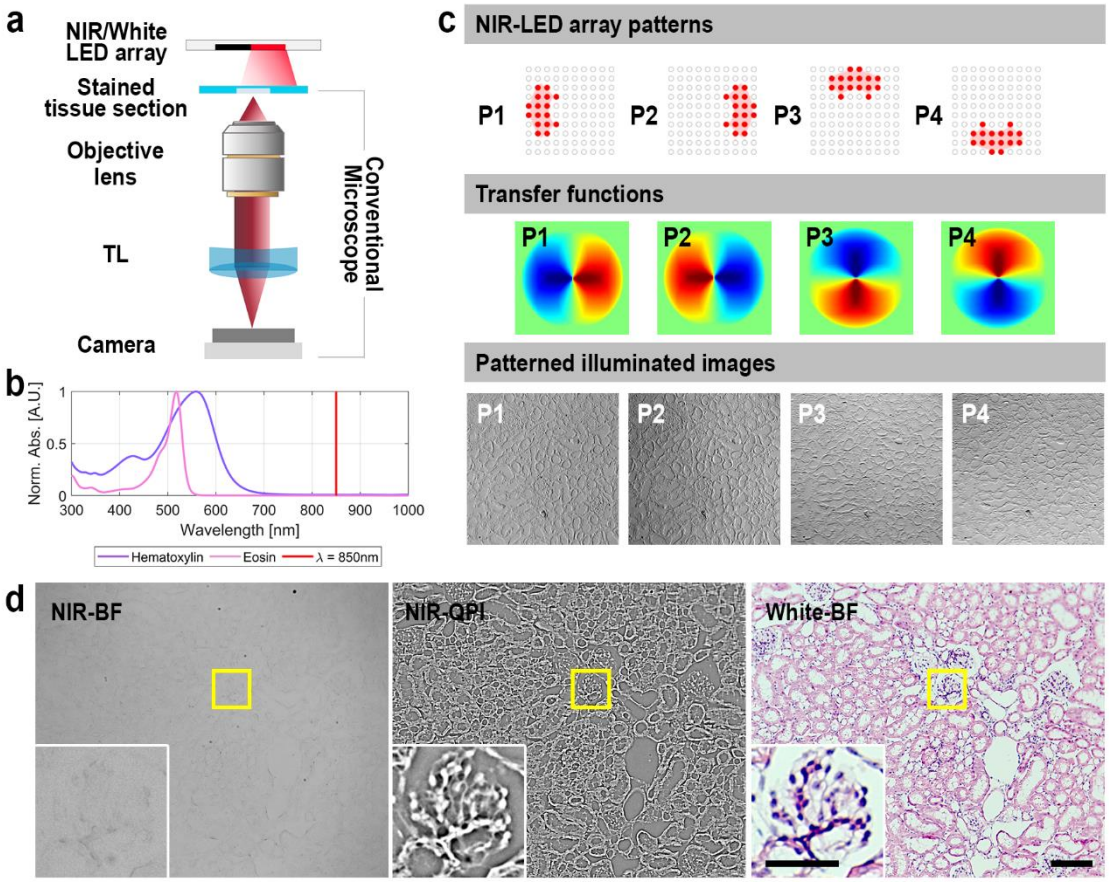

Figure 4. 9 Quantitative phase imaging using NIR LED array. (a) Optical configuration for the direct in-silico histology staining. Near-infrared (NIR)-/White-LED array is installed on the conventional inverted microscope setup. (b) Incoherent light emission of 850nm wavelength is from NIR-LED array (red line) and no hematoxylin/eosin absorption is shown. (c) QPI is carried out by illuminating NIR in four patterns, i.e. P1 to P4 in NIR-LED array patterns, which forms four transfer functions accordingly. Four patterned illuminated images are processed to create a quantitative phase image. (d) Brightfield image with NIR, QPI with NIR, and brightfield image with white LED illumination at a hematoxylin and eosin (H&E) stained kidney section. Scale bar: 100 μm or 50 μm for inset images.

4.2.2 Quantitative phase imaging

NIR-QPI system setup

Quantitative phase imaging (QPI) was carried out using the differential phase contrast microscopy (DPC) technique. An NIR LED matrix (LED Lamp Board Vo.1; Curiosis, Inc., South Korea) was installed on

ULSAN NATIONAL INSTITUTE OF SCIENCE AND TECHNOLOGY

a conventional inverted microscope body (Olympus, Japan). The NIR LED matrix is configured with a center wavelength at 850 nm and is specially designed to control all LEDs simultaneously by avoiding the rolling shutter effect. The distance between LEDs is 2.0 mm avoiding wave front interferences. 10× 0.25 NA achromatic finite-conjugate objective (#33-437; Edmund Optics, U.S.A) was configured to the system. Images were acquired using a color CMOS camera (CS505MU; Thorlabs, U.S.A.) without color filters. The acquisition system was controlled using a custom written software in MATLAB (Mathworks Inc. U.S.A.).

Near infrared (NIR) quantitative phase imaging (QPI) microscopy is essentially the same of the conventional brightfield microscope configured with NIR/white LED array illumination (Figure. 4.9a). The QPI images or brightfield stained section images are acquired by alternating the illumination color or pattern from a specimen. Thereby, no further registration is needed for the further deep learning analysis. The NIR-LEDs are configured at the center wavelength of 850 nm, which gives the least attenuation/absorption and the maximum quantum efficiency for the tissue imaging. In addition, there is no absorption from the staining of hematoxylin and eosin (H&E) at 850 nm (Figure. 4.9b) which brings an identical QPI image regardless of the staining (Figure. 4.12). We bring four NIR-LED illumination patterns which are a torus shape by helical cuts (inner illumination NA was 0.85) at 120 degrees and are centrically rotated by 120 degrees (Figure. 2c; NIR-LED array patterns). Four optical transfer functions (Figure. 4.9c; Transfer functions) form four images shown in Figure. 4.9c; patterned illuminated images P1 to P4. The phase information is recovered from these four patterned illuminated images. Figure. 4.9d shows an example of kidney section imaged by plane NIR illumination (NIR-BF), by four patterned illumination followed by the phase recovery (NIR-QPI), and by plane white-light illumination (White-BF). NIR-BF shows nearly nothing because of zero absorption/scattering by NIR, and NIR-QPI brings detailed phase features of the tissue which are well correlated with H&E staining in White-BF.

Quantitative phase recovery

Using NIR illumination may consider thick, absorbing H&E stained tissue as transparent specimen. This allows a weak object approximation with complex transmission function $\mathrm{t(r)} \approx 1 + -\mu(\mathrm{r}) + \mathrm{i}\phi(\mathrm{r})$, where μ denotes the absorption of the sample and $\phi(\mathrm{r})$ characterizes the phase [38, 40]. Under partially coherent illumination, the image intensity in Fourier plane can be still expressed as [40]

$$\tilde{\mathrm{I}}(\mathrm{u}) = \mathrm{B}\delta(\mathrm{u}) - H_{ab} \cdot \tilde{\mu}(u) + iH_{ph} \cdot \tilde{\phi}(u) \quad (1)$$

where u is spatial frequency coordinates, B is background term, H_{ab} is absorption transfer function, H_{ph} is phase transfer function (PTF or WOTF), $\tilde{\mu}(u)$, and $\tilde{\phi}(u)$ denotes absorption and phase,

ULSAN NATIONAL INSTITUTE OF SCIENCE AND TECHNOLOGY

respectively. Express of B, H_{ab}, H_{ph} are given by [40]

$$\mathrm{B} = \iint S(u')|P(u')|^2\, d^2u', \tag{2}$$

$$H_{ab} = \iint S(u')P^*(u')\, P(u'+u)d^2u' + \iint S(u')P(u')\, P^*(u'-u)d^2u', \tag{3}$$

$$H_{ph} = \iint S(u')P^*(u')\, P(u'+u)d^2u' - \iint S(u')P(u')\, P^*(u'-u)d^2u', \tag{4}$$

where u' denotes for spatial frequency coordinate of the tilted illumination, $S(u')$, and $P(u')$ denotes for illumination and pupil functions, respectively [38, 40]. To transform phase into measurable intensity or to acquire DPC images, annulus pattern was illuminated on the specimen and captured four phase shifted images. The DPC image then could be calculated by measured images from following equations [38, 40, 54]

$$\mathrm{I}_1^{DPC} = \frac{Im_1 - Im_2}{(Im_1 + Im_2)}, \quad \mathrm{I}_2^{DPC} = \frac{Im_3 - Im_4}{(Im_3 + Im_4)}. \tag{5}$$

where Im_n is image captured from nth pattern. Since $\mathrm{B}_1 = \mathrm{B}_2$, background terms were eliminated in numerator term of DPC measurements. In the aberration-free system, ideally DPC image doesn't contain any absorption information, leading $H_{ab} = 0$. Moreover, exact same illumination patterns on the corresponding axis would make phase term, $H_1^{ph} = -H_2^{ph}$ [38]. Thus, nth DPC equation could be simplified in linear form as $\tilde{\mathrm{I}}_n^{DPC} = \frac{H_{ph}}{B} \cdot i\tilde{\phi}(u)$. With all four DPC images, quantitative phase could be retrieved by simple deconvolution process with Tikhonov's regularization term γ [40].

$$\phi(r) = \mathcal{F}^{-1}\left\{\frac{\sum_i \tilde{H}_i(u) \cdot \tilde{I}_{DPC,i}(u)}{\sum_i |\tilde{H}_i(u)|^2 + \gamma}\right\} * \alpha, (\mathrm{i} = 1,2) \tag{6}$$

For this study, α, and γ was empirically set to 0.58, and ~ 0.08, respectively, from calibration experiment using phase resolution target (Benchmark Technology, Quantitative phase microscopy target).

4.2.3 Sample preparation and imaging

In order to avoid deformations found mostly after tissue staining, here, QPI and bright field imaging was achieved using corresponding stained tissue sample. All the samples that were used in this study were prepared by the Ulsan National Institute of Science and Technology Central Research Facility

ULSAN NATIONAL INSTITUTE OF SCIENCE AND TECHNOLOGY

(UCRF) at UNIST. All animals were sacrificed, and organs were harvested under accordance with a protocol approved by UNIST Institutional Animal Care and Use Committee (IACUC). In this experiment, coronal section of brain, and kidney were acquired for QPI imaging. For the tissue preparation, 10-week old Balb/c wild type male mouse was utilized. After harvesting brain and kidney from mouse, these tissues underwent through a formalin infiltration process. Then, dehydrated tissues were fixed in paraffin, making paraffin-embedding blocks. These paraffin blocks were sectioned along the coronal plane with a thickness of 5 μm using a microtome (RM2255, Leica Microsystems). To compare the NIR performance according to thickness, kidney tissue was sliced for 2, 5, 8, 11 μm thickness. Prior to staining process, tissue sections were completely deparaffinized using Xylene and a series of graded ethanol solutions on a standard glass slide. Following the deparaffinization, tissue is stained by hematoxylin and eosin dye through conventional staining protocol, then tissue specimen was sealed with coverslip. In prior to training process, using stained tissue presents several advantages. Cumbersome and complicated image registration algorithm is not mandatory since image can be captured in a single platform. In addition, avoiding deformation in tissue may improve the training performances in deep learning.

Following the tissue staining process, the specimen was imaged using a NIR-QPI microscope system to visualize quantitative phase information. Since our microscope system is implemented on the conventional bright field microscope configuration by alternating only illumination parts with LED matrix, bright field image could be acquired in same microscope by changing the illumination apparatus. No additional sample preparation process is needed. Both QPI and bright field H&E image was captured using 10x/0.25NA objectives.

4.2.4 Data processing methods

Data pre-processing for deep learning

A set of cropped images from acquired data was created for training and testing of in-silico staining model. Regions of interest (ROIs) in 100 × 100 pixels were found in each 2448 x 2048 pixels image producing 48,800 ROIs per image. We found 1,200 additional ROIs from random position to make a total 50,000 ROIs per Image. Images from four tissue sites were used for training and validation as 8:2 ratio, i.e. total 200,000 ROIs of 160,000 ROIs for training, and 40,000 ROIs for validation. We used additional images from 6 brain tissue sites or 16 kidney tissue sites for testing our results (Figure 4. 17 and Figure 4. 18). All the computation for data preparation were performed using a custom written software in MATLAB (Mathworks Inc., U.S.A.).

Image registration for evaluation of NIR-based QPI system

In this study, simple image registration algorithm was applied to evaluate the effect of phase on stained

ULSAN NATIONAL INSTITUTE OF SCIENCE AND TECHNOLOGY

and unstrained tissue QPI according while according to illumination wavelength variations. In order to find the phase deviations between quantitative phase images captured by different illumination wavelengths on stained and unstained tissues, here, we utilized M-estimator Sample Consensus (MSAC) algorithm [112] to register two QPI data set correctly. In addition, affine-based speeded-up robust features (SURF) was applied to detect the features between images. Figure 4. 10 simply illustrates the image registration process. Moreover, this phase deviation analysis based on image registration method was applied for each sliced thicknesses (3, 5, 8, 11 μm thick tissues).

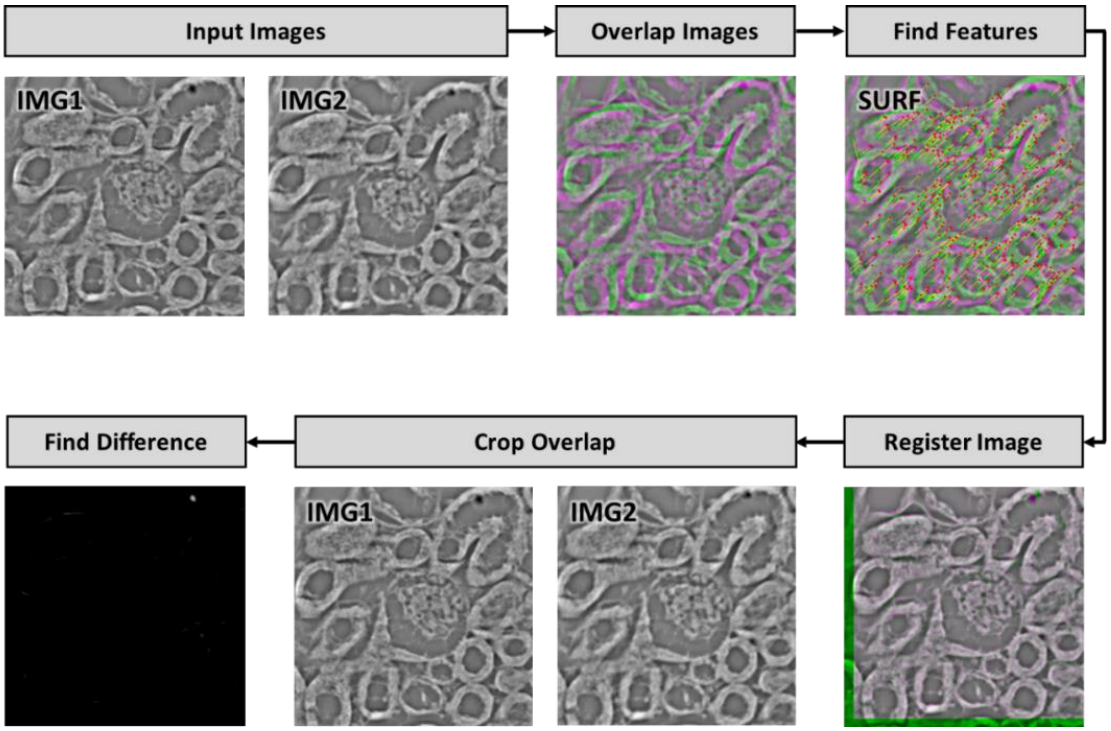

Figure 4. 10 Illustration of registration methods for analysis of effects on phase deviations between stained and unstained tissues according to illumination wavelength variations

4.2.5 GAN architecture and training

In-silico tissue staining with generative adversarial network

In-silico staining using GAN is a set of deep neural networks (DNNs) to transform the monochromatic quantitative phase information to color-based BF histological stained images. Here, in-silico stating model follows the SR-GAN approach [113]. Figure 4. 11 illustrates the architecture of in-silico staining model using GAN structures. In-silico GAN is composed three DNNs of a generator network (Figure 4. 11a), a discriminator networks (Figure 4. 11**b**), and a feature extraction network (Figure 4. 11c). The generator networks are structured in residual module by stacking a convolution layer, an activation layer with parametric ReLU (PReLU), batch normalization layer with a momentum 0.5, a convolution layer, and a batch normalization layer followed by an elementwise summation of input and output. The

ULSAN NATIONAL INSTITUTE OF SCIENCE AND TECHNOLOGY

residual module is repeated sixteen times followed by the other residual connection from the beginning of the residual module. These skip connections easy the training process at such a very deep neural network, avoiding the gradient vanishing problems and extracting more details in features. The discriminator network is a convolutional neural network to classify generated image or bright field color H&E stained tissue image (Figure 4.9c). As shown in Figure 4. 11**b**, it is composed of series of convolution layers, activation layers with LReLU at the slope 0.2, and batch normalization at a momentum 0.5 followed by a fully connected layer, an activation layer with LReLU at the slope 0.2, a fully connected layer in size 2, and an activation layer with Sigmoid. We took a part of pre-trained VGG19 network [114] to ImageNet database [106] as a feature extraction network (Figure 4. 11c). The feature extraction networks are composed of the convolution layers, activation layers of ReLU, and max-pooling layers of the VGG19. All layers in the feature extraction network set to inference only (no further training performed).

In-silico GAN uses a generative adversarial network architecture [111, 113] to create a chromatic stained tissue images with the same statistical features as labeling image $I^{H\&E}$ on top of the monochromatic QPI tissue image data I^{QPI}. Let in-silico GAN has a generator network G_{θ_G} in parameters θ_G creating intermediate data $G_{\theta_G}(I^{QPI})$, we optimize the generator network $G_{\widehat{\theta_G}}$ [113]:

$$\widehat{\theta_G} = \underset{\theta_G}{argmin} \frac{1}{N} \sum_{n=1}^{N} l_g \left(I_n^{H\&E}, G_{\theta_G}(I^{QPI}) \right), \tag{7}$$

with N training images, $n = 1, \dots, N,$ and the generator loss function l_g defined [113]

$$l_g = \frac{1}{W_{i,j} H_{i,j}} \sum_{x=1}^{W_{i,j}} \sum_{y=1}^{H_{i,j}} \left(\phi_{i,j}(I^{H\&E})_{x,y} - \phi_{i,j}\left(G_{\theta_G}(I^{QPI}) \right)_{x,y} \right)^2 + 10^{-3} \sum_n^N -\log\left(D_{\theta_D}\left(G_{\theta_G}(I^{QPI}) \right) \right), \tag{8}$$

where $\phi_{i,j}$ denotes the jth convolution in i^{th} activation layer output from the feature extraction network and D_{θ_D} denotes a discriminator network parametrized in θ_D distinguishing between generator output $G_{\theta_G}(I^{QPI})$ and label data $I^{H\&E}$. We optimize the discriminator network D_{θ_D} along with the generator network G_{θ_G} at each epoch by solving the adversarial problem [113]:

$$\min_{\theta_G} \max_{\theta_D} \mathbb{E}_{I^{H\&E} \sim p(I^{H\&E})} \left[\log D_{\theta_D}\left(I^{H\&E} \right) \right] + \mathbb{E}_{I^{QPI} \sim p_G(I^{QPI})} \left[\log\left(1 - D_{\theta_D}\left(G_{\theta_G}(I^{QPI}) \right) \right) \right] \tag{9}$$

In the in-silico GAN architecture, both the generator and discriminator network are optimized using an adaptive moment estimation (Adam) optimizer [115] with learning rates of 1×10^{-4}, exponential

ULSAN NATIONAL INSTITUTE OF SCIENCE AND TECHNOLOGY

decay rates β_1 = 0.9 and β_2 = 0.999, and a fuzz factor ε = 1×10^{-8}. These parameters were chosen empirically for the best performance. The discriminator network D_{θ_D} sets the loss function of binary cross-entropy l_d [113]:

$$l_d = -\frac{1}{N}\sum_{i=1}^{N} y_i \times \log\left(D_{\theta_D}(I_i)\right) + (1 - y_i) \times \log\left(1 - D_{\theta_D}(I_i)\right), \tag{10}$$

where y_i denotes the ith label of an image I_i, $i = 1, \ldots, N$. We took a part of pre-trained VGG19 for the feature extraction network and no further training was involved as mentioned above. The generator network and the discriminator network were trained alternatively in an adversarial manner over iterations. The in-silico GAN was trained for 500 epochs.

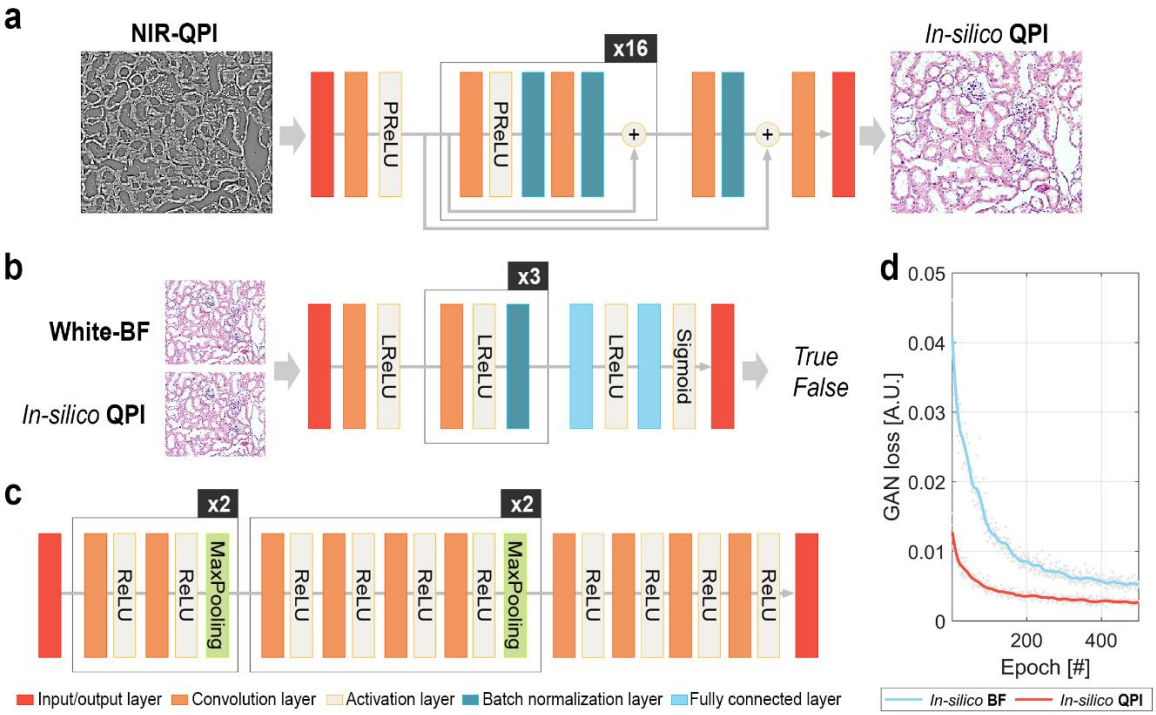

Figure 4. 11 Architecture of in-silico staining algorithm using GAN structure. In-silico staining is carried out using four deep neural networks (DNNs), i.e. (a) generator network, (b) discriminator network, (c) feature extraction network. (a) The generator network performs in-silico staining from input image (NIR-QPI). (b) The discriminator network evaluates the difference of the stained image (White-BF) and the generated image. (c) Image features are extracted using ImageNet pre-trained VGG19 network in (c). The outcome of (b) and (c) are used to train (a) in adversarial manner. (d) Generative adversarial network (GAN) losses over training. Two models were trained, i.e. In-silico BF to in-silico staining of NIR-brightfield image (NIR-BF), or In-silico QPI to in-silico staining of NIR-QPI image.

Image quality assessment

To evaluate the performance of the QPI-based in-silico staining, we further trained and analyzed GAN model by applying different contrast images such as bright field stained tissue image (ground truth, GT), NIR bright field, low-passed QPI, fully reconstructed QPI images. We calculated three full-reference

ULSAN NATIONAL INSTITUTE OF SCIENCE AND TECHNOLOGY

quality measurements of the mean-squared error (MSE), peak signal-to-noise ratio (pSNR), and structural similarity (SSIM) index between stained section image $S^{H\&E}$ versus the in-silico image S^{IS} from GAN scan [15, 16]:

$$MSE\left(S^{H\&E}, S^{IS}\right) = \frac{1}{N}\sum_{i=1}^{N}\left(S_i^{H\&E} - S_i^{IS}\right)^2, \tag{11}$$

$$pSNR\left(S^{H\&E}, S^{IS}\right) = 10 \times \log_{10}\left(\frac{pk^2}{MSE\left(S^{H\&E}, S^{IS}\right)}\right), \tag{12}$$

$$SSIM\left(S^{H\&E}, S^{IS}\right) = \frac{(2\mu_{H\&E}\mu_{IS}+C_1)(2\sigma_{H\&E,IS}+C_2)}{(\mu_{H\&E}^2+\mu_{IS}^2+C_1)(\sigma_{H\&E}^2+\sigma_{IS}^2+C_2)}, \tag{13}$$

where both $S^{H\&E}$ and S^{IS} has the same image size N with pixel $i = 1, \ldots, N$, pk denotes image bit depth, i.e. 8 bit, pk = 255, and μ_{GT}, μ_R, σ_{GT}, σ_R, or $\sigma_{GT,R}$ denote the local means μ, standard deviations σ or cross-covariance $\sigma_{H\&E,IS}$ of image $S^{H\&E}$ or S^{IS}. MSE, pSNR, or SSIM were calculated using MATLAB functions, `Immse`, `psnr`, or `ssim` subsequently.

4.2.6 Implementation details

Table 4. 2 Training details for the in-silico staining of QPI images using GAN

Patch size	Batch size	# of training images	# of validation images	Training time (h)	# of epochs
100 x 100	16	16,000	4,000	~ 72	< 500

Training details of deep neural network structures and parameters related to image patch size, number of training and validation images, and conditions are available in Table 4. 2. GAN was implemented using Keras version 2.2.4 front-end with tensorflow-gpu version 1.13.1 back-end running on Python version 3.7.3. Python libraries of tqdm version 4.31.1, numpy version 1.16.2, scipy version 1.2.1, scikit-image 0.14.2, h5py version 2.8.0, matplotlib version 3.0.3, os, and argparse were used. GAN algorithm was implemented on a desktop computer configured with a Core i7-7800X CPU at 3.5GHz (Intel), 128 GB of RAM, and a Titan V GPU (Nvidia) running a Windows 10 operating system (Microsoft). GAN was trained or inference using a GPU disabling the auto mixed-precision setting or a CPU. Data preprocessing and analysis were carried out using MATLAB R2019a (MathWorks). Furthermore, all image hardware was synchronized and controlled automatically by MATLAB (Mathworks, Inc., MATLAB).

ULSAN NATIONAL INSTITUTE OF SCIENCE AND TECHNOLOGY

4.2.7 Results & Discussion

Effect of NIR illumination in quantitative phase imaging

In order to evaluate the influence of NIR illumination for tissue quantitative phase imaging, kidney of mouse tissue sliced into 2, 5, 8, 11 μm thick were imaged with different types of illumination wavelength. Specifically, center wavelength of 480 nm, 530 nm, 650 nm, and 850 nm illumination was utilized for this imaging session. Depending on the light absorptions and scattering which may vary with wavelength of illumination and thickness of the tissue, we analyzed the phase variations ($\Delta\phi(r)$) and scattering coefficient (μ_s). The scattering coefficient was quantitatively extract using the measured phase information according to the scattering-phase theorem. In general, light attenuation is measured with respect to the depth of sample and converted to a scattering coefficient based on the Beer-Lambert law. However, the scattering-phase theorem can be applied for computation of the scattering coefficient utilizing only a 2D phase information in the following manner [116]:

$$\mu_s = \frac{\langle \Delta\phi^2(r) \rangle_r}{L}, \tag{14}$$

where $\Delta\phi(r)$ indicates spatial variance in phase image and L is thickness of the tissue. Here, L should be 2, 5, 8, 11 μm. The calculation was proceeded within window size of 512 x 512 pixels. According to the scattering-phase theorem, the scattering coefficient is directly influence by the phase variance, which means that scattering will present at the high phase fluctuation. In addition, phase measurements were demonstrated using very thin tissue slices, hence, the single scattering regime can be expected in this experiment. Therefore, dispersion and absorption were not significant for this experiment, especially for 850 nm illumination wavelength.

Figure 4. 12 illustrates the quantitative analysis of QPI that was captured by various illumination colors according to tissue thickness. As thickness increase, overall measured phase has been increased which follows the phase equation $\Delta\phi = \frac{2\pi}{\lambda_c}\Delta nL$ [116], where Δn, and L denotes variation of refractive index, and thickness, respectively. Furthermore, phase measurement was inversely proportion to illumination wavelength, which also follows the phase equation. Throughout this experiment, higher phases were measured in stained kidney tissue using visible wavelength illumination for the all thicknesses. Presence of high absorption in the specimen would yield phase error in computation (absorption information would be eliminated for DPC calculation, assuming to have highest phase

ULSAN NATIONAL INSTITUTE OF SCIENCE AND TECHNOLOGY

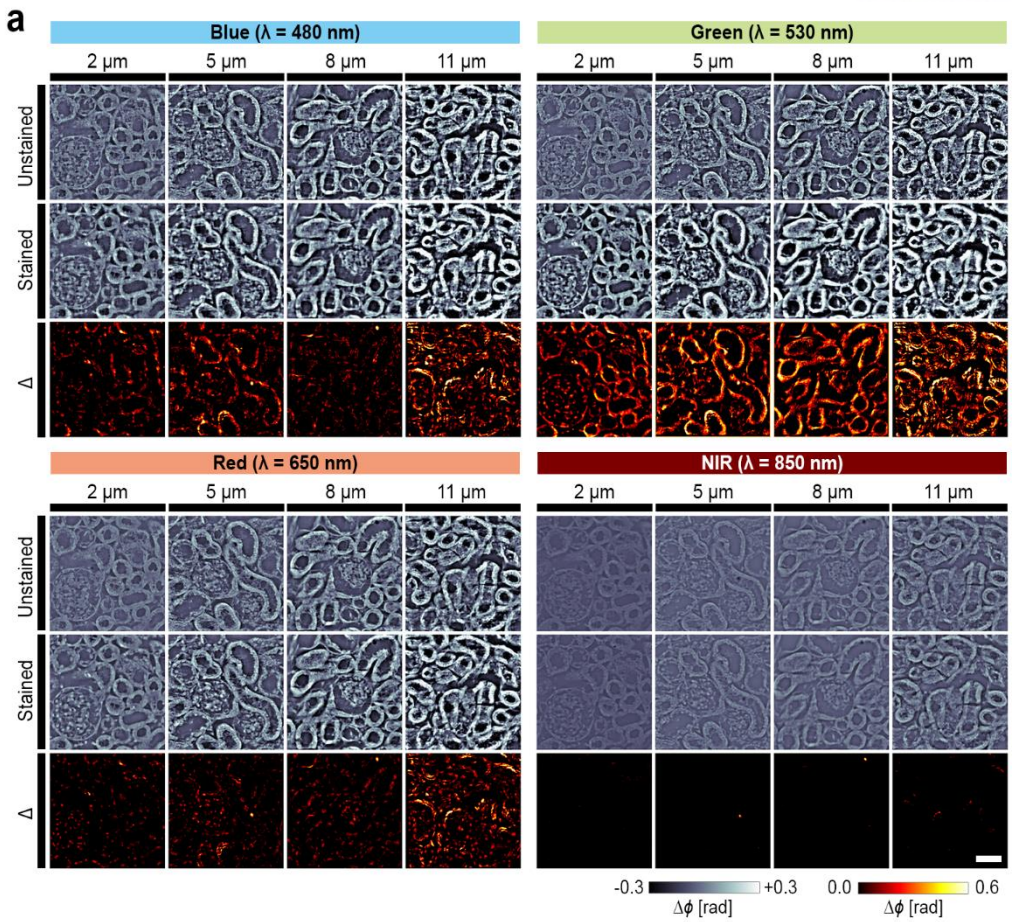

Figure 4. 12 Analysis of DPC driven QPI of mouse kidney tissue before and after H&E staining

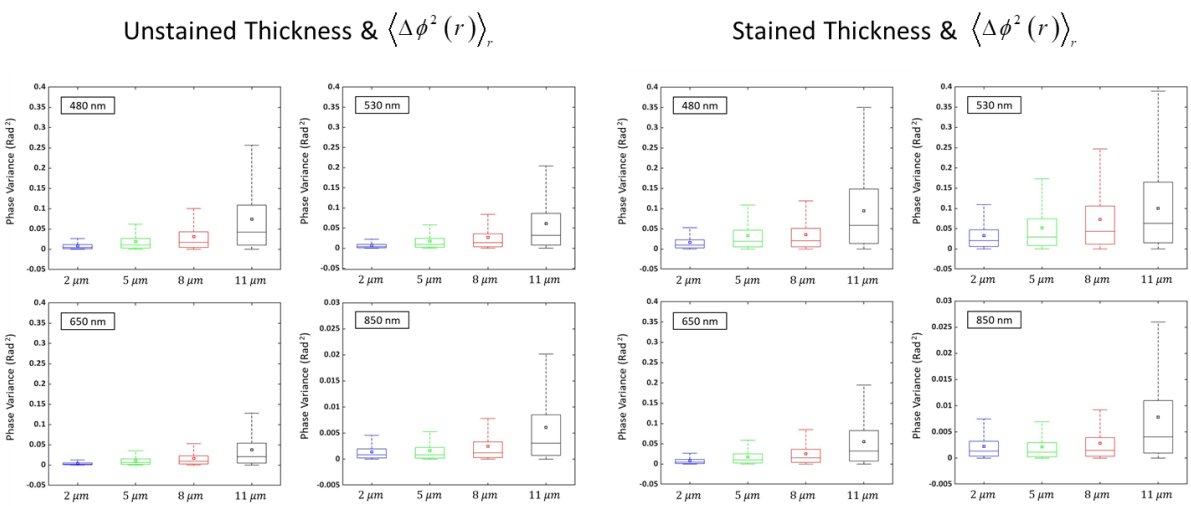

Figure 4. 13 Phase variation measurements on various illumination wavelength and tissue thickness using mouse kidney tissue before and after staining

ULSAN NATIONAL INSTITUTE OF SCIENCE AND TECHNOLOGY

presence), and structural information could be hidden in the DPC-based QPI system. However, minimal phase difference was shown between unstained and stained tissue when illumination wavelength of 850 nm (NIR). It is expected that absorption and scattering is minimally affecting the stained tissue in quantitative phase measurements when thickness is under ~10 μm. Figure 4. 13 graphically presents the average of phase variation measurements according to Figure 4. 12.

Furthermore, scattering coefficient was analyzed for thickness and illumination wavelength. Figure 4. 14 describes the average of scattering coefficient calculated in the image FOV according to scattering-phase theorem. Scatterings were highly presenting at low illumination wavelength as well as use of thicker specimens. Hence, wavelength of 480 nm showed highest while 850 nm showed the lowest scattering coefficients for all tissue thickness. In terms of thickness, 11 μm thick kidney tissue demonstrated the highest scattering coefficient for unstained kidney tissue. In the stained tissue imaging, trend of the scattering coefficient graph exactly follows the light absorption spectrum presented in

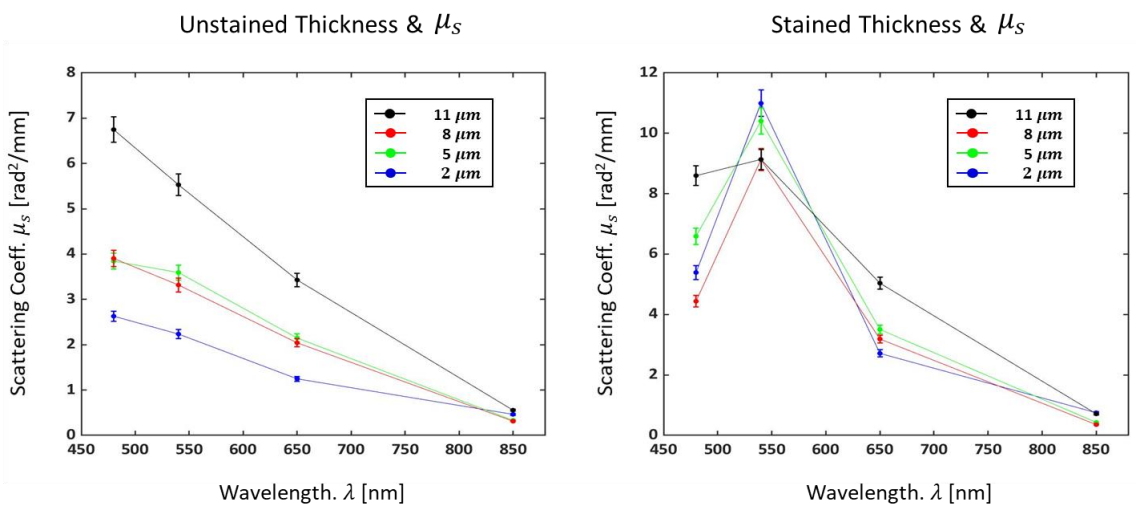

Figure 4. 14 Scattering coefficient on various illumination wavelength and tissue thickness using mouse kidney tissue before and after staining

Figure 4. 9a. High absorptions were presented for wavelength of 530 nm which also presents highest scattering coefficient. Similar to values found in the unstained tissue, lowest scattering coefficient was found when wavelength of 850 nm was utilized for stained tissue imaging. In addition, not much variations were found between stained and unstained tissue measured at 850 nm. Throughout this experiment, using NIR-illumination for QPI image illustrates and confirmed that stained tissue is available for data acquisition for the in-silico GAN training. Chromatic staining was found to be less affective to QPI imaging when NIR illumination was employed. One should note that staining tissue was only utilized for training/testing the GAN framework in this study to neglect the registration process and avoid tissue deformation from chemical staining process.

ULSAN NATIONAL INSTITUTE OF SCIENCE AND TECHNOLOGY

In-silico staining of tissue specimens

After validation of NIR-QPI system for stained tissue, we demonstrated the in-silico GAN models using coronally sectioned kidney and brain tissues. Following the training session, we blindly tested out the inference of trained networks by applying the fresh quantitatively retrieved phase image data sets which were not exposed during the training process. Figure 4. 15 illustrates the outcome for the in-silico GAN of phase image of mouse kidney tissue. These result demonstrates successful color conversion from QPI to bright-field equivalent image through trained GAN framework. Compare to bright field H&E kidney tissue image, colors of in-silico stained image were assigned correctly according to pathological constituents such as cell nuclei, proximal tubules, and glomerulus. Additional results of in-silico staining of QPI is illustrated in Figure 4. 16 for mouse brain tissue (also stained in H&E). For qualitative assessment, brain tissue seems to have less difference between in-silico and bright field images. This means that better training performance could be expected for GAN framework using brain tissue, which can be assume from less structural complexity compare to kidney tissue.

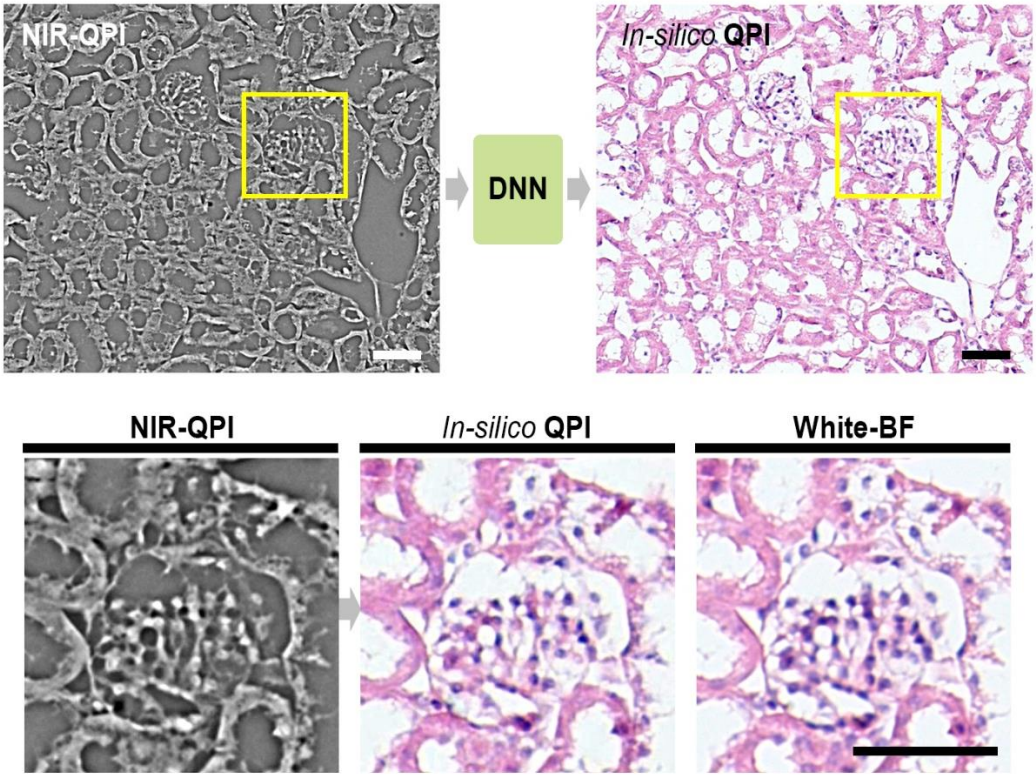

Figure 4. 15 In-silico staining of mouse kidney tissue using GAN frameworks

ULSAN NATIONAL INSTITUTE OF SCIENCE AND TECHNOLOGY

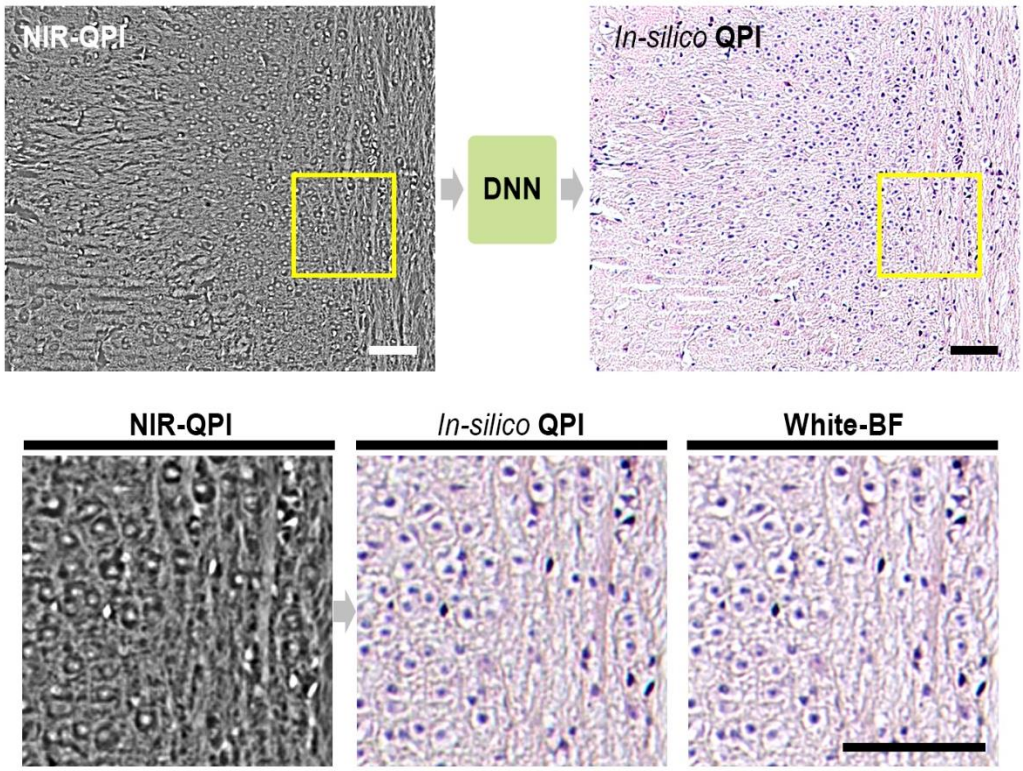

Figure 4. 16 In-silico staining of mouse brain tissue using GAN frameworks

Quantitative analysis of network output image quality

Similarity between the stained section images and the in-silico images were quantitatively and qualitatively evaluated for kidney and brain sections in Figure 4. 17 and Figure 4. 18, subsequently. Four images of the histological stained images by white light brightfield microscopy (white-BF), NIR-BF images, and NIR-QPI images were obtained from the tissue sections. NIR-BF and NIR-QPI images were in-silico stained using the trained generator networks. Figure 4. 17a shows the kidney section images of NIR-BF and NIR-QPI, and their in-silico stained images of In-silico BF and In-silico QPI, subsequently, with the corresponding stained tissue section image (white-BF). The In-silico QPI and the stained images are visually well matched even at the detailed podocyte structures shown in Fig. 6b. In-silico BF describes pinkish colors of convoluted tubule structures, yet the cellular morphologies are crumbled, especially, the podocyte cannot be recognized (Figure 4. 17b; In-silico BF). The cross-section intensity along the yellow dotted line in Figure 4. 17nwere plotted in Figure 4. 17c. The intensity from In-silico QPI and the stained image (white-BF) lines together, yet, In-silico BF intensity is apart. Correlation coefficients were calculated for the cross-section intensity measurements from in-silico stained image and the stained image (Figure 4. 17d). The very strong correlation (>0.9) appears for In-silico QPI and the weak correlation (<0.4) are for In-silico BF. Figure 4. 17e shows full referenced image quality measures of mean square error (MSE), peak signal-to-noise ratio (pSNR), structure

ULSAN NATIONAL INSTITUTE OF SCIENCE AND TECHNOLOGY

similarity (SSIM) from 19 tissue sections, and blind mean opinion scores (MOS) testing asked to the six trained histopathologists (Table 4. 3). In-silico QPI gives less MSE, higher pSNR, and better SSIM than In-silico BF. Six histopathologists could not differentiate the stained image (white-BF) to the In-silico QPI with good score (>3), and In-silico BF scored poor image quality (<2). Figure 4. 18 shows the same analysis with the brain tissue section. In-silico BF shows a very different morphology to the stained tissue section, yet In-silico QPI gives the exact same structure of the stained tissue section (Figs. Figure 4. 18 a and Figure 4. 18 b). The cross-section intensities along the dotted yellow lines from Fig. 7b and their correlation coefficients were analyzed (Figure 4. 18 c and Figure 4. 18 d). The In-silico QPI and the stained images are perfectly matched; however, the In-silico BF and the stained images are not matched and are anti-correlated. The image quality was evaluated using MSE, pSNR, and SSIM from 10 brain sections in addition to blind MOS testing from the six histopathologists (Figure 4. 18 and Table 4. 3). Similar to the kidney section case, In-silico QPI gives less MSE, higher pSNR, and better SSIM than In-silico BF. Again, six histopathologists could not differentiate the stained image (white-BF) to the In-silico QPI with good score (>3), and In-silico BF scored poor image quality (<2).

Discussion

We demonstrated the in-silico staining of quantitative phase contrast images using a generative adversarial network framework. Monochromatic information from QPI has been successfully transformed to chromatic images which corresponds to bright field H&E stained tissue or golden standard. Significance of this study could be describable to improvement of the conventional virtual staining methods. Using a stained tissue from the QPI acquisition for DNN input eliminates the complicated image alignment/registration algorithm and neglects the random loss or deformation of tissue constituents that typically happens during the staining process, making the training/learning procedure of DNN very simple and less times consuming. With a NIR-based QPI system, in-silico staining method could be potentially expanded using different stained tissue with various chemical dyes such as Masson's Trichrome, Jones stain, Toluidine Blue, Luxol Fast Blue, and etc [117], which usually have light absorption spectrum within the visible range. Following the training the network, stained tissue is not necessary anymore. The new stain-free quantitative phase images from unstained tissues (only kidney and brain) are available for the pretrained network to generate virtually stained images. Following the training process demonstrated here, any type of tissue is available for in-silico staining. Therefore, in-silico tissue staining method that we proposed in this study enables to bypass the cumbersome chromatic staining process in conventional histological procedure. This allows saving time, labor, and cost of the staining method, providing great benefits to the real clinic applications. To the best of our knowledge, it is the first time demonstrating the tissue as well as absorbing specimen acquisitions using DPC driven quantitative phase imaging method. Conventionally DPC imaging microscope [38, 40, 54] has shown great potentials in live cell imaging. Changing shape of the

ULSAN NATIONAL INSTITUTE OF SCIENCE AND TECHNOLOGY

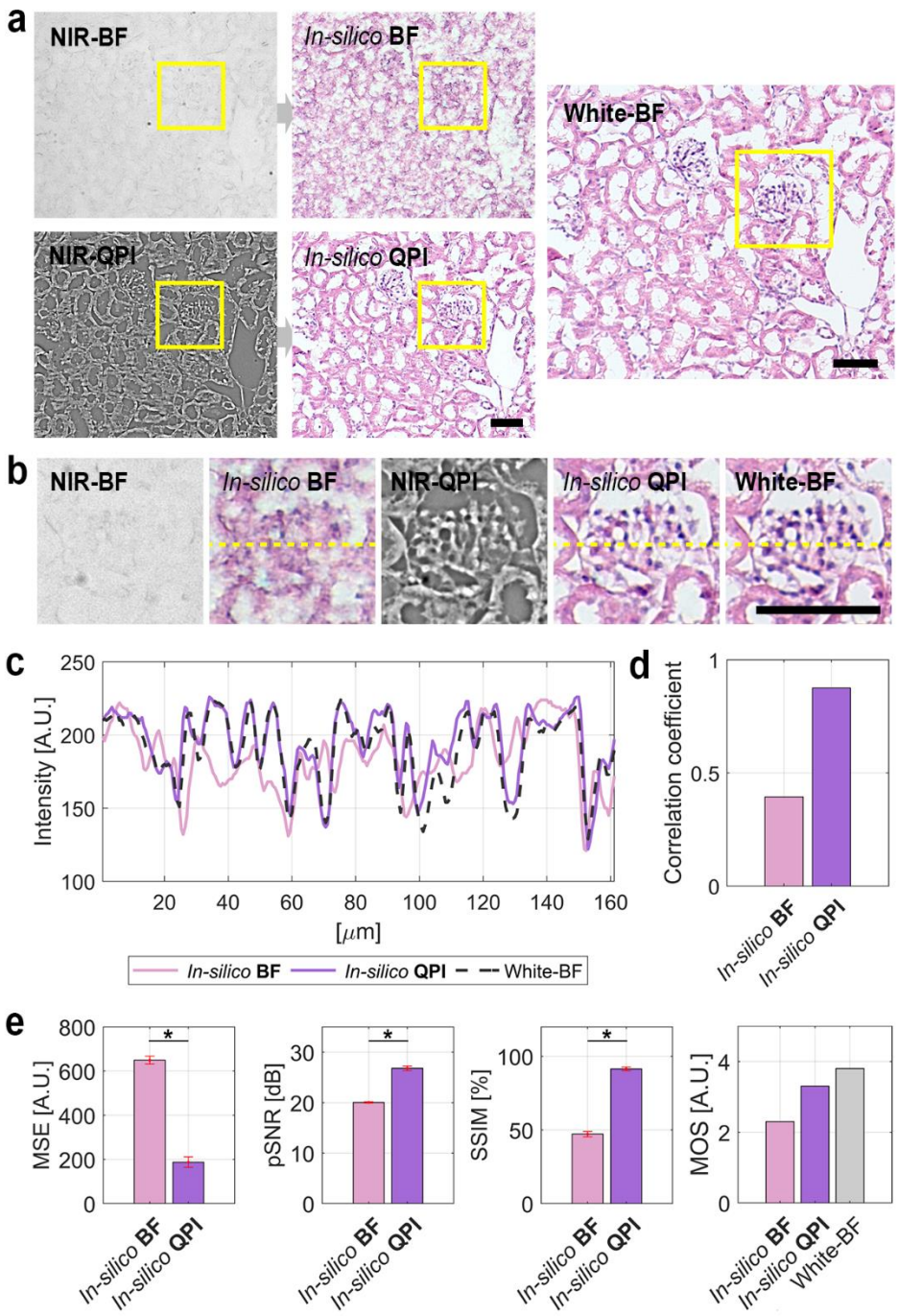

Figure 4. 17 In-silico staining from NIR-BF image NIR-BF or NIR-QPI image for a kidney section. (a, b) Images of NIR-BF or NIR-QPI followed by in-silico stained image of each (In-silico BF or In-silico QPI, subsequently) with a correspond stained kidney section image (White-BF). Yellow boxed regions are shown in (b). (c, d) Intensity profile along yellow dotted line in (b) are shown and the correlation coefficient between In-silico stained images (In-silico BF or In-silico QPI) and the stained section image (white-BF). (e) Quantitative analysis of image similarity between In-silico stained images (In-silico BF or In-silico QPI) and the stained section image (white-BF) by mean square error (MSE), peak signal to noise ratio (pSNR), structure similarity (SSIM), or mean opinion score (MOS) from six histopathologists. Scale bar: 100 μm.

ULSAN NATIONAL INSTITUTE OF SCIENCE AND TECHNOLOGY

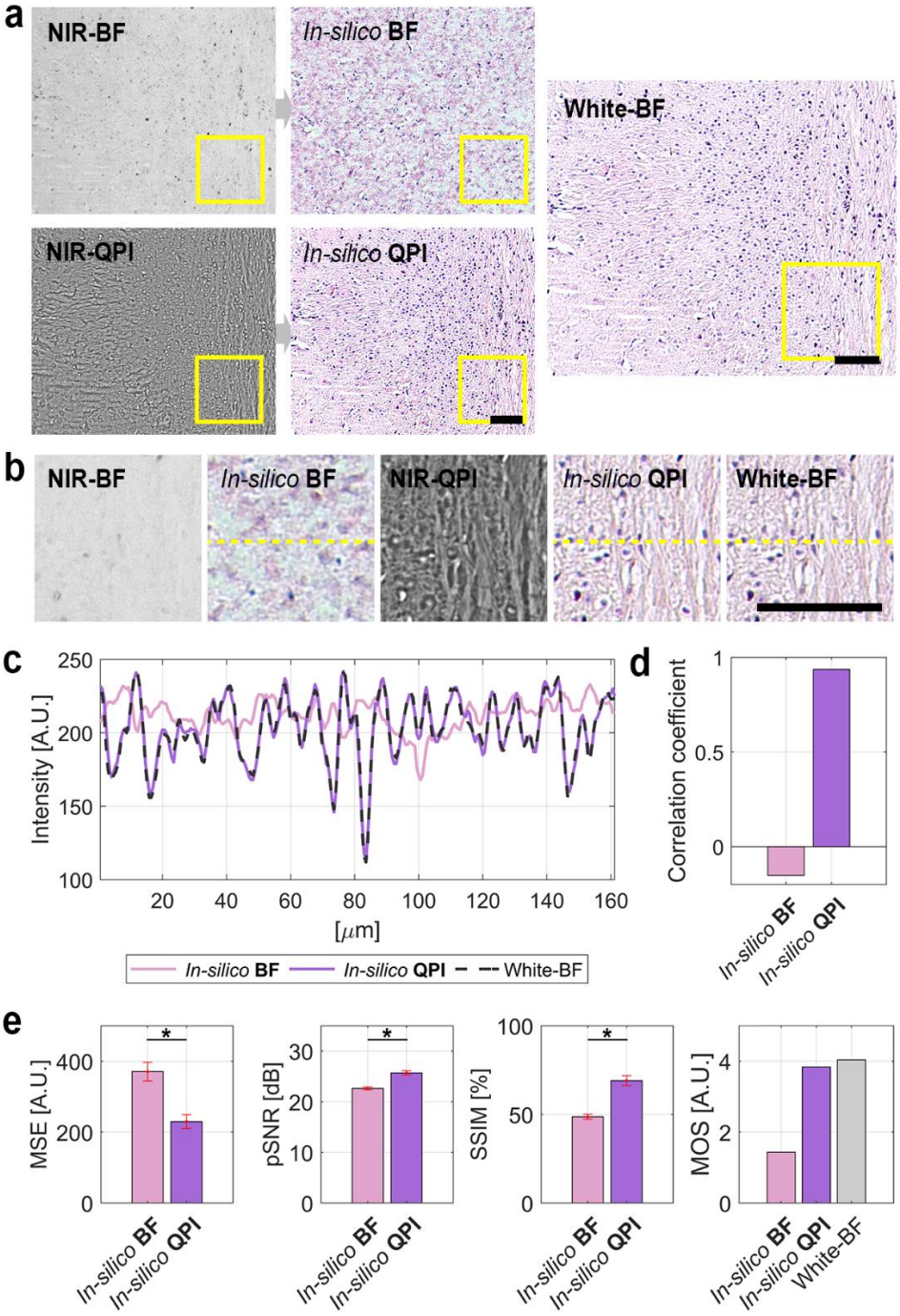

Figure 4. 18 In-silico staining from NIR-BF image NIR-BF or NIR-QPI image for a brain section. (a, b) Images of NIR-BF or NIR-QPI followed by in-silico stained image of each (In-silico BF or In-silico QPI, subsequently) with a correspond stained brain section image (White-BF). Yellow boxed regions are shown in (b). (c, d) Intensity profile along yellow dotted line in (b) are shown and the correlation coefficient between In-silico stained images (In-silico BF or In-silico QPI) and the stained section image (white-BF). (e) Quantitative analysis of image similarity between In-silico stained images (In-silico BF or In-silico QPI) and the stained section image (white-BF) by mean square error (MSE), peak signal to noise ratio (pSNR), structure similarity (SSIM), or mean opinion score (MOS) from six histopathologists. Scale bar: 100 μm.

ULSAN NATIONAL INSTITUTE OF SCIENCE AND TECHNOLOGY

Table 4. 3 Blind mean opinion score (MOS) testing for In-silico and H&E histological staining for kidney and brain sections.

	Kidney							Brain						
Tissue #	**P1**	**P2**	**P3**	**P4**	**P5**	**P6**	**Avg.**	**P1**	**P2**	**P3**	**P4**	**P5**	**P6**	**Avg.**
1 (HS)	5	4	5	5	5	5	4.8	2	4	3	5	5	5	4.0
1 (In-silico QPI)	5	4	4	4	5	5	4.5	3	4	4	4	4	3	3.7
1 (In-silico BF)	4	4	4	2	3	5	3.7	1	1	2	1	1	1	1.2
2 (HS)	4	2	4	4	5	4	3.8	2	4	3	3	5	4	3.5
2 (In-silico QPI)	4	2	4	3	4	5	3.7	5	4	4	4	4	5	4.3
2 (In-silico BF)	1	1	4	1	2	2	1.8	1	1	2	1	1	1	1.2
3 (HS)	3	2	3	4	4	3	3.2	4	5	4	4	5	5	4.5
3 (In-silico QPI)	3	2	3	4	3	4	3.2	5	4	4	4	4	5	4.3
3 (In-silico BF)	1	1	4	1	2	2	1.8	1	1	2	1	1	1	1.2
4 (HS)	4	3	3	3	4	3	3.3	4	4	3	3	5	5	4.0
4 (In-silico QPI)	3	1	3	4	3	3	2.8	3	4	3	3	4	5	3.7
4 (In-silico BF)	2	1	4	1	2	3	2.2	1	1	2	1	1	1	1.2
5 (HS)	4	2	4	4	4	4	3.7	4	4	3	2	4	5	3.7
5 (In-silico QPI)	4	2	4	4	3	4	3.5	4	4	4	4	3	5	4.0
5 (In-silico BF)	3	2	3	3	2	4	2.8	1	1	2	1	1	1	1.2
6 (HS)	4	4	3	4	3	3	3.5	3	3	4	4	4	5	3.8
6 (In-silico QPI)	3	1	3	4	2	4	2.8	3	4	4	3	3	4	3.5
6 (In-silico BF)	2	1	4	2	2	2	2.2	3	2	3	1	2	3	2.3
7 (HS)	5	5	5	5	4	4	4.7	3	3	4	5	4	5	4.0
7 (In-silico QPI)	4	1	5	5	2	4	3.5	4	4	4	3	3	4	3.7
7 (In-silico BF)	4	1	4	2	2	3	2.7	1	1	2	1	1	1	1.2
8 (HS)	3	4	4	3	4	3	3.5	4	3	4	5	4	5	4.2
8 (In-silico QPI)	2	2	4	2	2	3	2.5	4	3	4	4	3	5	3.8
8 (In-silico BF)	1	2	3	1	2	2	1.8	1	1	2	1	1	1	1.2
9 (HS)	4	2	3	3	4	2	3.0	4	4	4	4	4	5	4.2
9 (In-silico QPI)	2	3	3	2	3	2	2.5	3	4	4	4	3	4	3.7
9 (In-silico BF)	2	2	3	1	2	2	2.0	1	1	2	1	1	1	1.2
10 (HS)	5	3	4	5	5	5	4.5	4	5	4	5	4	5	4.5
10 (In-silico QPI)	5	3	4	4	4	4	4.0	3	4	4	3	3	5	3.7
10 (In-silico BF)	2	3	3	1	1	2	2.0	2	3	3	2	3	3	2.7
Average (HS)	4.1	3.1	3.8	4	4.2	3.6	3.8	3.4	3.9	3.6	4	4.4	4.9	4.0
Average (In-silico QPI)	3.5	2.1	3.7	3.6	3.1	3.8	3.3	3.7	3.9	3.9	3.6	3.4	4.5	3.8
Average (In-silico BF)	2.2	1.8	3.6	1.5	2	2.7	2.3	1.3	1.3	2.2	1.1	1.3	1.4	1.4

illumination benefits the imaging system, providing different contrast images including quantitative phase contrast in a single platform [37]. However, application of DPC imaging microscope was mostly limited to transparent cell imaging due to use of weak object approximation [40]. When object have

ULSAN NATIONAL INSTITUTE OF SCIENCE AND TECHNOLOGY

high absorption and scattering properties to the light, phase collapse is possible due to contradiction of linearized forward problem that is computed from weak object transfer function. Moreover, structural information may invisible in QPI, according to the light vanishing from absorption properties. Herein, patterned NIR illumination in the QPI system provides the potentials to expend the application field of the DPC driven QPI system. It enables to acquire not only thick tissue but also chromatic stained specimen, avoiding the absorption and scattering properties of H&E staining as shown in Figure 4. 9a. Therefore, stained tissue could be assumed as transparent specimen or slowly varying phase object (weak object approximation) that allows to maintain the quantitative phase retrieval principle, linearizing the complex field of the object. Currently, we have applied our system to paraffin embedded tissue sections. However, other fixation methods such as frozen tissue sections are applicable to in-silico tissue staining method with our NIR-based QPI approach.

Although virtually staining method is applicable with other QPI modalities such as interferometric microscopy, digital holography (DH), transport-of-intensity equation (TIE), Fourier ptychography (FP), we believe that our approach employing the DPC-based QPI system has advantages over other QPI systems. DH or interferometric approaches, in general, uses coherent light source, making the system expensive, sensitive to misalignments, speckle noises, and vibration [19, 21]. Alternative to coherent illumination system, TIE and FP are partially coherent illumination-based QPI techniques that quantitatively retrieve the phase from complex field of an object. However, these methods require multiple image acquisitions or iterative post-processing methods, which generally take time-consuming processes. Among others, DPC approach-based QPI, however, doesn't require any cumbersome optical alignments or expensive apparatus, rather simply alternates the illumination source to LED matrix [40]. In this study, it requires four images from partial coherent illumination patterns and provides promising non-interferometric performance. Due to illumination properties (partially coherent illumination), DPC approach offers twice better lateral resolution limit ($\frac{2\mathrm{NA}_{obj}}{\lambda}$), better optical sectioning, and speckle or diffraction-free imaging compare to coherent illumination-based QPI systems [17, 19]. This means that DPC-based approach incorporates two times better frequency information than that of coherent illumination-based QPI systems, which have could possibly influence the training of DNN in terms of computation performance and errors in loss functions. In addition, the first-order derivative response to phase in DPC based QPI system has less sensitivity to frequency noise compare to TIE approach [19, 21]. Therefore, additional noise reduction algorithm or post-process is unnecessary with DPC-based QPI system, which also allows simplifying the training method of DNNs. With tissue imaging capability and training as demonstrated in this study, relatively fast imaging speed of DPC-based QPI system provides the potential to perform on-site histopathology at the operation room where urgent golden standard results are required.

One of the challenges commonly facing for the DNN training/learning is data preparation. To

ULSAN NATIONAL INSTITUTE OF SCIENCE AND TECHNOLOGY

train the DNNs, great numbers of data is required to reduce the overfitting or bias problems [118]. Although data augmentation methods have been widely utilized showing stable training efficiencies, certain numbers of raw data are still required. Moreover, it is true that using larger number of raw data is much better than using larger number of artificially generated data from limited resources in terms of training/validation performance. However, it is very time-consuming, laborious, and complicated process to capture images over 100 for both before and after staining when different imaging modalities are utilized for each imaging sessions. One quick and simple way to overcome this problem is using already existing histology slide resources along with proposed approach in this study. Most of hospitals incorporates histopathology storages with enormous numbers of patient's stained histology slide. As following the proposed approach in this study, abundant resource of stained tissue slides could be utilized for data preparation with reduced data preparation time, complexity, and labors. In addition, more robust training networks could be expected along with data augmentation strategy.

One of the limitation that our approach incorporate is resolution reduction caused by use of NIR compare to use of visible light source. In addition, our NIR-based QPI is not aberration free system, which is susceptible to aberrations like all imaging systems. Resolution of the quantitative phase is sensitive to defocus of the image, where the field curvature blurs the image along the edges of the FoV. Fortunately, resolution reductions are overcome through our approach using SR-GAN as training framework of in-silico staining. This network model trains to generate stained tissue image by following the feature distributions of label images [111]. Thus, as shown in correlation coefficient in result, resolution of outcome has been enhanced following the resolution of the label image that captured by visible illumination source. Furthermore, aberrations can be computationally corrected by a deconvolution process while retrieving quantitative phase of object, from raw images captured by different source patterns. Without pre-calibration process, joint estimation of the sample complex-field and the spatially varying aberration recovers system pupil aberration, quantitative phase, and absorption of the specimen which influence to SNR and resolution [53].

4.2.8 Conclusion

To summarize, our proposed in-silico tissue staining method successfully demonstrate the transformation of stain-free quantitative phase image to colorful bright field H&E stained image. The use of NIR illumination for the QPI enables to capture light absorbing and scattering tissue, which shows minimal influence according to chromatic dyes. This approach offers the simple and fast training for virtual staining networks by acquiring both QPI and bright field label images after staining process. We believe that our proposed approach could also provide an innovative method for bypassing the cumbersome and costly conventional staining process in pathological diagnostic workflow.

ULSAN NATIONAL INSTITUTE OF SCIENCE AND TECHNOLOGY

4.3 Quantitative Screening of Cervical Cancers for Low-resource Settings: Pilot Study of Smartphone-based Endoscopic VIA using Machine Learning Technique

4.3.1 Introduction

According to the International Agency for Research on Cancer (IARC) and GLOBOCAN 2018, cervical cancer (CC) is the 4th most frequent cancer in women worldwide[119]. Approximately 90% of the global cervical cancer deaths in 2015 occurred in the low- and middle-income countries [120]. Although CC is regarded as highly preventable and curable cancer, CC is still one of the leading causes of mortality in low-resource settings and developing countries due to the lack of sustainable screening programs and limited infrastructures [121, 122]. CCs can be readily managed when it is found in the precancerous stages through routine screening method such as the cytology-based test. Most popular and affordable method for CC screening in low resource countries is to use visual inspection with acetic acid (VIA). Since VIA offers relatively simple, cost-effective visual feedback, it can even provide treatments on the same day of a screening visit [121-124]. In VIA, topical application of 4–5% acetic acid to the cervix transforms abnormal squamous epithelium to dense white color while normal epithelium presents light pink color. Despite its simplicity, VIA provides sufficient sensitivity and specificity to identify the cancerous lesion, hence, has been widely promoted and recommended as an alternative to the conventional cytology test (i.e. Pap smear) [121-125]. Nonetheless, visual inspection methods are found to be subjective, and the range of diagnostic performance varies widely, with significantly better results being obtained by physicians than by nurses [125]. Unfortunately, in many developing countries, trained physicians interpreting the VIA correctly may not be readily available [121, 123, 125].

Digital images of the cervix after application of acetic acid (D-VIA) or digital cervicography have been significantly important for improving quality control. It is a very efficient way of minimizing interpreters' subjectivity by capturing higher resolution images for post screening analysis [126-130]. Moreover, digital images can be transmitted or shared through internet with long-distance experts thus closing the gap in human resources [127]. Recent advances in smartphone technologies have opened new possibilities for cervical screening in low-resource settings, overcoming colposcopy's limitations such as the bulkiness, high-cost, electricity dependency and constant maintenance need [131-137]. The smartphone is highly integrated platform that includes various functionalities, easy accessibility, user-friendly interface, ubiquitous internet, and communication technologies [86]. Particularly, high-definition camera in a smartphone has made great impact on the practice of medicine by offering cost-effective, rapid, and non-invasive imaging capabilities [86, 138-141]. Smartphone-based cervical screening has been proven feasible and validated for quality assurance in low resource settings [131-137]. Smartphone-based D-VIA have been demonstrated for higher diagnostic accuracy and reduction

ULSAN NATIONAL INSTITUTE OF SCIENCE AND TECHNOLOGY

of the variability of detection rate. Although digital images are very effective in various ways [121], implementation of remote expert consultation is still challenging due to the lack of reliable broadband connections in remote areas [134]. On the other hand, automated interpretation of data and classification of cervical images for instant diagnostic conclusions will enable on-site treatments to be delivered without delays [142-146]. To date, various image processing and interpretation methods have been successfully applied to VIA using such features as aceto-whitening, blood vessel formation, and texture of the surface [143-145]. Prior works have shown that automated classification of VIA can perform as well as experts' qualitative assessment of colposcopic images [142, 146]. In addition, auxiliary processing methods such as elimination of speculum reflection (SR) and determination of region of interest (ROI) can further improve the overall performances of image processing outcomes [145]. Automated quantification of VIA based on modern image processing and machine learning techniques could be a very promising platform for cervical screening in low resource settings. However, the fully automated diagnostic performance using smartphone-based cervical images have not been introduced, despite a clear need and potential.

In this study, we demonstrate the new quantitative CC screening technique by implementing machine learning algorithm for smartphone based-endoscope VIA. Our method can provide digital images as well as automated diagnostic classification for comprehensive and intuitive feedback to a clinician. We have evaluated the diagnostic performance of the system through quantitative comparison to the gold standard of cytology and physicians' interpretation of the digital images. This approach would extend the cervical cancer screening to remote populations who do not have access to experienced colposcopists.

4.3.2 Smartphone-based endoscope system

We developed a miniaturized endoscope system by assembling the endoscopic probe and smartphone with customized ancillary components as reported previously [141]. The smartphone-based endoscope system and its components are illustrated in Figure 4. 19a. The system is composed of 3 major components. (1) Customized coupler for universal attachment of endoscopic probes and (2) smartphone case were generated from 3D printer (Stratasys, Objet260 Connex2). Magnification is achieved by (3) an optical adapter, which is placed between endoscopic probe and smartphone camera, as shown in Figure a1. Incorporating achromatic and aspherized achromatic lens having 40 mm, 14 mm focal lengths, (Figure 4. 19b) respectively, we obtained ~3x optical magnification. The image can be further magnified up to ~12x with smartphone's digital zoom feature. A portable light source (Medit, SPARK) was attached to the illumination port of an endoscopic probe. Images are acquired with the home-built android application that features control functions such as compensation of the rotated images caused by lens, camera controls including zoom, iso, white-balance, resolution size, and exposure adjustments,

and saving files.

Optical elements of the adapter significantly improved the cervix image captured with smartphone camera alone. Images of central part of USAF resolution target was captured with/without smartphone endoscope (Figure 4. 19c). The device was placed at 150 mm, 300 mm away from the target, where prior smartphone-based VIA [132-134, 137] and routine colposcopy [147] are conducted. For endoscope system, we placed the distal end of probe at 20 mm away from the target where whole ecto-cervix was well defined in the field-of-view. As shown in the Figure 1c, smartphone-based endoscopy achieved the best resolution from line-plot representing group 2, element 4 in resolution target.

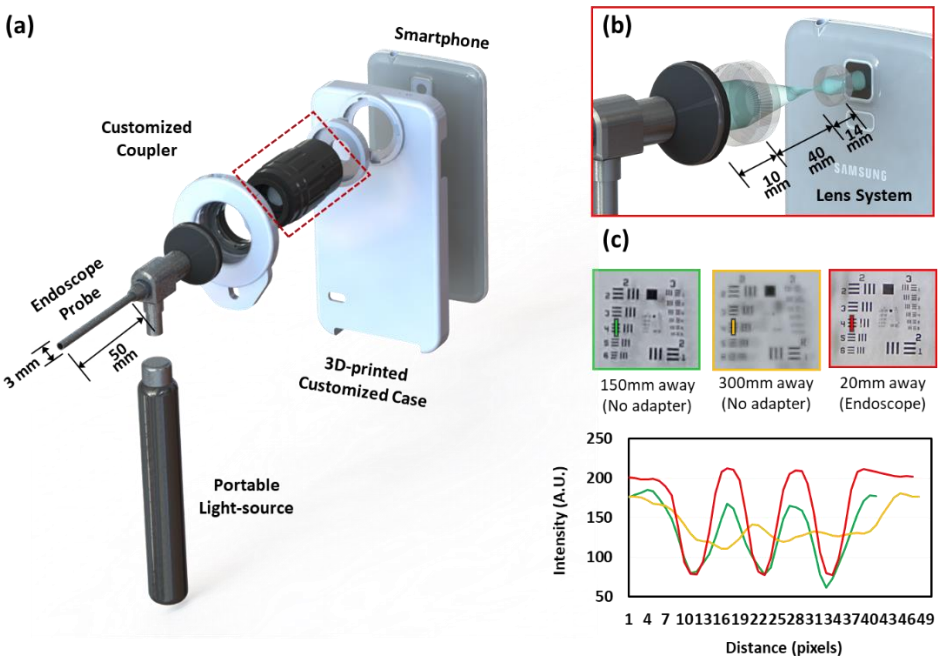

Figure 4. 19 Schematic of the system. (a) 3D modeling of the smartphone-based endoscope system. (b) Optics of the customized zoom lens. (c) Images of the resolution target taken by without any optics adapter and our system, respectively and group 2, element 4 from each image was described as line plot.

4.3.3 Image acquisition from clinic

In accordance with a protocol approved by the Ulsan University Hospital Institutional Review Board (IRB), we collected smartphone-based VIA images using endoscope in human subjects. In Ulsan University Hospital, VIA was routinely performed to visualize the margin before loop electrosurgical excision procedure (LEEP). Therefore, each imaging session was conducted prior to the LEEP at an operating room. A rigid endoscopic probe (Medstar, Otoscope, 0°, Ø4, and 50 mm length) was inserted inside a subject's vagina where speculum had already been placed. Since the endoscope is thin, smartphone-based endoscopic VIA imaging was performed in non-invasive and non-contact manner. All patients who underwent LEEP had already been found suspicious for having cervical intraepithelial neoplasia (CIN2+) through prior cytology-based test and colposcopy. Typical procedure in this study

ULSAN NATIONAL INSTITUTE OF SCIENCE AND TECHNOLOGY

took less than 5 minutes without causing undue burden on volunteers and delay of the treatment: first 1 minute was used for taking images before application of acetic acid, next 1-2 minute for applying of 3-5% of acetic acid, then another 1 minute for waiting, and last 1 minute for taking VIA images. Figure 2a-b shows the representative image of smartphone-based endoscopic VIA. For patients who underwent LEEP, 12 tissue sections were collected at each clock position from the excised ectocervix. For this study, physicians labeled the CIN grades in colors as shown in the center of Figure 4. 20c-e. Total 20 patients aged 20 or older participated in this study. Among them, 5 volunteers were normal (CIN1-), and 15 were confirmed abnormal (CIN1+) from gold standard cytology test. Normal cervix status of the 5 subjects were verified as such by cytology test and colposcopy, and therefore no LEEP was performed and no tissue was collected from them.

All the captured images including before and after application of the acetic acid were sent out to expert physicians for reviewing the smartphone-based endoscopic VIA. Total of four experts with professional experience ranging from 12 to 20 years participated while they were kept blind to the results of the machine learning and the cytology. Physicians' interpretation was based on only VIA features without any additional information given to them. During the image reviews, physicians labeled the directional information of tissue region that contained suspicious abnormal features (Figure 4. 20c-e). In this study, tissues including normal and CIN1 were considered to be normal and CIN2+ were considered to be abnormal because only CIN2+ requires treatment [142].

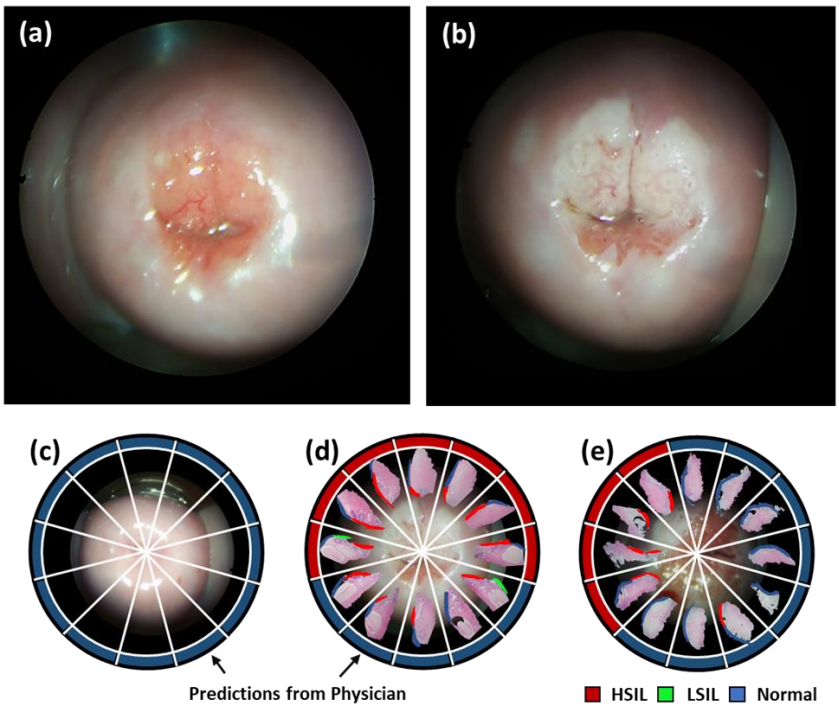

Figure 4. 20 Smartphone-based endoscopic cervicogram. (a) Cervicogram of before acetic acid application. (b) Cervicogram of after acetic acid application. (c) VIA- patient (d-e) VIA+ patients with predictions from best among four physicians. Prediction labeled the precancerous regions with colors at each clock position.

ULSAN NATIONAL INSTITUTE OF SCIENCE AND TECHNOLOGY

4.3.4 Pre-image processing

Images from smartphone-based endoscopic VIA contains unnecessary features such as vaginal walls, speculum, and specular reflections of light as commonly found in typical cervicograms [145, 146]. As these features may affect overall classification accuracy, we performed multi-step image processing to reduce their influence on data analysis (See Figure 4. 21a).

First, we determined and removed the specular reflections around the ecto-cervix area. Typical specular reflections appear white and saturated on the image. We primarily converted color space of the input image containing R, G, B to Hue, Saturation, Value (HSV). Saturation was used to identify the reflection with gradient computation in both x and y directions that quantitatively provide extent of directional gradient between adjacent pixels. Areas with specular reflection yield a dramatic change of intensity value from the neighboring pixels leading to abnormally high gradient magnitudes. Therefore, with proper threshold for gradients, area of specular reflections can be identified and then a binary mask can be applied to remove the reflections from the original image. In addition, removed pixels are then filled with colors by using the bicubic interpolation method. This method will minimally influence on the color distribution and provides numerical pixel information similar to that of adjacent pixels where high probability of similar color being expected.

Next, ROI was defined to segment the major cervix region. The major cervix region in images of both before and after application of acetic acid contains high red-channel values. For ROI detection, red-channel image was transferred to grayscale and separated into multilevel binary images. In here, 8-

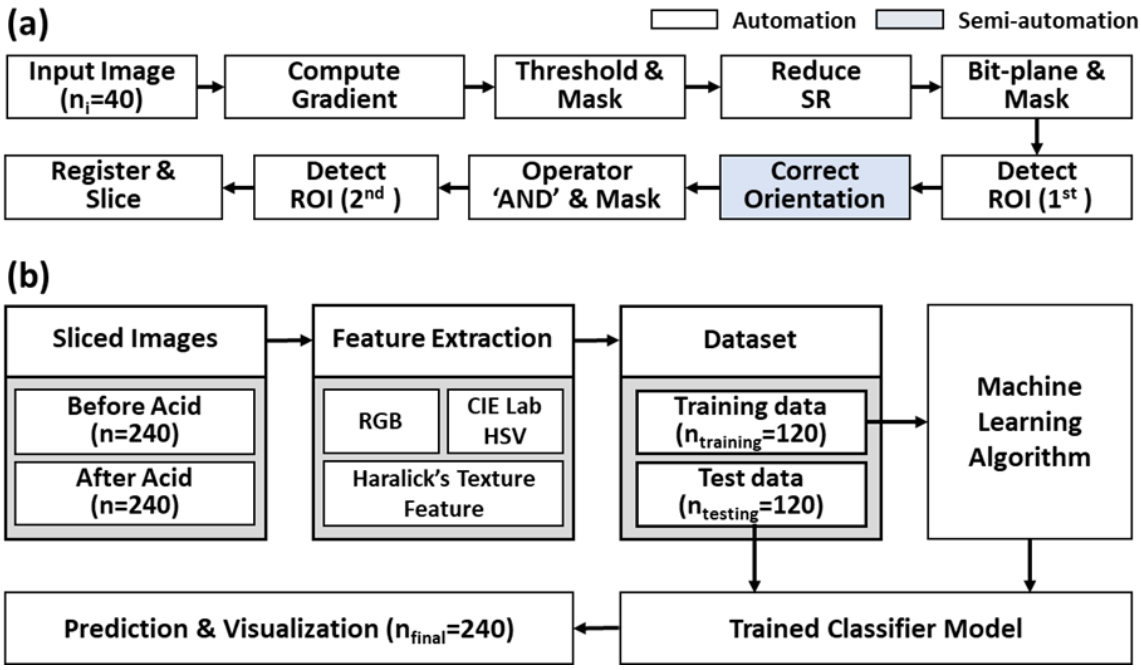

Figure 4. 21 Block diagram of image processing and classification. (a) Pre-image processing method, (b) Feature analysis and classification.

ULSAN NATIONAL INSTITUTE OF SCIENCE AND TECHNOLOGY

bit grayscale of red channel image was sliced into 8 planes ranging from the least significant bit 0 to the most significant bit 7. Most of 7th and 8th bit-planes present the major ecto-cervix regions, and hence we used these features to generate the mask for ROI segmentation. Due to the slight differences of cervix images between pre- and post-acetic acid application, we performed 'AND' operator to segment the overlapping regions.

Prior to VIA features extraction and classification, image pairs for pre- and post- acetic acid application had to be properly registered. As shown in Figure 4. 22, we manually provided three points as fiducials on each image to locate center of cervix (red dot), and both end of the cervical OS (2 black dots). Utilizing the center point, we correctly registered the center of cervix for every image pairs. In addition, we drew a line penetrating the other two points and found the angle of the line from each image. We made this line to be horizontal by rotating images with respect to the given central point. Moreover, we cropped the images into 12 pieces as sectioned in histology. In this image processing methods, we used total 20 image pairs acquired from volunteers as initial input (n_i=40) and obtained 240 pieces of images that have directional information for both before (n_{cb}=240) and after (n_{ca}=240) acetic acid application. All detailed procedures with representative images for each step could be found in Figure 4. 22.

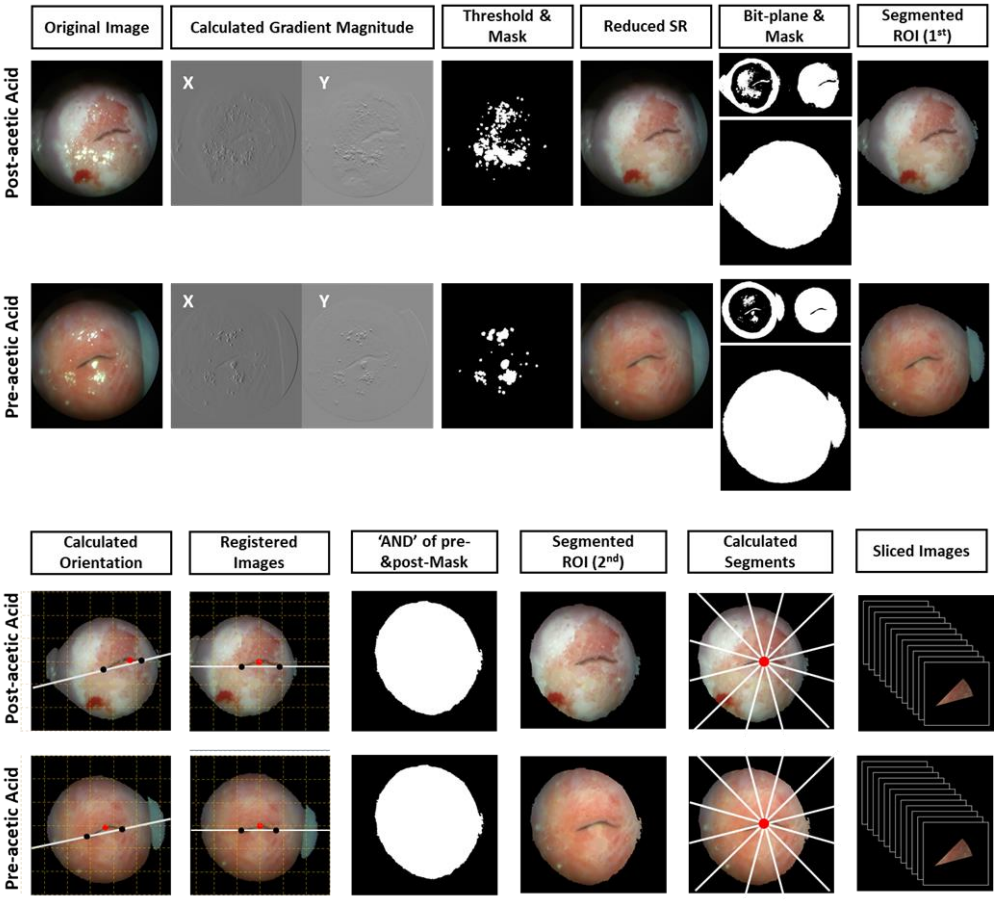

Figure 4. 22 Image pre-processing procedures with representative images.

ULSAN NATIONAL INSTITUTE OF SCIENCE AND TECHNOLOGY

4.3.5 Feature analysis and selection

After pre-processing of images, VIA features were analyzed to identify the images containing the suspicious lesions. To extract the abnormal features, we inspected RGB color intensity, values in extended color space, and Haralick's texture features [67]. Application of the acetic acid on squamous epithelial areas coagulates the cellular protein and dehydrates the cytoplasm. Images of VIA- cervix, hence, generally showed the light pink or very thin white appearances due to reflection of light from the underlying stroma. On the other hand, VIA+ tissues which is rich in cellular proteins were presented with thick white features blocking the colors of the stroma. Due to this reason, VIA+ incorporates larger thick-white areas in images which would exhibit more green and blue intensities in color space [142, 148]. Herein, we computed the green-to-red and blue-to-red intensity ratio and found the separation between histogram distributions of pre- and post-acetic acid application images. This approach would properly quantify changes in green and blue intensities independent of device variation and level of illumination. The differences of histogram distribution of average(D_{ave}), green-to-red ($D_{G/R}$),blue-to-red ($D_{B/R}$), and average histogram difference of green-to-red and blue-to-red (D_{ave}) can then be defined as:

$$D_{G/R} = I(mode)_{\frac{G}{R}Post} - I(mode)_{\frac{G}{R}Pre}$$

$$D_{B/R} = I(mode)_{\frac{B}{R}Post} - I(mode)_{\frac{B}{R}Pre}$$

$$D_{ave} = \frac{D_{G/R} + D_{B/R}}{2}$$

where I(mode) is intensity level or index at mode in histogram. Standard deviations (SD) of green and blue channels are another important extracted feature. Aceto-white features with higher green and blue channel intensities also exhibited higher standard deviations. It means more green and blue intensities are widely distributed in the histogram. In addition, different color space was utilized to find the features of VIA. CIE*Lab color space was computed to achieve perceptual uniform colors space which is useful to quantitatively distinguish colors of image. The great advantage of CIE*Lab is that it is independent of device and illumination [142]. In this study, major color included on cervix was defined calculating the average of a* channels from each post-acetic application. Due to abnormal vascular formation such as mosaicism and punctation, visualization of uneven surface of the ecto-cervix was another contrasting feature. Computation of Haralick's texture feature using gray-level co-occurrence matrix (GLCM) may quantify the spatial variation of gray intensity values related to the texture of an image. GLCM measures the probability distributions of different combinations of pixel values. Utilizing the GLCM, several

ULSAN NATIONAL INSTITUTE OF SCIENCE AND TECHNOLOGY

statistical information such as contrast, correlation, energy, and homogeneity can be derived quantitatively to exhibit the texture of image [149, 150]. Here, the GLCM was calculated in four different angles (0°, 45°, 90°, 135°) with inter pixel distance of 5 for difference of S channel (HSV color space) from pre- to post-acetic acid images. Different angles would measure the features of interest in every direction. Therefore, all four GLCMs were summed before texture calculation. In this study, we specifically utilized the correlation statistics which provides the extent of correlation between a pixel to its neighbor pixel over the whole image [114]. The correlation statistics exhibited a significant difference on the VIA+/- images, yet other texture statistics had shown very small difference down to third and fourth decimal points. Therefore, five VIA features were analyzed and selected as potentially useful for diagnostic classification: (1) Average difference of green/blue-to-red histogram index, (2) SD of green channel and (3) SD of blue channel from post-acetic acid images, (4) average value of a* channel , and (5) correlation values of Haralick's texture features from S channel information.

4.3.6 Classification training and validation

Using selected features of VIA as predictors, we interpreted the tissue abnormality of a localized region for the classification. Machine learning techniques are widely used and successfully supervised for VIA classification [141, 142, 145, 146]. In this work, we examined and selected an appropriate classifier by analyzing three different classifying methods. We designed K-nearest neighbor (KNN) with 5 neighbors based on Euclidian distance, supportive vector machine (SVM) with 4th degree of polynomial kernel function (cost=3, gamma=2.2), and decision tree (DT) with limit of maximum 10 nodes based on Gini's diversity split criterion. These parameters or known as hyperparameters in each classifying method were optimized through grid-search technique. All predictors were standardized using their corresponding weighted means and weighted standard deviations [146].

For data separation, we randomized the order of the images and used half (ntraining=120) for training classifiers. Other half of data, an untrained image set (ntesting=120), was used for testing set after the optimization of classification models. While in training, classifiers are validated using k-fold cross validation (k=10) with histopathology labels as the ground truth to avoid overfitting problem. In this method, data is evenly divided into k subsamples. Other k-1 subsamples are then used as training dataset and then held-out or excluded subsample are used for validation. Algorithm were repeated k times with each of subsamples being utilized only once as the validating data and performance accuracy were calculated by averaging the results from each k-folds. Receiver operating characteristic (ROC) curves with area under the curve (AUC), accuracy, sensitivity, and specificity of each trained classifier were computed and compared for selecting the best classifiers. Throughout the classifiers, each image was interpreted to either VIA+ or VIA-. Classification process is illustrated in Figure 4. 21b.

ULSAN NATIONAL INSTITUTE OF SCIENCE AND TECHNOLOGY

4.3.7 Result & Discussion

Direct evaluation of Smartphone-based endoscopic VIA

To determine the feasibility of the smartphone-based endoscope system for VIA application, four physicians participated and reviewed the image sets (n=20). On these 20 cases, both clinically normal and LSIL were designated as 'normal' and HSIL was designated as 'abnormal', resulting 8 normal and 12 abnormal for this study. The diagnostic performance assessed by pathologists is summarized in Table 4. 4. Sensitivity ranged from 33.3% to 83.3% and specificity was 100% for four physicians. Accuracy of the assessment ranged from 60.0% with kappa 0.286 (p=0.068) to 90.0% with kappa 0.800 (p=0.00023). Overall, average accuracy of 77.5% with kappa 0.571 (p<0.0001) was observed for the evaluation of the system.

Table 4. 4 Sensitivity, specificity, and cohen's kappa value, P-value for smartphone-based endoscopic VIA among all observers (n=20)

	Sensitivity (%)	Specificity (%)	Accuracy (%)	Kappa (κ)	*P*-value
Physician 1	0.75	100.0	85.0	0.706	0.001
Physician 2	33.3	100.0	60.0	0.286	0.068
Physician 3	83.3	100.0	90.0	0.800	0.000239
Physician 4	58.3	100.0	75.0	0.528	0.007
Average	62.5	100.0	77.5	0.571	< 0.0001

Result of image processing

Figure 4 shows the representative images from each image processing step. Specular reflections on the surface of the cervix are removed while preserving visually natural or smooth features. All areas of specular reflection with saturated intensity are correctly localized for all 20 image pairs including both pre- and post-acetic acid application images. Intensity threshold of 60% for specular reflection removal was most effective as the reflections on the ecto-cervix regions were identified clearly while minimally affecting general backgrounds. This was feasible because more reflection intensity was obtained in the focal plane compared to that of the unfocused regions. Next, major cervical region was selected as the ROI and was segmented by applying 7th and 8th bit-plane of the red channel image as primary mask. Although most of the artifacts such as unfocused background and speculum were successfully eliminated, some image still contained portions of vaginal wall. These results are likely found when cervix and virginal wall adjoined each other, or strong intensities were appeared on the virginal area by reflections. Through semi-automated registration algorithm, images were centered, aligned and rotated as shown in the fourth column of Figure 4. 23. Additional segmentation was conducted using overlapped

ULSAN NATIONAL INSTITUTE OF SCIENCE AND TECHNOLOGY

regions of pre- and post-acetic acid application images as secondary ROI mask. Furthermore, ROI images were sliced based on clock positions as they were collected for the histopathology. Each slice was then used to calculate color distribution histogram, CIELab, and HSV-based Haralick's texture features for VIA.

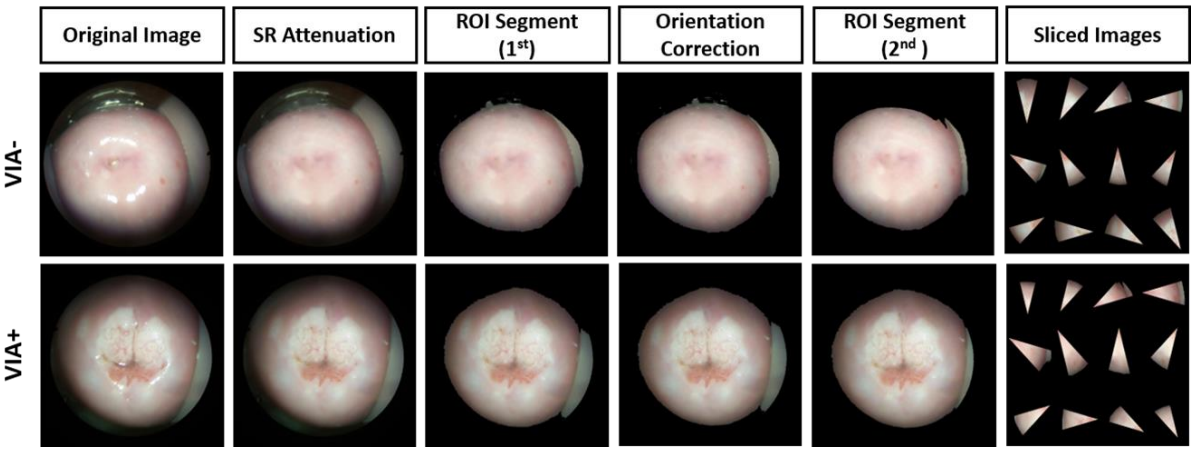

Figure 4. 23 Result of image processing result.

Feature extraction

In Figure 4. 24(a1, a5), representative images of sliced image are shown for VIA- and VIA+, respectively. Figure 4. 24(a2, a6) represents a* channel image using post-acetic acid images. Due to aceto-whitening areas, VIA+ showed significantly lower average values in a* channel from CIE*Lab color space, which represents lower for green and higher for magenta colors. Especially, lower values are localized on the area where aceto-white exist. In Figure 5(a3, a7), the images of difference of saturation channel from pre- to post-acetic acid application are shown. Higher values of saturation were obtained in aceto-whitening regions with VIA+ relative to those with VIA- where no aceto-whitening regions exist. Using images in in Figure 4. 24(a3, a7), correlation values were computed from Haralick's texture feature and visualized in Figure 4. 24(b3,a6). Contrary to expectation, higher correlation was found in VIA+ compare to that of VIA- (0-1, usually 1 for higher correlation); however, significant difference was observed with good trend for distinguishing the feature.

Among the 5 different features, representative data for green-to-red ratio was illustrated in Figure 4. 24b-c. There was relatively small effect of acetic acid application observed in green-to-red ratio in the VIA- images. The histogram of the green-to-red ratio in VIA- shows little changes between pre- and post-acetic acid application in terms of distribution and mode. However, the green-to-red ratio increased for VIA+ following application of acetic acid, as shown in the histogram in Figure 4c. Following application of acetic acid, distribution of green intensity histogram broadened along with increased intensity. Collecting all the statistical data, we derived the average difference of intensity level

ULSAN NATIONAL INSTITUTE OF SCIENCE AND TECHNOLOGY

in green/blue-to-red ratio, values of a* channels following application of acetic acid. In addition, standard deviation of green and blue intensity and correlation of Haralick's texture feature were calculated from the images after application of acetic acid. Figure 4. 24d summarizes these features with all predictors in abnormal tissues having greater values than those from normal tissues except a* values.

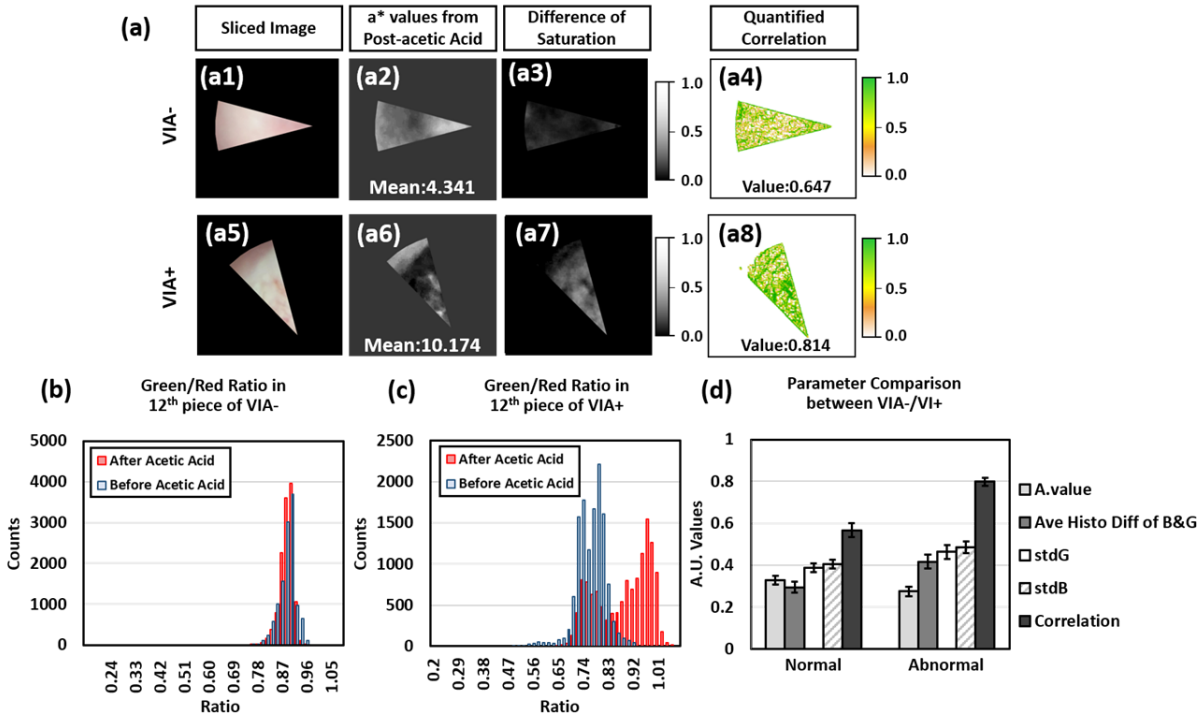

Figure 4. 24 Result of feature extraction. (a) Extracted VIA features from sliced VIA-/VIA+ images, showing graphical information in different color spaces. In addition, correlation map was calculated form Haralick's texture feature. (b,c) Representative histogram of green-to-red ratio in VIA-/VIA+. (d) Summarization of selected features as predictors for classifying model.

Classification comparison

Using all the extracted values from 120 sliced image sets, three different types of machine learning classifiers were trained and analyzed. As shown in Figure 4. 25a, KNN yielded the best performance in accuracy of 80.0% with sensitivity of 71.88%, specificity of 82.95%, and kappa of 0.517. The second most accurate classifier was SVM with accuracy of 78.33%, sensitivity of 62.50%, specificity of 84.09%, and kappa of 0.457. DT had the least accuracy for smartphone-based endoscopic VIA with accuracy of 73.33%, sensitivity of 65.63%, specificity of 76.14%, and kappa of 0.380. In the ROC curve shown in the Figure 4. 25b, KNN, SVM, and DT showed AUC of 0.852, 0.770, and 0.746, respectively. Figure 4. 25c illustrates the result of prediction scores from each classification on k-fold validation, indicating the probability of an image belonging to either the negative or positive class. From the box plot, separations of scores of abnormal and normal data were clearly distinguishable in KNN model

ULSAN NATIONAL INSTITUTE OF SCIENCE AND TECHNOLOGY

compared to that of DT and SVM. Most of abnormal data were distributed over 0.5 but those of normal data were shown under 0.5 in KNN and DT model. In SVM model, normal and abnormal data were separated positive and negative, respectively. As the best performing classifier in our study, KNN model was selected for evaluating the diagnostic accuracy of VIA. Confusion matrix of KNN in test set is illustrated in Figure 4. 25d.

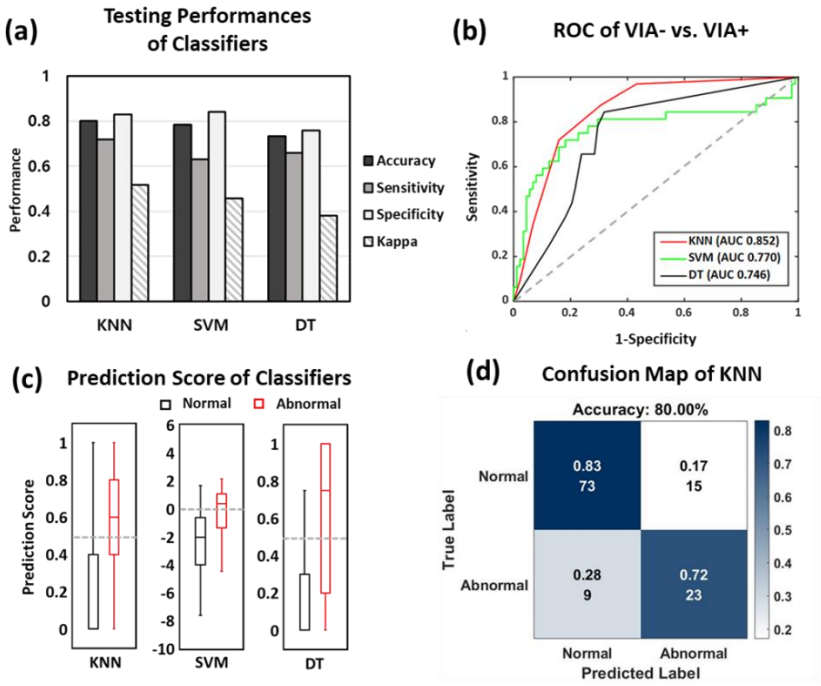

Figure 4. 25 Comparison & selection of classification model. (a) Graph of training performance comparing the VIA results from each classifier. (b) ROC curves comparing the VIA+ performances. (c) Box plots of prediction scores for each classifying method. (d) Confusion map of testing for KNN model.

Analysis of the KNN classification for Smartphone-based endoscopic VIA

Figure 4. 26 illustrates result of the classification with smartphone-based endoscopic VIA images for 10 patients that was used for testing set. Using all prediction results from testing data, locations of abnormal tissue were visualized as segmented annulus outside of each endoscopic image. Red and blue segment of annulus indicate VIA+ and VIA- at each clock position, respectively. Out of 120 slice images, 32 were determined positive, 88 negative according to the histopathology. As shown in Figure 4. 26a, all results of the gold standard for each patient are denoted as color lines inside the annulus and are aligned along each clock position as a line. Red, green, and blue lines denote abnormal tissues with HSIL (CIN2+), LSIL (CIN1), and normal, respectively. When KNN result is confirmed correctly as VIA+ by the golden standard, segments were labeled yellow on the perimeter of the annulus for each patient. Total 23 sliced regions were matched correctly for VIA+. Moreover, patient was estimated to have HSIL lesion if there is at least one VIA+ segment included among 12 locations. Out of total 10

ULSAN NATIONAL INSTITUTE OF SCIENCE AND TECHNOLOGY

patients, 7 patients were predicted to have HSIL through KNN prediction. Among the them, 6 patients were correctly estimated as VIA+ (true positive, TP). Among the 4 patients confirmed as VIA-, KNN identified 3 patients correctly (true negative, TN). However, there was no false negative predicted from KNN for 10 patients. Figure 4. 26b shows agreement between classification algorithm and individual physician's interpretation for each clock position. Classification algorithm shows moderate overall agreement ranging from 70.83% to 75.0%. For binary classification of patients, algorithm provides more accurate interpretations as shown in Figure 4. 26c. Algorithm yielded accuracy of 90.0% and average accuracy of physician achieved accuracy of 68.0% for 10 patients.

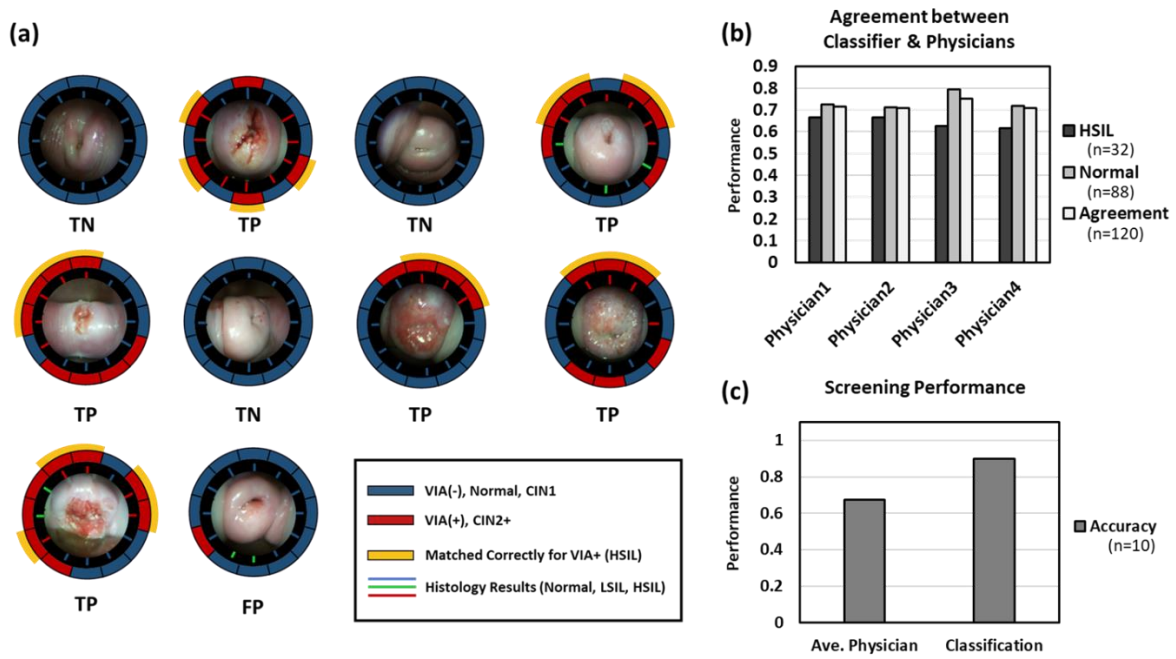

Figure 4. 26 Analysis of KNN for smartphone-based endoscopic VIA. (a) Visualization of KNN classifying result for 10 patients with VIA+/VIA-. Lines inside of annulus ring indicates the results of golden standard for each clock position. Annulus ring presents the result of KNN classification according to each clock position. Outer yellow mark represents the position where both golden standard and prediction results are matched. (b) Graph presenting the agreement of KNN to each physician. (c) Graph comparing the screening performance for 10 patients interpreted by KNN and physicians.

Discussion

The findings of this study suggested that the novel smartphone-based approach for VIA with endoscopy and machine learning technique could potentially be a useful tool for screening cervical cancer in the low-and-middle income countries. Smartphone-based endoscope system is simple and robust that screening could be performed outside of the office without cost, mobility, and electricity limitations. Here, moderate overall agreement (kappa 0.571) was achieved between interpretation of smartphone-based endoscopic cervicogram by physicians and histopathologic result. With support of machine learning and image processing technique, diagnostic performance was elevated for classifying

ULSAN NATIONAL INSTITUTE OF SCIENCE AND TECHNOLOGY

the VIA- or VIA+ patient. We had explored three different types of classifiers and selected KNN algorithm for this study due to its best performance of showing AUC of 0.8516 in classification among them. Both hardware and machine learned algorithm based on golden standard, over performed the conventional VIA. This was possible because our approach increased the sampling numbers of prediction for each patients as what was conventionally done in golden standard. In clinical point of view, finding abnormality out of normal tissue is critical, especially in low-resource settings. In addition, locations of abnormal tissue were identified and visualized at each clock position for each patient. With intuitive, perceptual color labels, VIA providers may easily understand where aceto-whitening has appeared and its degree of the abnormality. Had our algorithm been used to determine treatment pathway, the data would effectively assist the VIA providers with correct decision making.

To the best of our knowledge, this is the first smartphone-based endoscopic VIA work. Smartphone-based endoscopic approach provides some advantages over other smartphone-based VIA studies [131-137, 151, 152]. Many studies on diagnostic performances of smartphone VIA and have shown promising results with sufficient accuracies [131-137]. These methods mostly utilized the tripod or other hardware supports to obtain pictures, which poses challenges of limited space for maneuvering during the procedure. Recently, portable colposcope device with unique tampon form factor called pocket colposcope have been introduced with high concordance to clinical colposcope. Similar to our approach, pocket colposcope enables to capture images inside of the vagina. However, pocket colposcope requires wire-connection to smartphone as an accessory form with limited hardware variation availability [151, 152]. Here, using endoscopic probes within a speculum offers non-contact, non-invasive imaging capability, minimizing the cross-contamination risk between patients. Our endoscopic probe enhances resolution of the images and can achieve more details of mosaicism, punctation, and aceto-white regions. This could substantially improve the diagnostic accuracy as well as quality control of VIA. Moreover, various type of endoscopic probes brings flexibility to the system. Furthermore, smartphone-based endoscope is based on off-the-shelf optics to magnify the images while reducing the SNR by avoiding high digital zoom. Simple modification of optical components can enable additional functional imaging such as fluorescence, polarization, and multi-spectral imaging, and thus can further improve the visualization of the abnormal tissue [140, 153, 154]. Furthermore, manipulation of the endoscopic device inside of the vagina is very intuitive and easy compared to that of conventional approaches manipulating outside of the vagina. Hence, neither tripods nor stands are required for acquiring stable images, which in turn enhances the speed of imaging session.

Image processing algorithms have been developed to minimize external source of errors such as deviations of illumination power, imaging position, variations of device, specular reflections, and ROI of cervix. Especially method of ROI segmentation is unique as it uses bit-plane separation and finding overlapped regions to eliminate the insufficient information in smartphone-based endoscopic cervicograms. In addition, VIA features were mostly extracted based on statistical calculation of

ULSAN NATIONAL INSTITUTE OF SCIENCE AND TECHNOLOGY

histograms rather than just acquiring the quantitative pixel information from the raw images. This may minimize the dependencies on imaging environment and make image calculation confined to each image but still afford similar values of computation result when finding features. Extending the RGB images to other color space also provides benefits for calculation. Saturation value from HSV color space affords extent of purity of the hue data which results in more intuitive perceptual values between pre- and post-acetic acid application. Moreover, saturation value is separated from brightness (value), hence, it is illumination invariant. Empirically, using image of difference of pre- and post-acetic acid images in saturation channel for GLCM showed higher significant difference in correlation values between VIA- and VIA+. CIE*Lab color space is also very useful for finding device or illumination-independent quantitative color measurements. CIE*Lab also separates the luminance component (L*) from the color which makes color information less sensitive to illumination [146].

Even though our novel CC screening technique using smartphone based-endoscope VIA and machine learning demonstrated a positive outcome as pilot study, much improvement is needed before it can reach its practical potential. First, accuracy of our algorithm classifying the patients was calculated using small number of samples. No false negative data was predicted within small number of samples. We believe increasing sampling size could additively provide more number of sliced data for training and testing classifiers which possibly learn more of new cases that eventually leads to much reliable classification results. Therefore, overall estimation could be different with larger data set, however, it will still provide better performance compare to subjective estimation from physicians. Second, our approach for ROI segmentation aimed to precisely distinguish the ectocervix area from the images; however, there are still some portion of vaginal walls left that led to miss-classification. Moreover, location and area of cervix are substantially different in each image. For this reason, image processing algorithm for registering images of pre- and post-acetic acid application was done with manually providing positions of center and each distal end of cervical OS. Through image standardization by providing the visual guides in software, deviation of positioning and working distance can be minimized and further improve the ROI segmentation performance in an automated processing algorithm. Lastly, our image processing-based classification algorithm still was performed on a computer, limiting practical uses in developing countries in its current form. Due to the computational intensity, the current algorithm cannot be operated as a standalone in a smartphone. Recently, android based machine learning as well as image processing techniques have been introduced in various fields, using SVM, KNN, DT, and Deep Convolutional Neural Networks (CNN). As these functions are now available on mobile phones [155-158], we will embed the android based machine learning techniques to implement our algorithm on a smartphone alone.

ULSAN NATIONAL INSTITUTE OF SCIENCE AND TECHNOLOGY

4.3.8 Conclusion

In conclusion, we explored the smartphone-based endoscopic VIA and predicted the cervicogram as normal/abnormal using machine learning technique. Herein, histopathology results, acquired at each clock position on the excised cervical tissue, were provided as ground truth for classifications. VIA features were then extracted after image processing and utilized for training the classifiers. 120 sliced images obtained from cervicogram at each clock position were utilized and three classifiers such as KNN, DT, SVM were compared. Approach using KNN showed the best performance with accuracy of 80.0%, AUC of 0.852, specificity of 82.95%, and sensitivity of 71.88%, respectively. Prediction values were visualized with intuitive color labels, indicating the normal/abnormal tissue, at each clock position for each patient. Calculating the overlapped abnormal tissues between golden standard and predicted value, our KNN model for classifying the VIA-/VIA+ patients overperformed the interpretation results by physicians. Taken together, these results suggest that the smartphone-based endoscopic VIA and analysis based on the machine learning techniques would be a valuable tool for screening VIA in low-resource settings. Moreover, this approach can potentially minimize human subjectivity and be particularly useful in areas where experts or tele-consultations are unavailable.

ULSAN NATIONAL INSTITUTE OF SCIENCE AND TECHNOLOGY

Chapter 5. General conclusion and future perspectives

5.1 General conclusion of thesis

In conclusion, throughout this thesis, two major approaches have been introduced to overcome the limitations that was found in fields related to digital medicines, particularly in digital histopathology, and point-of-care diagnostics. Developments of quantitative differential phase contrast imaging using partially coherent illumination based computational microscope and smartphone-based endoscope system allows to label-free imaging as well as POC real-time medical imaging diagnosis, respectively. Furthermore, application of artificial intelligence technologies for phase microscope as well as POC device supports the proposed devices in data generation and analysis, which potentially alternate the diagnostic work flows as cost-effective and short, and experts were minimally required.

In chapter 2, utilization of our simple NIR illumination device successfully retrieved phases from thick and highly absorbing materials without any manipulations in QPI algorithm. Great advantage of using this method was maintaining the weak object transfer function for simplifying the complex field of object in optical system. In addition, using single LED source was another feature what makes our system fascinating. Although LED itself provides partial coherent illumination, single illumination would be considered as coherent illumination in spatial domain. Increasing only beam size would not provide solution for this situation. Spatially incoherent coherence condition is the main idea to make phase stable. With multiple diffuser implementation, randomly scattering on the surface of diffuser creates phase variations, that leads to incoherent conditions. As light passes the physical mask, phase gradient was generated and use of single LED with this configuration could provide DPC images. Since multiple LEDs are not required anymore, not only NIR wavelength but also various illumination spectrum could be applied. This could also offer advantages cost issue, provides possibility to develop QPI system in compact platform. We believe that, to the best of our knowledge, this work was the first method for not only imaging the tissue but also using only single point source illumination in DPC-based QPI system. Moreover, utilizing our approach would deliver label-free tissue imaging which could skip the staining process in digital pathology workflow.

Recent advances in technology such as 3D printing, smartphone, IOT have enabled the realization of cost-effective, portable point-of-care medical imaging devices. In this chapter 3, smartphone-based endoscope system demonstrated the feasibility as a stand-alone endoscope through clinical application. The unique advantages such as mobility and flexibility made system suitable for the point-of-care diagnostics. Throughout experiment, our device had shown sufficient imaging performance as a diagnostic tool. We believe this device could be applied in a wide range of nonclinical settings and ultimately, in some clinical settings. In particular, our device would be a very useful tool for health providers in low-resource settings and at remote locations with limited health care service.

In first part of chapter 4, proposed in-silico tissue staining method successfully transforms the

ULSAN NATIONAL INSTITUTE OF SCIENCE AND TECHNOLOGY

stain-free quantitative phase image to bright field H&E stained image. The use of NIR illumination for the QPI enables to capture light absorbing and scattering tissue. This approach offers the simple and fast training for virtual staining networks by acquiring both QPI and bright field label images after staining process. In addition, our QPI system outperforms other phase imaging contrasts in terms of in-silico GAN framework performance as well as simplicity. We believe that our proposed approach could also provide an innovative method for bypassing the cumbersome and costly conventional staining process in pathological diagnostic workflow.

In second part of chapter 4, we explored the smartphone-based endoscopic VIA and discriminated the cervicogram as normal/abnormal using machine learning technique. Herein, histopathology results, acquired at each clock position on the excised cervical tissue, were provided as ground truth for classifications. VIA features were then extracted after image processing and utilized for training the classifiers. 120 sliced images obtained from cervicogram at each clock position were utilized and three classifiers such as KNN, DT, SVM were compared. Approach using KNN showed the best training performance with accuracy. To validate the trained model, we used the other 120 sliced images and achieved accuracy 80%. Prediction values were visualized with intuitive color labels, indicating the normal/abnormal tissue, at each clock position of lesions. The overall accuracy of KNN model for classifying the VIA-/VIA+ patients was 90%, which was better than average image interpretation by physicians. Taken together, these results suggest that the smartphone-based endoscopic VIA and analysis based on the machine learning techniques would be a valuable tool for screening VIA in low-resource settings. Fully automated algorithm can potentially minimize human subjectivity and be particularly useful in areas where experts or tele-consultations are unavailable.

5.2 Future perspectives

In this section, we demonstrated QPI system and portable POC devices from the perspectives of improvement in healthcare to provide advanced medical services to patients. We believe there are possibilities improving the proposed devices in portability, cost issue, and expansion of functions. Moreover, the result from this device have shown great potentials to implements to other devices in the various application fields. Particularly, there are many promising imaging modalities introduced in biomedical fields which could be a potential candidates for integration.

Smartphone-based QPI system for POC diagnosis

From this thesis, we have developed label-free quantitative phase microscopy for tissue imaging. The principle behind this device was started from generating the differential phase contrast image by implementing patterned illumination sources in a simple bright field microscope setup [39, 40]. This means that differential phase contrast imaging could be realized in any type and size of digital bright field microscope configuration which compose of objective, tube lens, can camera. Recently, many

ULSAN NATIONAL INSTITUTE OF SCIENCE AND TECHNOLOGY

portable brightfield microscope system have been introduced for POC [7]. Most of them implemented on the smartphone, taking advantages of high-resolution imaging capabilities, portability, user friendly interface, easy accessibility, and internet infrastructures. In addition, using reversed smartphone camera module as objective in smartphone-based microscope system even make the system simpler and results in an aberration free system as well [159]. Applying all of these technologies, we believe the proposed QPI system, especially RGB patterned one, could be applied and single-shot portable QPI system could be realized for POC diagnosis. In fact, there are two mobile-based QPI systems were introduced using RGB LEDs and customized dome shape LEDs, respectively [43, 160]. However, quantitative phase contrast images were not provided in these existing methods.

Figure 5.1 illustrates the concept of smartphone-based QPI system for POC diagnostics and multi-contrast images that was captured from real smartphone-based QPI system. This smartphone utilizes reversed smartphone lens to implement the microscope system, offering optical magnification ~5X. Moreover, RGB pattern shown in Chapter 2.1was applied to provide a multi-contrast images from smartphone. DPC image was successfully realized which leads to QPI as shown in Figure 5.1c. This system was developed in android platform and homebuilt software that enables to control the imaging session as well as offers real-time DPC imaging capabilities as shown in Figure 5.2b. From this simple implementation and experiments, we have found the possibilities as well as its stability of smartphone-based QPI system as POC diagnosis device.

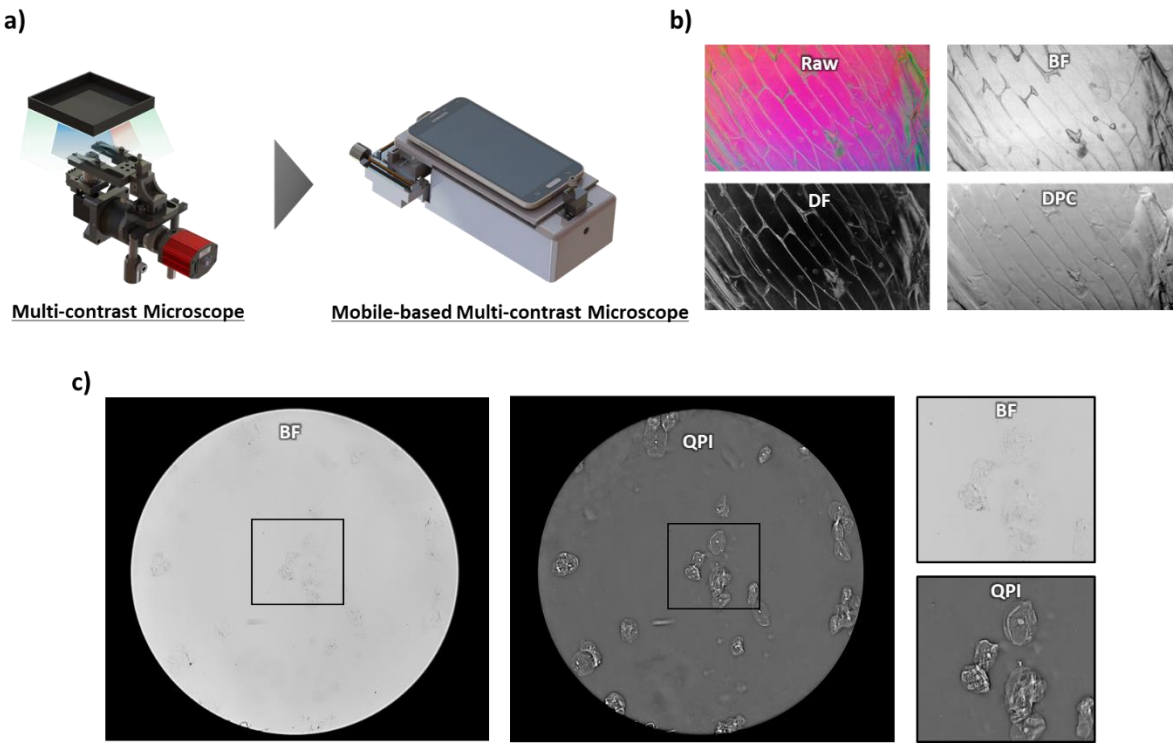

Figure 5.1 Smartphone-based QPI system for POC diagnostics

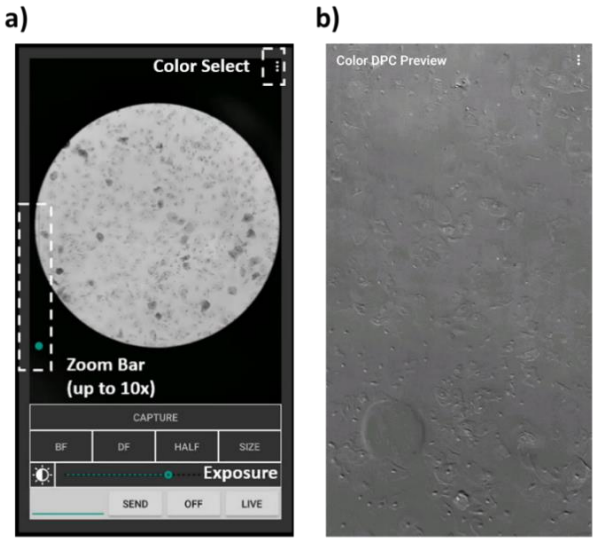

Figure 5.2 Development of QPI software in Android platform. a) Image capture screen. b) Real-time DPC computation screen imaging cells.

Utilizing portable QPI system, there are many possible applications in biomedical fields. Taking advantage of portability, we believe this system could be applied to cell imaging in low-resource settings. Particularly, visualizing the morphological information of cellular constituents could be useful for imaging disease cells that has difference between normal and abnormal. One of the candidate that we think about is cervical cancer cells. Nucleus to cytoplasm ratio mostly changes in cervical cell when there are abnormalities related to cancer [161]. Therefore, with image processing and machine learning technique, cervical cancer cells could be classified from smartphone-based QPI at the on-site (Figure 5.3a). If this method is performed before colposcope procedure as we proposed in Chapter 4.3, we believe that diagnosis accuracy could be improved significantly in POC cervical cancer screening.

Recently, deep learning methods have been implemented on smartphone and showed many possible applications in fields of biomedical [9]. As smartphone-based QPI system allows to capture transparent cells, label-free quantitative phase contrast tissue imaging would be possible as well. With

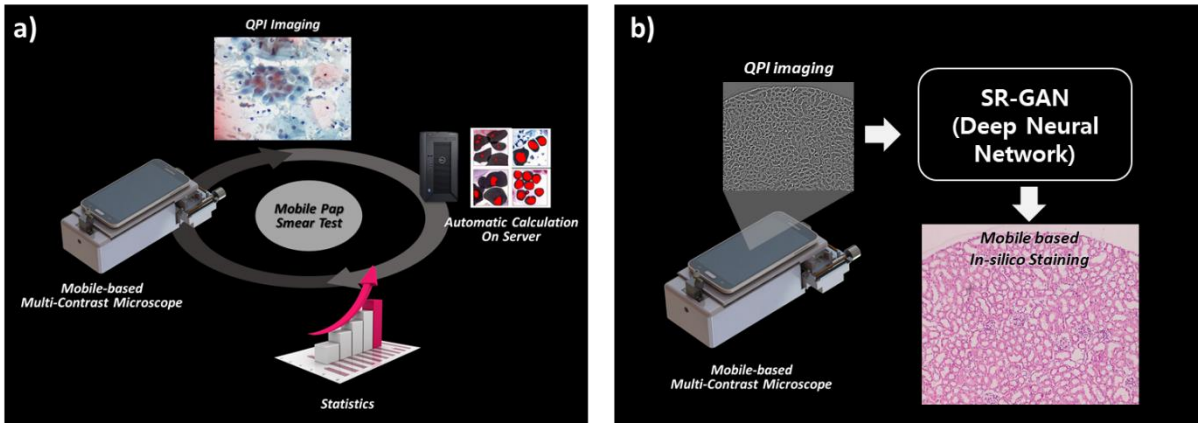

Figure 5. 3 Future perspective of POC-QPI system implemented on smartphone. a) automated cervical cancer cell screening. b) In-silico tissue staining from label free smartphone-QPI.

ULSAN NATIONAL INSTITUTE OF SCIENCE AND TECHNOLOGY

possibilities of deep learning in smartphone, already trained GAN models could be executable in smartphone, possibly realizing the in-silico tissue staining method as introduced in Chapter 4.2 as shown in Figure 5.3b.

Development of label-free whole slide scanner for digital histopathology

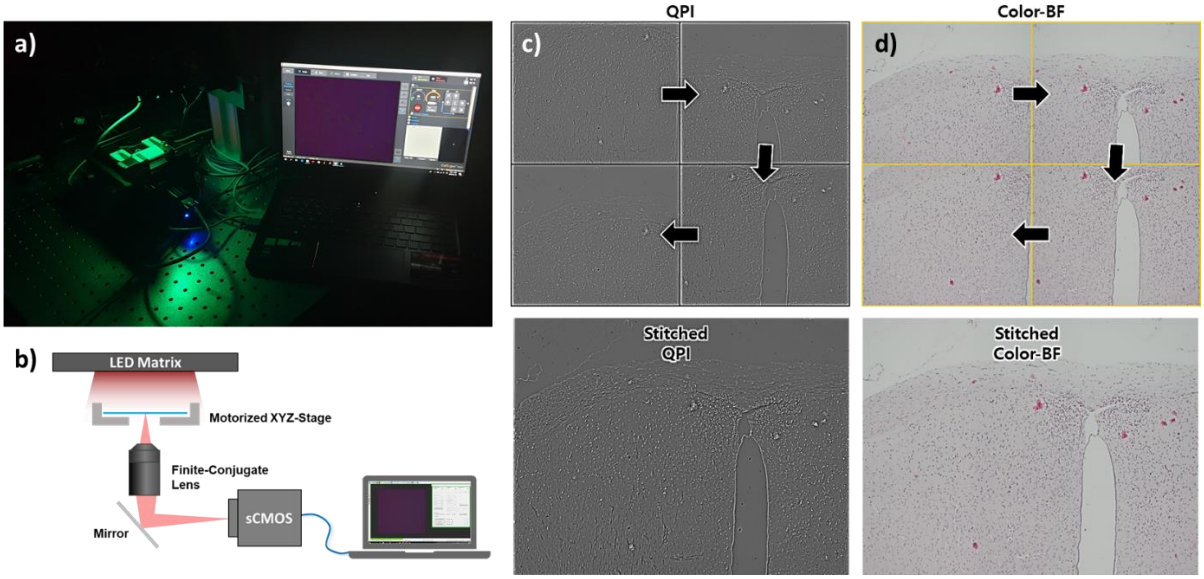

Figure 5.4 Development of portable high-throughput DPC-based QPI system. a) Real image of portable system connected to laptop. b) Simple schematic of proposed system. Reconstruction of large field-of-view (c) QPI and (d) color bright field image from a single platform.

In this thesis, QPI system was utilized for only fixed field-of-view. Since QPI system available to implement on simple conventional microscope system, the system could be transformed for high-throughput images using motorized stages. Large field-of-view QPI could be realized performing image processing method that stitches the QPI captured in different positions as stage moves as shown in Figure 5.4. This approach could be integrated with whole slide scanner and provide high-throughput QPI by just alternating the illumination source to LED matrix.

In chapter 4.2, in-silico staining approach using QPI system have shown great potentials to bypass staining process in digital pathology workflow. Although training the in-silico GAN framework took more than two days with our QPI image sets, in-silico staining using already trained network takes < 1 second for 100 x 100 image. This corresponds to ~7 minutes per whole field of view to virtually stain the QPI. With higher computational process device, it could shrink down less than ~3 minutes. This fast inference time means that our in-silico staining network can be also integrated with a QPI-based whole slide scanner and provide virtual slide image based on the label-free tissue imaging. If in-silico staining methods is strictly evaluated in clinic, we believe that this GAN integrated QPI whole slide scanner device would make paradigm shift in digital histopathology workflow.

ULSAN NATIONAL INSTITUTE OF SCIENCE AND TECHNOLOGY

Development of phase contrast optical projection tomography for small animal imaging

In biomedical fields, there are many imaging tools such as optical coherence tomography, confocal microscopy, ultrasound imaging, MRI, and CT that could provide cross-sectional images of the specimen [162, 163]. Among them optical projection tomography (OPT) has been introduced as promising optical instrument which allows to provide similar image of CT but in higher resolution [162]. OPT offers not only 2D cross sectional but 3D reconstructed images of specimen. Because OPT follows corresponding principle and light measuring method to CT reconstruction, most of OPT images are restricted to bright-field or fluorescence imaging. Therefore, totally transparent specimens are not appropriate to capture OPT images.

In this thesis, QPI demonstrated visualizing transparent specimens such as cells, and elegans by transforming the phase in intensity through illumination. It is very useful tool to image any kinds of transparent specimens. In addition, its simple implementation method may allow to integrate with other optical imaging modalities. Thus, we tested out to integrate the DPC-based QPI to conventional OPT system to provide new contrast which was not shown in other works. Since OPT uses visible ranged illumination, TFT liquid crystal display (LCD) was employed as programmable physical pattern and placed between illumination and specimen as shown in Figure 5.5. The illumination apparatus in this method follows similar concept shown in Chapter 2.2. Diffuser was utilized right after LCD pattern to provide partially coherent illumination in OPT system. At each angle, four images illuminated by four patterns were captured. This would allow to provide both bright field and phase contrast images for each angle as shown in Figure 5.6. After the OPT reconstruction, cross-sectional phase images could be obtained. Figure 5.6 illustrates that phase contrast cross-sectional image contains information which could not seen in bright field reconstructed cross-sectional images.

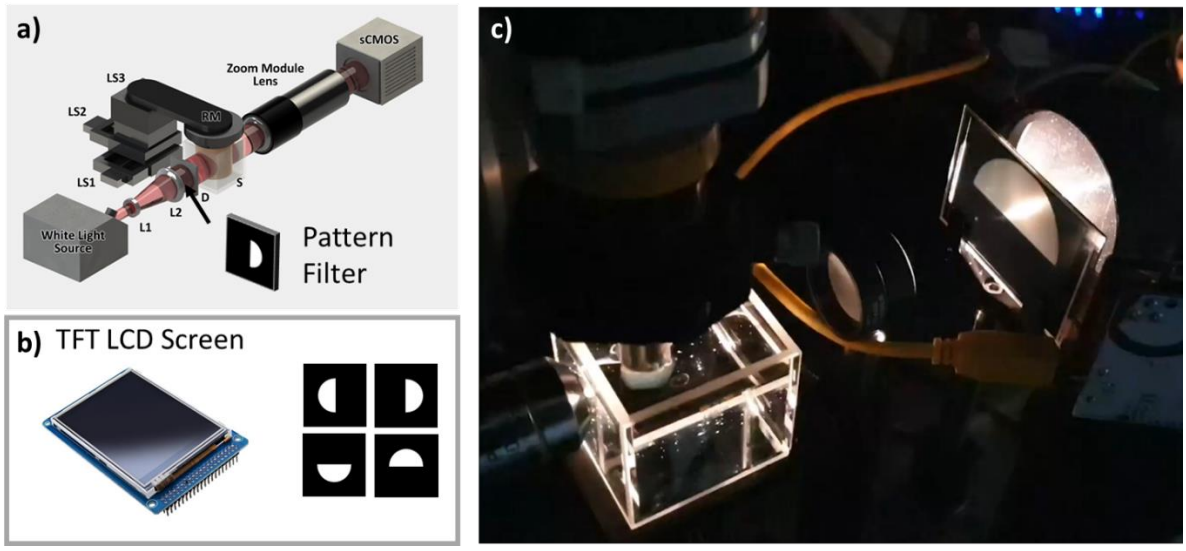

Figure 5.5 Development of phase contrast optical projection tomography. a) Schematic of phase contrast OPT, b) LCD for pattern filter, c) real image of the system.

ULSAN NATIONAL INSTITUTE OF SCIENCE AND TECHNOLOGY

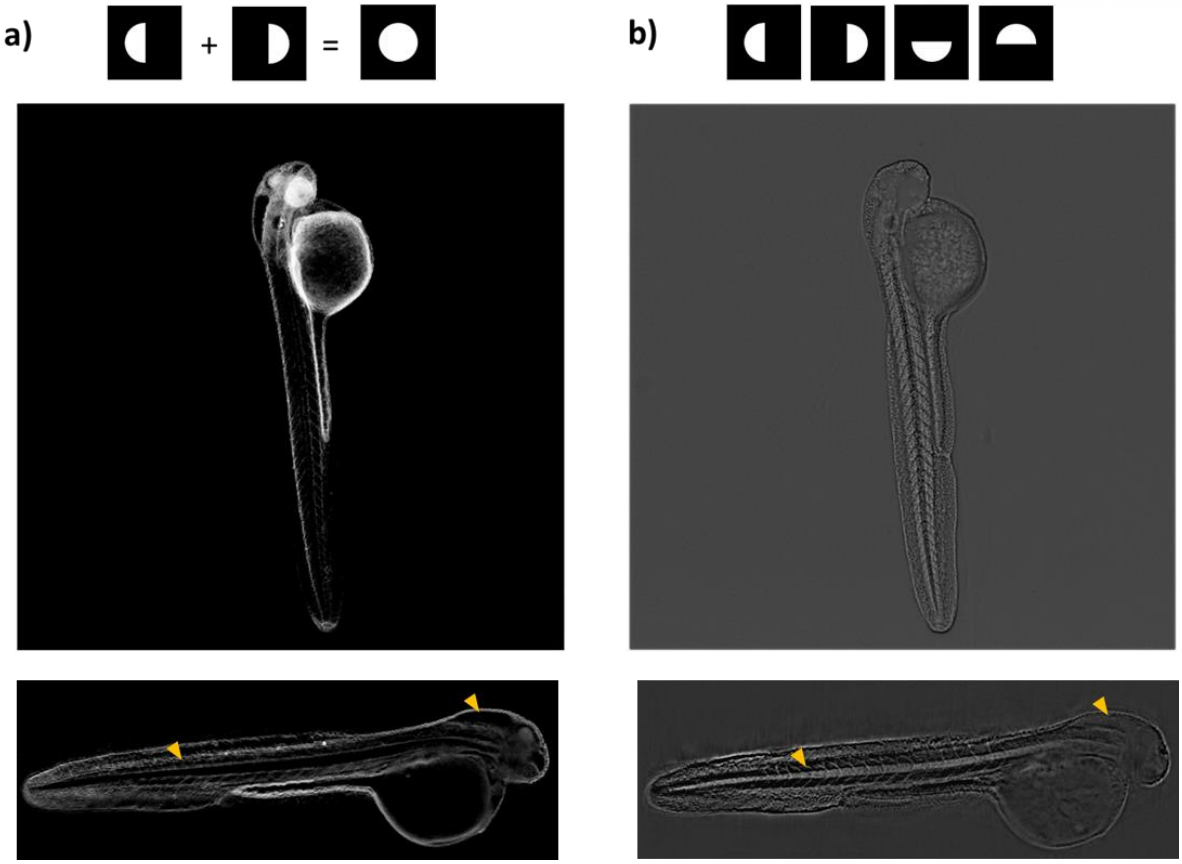

Figure 5.6 QPI reconstruction using LCD patterned illumination in OPT. a) Bright field, and phase contrast images are available in this OPT system.

References

1. Ghislieri, C., M. Molino, and C.G. Cortese, *Work and Organizational Psychology Looks at the Fourth Industrial Revolution: How to Support Workers and Organizations?* Frontiers in psychology, 2018. **9**: p. 2365-2365.
2. Schwab, K., *The Fourth Industrial Revolution*. 2017: Crown Publishing Group. 192.
3. Jee, Y.-S., *Exercise rehabilitation in the fourth industrial revolution.* Journal of exercise rehabilitation, 2017. **13**(3): p. 255-256.
4. Swabey, P. *Healthcare to benefit most from the Fourth Industrial Revolution, executives predict*. 2016 [cited 2019 11/28]; Available from: https://eiuperspectives.economist.com/technology-innovation/healthcare-benefit-most-fourth-industrial-revolution-executives-predict.
5. Coravos, A., et al., *Digital Medicine: A Primer on Measurement.* Digital Biomarkers, 2019. **3**(2): p. 31-71.
6. Elenko, E., L. Underwood, and D. Zohar, *Defining digital medicine.* Nature Biotechnology, 2015. **33**(5): p. 456-461.
7. Boppart, S.A. and R. Richards-Kortum, *Point-of-care and point-of-procedure optical imaging technologies for primary care and global health.* Science Translational Medicine, 2014. **6**(253): p. 253rv2.
8. Lee, J.Y. and J.Y. Lim, *The Prospect of the Fourth Industrial Revolution and Home Healthcare in Super-Aged Society.* Ann Geriatr Med Res, 2017. **21**(3): p. 95-100.
9. Litjens, G., et al., *A survey on deep learning in medical image analysis.* Medical Image Analysis, 2017. **42**: p. 60-88.
10. Aeffner, F., et al., *Introduction to Digital Image Analysis in Whole-slide Imaging: A White Paper from the Digital Pathology Association.* Journal of pathology informatics, 2019. **10**: p. 9-9.
11. Pantanowitz, L., et al., *Twenty Years of Digital Pathology: An Overview of the Road Travelled, What is on the Horizon, and the Emergence of Vendor-Neutral Archives.* Journal of pathology informatics, 2018. **9**: p. 40-40.
12. *Human Pathology Telepathology System Classification (2001) in Telemedicine and electronic medicine*. Halit Eren, John G. Webster ed. 2016, Boca Raton: CRC Press, Taylor & Francis Group.
13. Ho, J., et al., *Can digital pathology result in cost savings? A financial projection for digital pathology implementation at a large integrated health care organization.* Journal of pathology informatics, 2014. **5**(1): p. 33-33.
14. Intelligence, M., *Global Digital Pathology Market*. 2019, Mordor Intelligence: Hyderabad, IN.
15. Rivenson, Y., et al., *PhaseStain: the digital staining of label-free quantitative phase microscopy images using deep learning.* Light: Science & Applications, 2019. **8**(1): p. 23.
16. Rivenson, Y., et al., *Virtual histological staining of unlabelled tissue-autofluorescence images via deep learning.* Nature Biomedical Engineering, 2019. **3**(6): p. 466-477.
17. Ban, S., et al., *Effect of tissue staining in quantitative phase imaging.* Journal of Biophotonics, 2018. **11**(8): p. e201700402.
18. Dendere, R., N. Myburg, and T.S. Douglas, *A review of cellphone microscopy for disease detection.* Journal of Microscopy, 2015. **260**(3): p. 248-259.
19. Skandarajah, A., et al., *Quantitative Imaging with a Mobile Phone Microscope.* PLOS ONE, 2014. **9**(5): p. e96906.
20. *The Worldwide Market for Point-of-Care (POC) Testing (Infectious Disease Testing, POC Cancer Tests, Rapid Coagulation, Urine Testing, Lipid Tests, Pregnancy Testing, Glucose Testing and Other POC)*. Kalorama Information. p. 623.
21. Vashist, S.K., et al., *Cellphone-based devices for bioanalytical sciences.* Analytical and Bioanalytical Chemistry, 2014. **406**(14): p. 3263-3277.
22. Khan, H.N., D.A. Hounshell, and E.R.H. Fuchs, *Science and research policy at the end of Moore's law.* Nature Electronics, 2018. **1**(1): p. 14-21.
23. Fukushima, K., *Neocognitron: A self-organizing neural network model for a mechanism of*

ULSAN NATIONAL INSTITUTE OF SCIENCE AND TECHNOLOGY

pattern recognition unaffected by shift in position. Biological Cybernetics, 1980. **36**(4): p. 193-202.

24. Lo, S.B., et al., *Artificial convolution neural network techniques and applications for lung nodule detection.* IEEE Transactions on Medical Imaging, 1995. **14**(4): p. 711-718.
25. Krizhevsky, A., I. Sutskever, and G.E. Hinton, *ImageNet classification with deep convolutional neural networks*, in *Proceedings of the 25th International Conference on Neural Information Processing Systems - Volume 1*. 2012, Curran Associates Inc.: Lake Tahoe, Nevada. p. 1097-1105.
26. Campanella, G., et al., *Clinical-grade computational pathology using weakly supervised deep learning on whole slide images.* Nature Medicine, 2019. **25**(8): p. 1301-1309.
27. Ronneberger, O., P. Fischer, and T. Brox. *U-Net: Convolutional Networks for Biomedical Image Segmentation*. in *Medical Image Computing and Computer-Assisted Intervention – MICCAI 2015*. 2015. Cham: Springer International Publishing.
28. BenTaieb, A., J. Kawahara, and G. Hamarneh. *Multi-loss convolutional networks for gland analysis in microscopy*. in *2016 IEEE 13th International Symposium on Biomedical Imaging (ISBI)*. 2016.
29. Song, Y., et al., *Accurate Cervical Cell Segmentation from Overlapping Clumps in Pap Smear Images.* IEEE Transactions on Medical Imaging, 2017. **36**(1): p. 288-300.
30. Han, X.-H., J. Lei, and Y.-W. Chen. *HEp-2 Cell Classification Using K-Support Spatial Pooling in Deep CNNs*. in *Deep Learning and Data Labeling for Medical Applications*. 2016. Cham: Springer International Publishing.
31. Xu, Z. and J. Huang. *Detecting 10,000 Cells in One Second*. in *Medical Image Computing and Computer-Assisted Intervention – MICCAI 2016*. 2016. Cham: Springer International Publishing.
32. Goodfellow, I.J., et al. *Generative Adversarial Networks*. arXiv e-prints, 2014.
33. Wang, H., et al., *Deep learning enables cross-modality super-resolution in fluorescence microscopy.* Nature Methods, 2019. **16**(1): p. 103-110.
34. Weigert, M., et al., *Content-aware image restoration: pushing the limits of fluorescence microscopy.* Nature Methods, 2018. **15**(12): p. 1090-1097.
35. Ouyang, W., et al., *Deep learning massively accelerates super-resolution localization microscopy.* Nature Biotechnology, 2018. **36**(5): p. 460-468.
36. Chen, X., B. Zheng, and H. Liu, *Optical and digital microscopic imaging techniques and applications in pathology.* Analytical cellular pathology (Amsterdam), 2011. **34**(1-2): p. 5-18.
37. Lee, D., et al., *Color-coded LED microscopy for multi-contrast and quantitative phase-gradient imaging.* Biomedical optics express, 2015. **6**(12): p. 4912-4922.
38. Fan, Y., et al., *Wide-field anti-aliased quantitative differential phase contrast microscopy.* Optics Express, 2018. **26**(19): p. 25129-25146.
39. Liu, Z., et al., *Real-time brightfield, darkfield, and phase contrast imaging in a light-emitting diode array microscope.* Journal of Biomedical Optics, 2014. **19**(10): p. 1-5, 5.
40. Tian, L. and L. Waller, *Quantitative differential phase contrast imaging in an LED array microscope.* Optics Express, 2015. **23**(9): p. 11394-11403.
41. Hamilton, D. and C. Sheppard, *Differential phase contrast in scanning optical microscopy.* Journal of Microscopy, 1984. **133**: p. 27-39.
42. Mehta, S.B. and C.J.R. Sheppard, *Quantitative phase-gradient imaging at high resolution with asymmetric illumination-based differential phase contrast.* Optics Letters, 2009. **34**(13): p. 1924-1926.
43. Jung, D., et al., *Smartphone-based multi-contrast microscope using color-multiplexed illumination.* Scientific Reports, 2017. **7**(1): p. 7564.
44. Kemper, B. and G. von Bally, *Digital holographic microscopy for live cell applications and technical inspection.* Applied Optics, 2008. **47**(4): p. A52-A61.
45. Mann, C.J., et al., *High-resolution quantitative phase-contrast microscopy by digital holography.* Optics Express, 2005. **13**(22): p. 8693-8698.
46. Marquet, P., et al., *Digital holographic microscopy: a noninvasive contrast imaging technique*

ULSAN NATIONAL INSTITUTE OF SCIENCE AND TECHNOLOGY

allowing quantitative visualization of living cells with subwavelength axial accuracy. Optics Letters, 2005. **30**(5): p. 468-470.

47. Jingshan, Z., et al., *Transport of Intensity phase imaging by intensity spectrum fitting of exponentially spaced defocus planes.* Optics Express, 2014. **22**(9): p. 10661-10674.
48. Petruccelli, J.C., L. Tian, and G. Barbastathis, *The transport of intensity equation for optical path length recovery using partially coherent illumination.* Optics Express, 2013. **21**(12): p. 14430-14441.
49. Zuo, C., et al., *Transport-of-intensity phase imaging using Savitzky-Golay differentiation filter - theory and applications.* Optics Express, 2013. **21**(5): p. 5346-5362.
50. Ou, X., et al., *Quantitative phase imaging via Fourier ptychographic microscopy.* Optics Letters, 2013. **38**(22): p. 4845-4848.
51. Sun, J., et al., *Resolution-enhanced Fourier ptychographic microscopy based on high-numerical-aperture illuminations.* Scientific Reports, 2017. **7**(1): p. 1187.
52. Tian, L., et al., *Multiplexed coded illumination for Fourier Ptychography with an LED array microscope.* Biomedical Optics Express, 2014. **5**(7): p. 2376-2389.
53. Chen, M., Z.F. Phillips, and L. Waller, *Quantitative differential phase contrast (DPC) microscopy with computational aberration correction.* Optics Express, 2018. **26**(25): p. 32888-32899.
54. Fan, Y., et al., *Optimal illumination scheme for isotropic quantitative differential phase contrast microscopy.* Photonics Research, 2019. **7**(8): p. 890-904.
55. Vulović, M., et al., *When to use the projection assumption and the weak-phase object approximation in phase contrast cryo-EM.* Ultramicroscopy, 2014. **136**: p. 61-66.
56. Chen, H.-H., Y.-Z. Lin, and Y. Luo, *Isotropic differential phase contrast microscopy for quantitative phase bio-imaging.* Journal of Biophotonics, 2018. **11**(8): p. e201700364.
57. Lin, Y.-Z., K.-Y. Huang, and Y. Luo, *Quantitative differential phase contrast imaging at high resolution with radially asymmetric illumination.* Optics Letters, 2018. **43**(12): p. 2973-2976.
58. Lu, L., et al., *Quantitative Phase Imaging Camera With a Weak Diffuser.* Frontiers in Physics, 2019. **7**(77).
59. Zuo, C., et al., *High-resolution transport-of-intensity quantitative phase microscopy with annular illumination.* Scientific Reports, 2017. **7**(1): p. 7654.
60. Lee, W., et al., *Single-exposure quantitative phase imaging in color-coded LED microscopy.* Optics Express, 2017. **25**(7): p. 8398-8411.
61. Guo, K., et al., *Microscopy illumination engineering using a low-cost liquid crystal display.* Biomedical optics express, 2015. **6**(2): p. 574-579.
62. Wu, J., et al., *Coded aperture pair for quantitative phase imaging.* Optics Letters, 2014. **39**(19): p. 5776-5779.
63. Min, E., et al., *Measurement of multispectral scattering properties in mouse brain tissue.* Biomedical Optics Express, 2017. **8**: p. 1763.
64. Farrokhi, H., et al., *High-brightness laser imaging with tunable speckle reduction enabled by electroactive micro-optic diffusers.* Scientific Reports, 2017. **7**(1): p. 15318.
65. Redding, B., M.A. Choma, and H. Cao. *Speckle free laser imaging*. in *2012 Conference on Lasers and Electro-Optics (CLEO)*. 2012.
66. Albregtsen, F., *Statistical Texture Measures Computed from Gray Level Coocurrence Matrices.* Image Processing Laboratory, Department of Informatics, University of Oslo, 2008. **20**: p. 14.
67. Haralick, R.M., K. Shanmugam, and I. Dinstein, *Textural Features for Image Classification.* IEEE Transactions on Systems, Man, and Cybernetics, 1973. **SMC-3**(6): p. 610-621.
68. Zachary F. Phillips, M.C., *Technical Report: Benchmark Technologies Quantitative Phase Targ*. Benchmark Technology.
69. Sun, J., et al., *Refractive index measurement of acute rat brain tissue slices using optical coherence tomography.* Optics express, 2012. **20**(2): p. 1084-1095.
70. Davila, R.E., et al., *ASGE guideline: the role of endoscopy in the diagnosis, staging, and management of colorectal cancer.* Gastrointestinal Endoscopy, 2005. **61**(1): p. 1-7.
71. Morgenthal, C.B., et al., *The role of the surgeon in the evolution of flexible endoscopy.* Surgical

ULSAN NATIONAL INSTITUTE OF SCIENCE AND TECHNOLOGY

Endoscopy, 2007. **21**(6): p. 838-853.
72. Shah, J., *Endoscopy through the ages.* BJU International, 2002. **89**(7): p. 645-652.
73. Breslauer, D.N., et al., *Mobile Phone Based Clinical Microscopy for Global Health Applications.* PLOS ONE, 2009. **4**(7): p. e6320.
74. Fried, M.P., S.R. Parikh, and B. Sadoughi, *Image-Guidance for Endoscopic Sinus Surgery.* The Laryngoscope, 2008. **118**(7): p. 1287-1292.
75. Perneczky, A. and G. Fries, *Endoscope-assisted Brain Surgery: Part 1—Evolution, Basic Concept, and Current Technique.* Neurosurgery, 1998. **42**(2): p. 219-224.
76. Sohn, W., et al., *Endockscope: Using Mobile Technology to Create Global Point of Service Endoscopy.* Journal of Endourology, 2013. **27**(9): p. 1154-1160.
77. Shimizu, S., et al., *Remote transmission of live endoscopy over the Internet: Report from the 87th Congress of the Japan Gastroenterological Endoscopy Society.* Digestive Endoscopy, 2016. **28**(1): p. 92-97.
78. Wildi, S.M., et al., *Tele-endoscopy: a way to provide diagnostic quality for remote populations.* Gastrointestinal Endoscopy, 2004. **59**(1): p. 38-43.
79. Agu, E., et al. *The smartphone as a medical device: Assessing enablers, benefits and challenges*. in *2013 IEEE International Conference on Sensing, Communications and Networking (SECON)*. 2013.
80. Lee, Y.-G., W.S. Jeong, and G. Yoon, *Smartphone-Based Mobile Health Monitoring.* Telemedicine and e-Health, 2012. **18**(8): p. 585-590.
81. Navruz, I., et al., *Smart-phone based computational microscopy using multi-frame contact imaging on a fiber-optic array.* Lab on a Chip, 2013. **13**(20): p. 4015-4023.
82. Oresko, J.J., et al., *A Wearable Smartphone-Based Platform for Real-Time Cardiovascular Disease Detection Via Electrocardiogram Processing.* IEEE Transactions on Information Technology in Biomedicine, 2010. **14**(3): p. 734-740.
83. Pamplona, V.F., et al., *NETRA: interactive display for estimating refractive errors and focal range.* ACM Trans. Graph., 2010. **29**(4): p. 1-8.
84. Wojtczak, J. and P. Bonadonna, *Pocket mobile smartphone system for the point-of-care submandibular ultrasonography.* The American Journal of Emergency Medicine, 2013. **31**(3): p. 573-577.
85. Worringham, C., A. Rojek, and I. Stewart, *Development and Feasibility of a Smartphone, ECG and GPS Based System for Remotely Monitoring Exercise in Cardiac Rehabilitation.* PLOS ONE, 2011. **6**(2): p. e14669.
86. Xu, X., et al., *Advances in Smartphone-Based Point-of-Care Diagnostics.* Proceedings of the IEEE, 2015. **103**(2): p. 236-247.
87. Wu, C.-J., et al., *An Innovative Smartphone-Based Otorhinoendoscope and Its Application in Mobile Health and Teleotolaryngology.* J Med Internet Res, 2014. **16**(3): p. e71.
88. Koesveld, J.J.M., G.W.M. Tetteroo, and E.J.R. Graaf, *Use of head-mounted display in transanal endoscopic microsurgery.* Surgical Endoscopy And Other Interventional Techniques, 2003. **17**(6): p. 943-946.
89. Maithel, S.K., et al., *Simulated laparoscopy using a head-mounted display vs traditional video monitor: an assessment of performance and muscle fatigue.* Surgical Endoscopy And Other Interventional Techniques, 2005. **19**(3): p. 406-411.
90. Morisawa, T., et al., *Endoscopic Submucosal Dissection Using Head-mounted Display.* Gastroenterology, 2015. **149**(2): p. 290-291.e1.
91. van Lindert, E.J., J.A. Grotenhuis, and T. Beems, *The use of a head-mounted display for visualization in neuroendoscopy.* Computer Aided Surgery, 2004. **9**(6): p. 251-256.
92. Shin, D., et al., *A Fiber-Optic Fluorescence Microscope Using a Consumer-Grade Digital Camera for In Vivo Cellular Imaging.* PLOS ONE, 2010. **5**(6): p. e11218.
93. Roda, A., et al., *Smartphone-based biosensors: A critical review and perspectives.* TrAC Trends in Analytical Chemistry, 2016. **79**: p. 317-325.
94. Vashist, K.S., M.E. Schneider, and H.T.J. Luong, *Commercial Smartphone-Based Devices and Smart Applications for Personalized Healthcare Monitoring and Management.* Diagnostics,

2014. **4**(3).
95. Vashist, S.K., et al., *Emerging Technologies for Next-Generation Point-of-Care Testing.* Trends in Biotechnology, 2015. **33**(11): p. 692-705.
96. He, L., X. Ming, and Q. Liu, *A Medical Application Integrating Remote 3D Visualization Tools to Access Picture Archiving and Communication System on Mobile Devices.* Journal of Medical Systems, 2014. **38**(4): p. 44.
97. Jeong, C.-W., et al., *The development of a medical image information system environment using data synchronization based on cloud computing.* Multimedia Tools and Applications, 2016. **75**(23): p. 15479-15492.
98. Parikh, A. and N. Mehta, *PACS on mobile devices*. SPIE Medical Imaging. Vol. 9418. 2015: SPIE.
99. Jung, M., O. Niculita, and Z. Skaf, *Comparison of Different Classification Algorithms for Fault Detection and Fault Isolation in Complex Systems.* Procedia Manufacturing, 2018. **19**: p. 111-118.
100. Yang, Y.J. and C.S. Bang, *Application of artificial intelligence in gastroenterology.* World journal of gastroenterology, 2019. **25**(14): p. 1666-1683.
101. Rawat, W. and Z. Wang, *Deep Convolutional Neural Networks for Image Classification: A Comprehensive Review.* Neural Computation, 2017. **29**(9): p. 2352-2449.
102. Razzak, M.I., S. Naz, and A. Zaib, *Deep Learning for Medical Image Processing: Overview, Challenges and the Future*, in *Classification in BioApps: Automation of Decision Making*, N. Dey, A.S. Ashour, and S. Borra, Editors. 2018, Springer International Publishing: Cham. p. 323-350.
103. Hu, L.-Y., et al., *The distance function effect on k-nearest neighbor classification for medical datasets.* SpringerPlus, 2016. **5**(1): p. 1304-1304.
104. Smola, A.J. and B. Schölkopf, *A tutorial on support vector regression.* Statistics and Computing, 2004. **14**(3): p. 199-222.
105. *Support-vector machine*. Available from: https://en.wikipedia.org/wiki/Support-vector_machine.
106. Russakovsky, O., et al., *ImageNet Large Scale Visual Recognition Challenge.* International Journal of Computer Vision, 2015. **115**(3): p. 211-252.
107. Jo, Y., et al., *Quantitative Phase Imaging and Artificial Intelligence: A Review.* IEEE Journal of Selected Topics in Quantum Electronics, 2019. **25**(1): p. 1-14.
108. Nguyen, T., et al., *Deep learning approach for Fourier ptychography microscopy.* Optics Express, 2018. **26**(20): p. 26470-26484.
109. Sinha, A., et al., *Lensless computational imaging through deep learning.* Optica, 2017. **4**(9): p. 1117-1125.
110. Chatterjee, S., *Artefacts in histopathology.* Journal of oral and maxillofacial pathology : JOMFP, 2014. **18**(Suppl 1): p. S111-S116.
111. Goodfellow, I.J., et al., *Generative adversarial nets*, in *Proceedings of the 27th International Conference on Neural Information Processing Systems - Volume 2*. 2014, MIT Press: Montreal, Canada. p. 2672-2680.
112. Torr, P.H.S. and A. Zisserman, *MLESAC: A New Robust Estimator with Application to Estimating Image Geometry.* Comput. Vis. Image Underst., 2000. **78**(1): p. 138-156.
113. Ledig, C., et al. *Photo-Realistic Single Image Super-Resolution Using a Generative Adversarial Network*. in *2017 IEEE Conference on Computer Vision and Pattern Recognition (CVPR)*. 2017.
114. Simonyan, K. and A. Zisserman, *Very Deep Convolutional Networks for Large-Scale Image Recognition.* arXiv 1409.1556, 2014.
115. Kingma, D. and J. Ba, *Adam: A Method for Stochastic Optimization.* International Conference on Learning Representations, 2014.
116. Wang, Z., H. Ding, and G. Popescu, *Scattering-phase theorem.* Optics Letters, 2011. **36**(7): p. 1215-1217.
117. *Staining-Histology/Cytology*. [cited 2019 November 3]; Available from: https://www.polysciences.com/german/catalog-products/life-sciences/histology-

ULSAN NATIONAL INSTITUTE OF SCIENCE AND TECHNOLOGY

microscopy/staining-histology-cytology.
118. Shorten, C. and T.M. Khoshgoftaar, *A survey on Image Data Augmentation for Deep Learning.* Journal of Big Data, 2019. **6**(1): p. 60.
119. Bray, F., et al., *Global cancer statistics 2018: GLOBOCAN estimates of incidence and mortality worldwide for 36 cancers in 185 countries.* CA: A Cancer Journal for Clinicians, 2018. **68**(6): p. 394-424.
120. Cohen, P.A., et al., *Cervical cancer.* The Lancet, 2019. **393**(10167): p. 169-182.
121. Drummond, J.L., et al., *Cervical cancer data and data systems in limited-resource settings: Challenges and opportunities.* International journal of gynaecology and obstetrics: the official organ of the International Federation of Gynaecology and Obstetrics, 2017. **138 Suppl 1**: p. 33-40.
122. Huy, N.V.Q., et al. *The value of visual inspection with acetic acid and Pap smear in cervical cancer screening program in low resource settings - A population-based study.* Gynecologic oncology reports, 2018. **24**, 18-20 DOI: 10.1016/j.gore.2018.02.004.
123. Denny, L., M. Quinn, and R. Sankaranarayanan, *Chapter 8: Screening for cervical cancer in developing countries.* Vaccine, 2006. **24 Suppl 3**: p. S3/71-7.
124. World Health, O. and O. Pan American Health, *Monitoring national cervical cancer prevention and control programmes: quality control and quality assurance for visual inspection with acetic acid (VIA)-based programmes*. 2013, Geneva: World Health Organization.
125. Raifu, A.O., et al., *Determinants of Cervical Cancer Screening Accuracy for Visual Inspection with Acetic Acid (VIA) and Lugol's Iodine (VILI) Performed by Nurse and Physician.* PLOS ONE, 2017. **12**(1): p. e0170631.
126. Wright, T.C., *Chapter 10: Cervical cancer screening using visualization techniques.* Journal of the National Cancer Institute. Monographs, 2003(31): p. 66-71.
127. Nam, K., et al., *The performance of tele-cervicography for detection of preinvasive and invasive disease of the uterine cervix as an adjunctive test to Pap smears.* Contemporary oncology (Poznan, Poland), 2016. **20**(5): p. 402-406.
128. Firnhaber, C., et al., *Evaluation of a cervicography-based program to ensure quality of visual inspection of the cervix in HIV-infected women in Johannesburg, South Africa.* Journal of lower genital tract disease, 2015. **19**(1): p. 7-11.
129. Chen, Z.-P., H.-M. Chen, and T.-T. Lee, *Use of Compact Digital Cervicography: An Adjuvant Screening Tool for Precancerous Cervical Lesions.* Taiwanese Journal of Obstetrics and Gynecology, 2008. **47**(2): p. 187-191.
130. Bomfim-Hyppólito, S., et al., *Cervicography as an adjunctive test to visual inspection with acetic acid in cervical cancer detection screening.* International Journal of Gynecology & Obstetrics, 2006. **92**(1): p. 58-63.
131. Urner, E., et al. *A Smartphone-Based Approach for Triage of Human Papillomavirus-Positive Sub-Saharan African Women: A Prospective Study*. JMIR mHealth and uHealth, 2017. **5**, e72 DOI: 10.2196/mhealth.6697.
132. Tran, P.L., et al., *PERFORMANCE OF SMARTPHONE-BASED DIGITAL IMAGES FOR CERVICAL CANCER SCREENING IN A LOW-RESOURCE CONTEXT.* International journal of technology assessment in health care, 2018. **34**(3): p. 337-342.
133. Ricard-Gauthier, D., et al., *Use of Smartphones as Adjuvant Tools for Cervical Cancer Screening in Low-Resource Settings.* Journal of lower genital tract disease, 2015. **19**(4): p. 295-300.
134. Quinley, K.E., et al., *Use of mobile telemedicine for cervical cancer screening.* Journal of telemedicine and telecare, 2011. **17**(4): p. 203-209.
135. Catarino, R., et al. *Smartphone Use for Cervical Cancer Screening in Low-Resource Countries: A Pilot Study Conducted in Madagascar*. PloS one, 2015. **10**, e0134309 DOI: 10.1371/journal.pone.0134309.
136. Bagga, R., et al., *Feasibility of Using Mobile Smartphone Camera as an Imaging Device for Screening of Cervical Cancer in a Low-resource Setting.* Journal of Postgraduate Medicine Education and Research, 2016. **50**: p. 69-74.

ULSAN NATIONAL INSTITUTE OF SCIENCE AND TECHNOLOGY

137. Asgary, R., et al., *mHealth to Train Community Health Nurses in Visual Inspection With Acetic Acid for Cervical Cancer Screening in Ghana.* Journal of lower genital tract disease, 2016. **20**(3): p. 239-242.
138. Liu, J., et al., *Point-of-care testing based on smartphone: The current state-of-the-art (2017–2018).* Biosensors and Bioelectronics, 2019. **132**: p. 17-37.
139. Im, H., et al., *Digital diffraction analysis enables low-cost molecular diagnostics on a smartphone.* Proceedings of the National Academy of Sciences of the United States of America, 2015. **112**(18): p. 5613-5618.
140. Grant, B.D., et al., *A mobile-phone based high-resolution microendoscope to image cervical precancer.* PLOS ONE, 2019. **14**(2): p. e0211045.
141. Bae, J.K., et al., *Smartphone-Based Endoscope System for Advanced Point-of-Care Diagnostics: Feasibility Study.* JMIR Mhealth Uhealth, 2017. **5**(7): p. e99.
142. Park, S.Y., et al., *Automated image analysis of digital colposcopy for the detection of cervical neoplasia.* Journal of Biomedical Optics, 2008. **13**(1): p. 1-10, 10.
143. Liu, J., Y. Peng, and Y. Zhang, *A Fuzzy Reasoning Model for Cervical Intraepithelial Neoplasia Classification Using Temporal Grayscale Change and Textures of Cervical Images During Acetic Acid Tests.* IEEE Access, 2019. **PP**: p. 1-1.
144. Li, W., et al. *Computer-Aided Diagnosis (CAD) for Cervical Cancer Screening and Diagnosis: A New System Design in Medical Image Processing*. in *Computer Vision for Biomedical Image Applications*. 2005. Berlin, Heidelberg: Springer Berlin Heidelberg.
145. Fernandes, K., J.S. Cardoso, and J. Fernandes, *Automated Methods for the Decision Support of Cervical Cancer Screening Using Digital Colposcopies.* IEEE Access, 2018. **6**: p. 33910-33927.
146. Asiedu, M.N., et al., *Development of Algorithms for Automated Detection of Cervical Pre-Cancers With a Low-Cost, Point-of-Care, Pocket Colposcope.* IEEE Transactions on Biomedical Engineering, 2019. **66**(8): p. 2306-2318.
147. Ohri, N., et al., *An update on intraoral application of colposcopy.* Journal of oral and maxillofacial pathology : JOMFP, 2014. **18**(3): p. 403-410.
148. Sankaranarayanan, R. and R. Wesley, *A Practical Manual on Visual Screening for Cervical Neoplasia.* 2003. **41**.
149. Selvarajah, S. and S. Kodituwakku, *Analysis and Comparison of Texture Features for Content Based Image Retrieval.* 2011. **108**: p. 2045-5364.
150. Albregtsen, F., *Statistical Texture Measures Computed from Gray Level Coocurrence Matrices.* Image Processing Laboratory, Department of Informatics, 1995.
151. Mueller, J.L., et al., *International Image Concordance Study to Compare a Point-of-Care Tampon Colposcope With a Standard-of-Care Colposcope.* Journal of lower genital tract disease, 2017. **21**(2): p. 112-119.
152. Lam, C.T., et al. *An integrated strategy for improving contrast, durability, and portability of a Pocket Colposcope for cervical cancer screening and diagnosis*. PloS one, 2018. **13**, e0192530 DOI: 10.1371/journal.pone.0192530.
153. Vizet, J., et al., *In vivo imaging of uterine cervix with a Mueller polarimetric colposcope.* Scientific Reports, 2017. **7**(1): p. 2471.
154. Meena, B.L., et al., *Intrinsic fluorescence for cervical precancer detection using polarized light based in-house fabricated portable device.* Journal of biomedical optics, 2018. **23**(1): p. 1-7.
155. Taufiq, M.A., et al. *m-Skin Doctor: A Mobile Enabled System for Early Melanoma Skin Cancer Detection Using Support Vector Machine*. in *eHealth 360°*. 2017. Cham: Springer International Publishing.
156. Ramlakhan, K. and Y. Shang. *A Mobile Automated Skin Lesion Classification System*. in *2011 IEEE 23rd International Conference on Tools with Artificial Intelligence*. 2011.
157. Kim, H., et al., *Colorimetric analysis of saliva–alcohol test strips by smartphone-based instruments using machine-learning algorithms.* Applied Optics, 2017. **56**(1): p. 84-92.
158. Ech-Cherif, A., M. Misbhauddin, and M. Ech-Cherif. *Deep Neural Network Based Mobile Dermoscopy Application for Triaging Skin Cancer Detection*. in *2019 2nd International Conference on Computer Applications & Information Security (ICCAIS)*. 2019.

ULSAN NATIONAL INSTITUTE OF SCIENCE AND TECHNOLOGY

159. Switz, N.A., M.V. D'Ambrosio, and D.A. Fletcher, *Low-Cost Mobile Phone Microscopy with a Reversed Mobile Phone Camera Lens.* PLOS ONE, 2014. **9**(5): p. e95330.
160. Phillips, Z.F., et al., *Multi-Contrast Imaging and Digital Refocusing on a Mobile Microscope with a Domed LED Array.* PLOS ONE, 2015. **10**(5): p. e0124938.
161. Athanassiadou, P., et al., *Correlations between nuclear/cytoplasmic area ratio and classification of cervical smears.* Journal of experimental & clinical cancer research : CR, 2001. **20**: p. 481-6.
162. Ban, S., et al., *Label-free optical projection tomography for quantitative three-dimensional anatomy of mouse embryo.* Journal of Biophotonics, 2019. **12**(7): p. e201800481.
163. Cho, N.H., et al., *Development of SD-OCT for Imaging the in vivo Human Tympanic Membrane.* Journal of the Optical Society of Korea, 2011. **15**: p. 74-77.